High-Energy Astrophysics: Multi-Satellite Observations of X-ray Binaries

Dissertation
der Mathematisch-Naturwissenschaftlichen Fakultät
der Eberhard Karls Universität Tübingen
zur Erlangung des Grades eines
Doktors der Naturwissenschaften
(Dr. rer. nat.)

vorgelegt von
Xiaohang Dai
aus Jilin, China

Tübingen
2025

Gedruckt mit Genehmigung der Mathematisch-Naturwissenschaftlichen Fakultät der Eberhard Karls Universität Tübingen.

Tag der mündlichen Qualifikation:	05.05.2025
Dekan:	Prof. Dr. Thilo Stehle
1. Berichterstatter:	Prof. Dott. Andrea Santangelo
2. Berichterstatter:	Prof. Chen Yupeng

Ich erkläre, dass ich die zur Promotion eingereichte Arbeit mit dem Titel "Hochenergie-Astrophysik: Multi-Satelliten-Beobachtungen von Röntgendoppelsternen" selbstständig verfasst, nur die angegebenen Quellen und Hilfsmittel benutzt und wörtlich oder inhaltlich übernommene Stellen als solche gekennzeichnet habe. Ich versichere an Eides statt, dass diese Angaben wahr sind und dass ich nichts verschwiegen habe. Mir ist bekannt, dass die falsche Abgabe einer Versicherung an Eides statt mit Freiheitsstrafe bis zu drei Jahren oder mit Geldstrafe bestraft wird.

Ort/Place, Datum/Date

Unterschrift/Signature

Abstract

X-ray binaries, consisting of a compact object (either a black hole or a neutron star) accreting matter from a companion star, are among the most luminous sources of high-energy radiation in the universe. These systems serve as natural laboratories for studying fundamental physics under extreme conditions, including strong gravitational fields, rapid rotation, and intense magnetic fields. Despite decades of study, critical questions remain unanswered regarding the accretion processes, variability mechanisms, and the interplay between accretion and outflows in X-ray binaries. This thesis addresses these challenges by investigating the spectral and timing properties of X-ray binaries through multi-satellite observations and advanced data analysis techniques. The content includes several published articles (see the Appendix).

The first chapter introduces the motivation and significance of the study, highlighting key challenges in high-energy astrophysics. It begins with an overview of X-ray binaries, emphasizing their unique characteristics and astrophysical relevance. Historical developments in X-ray astronomy, from the discovery of Sco X-1 to the contributions of modern observatories such as eROSITA, NICER, NuSTAR, XMM-Newton, and Insight-HXMT, are discussed. Additionally, the study's novel contributions are outlined, particularly the application of advanced time-domain analysis methods and the integration of multi-mission data to achieve comprehensive insights.

The second chapter establishes the theoretical and observational foundations of X-ray binary research. This includes a detailed explanation of essential concepts such as accretion physics, quasi-periodic oscillations (QPOs), spectral state transitions, and spin dynamics, which are critical for understanding the physical mechanisms governing X-ray binaries. The chapter also summarizes unresolved scientific questions, such as the physical origins of QPOs, the role of magnetic fields in accretion processes, and the coupling between spectral state transitions and relativistic jets.

The methodological framework and data sources are presented in a dedicated chapter. This study employs multi-satellite observations to analyze the spectral and timing properties of X-ray binaries across a broad energy range. The contributions of each observatory are detailed: eROSITA's wide-field surveys reveal variability patterns in transient X-ray sources, NICER's high temporal resolution facilitates precise timing analysis, NuSTAR provides critical insights into high-energy spectral components, XMM-Newton delivers high-resolution spectroscopy of accretion disks, and Insight-HXMT contributes to the study of transient phenomena and hard X-ray emissions.

The results are divided into two main sections, focusing on black hole and neutron star X-ray binaries, respectively. For black hole systems, the findings highlight significant spectral and temporal variability, with key phenomena such as state transitions and disk wind launching explored in detail. Spectral analyses reveal correlations between changes in disk structure and relativistic outflows, while timing analyses of

QPOs provide insights into accretion dynamics near the event horizon. These results contribute to a deeper understanding of accretion-ejection coupling and the feedback processes associated with black hole growth and galaxy evolution.

For neutron star systems, the study investigates spin evolution and variability patterns. High-resolution timing data uncover complex pulsation profiles and anti-glitch phenomena, offering new perspectives on magnetospheric accretion and dense matter physics.

This thesis also highlights the limitations of current observational and analytical methods, such as the challenges posed by faint signals and incomplete temporal coverage. It identifies opportunities for future research, including the integration of multi-wavelength and multi-messenger data to further explore compact object dynamics.

In conclusion, this thesis advances the understanding of X-ray binaries by providing a comprehensive analysis of their spectral and timing properties through multi-mission observations. The findings contribute to a deeper understanding of accretion processes, and variability mechanisms in X-ray binaries, addressing critical gaps in current knowledge. Furthermore, the study establishes a foundation for future research aimed at bridging observational and theoretical aspects of high-energy astrophysics, ultimately enhancing our understanding of the universe's most extreme environments.

Zusammenfassung

Röntgendoppelsterne, die aus einem kompakten Objekt (entweder einem Schwarzen Loch oder einem Neutronenstern) bestehen, das Materie von einem Begleitstern akkreditiert, gehören zu den leuchtstärksten Quellen hochenergetischer Strahlung im Universum. Diese Systeme dienen als natürliche Labore zur Untersuchung grundlegender physikalischer Prozesse unter extremen Bedingungen, einschließlich starker Gravitationsfelder, schneller Rotation und intensiver Magnetfelder. Trotz jahrzehntelanger Forschung bleiben zentrale Fragen zu Akkretionsprozessen, Variabilitätsmechanismen und der Wechselwirkung zwischen Akkretion und Ausflüssen in Röntgendoppelsternen unbeantwortet. Diese Dissertation widmet sich diesen Herausforderungen, indem sie die spektralen und zeitlichen Eigenschaften von Röntgendoppelsternen mithilfe von Multisatellitenbeobachtungen und fortschrittlichen Datenanalysetechniken untersucht. Der Inhalt umfasst mehrere veröffentlichte Artikel (siehe Anhang).

Das erste Kapitel führt in die Motivation und Bedeutung dieser Studie ein und beleuchtet zentrale Herausforderungen der hochenergetischen Astrophysik. Es beginnt mit einem Überblick über Röntgendoppelsterne und betont deren einzigartige Eigenschaften und astrophysikalische Relevanz. Historische Entwicklungen der Röntgenastronomie, von der Entdeckung von Sco X-1 bis zu den Beiträgen moderner Observatorien wie eROSITA, NICER, NuSTAR, XMM-Newton und Insight-HXMT, werden diskutiert. Darüber hinaus werden die neuartigen Beiträge dieser Studie skizziert, insbesondere die Anwendung fortschrittlicher Zeitbereichsanalysemethoden und die Integration von Daten aus mehreren Missionen, um umfassende Einblicke zu gewinnen.

Das zweite Kapitel legt die theoretischen und beobachtungsbezogenen Grundlagen der Forschung zu Röntgendoppelsternen dar. Es umfasst detaillierte Erklärungen grundlegender Konzepte wie Akkretionsphysik, Quasiperiodische Oszillationen (QPOs), spektrale Zustandsübergänge und Spindynamik, die für das Verständnis der physikalischen Mechanismen von Röntgendoppelsternen entscheidend sind. Das Kapitel fasst auch ungelöste wissenschaftliche Fragen zusammen, wie die physikalischen Ursprünge von QPOs, die Rolle von Magnetfeldern in Akkretionsprozessen und die Kopplung zwischen spektralen Zustandsübergängen und relativistischen Jets.

Der methodische Rahmen und die Datenquellen werden in einem eigenen Kapitel präsentiert. Diese Studie nutzt Multisatellitenbeobachtungen, um die spektralen und zeitlichen Eigenschaften von Röntgendoppelsternen über einen breiten Energiebereich hinweg zu analysieren. Die Beiträge der einzelnen Observatorien werden detailliert beschrieben: Die großflächigen Himmelsdurchmusterungen von eROSITA decken Variabilitätsmuster in transienten Röntgenquellen auf, NICERs hohe zeitliche Auflösung ermöglicht präzise Zeitmessungen, NuSTAR liefert wichtige Erkenntnisse zu hochenergetischen Spektralkomponenten, XMM-Newton bietet hochauflösende Spektroskopie

von Akkretionsscheiben, und Insight-HXMT trägt zur Untersuchung von transienten Phänomenen und harter Röntgenstrahlung bei.

Die Ergebnisse sind in zwei Hauptabschnitte unterteilt, die sich auf Schwarze Löcher und Neutronensterne in Röntgendoppelsternen konzentrieren. Bei Systemen mit Schwarzen Löchern heben die Ergebnisse signifikante spektrale und zeitliche Variabilität hervor, wobei Schlüsselphänomene wie Zustandsübergänge und das Starten von Scheibenwinden im Detail untersucht werden. Spektralanalysen zeigen Korrelationen zwischen Änderungen in der Scheibenstruktur und relativistischen Ausflüssen, während Zeitanalysen von QPOs Einblicke in die Akkretionsdynamik nahe dem Ereignishorizont liefern. Diese Ergebnisse tragen zu einem tieferen Verständnis der Akkretions-Ausstoß-Kopplung und der Rückkopplungsprozesse bei, die mit dem Wachstum von Schwarzen Löchern und der Galaxienevolution verbunden sind.

Für Neutronensterne untersucht die Studie die Spinentwicklung und Variabilitätsmuster. Hochauflösende Zeitdaten zeigen komplexe Pulsationsprofile und Anti-Glitch-Phänomene, die neue Perspektiven auf magnetosphärische Akkretion und dichte Materiephysik bieten.

Diese Dissertation hebt auch die Einschränkungen aktueller Beobachtungs- und Analysemethoden hervor, wie die Herausforderungen durch schwache Signale und unvollständige zeitliche Abdeckung. Sie identifiziert Möglichkeiten für zukünftige Forschungen, einschließlich der Integration von multiwellenlängen- und multimessenger-Daten, um die Dynamik kompakter Objekte weiter zu erforschen.

Abschließend trägt diese Dissertation wesentlich zum Verständnis von Röntgendoppelsternen bei, indem sie eine umfassende Analyse ihrer spektralen und zeitlichen Eigenschaften auf der Grundlage von Multimissionsbeobachtungen liefert. Die Ergebnisse schließen entscheidende Wissenslücken und schaffen eine Grundlage für zukünftige Forschungen, die beobachtende und theoretische Aspekte der hochenergetischen Astrophysik miteinander verbinden, um unser Verständnis der extremsten Umgebungen des Universums zu erweitern.

Contents

Abstract **vii**

Zusammenfassung **ix**

1 Introduction **2**
1.1 Background . . . 2
1.2 Current State of Research and Motivation . . . 5
1.3 Research Scope and Objectives . . . 7
1.4 Thesis Structure . . . 10

2 X-ray Binaries and X-ray Missions **12**
2.1 Studies of X-ray Binaries . . . 12
2.1.1 Basic Concept . . . 12
2.1.2 X-ray Binary Systems: Classification and Physical Processes . . . 17
2.1.3 Spectral and Temporal Evolution of Low-Mass Black Hole X-ray Binaries . . . 19
2.1.4 Accretion Flow Models During Outbursts . . . 21
2.1.5 Outflows in X-ray Binaries . . . 27
2.2 Major Satellite Missions and Their Contributions . . . 29
2.2.1 Advancements in X-ray Astronomical Instrumentation . . . 29
2.2.2 Advancements in Observatories . . . 32
2.3 Advantages of Multi-Satellite Observations . . . 47

3 Data and Methods **50**
3.1 Data Sources and Preprocessing . . . 50
3.1.1 eROSITA . . . 50
3.1.2 NICER . . . 51
3.1.3 NuSTAR . . . 53
3.1.4 XMM-Newton . . . 55
3.1.5 Insight-HXMT . . . 57
3.2 Data Analysis . . . 58
3.2.1 X-ray Timing Analysis . . . 58
3.2.2 X-ray Spectral Analysis . . . 59
3.2.3 Spectral Fitting with XSPEC . . . 59
3.3 Spin Measurement Methods . . . 61
3.3.1 PDS and RMS Calculation . . . 61
3.3.2 Pulsar Period Analysis . . . 62
3.3.3 Solar System Barycenter Correction . . . 62

3.3.4 Binary Orbital Correction 63
3.3.5 Pulse Folding and Phase Alignment 65
3.3.6 Phase-Resolved Spectroscopy 66

4 Black Holes Research Results 67
4.1 Summary: Evolution of Disc and Corona in MAXI J1348-630 During the 2019 Reflare (Dai et al., 2023 [1]) 67
4.1.1 Aim of the Research 67
4.1.2 Conclusions 67
4.1.3 Creative Ideas and Novel Contributions 68
4.1.4 Main Results 69
4.2 Unveiling the Rebrightening Mechanism of GRS 1915+105: Insights from QPOs and Disk Winds (Dai et al., 2024 [2]) 70
4.2.1 Aim of the Research 70
4.2.2 Conclusion 70
4.2.3 Creative Ideas and Novel Contributions 70
4.2.4 Main Results 71
4.3 Search for Quiescent Black Holes with eROSITA 72
4.3.1 Cataloging of Quiescent Black Holes 72
4.3.2 Observation Results of Luminosity Changes 77

5 Neutron Star Research Results 79
5.1 Spin Measurement and Evolution Analysis of SXP726(Haberl et al.,2022 [3]) 79
5.1.1 XMM-Newton Data Analysis 81
5.1.2 Spin evolution combined with eROSITA 82
5.1.3 Flux evolution combined with eROSITA 86
5.2 Anomalies in Swift J0243.6+6124 87
5.2.1 Search for Anti-glitch 88
5.2.2 Finding and Analysis of Slight glitches 94

6 Discussion and Conclusion 99
6.1 Summary of Work 99
6.2 Comprehensive Discussion of Research Results 99
6.2.1 Black Hole X-ray Binaries 100
6.2.2 Neutron Star X-ray Binaries 100
6.3 Future Work 100
6.4 Conclusion 101

Acknowledgements 102

References 104

Appendices 116

1 Introduction

This chapter provides an overview of the foundational concepts and background knowledge required to understand the research presented in this thesis. It begins with a broad introduction to X-ray binaries, which consist of black holes and neutron stars as compact objects of a binary stellar system, highlighting their astrophysical significance and unique characteristics. The chapter then discusses the observational challenges and technological advancements in high-energy astrophysics that have shaped modern approaches to studying these systems. Particular emphasis is placed on the gaps in current knowledge that motivate this research, including unresolved questions about the variability and spectral characteristics of X-ray binaries. Historical developments in X-ray astronomy are also summarized to contextualize the rationale for utilizing multi-mission observational data. Finally, the structure of this thesis is outlined to provide a road map for the discussion and analysis that follows.

1.1 Background

Understanding the physics of matter under extreme conditions is essential for advancing astrophysics and even fundamental physics as a whole. Compact objects, such as neutron stars and black holes, are at the forefront of high-energy astrophysics due to their extreme physical conditions, including intense gravitational and magnetic fields, rapid rotation, and high-energy particle interactions. In X-ray binary systems, these compact objects accrete matter from a companion star, releasing gravitational energy in the form of powerful X-ray emissions. Such systems serve as natural laboratories for studying fundamental astrophysical processes, ranging from relativistic effects to accretion dynamics, under conditions unattainable in terrestrial experiments [4, 5].

Black holes, one of the primary compact objects in X-ray binaries, are end stages of massive stellar evolution and are characterized by an event horizon beyond which no information can escape [6]. Owing to its strong gravity, material from the companion star is transferred to the black hole via Roche lobe overflow or stellar wind, typically forming a disk-like accretion structure. In particular, black hole X-ray binaries are ideal for examining phenomena like jet production, energy release near the event horizon, and accretion disk instability, which are critical for understanding the role of black holes in galaxy evolution and feedback processes [7]. Neutron stars are another class of compact objects in X-ray binaries. With masses comparable to the Sun but radii of only about 10 kilometers, neutron stars are extraordinarily dense, making them unique environments to test theories of dense matter physics [8, 9]. Neutron stars in X-ray binaries often exhibit pulsations due to their rapid rotation and strong magnetic fields, which can channel accreting material onto the magnetic poles, producing observable X-ray pulses [10, 11]. These systems provide a valuable platform for studying magnetic field evolution, spin dynamics, and nuclear reactions under extreme pressure, thus enriching

our understanding of high-energy astrophysics and fundamental particle interactions [12]. Observations of their high-energy missions (see Section 2.3) have enabled detailed studies of these compact objects, revealing their variable emission, spectral features, and timing properties, which have direct implications for accretion theory, compact object formation, and high-energy astrophysical processes [13–15]. Therefore, the study of X-ray binaries not only enhances our knowledge of compact objects but also contributes to broader fields like cosmology and stellar evolution, positioning these systems as crucial observational targets for advancing modern astrophysics.

The field of X-ray astronomy was born in the early 1960s with the groundbreaking discovery of the first cosmic X-ray source, Scorpius X-1 (Sco X-1), by Riccardo Giacconi and colleagues [16]. Using a rocket-mounted X-ray detector, they detected Sco X-1 as the brightest point source of X-rays in the sky [17]. This discovery marked the first evidence of X-ray emission from sources beyond the solar system, opening a new window into high-energy astrophysics. In the following years, several more X-ray sources were identified using rocket and balloon-based instruments, but their nature remained unclear until the advent of satellite-based X-ray observatories. The Uhuru X-ray Explorer Satellite (Uhuru) satellite, launched in 1970, was the first dedicated X-ray astronomy mission. It conducted the first systematic survey of the X-ray sky, revealing that many of these sources were binary systems containing either a neutron star or a black hole accreting material from a companion star [18]. The discovery of Centaurus X-3 (Cen X-3) in 1971 provided definitive evidence of a neutron star in an X-ray binary system, as its regular pulsations clearly indicated the presence of a rapidly spinning magnetized compact object [19]. Another milestone was reached in the 1970s with the confirmation of Cygnus X-1 (Cyg X-1) as the first stellar-mass black hole. Through radial velocity measurements and observations of the system's orbital parameters, it was established that the unseen companion of the supergiant star in Cyg X-1 exceeded the mass limit for a neutron star, confirming it as a black hole [20]. The 1980s and 1990s saw the deployment of more sophisticated X-ray observatories, such as the European X-ray Observatory Satellite (EXOSAT) and the Rossi X-ray Timing Explorer (RXTE) [21, 22]. These missions expanded the scope of X-ray astronomy by enabling high-resolution timing studies and the detection of quasi-periodic oscillations (QPOs), which provided insights into accretion disk instabilities and the relativistic effects near compact objects [23, 24]. The discovery of millisecond X-ray pulsars further deepened our understanding of neutron stars and their evolution [25]. The turn of the century brought revolutionary advancements with the launch of observatories like Chandra and X-ray Multi-Mirror observatory (XMM-Newton), which combined high spatial and spectral resolution to study faint X-ray sources in unprecedented detail. For example, Chandra's sub-arcsecond imaging resolved crowded regions like the galactic center, while XMM-Newton's large effective area enabled detailed studies of accretion disks and emission lines [26]. More recently, missions such as the Nuclear Spectroscopic Telescope Array (NuSTAR), the Neutron Star Interior Composition Explorer Mission (NICER), the extended ROentgen Survey with an Imaging Telescope Array (eROSITA) and the Hard X-ray Modulation Telescope (Insight-HXMT, HXMT) have further advanced X-ray astronomy.

Missions such as eROSITA have provided all-sky surveys, revealing previously undetected X-ray binaries and adding to the known population of compact objects [27]. NICER's high temporal resolution has enabled studies of neutron stars in unprecedented detail, offering insights into dense matter physics and the equation of state

[14]. NuSTAR's capability to observe hard X-rays has expanded the observational range for X-ray binaries, allowing for more detailed studies of high-energy processes [15]. Insight-HXMT provides a very broad energy band of $2 - 250$ keV, and extramely large effective area above 30 keV [28, 29].

These missions have unveiled a wealth of phenomena, including Fe K_α emission lines used to measure black hole spin, thermonuclear bursts on neutron stars, and the coupling between accretion flows and outflows in the form of jets or winds. The development of multi-wavelength observational strategies and advanced analytical techniques has also enriched our understanding of the dynamic and energetic processes in X-ray binaries.

One of the key aspects of studying X-ray binaries is understanding the interplay between accretion processes and outflows, such as jets. In systems with neutron stars, the presence of a strong magnetic field plays a critical role in shaping the accretion flow and modulating X-ray emissions. Black hole systems, on the other hand, provide unique opportunities to study relativistic effects near the event horizon and the nature of the accretion disk's inner regions. Both classes of systems exhibit state transitions, wherein the spectral properties and timing behavior of the system change dramatically, often accompanied by the launching or suppression of relativistic jets. These transitions offer a window into the physics of accretion and energy release in the vicinity of compact objects.

In addition to the significant progress made through individual observations of neutron stars and black holes, there has been a growing emphasis on multi-wavelength and multi-messenger approaches to studying these objects. By combining X-ray data with observations in other parts of the electromagnetic spectrum, such as radio and optical, researchers can gain a more comprehensive understanding of the processes driving the behavior of these systems. Furthermore, the advent of gravitational wave astronomy, pioneered by observatories such as the Laser Interferometer Gravitational-Wave Observatory (LIGO) and the Virgo interferometer (Virgo), has added a new dimension to the study of compact objects. The detection of gravitational waves from black hole and neutron star mergers has provided direct evidence of the violent and energetic processes involved in the final stages of binary evolution, opening new avenues for research into the life cycles of these systems.

Despite these advances, significant gaps in knowledge remain. For instance, the physical mechanisms behind Quasi Periodic Oscillations (QPOs) are still not fully understood, and debates continue regarding the relationship between QPO frequencies and the spin of black holes [24]. The structure and behavior of the magnetic fields of neutron stars also pose challenges, especially as certain phenomena, like anti-glitches, remain unexplained within current models [30]. Additionally, the detection of transient X-ray sources continues to raise questions about the origins and evolutionary paths of these systems. Addressing these gaps is crucial for a comprehensive understanding of compact objects, and this research aims to contribute to these areas by exploring variability in X-ray binaries.

One major challenge in observing X-ray binaries and other high-energy sources is their variability. Many of these sources exhibit complex temporal changes, such as periodic pulsations, QPOs, and random flares, which require precise timing analysis [5]. Additionally, the emission can vary significantly due to changes in the accretion rate or magnetic field, making it essential to have continuous or repeated observations over

time [31]. The need for multi-satellite observations further arises from the diversity in X-ray binaries, as no single observatory can cover the entire X-ray spectrum or provide continuous monitoring. Combining data from multiple missions allows for a comprehensive view of these dynamic systems [32].

The analysis of high-energy astrophysical data also presents challenges due to the variable nature of X-ray signals and the need to disentangle complex physical processes in the data. Advanced analytical methods, such as Fourier and wavelet transforms for timing analysis and spectral fitting techniques, are essential to extracting meaningful information from observations [23]. Machine learning approaches are increasingly applied to classify and interpret large datasets, further enhancing observational studies of X-ray binaries [33].

Building on recent advances and addressing existing gaps, this thesis focuses on investigating X-ray binaries and compact objects through multi-mission observations and advanced data analysis techniques. Utilizing data from eROSITA, NICER, and NuSTAR, this research examines variability patterns and spectral features in black holes and neutron stars, aiming to provide insights into their accretion processes and magnetic fields. The combination of spectral and temporal analyses, along with innovative methods such as the Hilbert-Huang Transform (HHT), offers a novel approach to understanding these complex systems [13, 15]. By applying these observational and analytical strategies, this work aims to address unresolved questions in high-energy astrophysics and contribute to the broader understanding of X-ray binaries and compact objects.

1.2 Current State of Research and Motivation

In the first 15 years of X-ray binaries, only the limited brightest sources could be found due to the instrument limitation. Until in the late of 1970s, the first non-solar point source and a fainter one was discovered [17, 34] due to the advence of X-ray imaging instruments. X-ray binaries began the stage of a hundred flowers blooming. Figure 1.1 illustrates the sky distribution of the brightest cosmic X-ray sources, based on early X-ray astronomy studies, highlighting their clear association with the Milky Way Galaxy. In 1966, Sandage et al. identified Sco X-1 with a faint blue star characterized by emission lines in its spectrum. It was one year later discovered by Shklovskii that these sources are binary systems consisting of a normal star and a neutron star or black hole [18].

Extensive observational and theoretical studies have been conducted to unravel the complexities of these systems. Modern X-ray observatories, equipped with advanced instrumentation, have enabled astronomers to observe these objects with unprecedented detail and accuracy. These observations have revealed a wealth of information about the physical characteristics of X-ray binaries, including their spectral properties, timing behavior, and variability. For instance, the periodicity observed in some X-ray binaries has provided valuable data on the orbital dynamics and the nature of the compact object. In addition to observational advancements, significant progress has been made in theoretical modeling and numerical simulations, which have been instrumental in interpreting the data and understanding the underlying physics of X-ray binaries. These models explore various aspects, such as the structure and evolution of accretion disks, the impact of magnetic fields on the accretion process, and the generation of

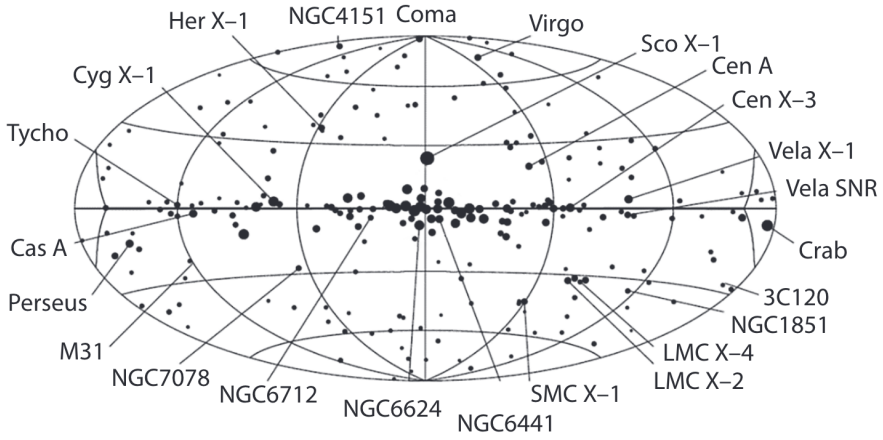


Figure 1.1: Sky distribution of the brightest cosmic X-ray sources, as recorded by UK+NASA's Ariel 5 X-ray satellite (Warwick et al., 1981; McHardy et al., 1981) (Aitoff equal area Galactic coordinate plot). Sources are represented by circles, with size indicating the strength of the source as recorded by the detector. The horizontal axis is along the Milky Way, and the center of the picture is the Milky Way center. The brightest source of the sky, above the center, is Sco X-1, a LMXB with an orbital period of 19.2 hr. The great majority of the bright circles along the Galactic plane are X-ray binaries; some of the most prominent sources are indicated by name: LMC, Large Magellanic Cloud; SMC, Small Magellanic Cloud; NGC 6624, globular cluster. Coma and Virgo are clusters of galaxies, like the Perseus Cluster. After Pounds (2020).(From Tauris et al. 2023) [35]

X-ray emissions. The observational data and theoretical models has led to a more comprehensive understanding of these systems.

However, fundamental questions remain unanswered. Among the others we have:

- What physical mechanisms underlie the variability observed in X-ray binaries, such as quasi-periodic oscillations (QPOs) and state transitions?
- How do magnetic fields influence accretion flows and drive phenomena like pulsations and jets?
- What are the connections between spectral and timing properties in X-ray binaries, and how do these relate to the compact object's spin and magnetic field?

These open questions motivate this thesis, which aims to investigate the spectral and timing properties of X-ray binaries using data from multiple X-ray observatories. By leveraging advanced analysis techniques, this study seeks to:

1. Explore variability mechanisms, such as QPOs, in both neutron star and black hole systems.
2. Investigate the role of magnetic fields in shaping the accretion dynamics of compact stars.
3. Examine the coupling between spectral state transitions and relativistic outflows in black hole binaries.

The motivation for this research stems from the need to deepen our understanding of the complex processes governing neutron stars and black holes in X-ray binaries. By addressing key questions related to accretion-ejection coupling, QPOs and neutron star spin evolution, this thesis aims to contribute to the broader field of high-energy astrophysics. The use of multi-satellite datasets offers a powerful approach to probing these extreme systems, with the potential to uncover new insights into the nature of compact objects and the extreme environments in which they exist.

The findings of this study are expected to contribute to a deeper understanding of the physical processes governing X-ray binaries. Moreover, they address broader scientific challenges, such as the nature of dense matter in neutron stars and the feedback mechanisms of black holes in galactic evolution.

1.3 Research Scope and Objectives

The scope of this thesis involves the detailed study of neutron stars and black holes within X-ray binary systems, with a particular focus on their spectral and timing properties. The research is centered on understanding the physical mechanisms driving accretion processes, the behavior of matter in extreme gravitational and magnetic fields, and the interaction between accretion disks and corona.

Focus on Neutron Stars and Black Holes in X-ray Binaries

The primary focus of this research is on neutron stars and black holes in low-mass X-ray binaries (LMXBs) and high-mass X-ray binaries (HMXBs). These systems are characterized by their accretion of matter from a companion star, which leads to the emission of X-rays and the production of relativistic outflows. The specific areas of focus within these systems include:

Spin evolution and timing behavior of neutron stars, particularly the detection and analysis of periodic and quasi-periodic oscillations. Spectral state transitions in black hole binaries, including the interplay between accretion states and the launching or suppression of jets or corona. Accretion-ejection coupling, which refers to the relationship between the inflow of material via accretion and the outflow in the form of relativistic jets or winds.

Multi-Satellite X-ray Observations

This research utilizes data from multiple X-ray observatories, each contributing different observational strengths that allow for a comprehensive analysis of X-ray binary systems:

XMM-Newton for precise timing measurements, providing insights into the spin periods and pulse profiles of neutron stars. NICER for high-resolution spectroscopy in the low energy band, essential for studying thermal emission and relativistic reflection features in accretion disks, as well as the detection of QPOs. NuSTAR for precise spectral measurements, providing a reference in spectral and temporal analysis. eROSITA for wide-field X-ray surveys, enabling the study of long-term variability and population statistics of X-ray binaries. Insight-HXMT for observations in the hard X-ray regime, allowing the investigation of non-thermal emission components and the properties

of black hole corona. The combination of these observatories offers a broad energy range (from soft to hard X-rays) and temporal resolution, enabling the study of both short-term variability and long-term evolutionary trends in X-ray binaries.

The overall goal of this thesis is to advance our understanding of the physical processes governing neutron stars and black holes in X-ray binary systems, with a specific focus on their spectral and timing properties. This research aims to address several critical questions in high-energy astrophysics. The following research objectives have been defined to guide this investigation:

Analyze Spectral State Transitions in Black Hole X-ray Binaries

One of the most intriguing aspects of X-ray binaries is the complex interaction between the inflow of matter via accretion and the outflow of energy and material in the form of relativistic jets. Black hole systems often undergo state transitions, where their X-ray spectra and timing properties change dramatically. These transitions are typically associated with the accretion process, but the precise mechanism driving this accretion-ejection coupling remains limited understood.

Current models suggest that changes in the inner accretion disk, magnetic field interactions, or the properties of the corona may play a role, but more detailed data are needed to clarify these mechanisms. The study aims to explore how accretion processes influence disk-corona formation and to provide new insights into the conditions under which corona are launched or suppressed.

A detailed analysis of these transitions is essential for understanding the physical mechanisms that drive shifts between different accretion states. The specific objectives are:

- Investigate the spectral evolution during state transitions, focusing on the specific state, which may be in the low/hard state (dominated by non-thermal emission and jet activity) and the high/soft state (dominated by thermal emission from the accretion disk).
- Analyze the relationship between spectral changes and corona activity by integrating simultaneous multi-observations to explore how variations in the inner accretion disk influence the launching or suppression of corona.
- Compare the properties of state transitions across multiple black hole systems to identify commonalities in accretion physics and understand the role of relativistic effects near the event horizon.

These analyses aim to deepen our knowledge of accretion-ejection coupling and the dynamic behavior of black hole systems under varying accretion conditions.

Examine Pulse Profiles and Spin Evolution in Neutron Stars

Neutron stars are among the most magnetized objects in the universe, and their strong magnetic fields play a critical role in shaping the accretion flow and modulating their X-ray emission. The interaction between the magnetic field and the accretion

disk can lead to the formation of magnetospheric boundaries and the generation of quasi-periodic oscillations. Additionally, neutron stars exhibit complex spin behaviors, including spin-up due to accretion and spin-down from magnetic braking.

While observational studies have provided measurements of neutron star spin periods and magnetic field strengths, the long-term evolution of these properties remains a subject of active research. The precise relationship between accretion processes and the spin evolution of neutron stars, particularly in millisecond pulsars, is still not fully understood. The study seeks to contribute to neutron star spin evolution by analyzing detailed timing data and researching in shaping neutron star accretion dynamics.

The spin evolution of neutron stars in X-ray binaries is a key to understanding complex accretion process. The specific objectives include:

- Measure spin periods and their evolution over time using long-term monitoring data from X-ray observatories such as NICER and XMM-Newton.
- Investigate the presence of gliches and anti-gliches.

Investigate QPOs in Neutron Star and Black Hole Systems

Quasi-periodic oscillations (QPOs) are observed in the X-ray light curves of both neutron star and black hole X-ray binaries and offer a valuable probe of the innermost regions of these systems. QPOs are thought to arise from disk oscillations, interactions with the compact object's magnetic field, or general relativistic effects near the innermost stable circular orbit (ISCO) of black holes. However, the exact origin and physical mechanism behind QPOs remain unclear.

High-frequency QPOs (HFQPOs) in particular are believed to be linked to the strong gravitational fields close to black holes and could provide a direct test of general relativity in extreme environments. In neutron star systems, low-frequency QPOs (LFQPOs) may be related to interactions between the magnetic field and accretion disk. This thesis is motivated by the need to better understand the origins of QPOs through detailed timing and spectral analysis, using multi-satellite data to capture these oscillations across different energy bands.

The specific objectives are:

- Detect and characterize QPOs in the X-ray light curves of neutron star and black hole systems using high-precision timing data from multi-satellite observations.
- Analyze the frequency, amplitude, and energy dependence of QPOs to infer the physical properties of the inner accretion disk, including its structure, magnetic interactions, and relativistic effects near compact objects.
- Compare the characteristics of QPOs in neutron star and black hole systems to uncover similarities and differences in the accretion processes and relativistic effects that generate these oscillations.

1.4 Thesis Structure

This thesis is organized into six chapters, each addressing specific aspects of the study of neutron stars and black holes in X-ray binaries. The overall structure is designed to guide the reader through the background, methodology, key findings, and broader implications of the research. The structure of the thesis is outlined as follows:

Chapter 1: Introduction

This chapter provides an overview of the research topic and its significance in the field of high-energy astrophysics. It includes the motivation behind the study, the scope of the research, the specific objectives to be addressed, and a summary of the overall structure of the thesis. The introduction sets the stage for the detailed investigation of neutron stars and black holes in X-ray binaries, with a focus on their spectral and timing properties.

Chapter 2: X-ray Binaries and X-ray Missions

The chapter presents a comprehensive summary of the current state of research in X-ray binary systems. It covers basic concepts, key developments in the study of accretion processes and the behavior of compact objects in extreme gravitational and magnetic fields. The chapter also reviews the major observational techniques used to study neutron stars and black holes and introduces the main X-ray missions used in the study, as well as the contributions of past and ongoing X-ray satellite missions. This chapter establishes the foundation upon which the subsequent chapters build.

Chapter 3: Data and Methods

This chapter details the observational data and analytical methods used in the study. It describes the X-ray observatories (such as XMM-Newton, NICER, eROSITA, and Insight-HXMT) and the specific datasets acquired for the investigation. The chapter also explains the techniques used for timing and spectral analysis, including the methods for detecting and characterizing QPOs, measuring neutron star spin evolution, and analyzing spectral state transitions in black hole systems. The multi-satellite approach and its advantages are also discussed.

Chapter 4: Black Hole Research Results

This chapter focuses on the black hole systems in X-ray binaries, with an emphasis on their spectral state transitions and the relationship between accretion and corona activity. The chapter presents detailed analyses of the timing and spectral behavior of black hole X-ray binaries during state transitions, exploring the mechanisms that drive these changes. It also examines the detection of QPOs and their relevance to the study of strong gravitational fields near the event horizon of black holes.

Chapter 5: Neutron Star Research Results

This chapter presents the findings from the detailed study of neutron stars in X-ray binaries, focusing on their timing and spectral properties. It includes results on neutron star spin evolution, the role of magnetic fields in accretion processes, and the detection and analysis of QPOs. The chapter also discusses the open questions about neutron stars.

Chapter 6: Discussion and Conclusion

The final chapter synthesizes the key findings of the thesis and discusses their broader implications for the field of high-energy astrophysics. It addresses the research objectives set out in Chapter 1 and evaluates how the results contribute to a deeper understanding of neutron stars and black holes in X-ray binaries. The chapter also identifies the limitations of the current study and proposes potential directions for future research. Finally, it offers concluding remarks on the significance of the work and its contribution to the ongoing study of compact objects in extreme environments.

2 X-ray Binaries and X-ray Missions

This chapter aims to provide a comprehensive overview of the theoretical background and observational advancements relevant to the study of X-ray binaries (XRBs) and the X-ray missions that have significantly contributed to this field. The first part of this chapter, Studies of X-ray binaries, outlines the fundamental concepts understanding XRB research, including accretion energy and nuclear reactions, Eddington luminosity, Kerr black holes, innermost stable circular orbits (ISCO), and their astrophysical applications. This section also includes the classification of XRB systems, the mechanisms of accretion, disk structures, spectral properties, and the impact of relativistic effects, alongside a discussion of recent progress in the field.

The second part, X-ray Missions, highlights the technological evolution and scientific achievements of X-ray astronomy. It begins with a review of the development of proportional counters, which have played a pivotal role in X-ray detection, followed by an overview of major observatories that have shaped our understanding of XRBs. Special emphasis is placed on current operational satellites such as the extended ROentgen Survey with an Imaging Telescope Array (eROSITA), the Hard X-ray Modulation Telescope (Insight-HXMT, HXMT), X-ray Multi-Mirror (XMM-Newton), the Nuclear Spectroscopic Telescope Array (NuSTAR) and the Neutron Star Interior Composition Explorer Mission (NICER), which form the cornerstone of the observational data used in this thesis. The unique capabilities of each satellite are discussed, particularly in relation to their contributions to multi-mission studies, which leverage complementary observations to achieve higher precision and a broader understanding of XRB systems.

By bridging theoretical insights with observational capabilities, this chapter sets the foundation for the detailed analyses and discussions presented in subsequent sections of the thesis.

2.1 Studies of X-ray Binaries

X-ray binary systems are a fascinating and crucial class of binary star systems that emit substantial amounts of X-rays. These systems consist of a normal star, which can be either a main-sequence star, giant, or supergiant, and a compact object, which is typically a neutron star or a black hole. The intense X-ray emissions in these systems are produced by the accretion of matter from the normal star onto the compact object.

2.1.1 Basic Concept

Astrophysical processes around compact objects, such as black holes and neutron stars, are governed by extreme physical conditions involving strong gravitational fields, high temperatures, and intense magnetic fields. This section outlines several fundamental

concepts, which together form the theoretical basis for understanding X-ray binaries.

Accretion Energy and Nuclear Reactions

Accretion and nuclear reactions are two fundamental energy-generation mechanisms in astrophysics, with crucial roles in powering various astrophysical systems. Nuclear reactions dominate the energy production in stellar interiors, sustaining the long-term stability of main-sequence stars. In contrast, accretion provides the primary energy source for systems like X-ray binaries, active galactic nuclei, and other compact-object environments.

In the accretion process, matter falling onto a compact object releases gravitational potential energy. This energy can be estimated as:

$$\Delta E_{\rm acc} \sim \frac{GM}{r}, \tag{2.1}$$

where G is the gravitational constant, M is the mass of the compact object, and r is the radius at which the matter is deposited. For a typical neutron star with a mass of $M \sim M_\odot$ and a radius of $r \sim 10\,\mathrm{km}$, the energy released per unit mass of accreted material is approximately $\sim 10^{20}\,\mathrm{erg\ g^{-1}}$. This immense energy makes accretion the dominant power source in compact-object systems, producing high-energy radiation, such as X-rays and gamma rays, which serve as valuable observational probes of these extreme environments.

On the other hand, nuclear reactions, such as hydrogen fusion into helium in stellar cores, are responsible for the energy output of stars during their main-sequence lifetimes. The energy released in nuclear fusion can be expressed as:

$$\Delta E_{\rm fus} \sim 0.007 mc^2, \tag{2.2}$$

where m is the mass of the reacting material, and c is the speed of light. This corresponds to an energy release of approximately $\sim 10^{18}\,\mathrm{erg\ g^{-1}}$, which is two orders of magnitude smaller than the energy released during accretion.

Thus, accretion emerges as the dominant energy-generation mechanism in compact-object systems, particularly in X-ray binaries. The variability in accretion rates, the structure of accretion disks, and interactions between the compact object and its companion star lead to diverse observational phenomena, such as periodic or quasi-periodic variability in X-ray emissions.

In conclusion, accretion and nuclear reactions provide complementary insights into astrophysical energy production. While nuclear reactions drive stellar evolution, accretion governs the dynamics of compact-object systems. The high-energy radiation from accretion processes, especially in X-ray binaries, serves as a critical tool for exploring the extreme physical conditions around compact objects.

Eddington Luminosity

For a spherically symmetric accretion system, the radiation pressure from emitted photons counteracts the ram pressure of the accreting plasma. When these forces

reach equilibrium, accretion halts, and the luminosity reaches the Eddington limit:

$$L_{\rm Edd} = \frac{4\pi G M m_p c}{\sigma_T} \sim 1.3 \times 10^{38} \left(\frac{M}{M_\odot}\right) \,{\rm erg\,s^{-1}}, \tag{2.3}$$

where σ_T is the Thomson scattering cross-section, m_p is the proton mass, and $M_\odot$ is the solar mass. For super-Eddington accretion, such as in highly magnetized neutron stars, the actual accretion rate may exceed this limit due to anisotropic emission or strong magnetic confinement. These deviations play a critical role in understanding extreme systems such as ultraluminous X-ray sources (ULXs) [36].

Kerr Metric and Black Hole Spin

The Kerr metric describes the spacetime geometry around a rotating black hole. Unlike a non-rotating Schwarzschild black hole, a Kerr black hole is characterized by two key parameters: the mass M and the spin parameter $a = J/M$, where J is the black hole's total angular momentum. This metric is a solution to Einstein's field equations in general relativity, extending the Schwarzschild solution to include rotation. The Kerr metric is essential for understanding the dynamics of accretion disks, relativistic jets, and other high-energy phenomena near black holes. In observations, it can be characterized with dimensionless spin, defined as:

$$a_* = \frac{a}{R_g} = \frac{Jc}{GM^2}, \tag{2.4}$$

where R_g is called the gravitational radius, M is the mass of the black hole, c is the speed of light in a vacuum, and G is the gravitational constant. The spin parameter a_* ranges from -1 to 1, with $a_* = 0$ corresponding to a non-rotating Schwarzschild black hole. The Kerr metric allows us to compute the event horizon radius and energy situatios, both of which influence accretion processes and relativistic jet formation.

In flat spacetime (Minkowski spacetime), the line element ds can be simply written as:

$$ds^2 = -dt^2 + dx^2 + dy^2 + dz^2,$$

using natural units ($G = c = 1$, $R_g = M$).

In Boyer-Lindquist coordinates (t, r, θ, ϕ)[37], the line element of the Kerr metric is given by:

$$\begin{aligned} ds^2 = &-\left(1 - \frac{2Mr}{\rho^2}\right) dt^2 - \frac{4Mar\sin^2\theta}{\rho^2} dt d\phi + \frac{\rho^2}{\Delta} dr^2 + \rho^2 d\theta^2 + \\ &\left(r^2 + a^2 + \frac{2Ma^2 r \sin^2\theta}{\rho^2}\right) \sin^2\theta d\phi^2, \end{aligned} \tag{2.5}$$

where

$$\Delta = r^2 - 2Mr + a^2,$$
$$\rho^2 = r^2 + a^2\cos^2\theta.$$

Here, M represents the mass of the black hole, a is the spin parameter, and Δ determines the location of the event horizon. When $a = 0$, the metric reduces to the Schwarzschild metric.

The event horizons occur where $\Delta = 0$, leading to:

$$r_{\pm} = M \pm \sqrt{M^2 - a^2},$$

where r_+ is the outer event horizon and r_- is the inner horizon.

The Kerr metric also introduces frame-dragging effects, where spacetime itself is dragged in the direction of the black hole's rotation. This effect is significant near the black hole and influences the angular momentum of accreting matter [38]. The dimensionless spin parameter a_* plays a critical role in determining the physical processes near the black hole, such as the location of the innermost stable circular orbit (ISCO) and the efficiency of energy extraction mechanisms like the Penrose process [39] or Blandford-Znajek process [40].

The Kerr metric forms the theoretical basis for analyzing relativistic phenomena around rotating black holes, making it an essential tool for interpreting observational data from X-ray binaries and active galactic nuclei [41, 42].

Innermost Stable Circular Orbit (ISCO)

The innermost stable circular orbit (ISCO) is the smallest radius at which matter can maintain a stable orbit around a compact object. For black holes, the ISCO depends on the spin parameter a_*, given by:

$$r_{\rm ISCO} = M[3 + Z_2 \mp \sqrt{(3 - Z_1)(3 + Z_1 + 2Z_2)}], \tag{2.6}$$

where

$$Z_1 = 1 + \left(1 - \frac{a_*^2}{M^2}\right)^{1/3} \left[\left(1 + \frac{a_*}{M}\right)^{1/3} + \left(1 - \frac{a_*}{M}\right)^{1/3}\right], \tag{2.7}$$

$$Z_2 = \sqrt{3\frac{a_*^2}{M^2} + Z_1^2}. \tag{2.8}$$

The ISCO determines the efficiency of accretion and the boundary of the inner accretion disk, influencing observed X-ray spectra and variability. It represents the smallest radius at which a particle can stably orbit a black hole without being drawn into it. The radius of ISCO, denoted as $R_{\rm ISCO}$, depends on the black hole's spin parameter a_*, with higher spin values resulting in a smaller $R_{\rm ISCO}$ when the orbit corotates with the black hole ($a_* > 0$). Conversely, for counter-rotating orbits ($a_* < 0$), $R_{\rm ISCO}$ increases. In the case of a non-spinning black hole ($a_* = 0$), the ISCO is located at $6GM/c^2$, corresponding to the Schwarzschild case. The Figure 2.1 shows the relation of $R_{\rm ISCO}$ and a_*.

The ISCO is significant because it marks the transition where circular orbits become unstable. For radii smaller than $R_{\rm ISCO}$, matter spirals inward, losing angular momentum and falling into the black hole. Observationally, variations in the ISCO's position, angular velocity, and binding energy of orbiting particles can provide insights into the black hole's spin and the dynamics of accreting matter. Measurement techniques often rely on X-ray spectral features and other observational signatures to estimate the ISCO and thereby infer the black hole's spin parameter a_*.

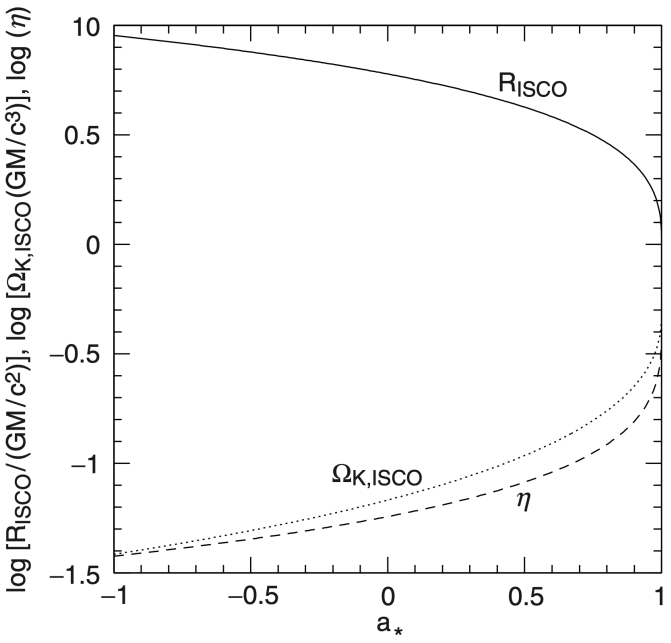


Figure 2.1: The radius of the innermost stable circular orbit $R_{\rm ISCO}$, the Keplerian frequency at this radius $\Omega_{\rm K,ISCO}$, and the binding energy at this radius η, as functions of the BH spin parameter a_*. Positive values of a_* imply that the BH corotates with the orbit, and negative values mean that the BH counter-rotates. By measuring the quantity $R_{\rm ISCO}/M$, $\Omega_{\rm K,ISCO}M$, or η, one could estimate a_*. (From Ramesh Narayan, 2005) [41]

Critical Luminosity in X-ray Binaries

In X-ray binaries, the term critical luminosity ($L_{\rm crit}$) refers to a specific luminosity level at which a significant change in the accretion process or radiation mechanism is observed. In this thesis, the critical luminosity is lower than the Eddington luminosity ($L_{\rm Edd}$) but is high enough to alter the physical conditions in the accretion flow.

When the luminosity of an X-ray binary reaches $L_{\rm crit}$, various transitions in accretion dynamics and radiative properties can occur, depending on the nature of the compact object (neutron star or black hole) and the characteristics of the accretion flow. These changes may include:

- Transitions between different accretion modes (e.g., disk accretion to column accretion in neutron star systems).
- The emergence or suppression of certain radiation mechanisms.
- Sudden changes in plasma temperature and spectral properties.

In high-magnetic-field neutron stars, such as X-ray pulsars (XRPs), accreted matter follows magnetic field lines and forms an accretion column. At low luminosities, most energy is released through direct impact on the neutron star surface. However, when the luminosity exceeds a critical threshold, strong radiation pressure can create a radiation-dominated shock at the top of the accretion column [43, 44].

Observationally, this transition results in spectral softening, as radiation pressure

modifies the structure of the accretion column and enhances Comptonized emission [45].

In black hole X-ray binaries, the accretion disk can exhibit state transitions around a critical luminosity. Below L_{crit}, the system is typically in a low-hard state dominated by Comptonized hard X-rays. As luminosity increases, the inner disk moves closer to the black hole, leading to a high-soft state, where thermal disk emission dominates [5, 46].

Critical luminosity plays a vital role in understanding the accretion physics of X-ray binaries, marking the transition between different accretion regimes, spectral states, and radiative processes. Observations of L_{crit} provide insights into the structure of accretion flows, the impact of magnetic fields, and the fundamental properties of compact objects.

2.1.2 X-ray Binary Systems: Classification and Physical Processes

XRBs are classified based on the nature of the donor star and the mass transfer mechanism into low-mass X-ray binaries (LMXBs) and high-mass X-ray binaries (HMXBs). LMXBs, characterized by a companion star with $M \leq 1M_{\odot}$, predominantly accrete matter via Roche-lobe overflow, forming a thin accretion disk around the compact object [47]. In contrast, HMXBs typically accrete mass through stellar wind capture, as their massive companions are unable to fill their Roche lobes [12]. This dichotomy in the accretion mechanisms leads to distinct observational characteristics in the X-ray spectra and variability profiles of these systems.

Figure 2.2 illustrates two primary regimes of matter accretion in a binary system involving a black hole and a companion star. In the first scenario, when the companion star fills its Roche lobe (top panel), matter flows through the inner Lagrangian point directly towards the black hole. This transfer of material forms an accretion disk around the black hole due to the angular momentum of the infalling matter. This process, known as Roche-lobe overflow, typically occurs in systems where the companion star is in close proximity to the black hole, allowing gravitational forces to dominate the dynamics of mass transfer.

In the second regime (bottom panel), the companion star does not fill its Roche lobe but instead ejects matter through stellar winds. The black hole captures a fraction of this wind material, which loses kinetic energy in shock waves before becoming gravitationally bound. This mode of accretion is common in systems with larger separations between the two components, where the influence of the stellar wind surpasses that of Roche-lobe dynamics. The arrows in the figure represent the flow of matter in both regimes, demonstrating how the physical configuration of the binary system dictates the accretion process and its resulting structures.

Beyond mass-based classification, neutron stars can also be classified according to other intrinsic properties. Figure 2.3 presents various classification schemes for X-ray binaries.

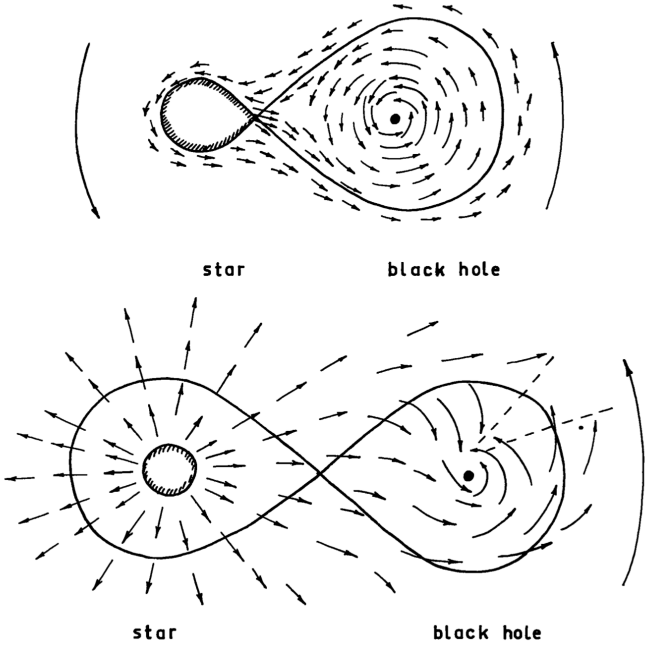


Figure 2.2: Two regimes of matter capture by a collapsar: (a) a normal companion fills up its Roche lobe, and the outflow goes, in the main, through the inner Lagrangian point; (b) the companion's size is much less than the Roche lobe, and the outflow is connected with a stellar wind. The matter loses part of its kinetic energy in the shock wave, and thereafter, gravitational capture of accreting matter becomes possible. (from N. I. Shakura, 1973) [47]

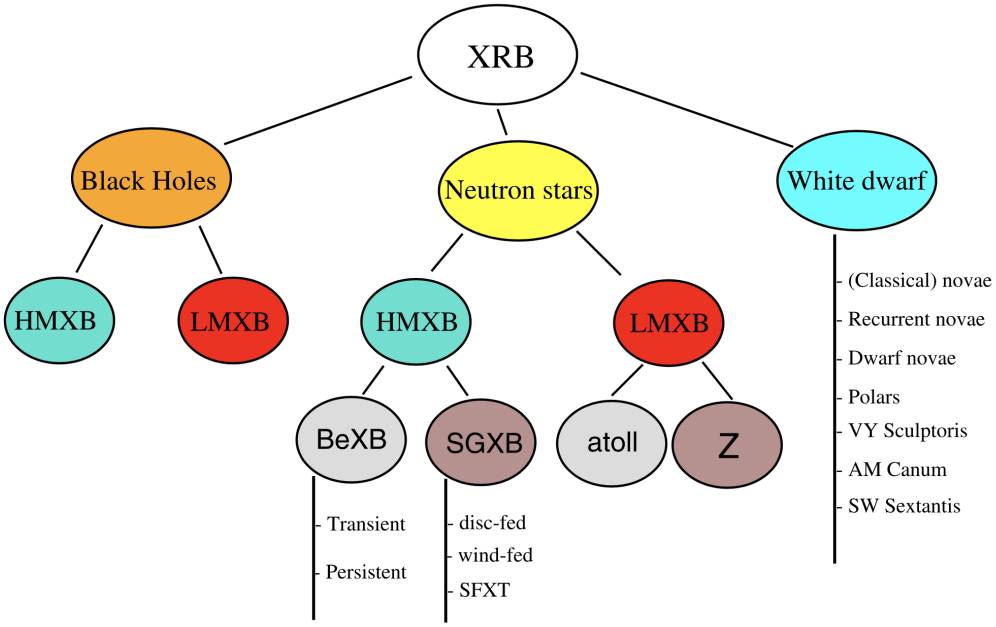


Figure 2.3: Classification of X-ray binaries. (From Pablo Reig, 2011) [12]

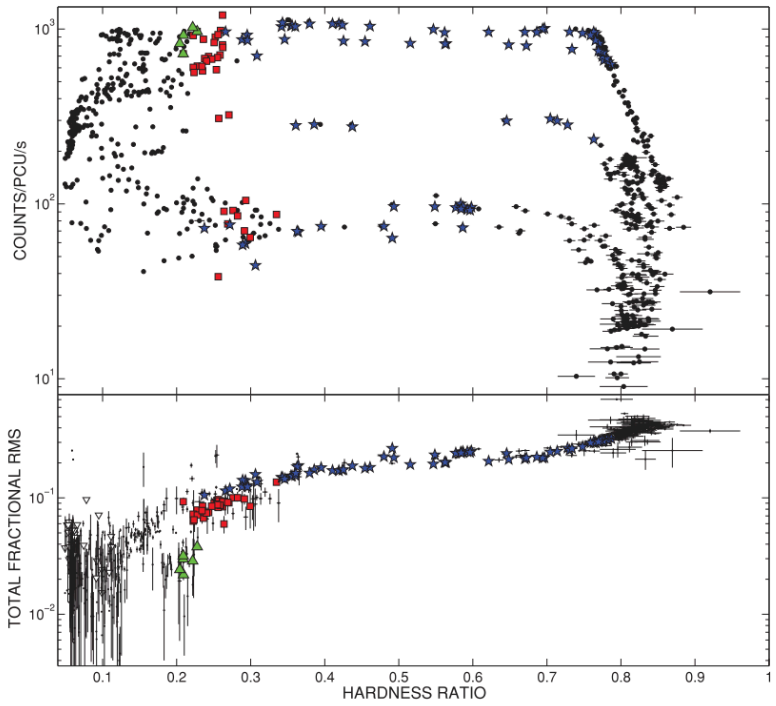


Figure 2.4: Top panel: HID for the 2002, 2004, 2007 and 2010 outburst of GX 339-4. Each point represents a single RXTE observation. Blue stars mark type C QPOs, red squares mark type B QPOs and green triangles mark type A QPOs. Black dots mark all the other RXTE observations of GX 339-4 that do not show low-frequency QPOs. Bottom panel: corresponding Rms–Hardness Diagram (RID). Empty triangles stand for upper limits. (From Motta et al., 2011 [48])

2.1.3 Spectral and Temporal Evolution of Low-Mass Black Hole X-ray Binaries

Hardness-Intensity Diagrams and RMS Evolution

The spectral and temporal evolution of low-mass black hole X-ray binaries (LMXBs) during outbursts can be effectively described using Hardness-Intensity Diagrams (HIDs), Hardness-RMS Diagrams (HRDs), and RMS-Intensity Diagrams (RIDs) (see Figure 2.4 and Figure 2.5). The HID tracks the evolution of spectral hardness with accretion rate, while HRDs and RIDs represent the variability properties as functions of accretion rate.

Phenomenologically, most sources exhibit a counterclockwise "q"-shaped loop in their HIDs during outbursts, where the luminosity differs significantly between the rise and decay phases at the same hardness. This behavior, termed "hysteresis," reflects the intrinsic complexity of accretion physics. In parallel, Power Density Spectra (PDS) evolve significantly during outbursts, revealing distinct temporal variability characteristics (see Figure 2.6). These properties provide a basis for classifying spectral states during outbursts [5, 49–51].

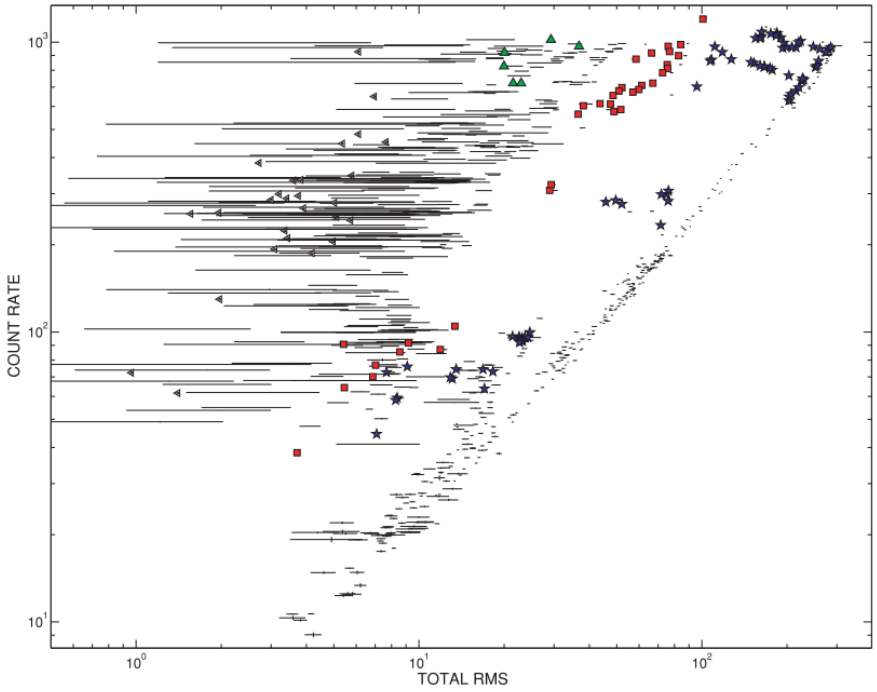


Figure 2.5: Rms-Intensity Diagram (RID) for the 2002, 2004, 2007 and 2010 outburst of GX 339-4. The symbols follow the same criteria as in Figure 2.5. (From Motta et al., 2011 [48])

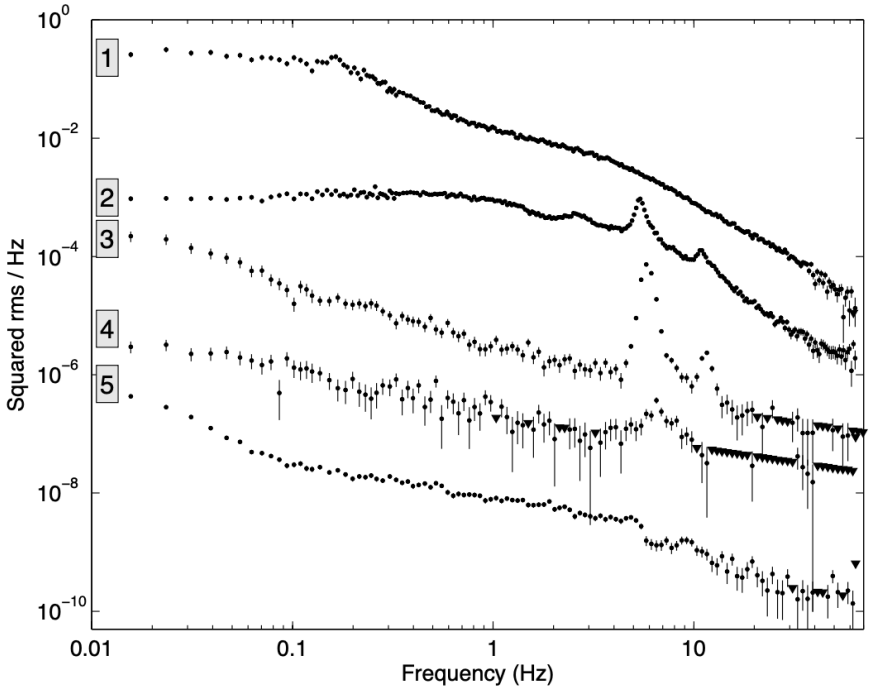


Figure 2.6: Examples of the five types of PDS described in the text (labeled on the left). The data are from the 2002/2003 outburst GX 339-4 and correspond to the energy range 3.8–21.2 keV. The PDS are shifted in power for clarity. (From Belloni et al., 2010 [50])

Spectral States and Temporal Properties

Low-Hard State (LHS). During the early and late stages of an outburst, the system resides in the Low-Hard State (LHS). In this state, the accretion rate undergoes significant changes, but the spectral hardness remains high. The spectrum is predominantly composed of three components:

- A multi-temperature blackbody component from the accretion disk (Diskbb),
- A power-law component with a high-energy cutoff attributed to a hot corona or jet (cutoffpl),
- Reflection features from the disk-corona interaction.

The PDS in this state typically shows strong broadband noise (30–40% RMS) and occasionally low-frequency quasi-periodic oscillations (LFQPOs) of type C (see PDS labeled 1 in Figure 2.6).

Transition to High-Intermediate State (HIMS). As the system evolves, the accretion rate increases, leading to a transition into the High-Intermediate State (HIMS). In this state, the spectral hardness decreases, and the overall RMS drops to 10–20%. The QPOs transition from type C to type B, and the PDS shifts towards weaker variability dominated by low-amplitude noise (see PDS labeled 2–3 in Figure 2.6). This state is characterized by rapid spectral changes as the system approaches the soft-intermediate state (SIMS).

High-Soft State (HSS). In the High-Soft State (HSS), the disk component dominates the spectrum, with minimal contributions from non-thermal emission. The PDS is weak, with RMS values below 1%. Occasionally, weak type A QPOs can be observed in the 10–30 Hz range. This state corresponds to the peak of accretion efficiency (see PDS labeled 4–5 in Figure 2.6).

Return to Low-Hard State. As the system transitions back to quiescence, it re-enters the Low-Hard State. Although the RMS and spectral hardness return to values similar to the rise phase, the hysteresis effect causes notable differences in the overall spectral evolution.

2.1.4 Accretion Flow Models During Outbursts

During outbursts, two distinct accretion flows can be identified based on the evolution of the spectral components and hardness ratios:

- A cold, optically thick, and geometrically thin accretion flow (standard thin disk; SS).
- A hot, optically thin, and geometrically thick flow (Advection-Dominated Accretion Flow; ADAF).

Standard Thin Disk (SS)

The Standard Thin Disk (SS) model describes a geometrically thin and optically thick accretion flow. Proposed by Shakura et al. (1973) [47], this model has been widely applied to X-ray binaries, active galactic nuclei (AGN), and other systems involving accreting compact objects. In the SS disk, the accretion flow is radiatively efficient, and the disk remains geometrically thin with subsonic orbital velocities. The temperature distribution along the radial axis results in a multi-temperature blackbody spectrum.

The total spectral flux from the disk can be expressed as:

$$F(E) = \frac{4\pi E^3 \cos\theta}{c^2 D^2 h^2} \int_{R_{\rm in}}^{R_{\rm out}} \frac{R\, dR}{e^{E/kT_{\rm eff}(R)} - 1}, \tag{2.9}$$

where $T_{\rm eff}(R)$ is the effective temperature of the disk at radius R. Rewriting the above integral in terms of temperature, we have:

$$F(E) = \frac{8\pi}{3} r_{\rm in}^2 \cos\theta \int_{T_{\rm out}}^{T_{\rm in}} \left(\frac{T}{T_{\rm in}}\right)^{-11/3} B(E,T) dT/T_{\rm in}, \tag{2.10}$$

where $B(E,T)$ represents the Planck function, and $T_{\rm in}$ and $T_{\rm out}$ denote the temperatures at the inner and outer edges of the disk, respectively.

The effective temperature at a given radius R is given by:

$$T_{\rm eff}(R) = \left(\frac{3G\dot{M}M}{8\pi R^3 \sigma_B}\right)^{1/4} \left[1 - \left(\frac{R_{\rm in}}{R}\right)^{1/2}\right]^{1/4}, \tag{2.11}$$

where $\dot{M}$ is the accretion rate, M is the mass of the compact object, σ_B is the Stefan-Boltzmann constant, and $R_{\rm in}$ is the inner radius of the accretion disk. The inclination angle θ describes the angle between the disk plane and the observer's line of sight, while D is the source distance.

For $R \gg R_{\rm in}$, the temperature distribution follows a power law, $T \propto R^{-3/4}$. Thus, the temperature profile at each radius defines the emission, with the maximum temperature reached at the innermost stable circular orbit ($R_{\rm in}$). The disk emission is characterized by two primary parameters:

- $R_{\rm in}\cos(\theta)^{1/2}$, which determines the cutoff in the spectral energy distribution,
- $T_{\rm in}$, which represents the maximum temperature of the disk.

The disk's emission is dominated by photons with energies above $2kT_{\rm in}$, forming a blackbody spectrum that peaks around $0.77T_{\rm in}$. These characteristics make the SS disk an essential model for interpreting X-ray spectra and understanding accretion processes in compact-object systems.

Advection-Dominated Accretion Flow (ADAF)

The Advection-Dominated Accretion Flow (ADAF) model, proposed by Narayan and Yi [52] and Abramowicz et al. [53], describes an accretion flow that is radiatively

inefficient but dynamically stable. This model provides an effective explanation for the hard state observed during the onset of outbursts in black hole X-ray binaries, as well as their quiescent states. Subsequent studies [49] extended the ADAF framework to interpret the transition from hard to soft states during outbursts.

In the ADAF regime, the density of the accretion flow is low, and the mean free path of particles is large, allowing ions to retain most of their energy without radiative losses. This leads to inefficient radiation and a high-temperature, optically thin plasma. Despite its inefficiency, ADAF can still support accretion through viscous heating, which balances the energy lost to advection. The system transitions to an efficient accretion regime as the accretion rate increases, leading to the development of a standard thin disk (SS disk). This transition is often used to explain the evolution from the hard state to the soft state during black hole outbursts. The ADAF model predicts a critical accretion rate, $\dot{M}_{\rm crit} \sim \alpha^2$, below which the ADAF regime is stable. Here, α represents the viscosity parameter. The maximum accretion rate at which ADAF can exist corresponds to $\dot{M}_{\rm low}$, typically on the order of $2.6 \times 10^{-8} M_\odot\,{\rm yr}^{-1}$. Between $\dot{M}_{\rm low}$ and $\dot{M}_{\rm crit}$, the accretion flow can exhibit a hybrid state, where both ADAF and SS disk components coexist.

Figure 2.7 illustrates the parameter space of ADAF and SS disk configurations, highlighting the accretion rate thresholds for these regimes. During outbursts, ADAF explains the transition between low-hard and high-soft states. In this process, high-energy electrons in the inner regions of the disk scatter thermal photons from the SS disk, generating significant non-thermal emission (hard X-rays). As the accretion rate increases, the ADAF region shrinks, and the flow transitions into a fully radiatively efficient SS disk. The ADAF model has become a cornerstone for interpreting the spectral and temporal evolution of black hole systems, particularly in explaining the hard state and the transition to the soft state during outbursts [49, 54]. The transition between accretion regimes offers a unique opportunity to study the interaction between the accretion disk, corona, and jet. These findings contribute to the broader understanding of black hole accretion processes and their role in high-energy astrophysical phenomena.

X-ray Variability in time domain

The temporal variability, often characterized by QPOs, arises from the dynamic interplay between the disk, corona, and magnetic fields. QPOs, classified into low-frequency (LF) and high-frequency (HF) categories, serve as diagnostics for the inner disk regions and relativistic effects [50].

Lense-Thirring Precession

Lense-Thirring precession arises from the additional torque exerted on the accretion flow by the frame-dragging effect. When the angular momentum of the accretion flow is misaligned with the black hole's spin axis, the differential precession caused by frame-dragging leads to an additional torque, influencing the flow dynamics. This torque can drive the inner accretion flow to align with the black hole's spin axis. This alignment leads to the precession of the accretion flow at specific radii, which manifests observationally in phenomena such as QPOs in the power density spectra of X-ray

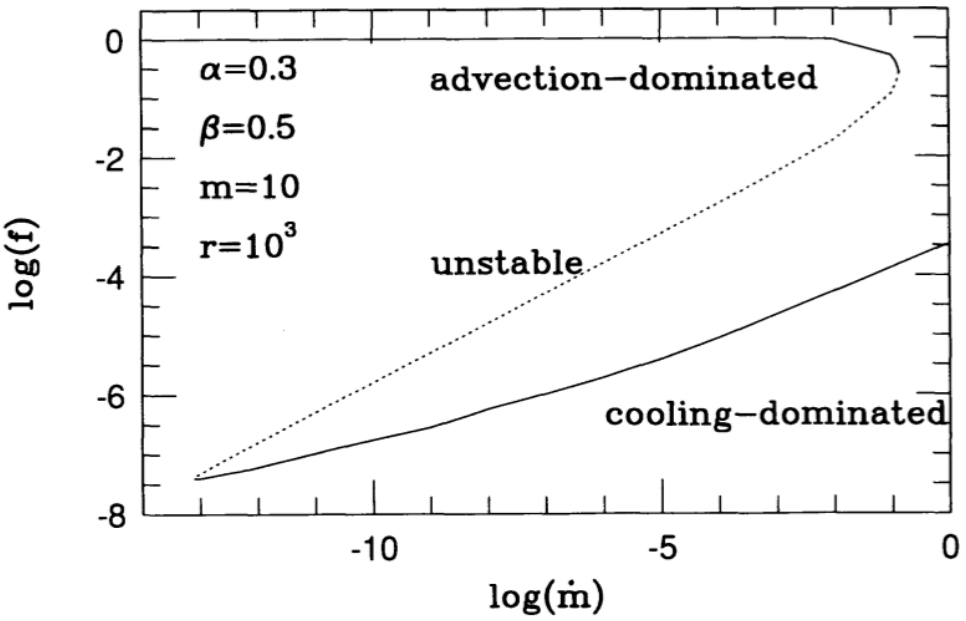


Figure 2.7: The three solution branches for an accreting $10M_\odot$ black hole at a radius of $r = 10^3$. The uppermost branch is the new advection-dominated branch. The lowermost branch corresponds to the standard cooling-dominated thin accretion disk solution. These two stable branches are connected by an unstable middle branch, indicated by a dotted line. (From Narayan et al., 1995 [52])

binaries [55].

Power Density Spectrum (PDS) and Quasi-Periodic Oscillations (QPOs)

To investigate the origin of QPOs, we first introduce the characteristics of QPOs and PDS. As mentioned earlier, during state transitions in black holes, significant spectral and timing variations are observed. The PDS changes significantly, consisting of two main components: broad-band noise and QPOs. The noise component is usually classified into Band-Limited Noise (BLN) and Power-Law Noise (PLN).

In the BLN component, the noise remains constant at low frequencies but decays rapidly above a break frequency (f_{break}). For PLN, the PDS follows the power-law form:

$$P(f) \propto f^{-\gamma}, \quad \text{where } \gamma = 0 \text{ for white noise and } \gamma \leq 2 \text{ for red noise.} \tag{2.12}$$

QPOs generally exhibit central frequencies in the range of 0.1–10 Hz and are associated with accretion dynamics in the inner region of the accretion disk. Low-Frequency QPOs (LFQPOs) are defined with Q values greater than 2, where Q is the quality factor given by:

$$Q = \frac{f_0}{\sigma}, \tag{2.13}$$

where f_0 represents the central frequency, and σ is the width of the peak. The

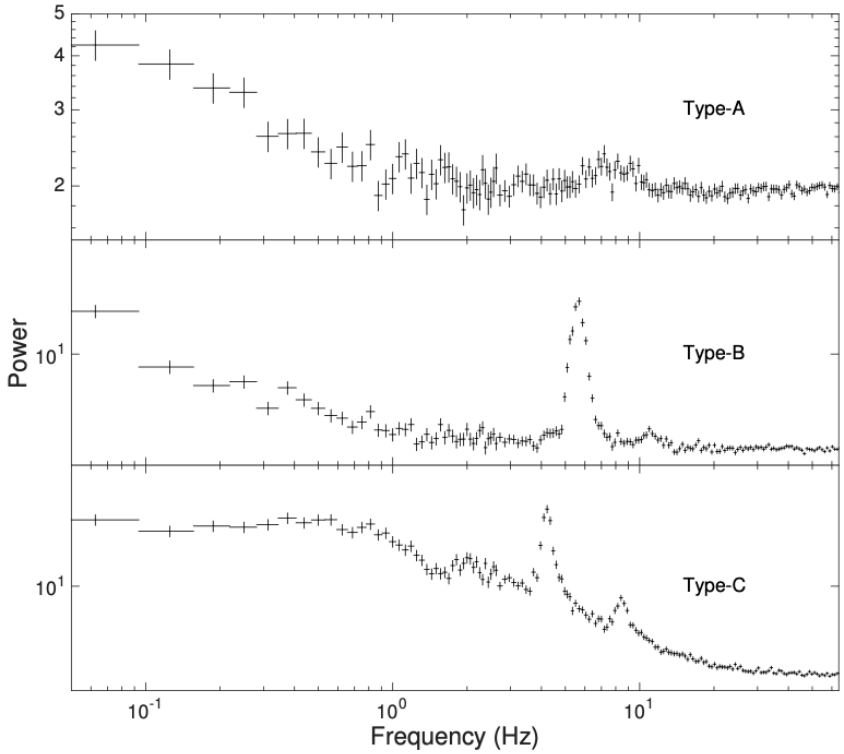


Figure 2.8: Examples of types A, B and C QPOs from our GX 339-4 observations. (From Motta et al., 2011 [48])

Lorentzian function used to describe QPOs is:

$$P(f) \propto \frac{\sigma}{(f - f_0)^2 + (\sigma/2)^2}. \tag{2.14}$$

The QPO strength is typically measured by the fractional root-mean-squared (RMS) amplitude, providing insights into the variability of the X-ray emission. Through integrating specific frequency ranges of the PDS, the contribution of QPOs to the total RMS variability can be quantitatively analyzed. This approach is crucial for understanding the timing properties of black hole binaries and the physical mechanisms driving accretion and ejection processes in these systems.

Classification of Low-Frequency QPOs

Low-frequency QPOs exhibit distinct differences in their RMS amplitude, PDS shape, and frequency. Based on these characteristics, low-frequency QPOs can be classified into three main types: Type-C, Type-B, and Type-A QPOs, as illustrated in Figure 2.8.

Type-C QPO: Type-C QPOs are the most commonly observed QPOs in black hole systems and exhibit the strongest signals. They have a high quality factor $Q \geq 8$ and RMS amplitude reaching up to $\sim 20\%$. The centroid frequency of Type-C QPOs can vary from a few mHz to around 20 Hz. These QPOs display a gradual increase in frequency and RMS amplitude as the accretion rate rises, often accompanied by

harmonic and overtone signals [48]. The PDS of Type-C QPOs frequently includes a broad noise component (BLN), with an RMS amplitude of $\sim 40\%$, which is correlated with the central frequency of the QPO [56].

Type-B QPO: Type-B QPOs typically have frequencies in the range of 4–6 Hz, often accompanied by weak harmonic and overtone signals. These QPOs exhibit relatively strong peaks with $Q \geq 6$ and RMS amplitude of 4–6%. Type-B QPOs are usually observed during transitions between hard-intermediate and soft-intermediate states. Occasionally, a weak red noise component below ~ 0.1 Hz can be detected in the PDS. Type-B QPOs are transient in nature and often vanish abruptly or evolve into Type-C QPOs. The appearance and disappearance of Type-B QPOs are associated with discrete jet ejections and changes in the inner accretion flow [57, 58].

Type-A QPO: Type-A QPOs are relatively rare and have a centroid frequency concentrated between 6–8 Hz. These QPOs have low quality factors, with $Q \leq 3$, and weak RMS amplitude of $\sim 2\%$. They are typically observed in soft spectral states and exhibit weak or no harmonic signals. The PDS of Type-A QPOs is dominated by low-amplitude noise components.

The distinct characteristics of Type-C, Type-B, and Type-A QPOs provide crucial insights into the physical processes of accretion flows and their coupling with relativistic jets. These classifications help reveal the dynamic evolution of X-ray binaries across different accretion states.

The Origin and Non-Thermal Nature of QPOs

The detection and study of LFQPOs have persisted for decades, yet their physical origin and mechanisms remain uncertain. Observationally, low-frequency QPOs are tightly associated with accretion processes and variability in X-ray binaries, providing valuable insights into the physics of accretion flows and relativistic phenomena near compact objects.

Currently, two dominant models explain the origin of low-frequency QPOs: the accretion instability model and the Lense-Thirring precession model. The accretion instability model attributes QPOs to the interaction between accretion flows and magnetohydrodynamic instabilities [59–61]. In contrast, the Lense-Thirring precession model associates QPOs with the relativistic frame-dragging effect, leading to the precession of the inner accretion flow or outflow e.g. disk, corona, and jet [55, 62–64].

Low-Frequency QPO Characteristics In the context of geometrically thick accretion flows, the Lense-Thirring precession model aligns well with observational findings. For example, within the framework of disk instability models and ADAF, the Type-C QPOs exhibit clear correlations between their frequencies and the accretion energy distribution across the disk. With increasing energy, the QPO root-mean-squared (RMS) amplitude also increases, reaching maximum values in the 10–50 keV range, which supports their non-thermal nature [63, 65].

RMS and Energy Correlations A particularly noteworthy aspect is the relationship between RMS and QPO frequencies across various energy ranges. For instance, RXTE observations were limited to energies below 30 keV, where RMS variability remained poorly constrained. Recent studies, such as those using Insight-HXMT, extended the energy range to 50 keV and beyond, revealing strong RMS dependencies up to 100 keV for sources like MAXI J1535-571. Similarly, Ma et al. [64] reported robust QPO RMS evolution up to 250 keV in MAXI J1820+070, underscoring the non-thermal nature of QPOs.

New Perspectives on QPO Studies Through these observations, it becomes evident that the RMS amplitude serves not only as a tracer for QPO energy dependencies but also as a diagnostic tool for probing accretion flow dynamics and the energetic contributions of jet emission. Recent efforts have explored correlations between QPO RMS and their harmonic modes, providing fresh insights into energy partitioning mechanisms in accretion disks. For example, studies of MAXI J1535-571 reveal that RMS amplitudes in QPO signals correspond closely with jet launching regions and accretion instabilities, solidifying the role of RMS in understanding the physics of QPO generation and evolution.

These findings collectively emphasize the importance of extending observational constraints to higher energies and refining theoretical models to capture the full complexity of QPO phenomena. Future research is expected to leverage multi-mission data to further constrain the interaction between accretion dynamics and QPO mechanisms, offering deeper insights into the nature of compact object environments.

2.1.5 Outflows in X-ray Binaries

In X-ray binaries, apart from the accretion flow within the disk (thermal and non-thermal components), outflows such as winds and jets constitute an essential component, closely linked to the system's evolutionary state. These outflows are generally observed in two primary forms: disk winds associated with soft states, and relativistic jets typically linked to hard states.

Disk Winds

Disk winds are commonly detected during the soft spectral state, where the accretion flow is geometrically thin but optically thick. Observations with high-resolution X-ray spectrometers, such as those on Chandra, XMM-Newton, and Suzaku, have revealed strong Fe K-shell absorption lines (e.g., Fe XXV and Fe XXVI), indicative of ionized winds originating from the inner regions of the accretion disk . The strength of these winds often correlates with the system's luminosity, suggesting a radiation-driven mechanism. In high-inclination LMXBs, these winds are more prominent [66].

The wind properties, including density, velocity, and ionization state, provide critical insights into the accretion dynamics. The ionization parameter ξ is defined as:

$$\xi = \frac{L}{nr^2}, \tag{2.15}$$

where L is the source luminosity, n is the electron density, and r is the distance from the source. In LMXBs, ξ values typically range between 10^{21}–10^{24} cm^{-2}, reflecting the highly ionized nature of these outflows.

Outflow Mechanisms

The origins of these outflows are attributed to three primary mechanisms:

- **Thermal Driving:** Disk winds driven by thermal pressure gradients, often observed in soft states. Thermal driving occurs in systems where the accretion disk is heated to temperatures exceeding 10^7 K. In such scenarios, the thermal energy is sufficient to overcome the gravitational potential and launch material from the disk's surface. The driving radius, R_c, depends on the sound speed and temperature of the disk. For optically thin regions, Begelman et al. (1983) showed that thermal driving can occur at radii larger than $0.1R_c$, where R_c is the Compton radius [67, 68].

- **Radiation Driving:** Outflows accelerated by radiation pressure on highly ionized gas. Radiation pressure can transfer momentum to the disk material through scattering processes. This mechanism is particularly effective when the electron scattering optical depth, τ_e, is significant. The radiation-driven momentum transfer can be expressed as:

$$\dot{p}_w = \tau_e \frac{L}{c}, \tag{2.16}$$

  where L is the luminosity, and c is the speed of light. Systems with high luminosity approaching the Eddington limit can exhibit strong radiation-driven winds. However, Reynolds (2012) noted that this mechanism is often accompanied by thermal driving [69].

- **Magnetic Driving:** Magnetocentrifugal acceleration of outflows, typically linked to jet formation in hard states. Magnetic fields within the disk can exert magnetic pressure to drive outflows. Blandford & Payne (1982) proposed that magnetic field lines anchored to the disk can accelerate material to form winds [70]. The Alfven radius, R_A, determines the region where magnetic forces dominate over gravity and thermal pressure. Studies by Pudritz et al. (2007) and Reynolds (2012) suggest that this mechanism is crucial for systems with strong magnetic fields [69, 71].

Recent studies, such as Kong et al. [72], have observed rapid transitions between winds and jets in systems like GRS 1915+105, demonstrating the dynamic nature of accretion-related outflows. These transitions occur on timescales of seconds, underscoring the complexity of the accretion-ejection interplay.

Outflows in X-ray binaries play a pivotal role in the evolution of these systems. By studying the properties of disk winds and jets, we gain critical insights into the mechanisms governing accretion and their impact on the surrounding environment.

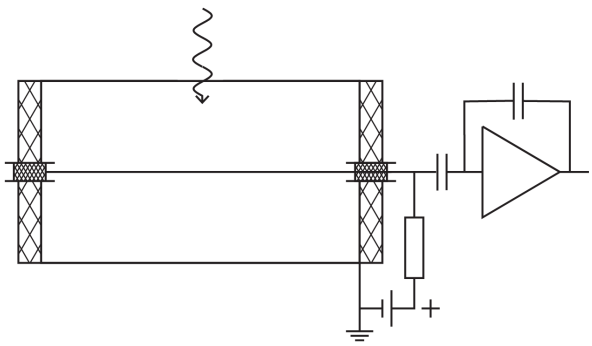


Figure 2.9: Single wire proportional counter (from E. Pfeffermann, 2008) [75]

2.2 Major Satellite Missions and Their Contributions

X-ray astronomy has benefited immensely from the development and deployment of numerous space-based observatories, each contributing unique capabilities for observing the high-energy universe. These missions have been crucial in advancing our understanding of X-ray binaries, neutron stars, black holes, and other compact objects. In addition to the satellites utilized in this study, several other major X-ray observatories have played key roles in the field. This section reviews some of the most significant X-ray satellite missions and their contributions to high-energy astrophysics.

2.2.1 Advancements in X-ray Astronomical Instrumentation

Scintillation counters were one of the earliest types of detectors used in X-ray astronomy, providing the ability to detect high-energy photons with relatively high sensitivity. These detectors operate based on the principle of scintillation: when X-rays interact with a scintillating material (such as sodium iodide doped with thallium, NaI(Tl)), they produce light flashes. These light flashes are subsequently converted into electrical signals by a photomultiplier tube (PMT). The amplitude of the electrical signal is proportional to the energy of the incident X-ray photon, enabling scintillation counters to measure both the intensity and energy of X-ray sources.

The development of proportional counters marked a transformative phase in the field of X-ray astronomy. These detectors, with their ability to provide moderate energy resolution and high detection efficiency, became integral components of numerous space-based observatories. Early X-ray astronomy missions, such as Uhuru X-ray Observatory (Uhuru, 1970), High Energy Astronomy Observatory-1 (HEAO-1,1977), and European X-ray Observatory Satellite (EXOSAT 1983), employed proportional counters to measure cosmic X-ray sources with unprecedented sensitivity and accuracy [19, 73].

The basic principle of a proportional counter relies on gas ionization. Incoming X-rays interact with the detector gas, producing electron-ion pairs. These primary electrons are subsequently accelerated by a strong electric field, initiating a cascade of secondary ionizations. The resulting amplified charge provides a proportional signal to the energy of the incident X-ray photon, enabling precise spectral analysis [74]. A gas-filled cylindrical conductive tube with a coaxial thin wire as shown in Figure 2.9 is the simplest geometry of a proportional counter[75].

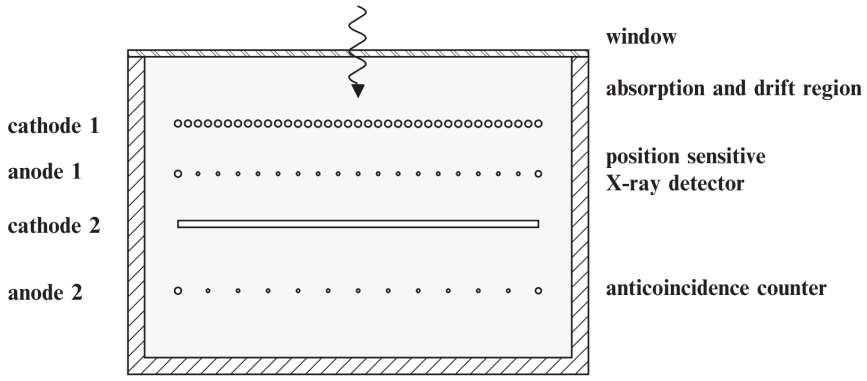


Figure 2.10: Multiwire proportional counter for X-ray astronomy (from E. Pfeffermann, 2008) [75]

One of the significant advancements in proportional counter technology was the implementation of large-area multiwire configurations (shown in Figure 2.10), which increased the detection area and improved spatial resolution. Detectors aboard satellites such as the Rossi X-ray Timing Explorer (RXTE, 1995) proportional counter array (PCA) featured multiple layers of anode wires and cathode grids, allowing for efficient background rejection and enhanced sensitivity to faint X-ray sources. These improvements enabled the detailed study of phenomena like QPOs and spectral state transitions in X-ray binaries [76].

Further refinements included the introduction of quench gases, such as CO_2 or CH_4 , to stabilize the electron avalanche process and minimize detector aging effects. The proportional counters on EXOSAT and later missions employed optimized gas mixtures to improve energy resolution and longevity under the harsh conditions of space. These advancements were particularly crucial for studying transient X-ray sources, where consistent detector performance over extended observation periods was essential [75].

Additionally, proportional counters played a vital role in exploring hard X-ray emissions. Detectors on missions like Ginga (1987) with the large area counter (LAC) and Beppo Satellite per Astronimia a raggi X (BeppoSAX, 1996) were designed to operate across extended energy ranges, capturing high-energy X-rays crucial for probing relativistic processes near compact objects. The ability to detect photons up to tens of keV significantly broadened the scope of X-ray astronomy, providing insights into the physics of accretion disks and jet formation [76].

Despite their successes, proportional counters have limitations, including moderate energy resolution and susceptibility to background noise. However, their relatively simple design, robustness, and adaptability to various space environments have ensured their continued relevance in X-ray astronomy. The legacy of these detectors is evident in their contributions to our understanding of neutron stars, black holes, and the broader dynamics of high-energy astrophysical systems.

Aperture modulation telescopes are another one designed to measure X-ray intensities from celestial sources by modulating the incoming X-ray flux through a predefined aperture pattern. This technique is particularly effective for imaging and source localization. By employing rotating grids or collimators, aperture modulation telescopes can reconstruct the position and structure of X-ray sources even in crowded fields [75]. It provides an actual coded-mask telescope. Early missions such as UHURU

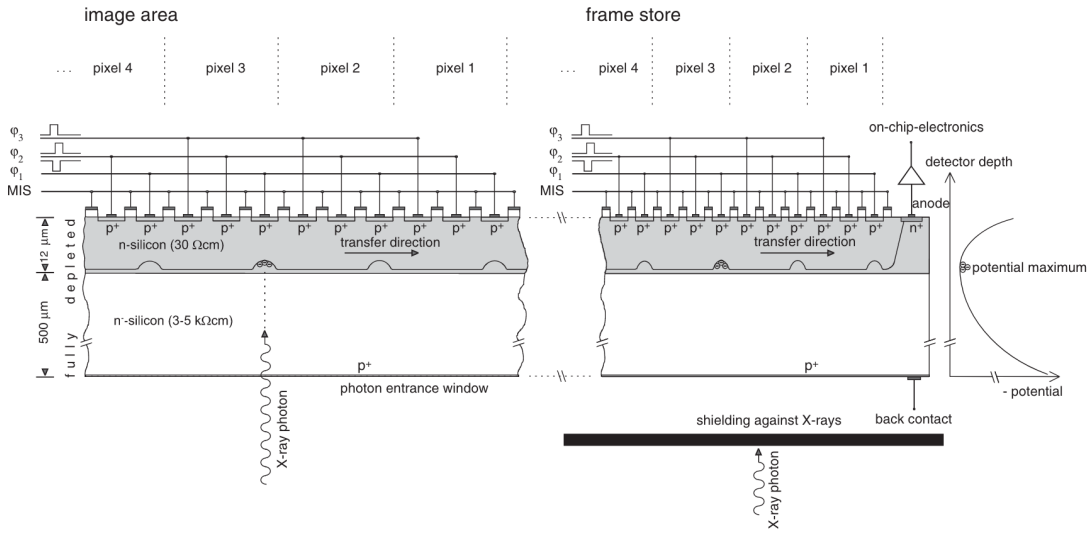


Figure 2.11: Schematic cross-section through a frame-store pnCCD channel and to the right electric potential in the device vs. depth. The chip thickness of about 450 mm is fully depleted by reverse-biased pn-junctions on the front and back sides of the device. The signal charge is stored and transferred in a depth of about 7 mm below the front side. The frame store of the back-illuminated pnCCD is shielded against radiation. Each transfer channel is equipped with an anode and a JFET for on-chip signal amplification. (from Meidinger et al., 2006) [80]

and HEAO-1 utilized aperture modulation to map the X-ray sky with unprecedented sensitivity and spatial resolution.

Aperture Modulation Telescopes and coded-mask telescopes share a similar principle of modulating incoming X-rays to reconstruct source positions. While aperture modulation uses simpler rotating collimators or grids, coded-mask telescopes employ a more advanced fixed mask with a predefined pattern, allowing for improved imaging capabilities and higher angular resolution. Coded-mask telescopes, such as those used in INTEGRAL and Swift-BAT, are a direct evolution of aperture modulation designs, optimized for modern astrophysical observations.

These telescopes are particularly beneficial for point-source detection and sky surveys where high angular resolution is secondary to sensitivity. However, their inability to produce direct images limited their application as more advanced imaging techniques were developed.

Charge-coupled devices (CCDs) revolutionized X-ray astronomy by offering high-resolution imaging and spectroscopy in a compact format. CCDs are semiconductor devices that detect X-rays by converting incident photons into electron-hole pairs. The number of generated charge carriers is proportional to the photon energy, allowing for precise energy resolution [77, 78]. The 3-phase frame-store pnCCD is shown in Figure 2.11, which is a chip fully depleted by reverse-biased pn-junctions. Modern X-ray missions, such as XMM-Newton, employ CCD detectors in their European Photon Imaging Camera (EPIC), which enables simultaneous imaging and spectroscopy across a broad energy range (0.2–12 keV) [79].

The first mission dedicats to imaging X-ray polarimetry, the Imaging X-ray Polarimetry Explorer (IXPE, 2021) utilizes Gas Pixel Detectors (GPDs) for polarimetry measure-

ments. These detectors consist of a gas-filled chamber where incoming X-ray photons interact with gas atoms to produce electron clouds. The spatial distribution and direction of the electrons are tracked using a finely pixelated readout system, allowing IXPE to measure the degree and angle of X-ray polarization [81].

In summary, the evolution of X-ray astronomical instrumentation has been a cornerstone of modern astrophysical discoveries. From early proportional counters and scintillation detectors to advanced CCDs, coded-mask telescopes, and polarimetric detectors, each innovation has significantly enhanced sensitivity, energy resolution, and imaging capabilities. These advancements have enabled the detailed study of diverse X-ray sources, such as black holes, neutron stars, and galaxy clusters, while missions like NuSTAR, NICER, eROSITA, HXMT, and IXPE continue to push the boundaries of X-ray astronomy. Together, these technological breakthroughs provide a deeper understanding of the high-energy universe and its underlying physical processes.

2.2.2 Advancements in Observatories

The development of X-ray observatories has been a pivotal aspect of modern astrophysics, providing groundbreaking insights into the high-energy universe. Over the past several decades, advancements in satellite technology have significantly enhanced the ability to observe X-ray emissions from compact objects such as black holes and neutron stars, as well as from supernova remnants and active galactic nuclei. This section provides an overview of some of the most influential X-ray observatories, their contributions, and their technological advancements.

Early X-ray observatories, such as Uhuru, HEAO-1, and EXOSAT, marked the first dedicated efforts to systematically study X-ray sources in the universe [17, 75]. Uhuru, launched by NASA, was the first satellite dedicated to X-ray astronomy and provided the first all-sky survey of X-ray sources, leading to the discovery of many X-ray binaries and supernova remnants. The subsequent HEAO-1 and EXOSAT missions expanded on this foundation by introducing proportional counters and extended monitoring capabilities, enabling more detailed studies of transient X-ray phenomena.

The 1990s witnessed a significant leap in X-ray observational technology. The RXTE brought high-time-resolution observations to the forefront, revolutionizing the study of variability in X-ray binaries [82]. Simultaneously, BeppoSAX pioneered the study of gamma-ray bursts (GRBs) by detecting their X-ray afterglows, allowing the precise localization of these events and linking them to distant galaxies. Chandra X-ray Observatory (1999) further advanced the field with its exceptional angular resolution, producing the sharpest X-ray images of cosmic sources to date. Its observations of supernova remnants, accretion flows, and pulsar wind nebulae have provided unparalleled insights into high-energy astrophysical processes [83].

In the 21st century, X-ray observatories have continued to evolve, incorporating cutting-edge technologies to address increasingly complex scientific questions. The Suzaku satellite (2005) introduced instruments with high spectral resolution, allowing detailed studies of relativistic reflection and the hard X-ray spectra of compact objects [84]. The Swift Gamma-Ray Burst Mission (2004) expanded the study of GRBs with its rapid-response capabilities, while its X-ray Telescope (XRT) contributed to the understanding of transient X-ray sources [85].

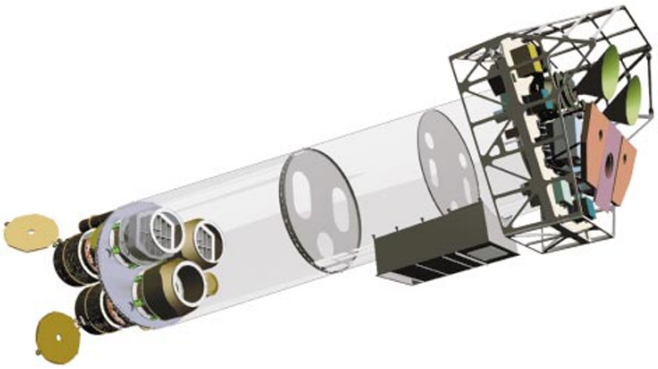


Figure 2.12: "Open" view of the XMM-Newton observatory. To the left the three mirror modules (with the RGA units mounted behind two of them) can be seen, while at the right the back end of the instrument platform with all the radiators is visible (from Jansen et al., 2001) [26]

The launch of NuSTAR (2012) marked a major breakthrough in high-energy X-ray astronomy, being the first satellite capable of focusing hard X-rays up to 79 keV. Its imaging capabilities have been critical in probing the coronae of black holes and the relativistic effects near the innermost stable circular orbit (ISCO) [15]. Meanwhile, the NICER mission (2017) has specialized in timing studies of neutron stars, offering precision measurements of pulsars and accreting binaries [86]. The eROSITA (2019), with its wide-field X-ray imaging, has conducted the most sensitive all-sky X-ray survey to date, uncovering thousands of new sources [27]. Finally, The insight-HXMT (2017) has contributed to broadband spectral studies, particularly in the hard X-ray band, facilitating investigations of accretion physics and relativistic jets [87].

These observatories represent a continuous trajectory of innovation, each building on the achievements of its predecessors. From mapping the X-ray sky to resolving faint sources and probing relativistic environments, these missions have profoundly advanced our understanding of the universe's most extreme environments. Looking ahead, the legacy of these observatories will inspire the next generation of X-ray missions, paving the way for even deeper explorations of high-energy astrophysics.

XMM-Newton

The XMM-Newton satellite, launched by the European Space Agency (ESA) on December 10, 1999, is one of the most successful and versatile X-ray observatories to date. It was designed to study a wide range of high-energy astrophysical phenomena, from black holes and neutron stars to galaxy clusters and supernova remnants. With its exceptional sensitivity, broad energy range, and long operational lifetime, XMM-Newton has significantly advanced our understanding of the X-ray universe [26].

This schematic (shown in Figure 2.12)illustrates the internal architecture of the XMM-Newton observatory. The three mirror modules on the left, equipped with reflection grating array (RGA) units, demonstrate the observatory's advanced optical capabilities for focusing X-rays. To the right, the back end of the instrument platform, complete with radiators, highlights the engineering innovations essential for thermal management and operational stability in space. This design underscores XMM-Newton's precision and efficiency in conducting X-ray observations of celestial phenomena. To enhance

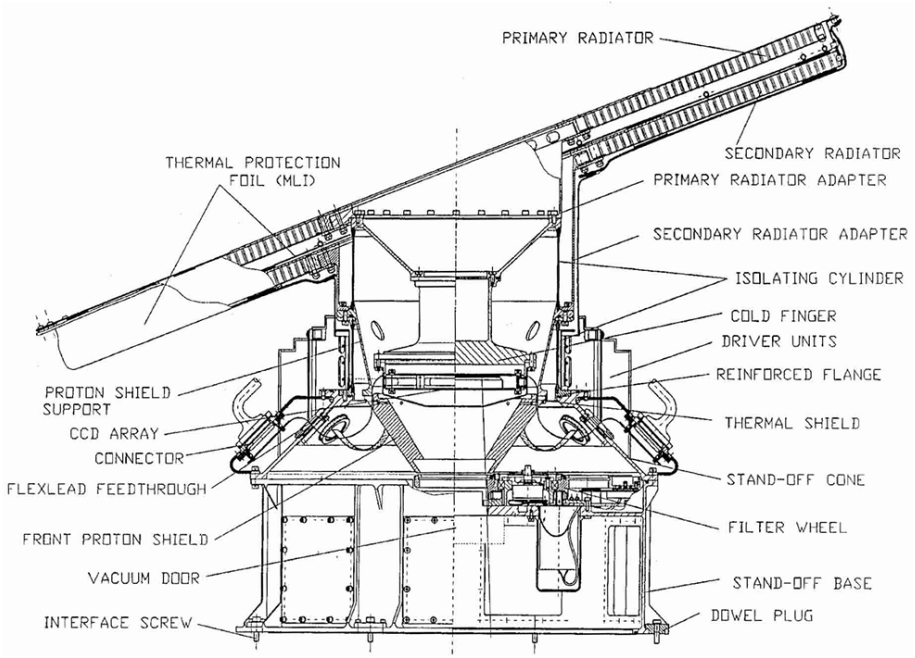


Figure 2.13: Mechanical structure of the pn-CCD camera system. X-rays imaged through the telescope enter the detector from the bottom (from Strüder et al., 2001) [79]

the understanding of X-ray imaging technology employed in astronomical observations, Figure 2.13 illustrates the detailed mechanical structure of the pn-CCD camera system. The figure highlights key components, such as the CCD array for detection, the proton shield for protection against charged particles, and the thermal shield to maintain operational stability. These features collectively ensure the reliability and sensitivity of the instrument in the harsh environment of space.

XMM-Newton's primary objectives include:

- Conducting detailed spectroscopic and imaging studies of X-ray sources across a wide energy range (0.2–12 keV).
- Investigating the properties of hot gas in galaxy clusters and intergalactic filaments.
- Understanding the physical processes driving X-ray emissions in compact objects such as black holes, neutron stars, and white dwarfs.
- Exploring the evolution of active galactic nuclei (AGN) and their role in galaxy evolution [26].

XMM-Newton is equipped with three advanced X-ray telescopes, each employing a Wolter-I mirror design. These telescopes focus X-rays onto their respective detectors, achieving exceptional sensitivity and spatial resolution. Key instruments onboard XMM-Newton include:

- **European Photon Imaging Camera (EPIC):** Comprising three cameras (two MOS detectors and one PN detector), EPIC provides high-resolution imaging and moderate spectral resolution across a broad energy range.

- **Reflection Grating Spectrometer (RGS):** Designed for high-resolution spectroscopy in the soft X-ray band (0.2–2 keV), the RGS enables detailed studies of emission and absorption lines in various astrophysical environments.
- **Optical Monitor (OM):** A unique feature of XMM-Newton, the OM is a UV/optical telescope that provides simultaneous multi-wavelength coverage, complementing X-ray observations [79].

With its large effective area and long uninterrupted observing periods, XMM-Newton excels in studying faint and extended X-ray sources, such as galaxy clusters and supernova remnants.

XMM-Newton has made numerous groundbreaking discoveries, including:

- **Galaxy Clusters and Cosmology:** XMM-Newton has provided precise measurements of the temperature and metallicity distributions in galaxy clusters, offering insights into their formation and evolution.
- **Relativistic Effects in Accretion Disks:** Observations of Fe Kα emission lines from the inner regions of accretion disks around black holes have revealed relativistic broadening, confirming the effects of strong gravity [42].
- **Neutron Star Emission:** XMM-Newton has enabled detailed studies of the thermal and non-thermal emissions from isolated neutron stars, helping to constrain their magnetic field strengths and cooling mechanisms.
- **AGN Evolution:** By conducting large surveys, XMM-Newton has traced the growth and activity cycles of supermassive black holes, contributing to our understanding of AGN feedback and galaxy evolution [88].
- **Star Formation and Stellar Flares:** XMM-Newton has observed high-energy flares from young stellar objects, shedding light on the processes that drive star formation and magnetic reconnection events.

XMM-Newton has remained operational for over two decades, far exceeding its original mission timeline. Its extensive dataset serves as a cornerstone for multi-wavelength and multi-messenger astronomy, often used in conjunction with data from ground-based observatories and other space missions. XMM-Newton's legacy includes one of the most comprehensive X-ray source catalogs, which continues to drive discoveries across diverse fields in astrophysics.

Future missions, such as Advanced Telescope for High-ENergy Astrophysics (ATHENA), are expected to build on XMM-Newton's achievements by providing even greater sensitivity and spectral resolution. However, XMM-Newton's contributions to high-energy astrophysics remain unparalleled, making it one of the most influential X-ray observatories in history.

NuSTAR

The Nuclear Spectroscopic Telescope Array (NuSTAR) is the first X-ray observatory capable of focusing high-energy X-rays (3–79 keV), providing unprecedented sensitivity

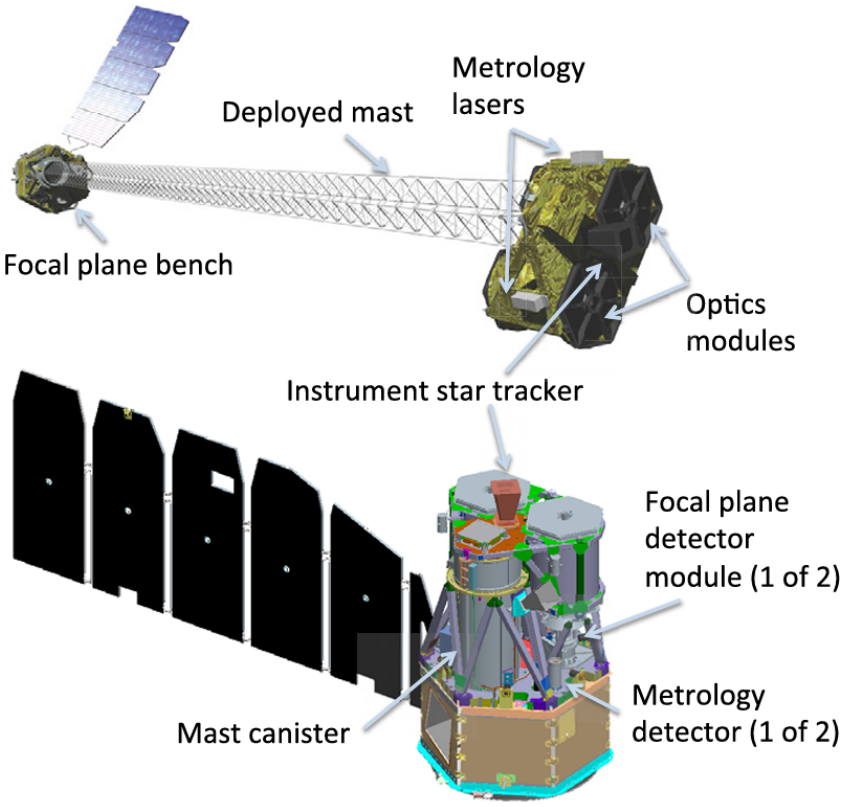


Figure 2.14: Diagram of the observatory in the stowed (bottom) and deployed (top) configurations. (from Harrison et al., 2013) [15]

and spatial resolution in the hard X-ray band. Launched by NASA on June 13, 2012, NuSTAR has revolutionized high-energy astrophysics by enabling detailed studies of compact objects, supernova remnants, and active galactic nuclei (AGN) in the previously challenging hard X-ray regime [15]. This innovative design and configurations of the NuSTAR observatory is shown in Figure 2.14

NuSTAR's primary objectives include:

- Studying the structure and dynamics of supernova remnants, including the distribution of radioactive isotopes like ^{44}Ti.
- Investigating the properties of black hole coronae and measuring the spin of stellar-mass and supermassive black holes through relativistic reflection features.
- Exploring the emission mechanisms in magnetars, neutron stars, and pulsars.
- Constraining the population of obscured AGN and their contribution to the cosmic X-ray background [15].

NuSTAR's ability to detect high-energy X-rays complements other missions, such as Chandra and XMM-Newton, which are optimized for lower energy bands.

NuSTAR employs a unique design to achieve its groundbreaking capabilities:

- **Focusing Optics:** NuSTAR uses two co-aligned telescopes equipped with Wolter-I mirrors, capable of focusing hard X-rays. This allows for significantly

improved sensitivity and spatial resolution compared to previous non-focusing instruments.

- **Focal Plane Detectors:** Each telescope is paired with a Cadmium Zinc Telluride (CdZnTe) detector, which provides high spectral resolution and sensitivity across the energy range of 3–79 keV.
- **Deployable Mast:** NuSTAR features a 10-meter deployable mast that separates the mirrors and detectors, enabling the long focal length required for focusing hard X-rays [15].

This innovative design allows NuSTAR to detect faint sources with high angular resolution, making it a key instrument for studying high-energy phenomena.

NuSTAR has made numerous significant contributions to astrophysics, including:

- **Black Hole Coronae:** NuSTAR has provided critical insights into the properties of black hole coronae, measuring their temperatures, sizes, and dynamics through observations of high-energy spectral features, such as the Compton hump and broad Fe Kα emission lines.
- **Neutron Stars and Magnetars:** The observatory has studied hard X-ray emissions from magnetars and accreting neutron stars, revealing non-thermal emission processes and magnetic field effects.
- **Supernova Remnants:** NuSTAR has mapped the distribution of radioactive ^{44}Ti in supernova remnants like Cassiopeia A, providing insights into explosion mechanisms and nucleosynthesis.
- **AGN Population Studies:** By detecting obscured AGN in the hard X-ray band, NuSTAR has contributed to our understanding of the cosmic X-ray background and the growth of supermassive black holes [15, 89].

Notably, NuSTAR's measurements of black hole spin parameters have advanced our understanding of relativistic effects and the growth history of accreting black holes. NuSTAR's ability to focus hard X-rays has established it as a cornerstone of modern X-ray astronomy. Its data have been widely used in combination with other X-ray observatories, such as Chandra, XMM-Newton, and NICER, to provide comprehensive multi-wavelength analyses of high-energy phenomena. As a pioneer in the hard X-ray band, NuSTAR has paved the way for future missions, such as the planned High-Energy X-ray Probe (HEX-P), which aims to build upon NuSTAR's legacy with enhanced sensitivity and broader spectral coverage.

NICER

The Neutron Star Interior Composition Explorer (NICER) is an X-ray observatory designed specifically for the study of neutron stars and other compact objects. Launched aboard the International Space Station (ISS) on June 3, 2017, as part of NASA's Explorers program, NICER is optimized for high-precision timing and spectroscopy in the soft X-ray band (0.2–12 keV). Its unique design and observational strategy have made it a powerful tool for probing the extreme physics of compact objects [86].

NICER's primary objectives include:

- Measuring the masses and radii of neutron stars with unprecedented precision to constrain the equation of state (EoS) of dense matter.
- Investigating the dynamics of accretion in neutron star and black hole systems, particularly through the detection of QPOs and burst oscillations.
- Studying time-variable phenomena in X-ray binaries, including pulsations, flares, and state transitions.
- Characterizing X-ray emission from isolated neutron stars, magnetars, and other high-energy astrophysical phenomena [86, 90].

NICER also contributes to multi-messenger astrophysics by following up gravitational wave detections of neutron star mergers to study their electromagnetic counterparts.

NICER features a compact X-ray Timing Instrument (XTI) with the following key design elements:

- **56 Concentrator Optics:** NICER uses lightweight, grazing-incidence optics to focus X-rays onto its detectors. These optics provide a large effective area (up to 1,900 cm^2 at 1.5 keV), making NICER highly sensitive to faint X-ray sources.
- **Silicon Drift Detectors (SDDs):** The SDDs measure X-ray energies with high spectral resolution (energy resolution of 85 eV at 1.5 keV) and enable precise photon timing with microsecond accuracy.
- **Time-Resolved Observations:** NICER is capable of high time-resolution studies, allowing for the detection of millisecond pulsations and short-term variability in X-ray binaries.

As a payload on the International Space Station (ISS), NICER benefits from a flexible observational strategy, allowing for frequent target switching and real-time event monitoring. Figure 2.15 illustrates the NICER in both its stowed and deployed configurations. The diagram highlights key components of the instrument, including the X-ray Timing Instrument (XTI), Deploy and Pointing System (DAPS), and supporting modules such as the Main Electronics Box (MEB) and the Modular Power Unit (MPU).

Since its deployment, NICER has made numerous contributions to the study of compact objects:

- **Neutron Star Equation of State:** NICER's precise timing and spectral data have provided the most accurate measurements of neutron star masses and radii, notably for PSR J0030+0451, placing significant constraints on the EoS of ultra-dense matter [91, 92].
- **Pulsar Timing and Emission:** NICER has observed millisecond pulsars with unparalleled timing precision, enabling studies of pulse profiles and emission mechanisms.

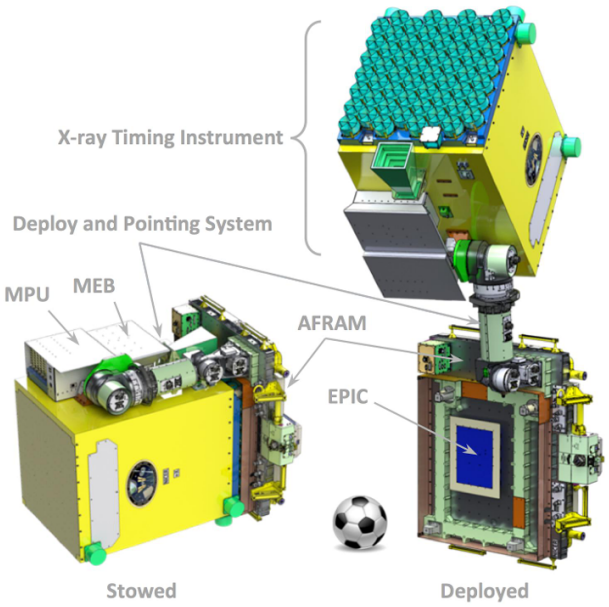


Figure 2.15: NICER in its stowed and deployed configurations. (from Gendreau et al., 2016) [86]

- **X-ray Bursts and Accretion Dynamics:** NICER has detected thermonuclear bursts and oscillations from accreting neutron stars, shedding light on accretion processes and nuclear burning on neutron star surfaces.
- **Gravitational Wave Follow-Up:** NICER has played a key role in studying X-ray emissions from neutron star mergers detected by gravitational wave observatories, providing insights into the post-merger environment [93].

One of NICER's groundbreaking achievements is its contribution to the emerging field of pulse-profile modeling, which uses precise timing data to map the emission regions on neutron star surfaces and test theories of general relativity.

The NICER observatory offers a unique set of capabilities for studying neutron stars, particularly in measuring radii and probing the stability of their spin and clock properties. Figure 2.16 illustrates how NICER's contributions are complemented by other observational facilities across the electromagnetic spectrum, including X-ray polarimeters, radio telescopes, and gamma-ray observatories like Fermi. This collaborative framework amplifies the scientific return by integrating diverse data products, such as pulsation period discoveries and magnetic field diagnostics. Such synergies highlight the value of multi-instrument approaches in advancing our understanding of compact objects and their environments.

Insight-HXMT

Insight-HXMT (Hard X-ray Modulation Telescope), China's first X-ray space observatory, was launched on June 15, 2017. Developed by the Institute of High Energy Physics (IHEP) under the Chinese Academy of Sciences (CAS), Insight-HXMT is designed to observe a wide range of X-ray sources, including black holes, neutron stars, and gamma-ray bursts, with an emphasis on hard X-ray observations [95]. An

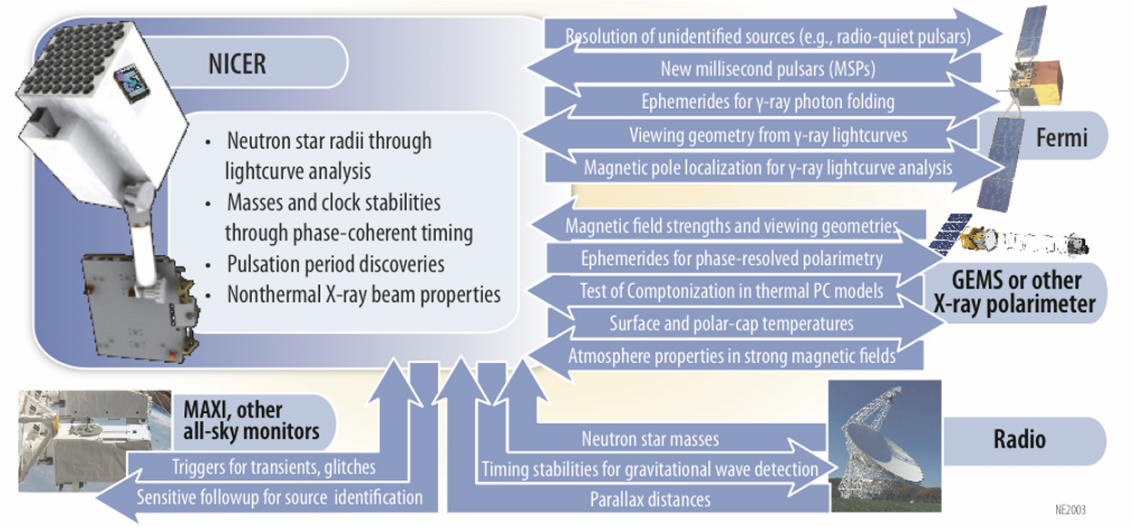


Figure 2.16: NICER capabilities and measurement products are highly complementary to those of other X-ray, radio, and γ-ray facilities for neutron star studies. Interplay between them amplifies the scientific returns from all. (from Gendreau et al., 2012) [94]



Figure 2.17: An artist's illustration of Insight-HXMT in space (from Zhang et al., 2020) [95]

artist's illustration of the Insight-HXMT satellite is shown in Figure 2.17, showcasing its structural design.

The Figure 2.18 outlines the mission profile of Insight-HXMT, detailing its orbital parameters, weight, payload mass, mission lifetime, observation modes, and precision capabilities. These specifications highlight the satellite's key contributions to high-energy X-ray astronomy, such as its ability to perform high-speed scanning and achieve precise pointing accuracy.

The primary goals of Insight-HXMT include:

- Conducting broadband X-ray observations (1–250 keV) of both transient and persistent high-energy sources.
- Investigating the spectral and timing properties of black holes, neutron stars, and AGN.
- Detecting and studying GRBs and other high-energy transient phenomena.

Items	Value
Orbit	550 km, 43°
Weight	2500 kg
Payload mass	1000 kg
Lifetime	4 years
Observation modes	With collimator: Pointed, Scanning Without collimator: gamma-ray monitoring
Scanning speed	0.01° /s, 0.03° /s, 0.06° /s
Pointing accuracy (3 σ)	±0.1°
Attitude measurement accuracy (3σ)	±0.01°
Attitude stability	±0.005° /S
Telemetry rate	120 Mbps
ToO response time	~5 hours

Figure 2.18: Mission profiles of Insight-HXMT (from Zhang et al., 2020) [95]

- Mapping the Galactic plane to identify new X-ray sources and study diffuse X-ray emissions [95].

Insight-HXMT's focus on hard X-rays complements other contemporary X-ray missions, enabling a deeper exploration of non-thermal processes in high-energy environments.

Insight-HXMT features three types of co-aligned instruments, covering a broad energy range:

- **High Energy X-ray Telescope (HE, 20–250 keV):** Based on NaI(Tl)/CsI detectors (shown as in Figure 2.19), this instrument is optimized for hard X-ray observations and is particularly effective for detecting non-thermal emission from compact objects and gamma-ray bursts. Figure 2.20 illustrates the intricate design of the HE telescope onboard the Insight-HXMT satellite. The diagram highlights key components such as the main detectors, collimators, anti-coincidence shield (HVT, high voltage threshold) detectors and particle monitors, along with the auto-gain control (HGC, high gain control) detectors. The HGC detectors are specifically designed to handle the high dynamic range of incoming X-rays, ensuring accurate measurements even for the brightest X-ray sources. This advanced configuration allows the HE telescope to effectively measure high-energy X-rays while minimizing background noise, providing critical data for studying hard X-ray emissions from compact objects like neutron stars and black holes.

- **Medium Energy X-ray Telescope (ME, 5–30 keV):** Employing Si-PIN detectors, the ME telescope provides intermediate spectral coverage, ideal for studying thermal and non-thermal emission in neutron stars and black holes.

- **Low Energy X-ray Telescope (LE, 1–15 keV):** Using Swept Charge Device (SCD) technology, the LE telescope enables soft X-ray observations, complementing the medium and high-energy instruments .

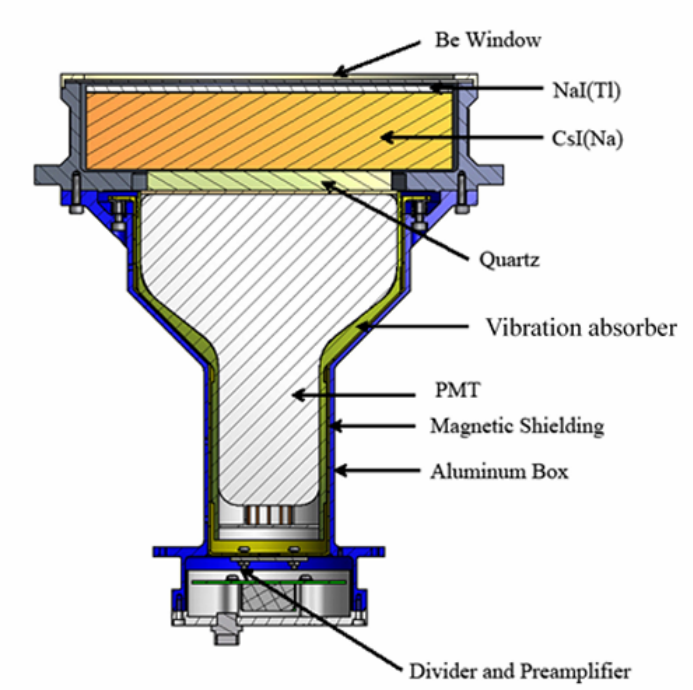


Figure 2.19: A cutaway view of an high energy detector (HED). (from Liu et al., 2020) [96]

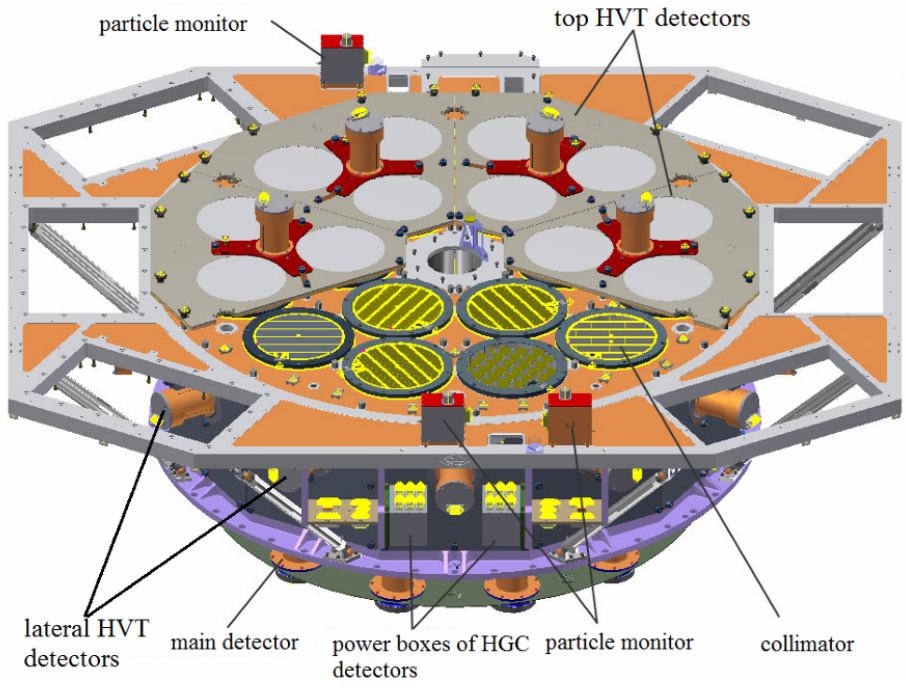


Figure 2.20: Illustration of the HE telescope onboard the Insight-HXMT astronomy satellite. The HE telescope is composed of main detectors, collimators, auto-gain control detectors (not shown), anti-coincidence shield detectors (HVT) and particle monitors. (from Liu et al., 2020) [96]

These instruments are mounted on a three-axis stabilized platform, allowing Insight-HXMT to perform pointed observations as well as Galactic plane scans. The satellite's broadband coverage and high sensitivity make it uniquely suited for studying X-ray binaries and transient sources.

Since its launch, Insight-HXMT has made several notable contributions to X-ray astronomy:

- **Black Hole and Neutron Star Studies:** Insight-HXMT has provided detailed timing and spectral analyses of black hole and neutron star systems, offering new insights into accretion processes and spectral state transitions.
- **Detection of X-ray Pulsations:** The mission has detected coherent pulsations from accreting neutron stars, improving our understanding of spin evolution and magnetospheric interactions.
- **Gamma-ray Bursts:** Insight-HXMT has observed and characterized gamma-ray bursts, contributing to multi-wavelength and multi-messenger studies of these events.
- **Mapping the Galactic Plane:** The satellite has conducted large-scale surveys of the Galactic plane, identifying new X-ray sources and studying diffuse X-ray emissions from the interstellar medium [29, 97].

One of its key findings includes detailed observations of the black hole X-ray binary MAXI J1820+070, where Insight-HXMT captured high-energy spectral features associated with disk-jet interactions and coronal activity during outbursts [98].

Insight-HXMT represents a significant milestone in China's space exploration program, showcasing advanced X-ray instrumentation and providing a platform for high-energy astrophysics research. Its broadband spectral coverage and ability to monitor transient phenomena make it an invaluable resource for the global astrophysics community.

As the mission continues, Insight-HXMT is expected to contribute further to our understanding of compact objects and high-energy processes in the universe. Its data, combined with observations from other X-ray observatories, will enhance our knowledge of the most energetic phenomena in astrophysics. Insight-HXMT's unique combination of hard X-ray sensitivity and broadband coverage has made it a vital tool in the study of high-energy astrophysical processes. Its contributions to black hole and neutron star research, along with its role in multi-wavelength and multi-messenger astronomy, highlight the importance of this mission in advancing X-ray astronomy.

eROSITA

The eROSITA, part of the Russian-German Spektr-RG mission, was launched on July 13, 2019 and is designed for high-sensitivity X-ray surveys. Developed by the Max Planck Institute for Extraterrestrial Physics (MPE) in Germany, eROSITA aims to conduct the most sensitive all-sky survey in the soft X-ray energy band (0.2–8 keV), vastly improving upon its predecessor, ROSAT [27, 75]. Its high data volume and wide field of view make it ideal for studying extended objects like clusters of galaxies, as well as individual sources such as neutron stars and black holes.

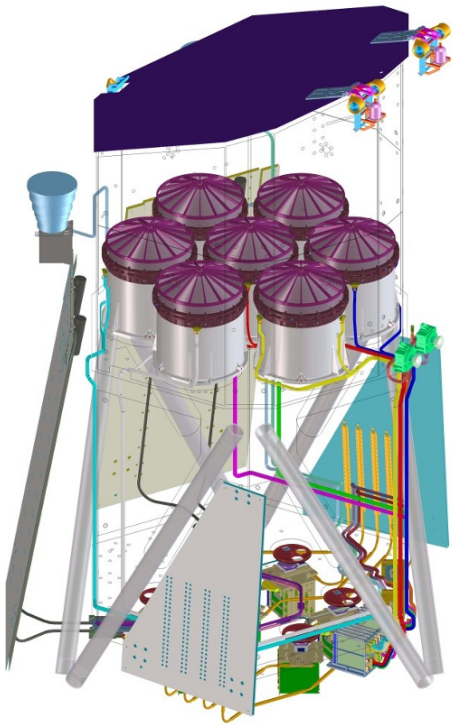


Figure 2.21: Schematic view of the eROSITA telescope with (from top):front cover, 7 MAs (baffle, mirror, electron deflector), and 7 CAs (filter wheel, camera, electronics box). In addition ther are two star trackers (one seen) and fourlarge radiators to cool the cameras and their electronics. The telescope structure is lightly shaded. (from Predehl et al., 2021) [27]

The eROSITA telescope, as illustrated in Figure 2.21, showcases its sophisticated design and advanced components. This schematic highlights its primary elements, including seven mirror assemblies (MAs), each consisting of a baffle, mirror, and electron deflector, and seven camera assemblies (CAs) comprising a filter wheel, camera, and associated electronics box. Supporting the telescope's operations are two star trackers (one visible in the figure), essential for precise attitude control, and four radiators for thermal regulation, ensuring optimal performance of the cameras and electronics. The lightly shaded structure outlines the telescope's framework, emphasizing its well-integrated system designed for efficient X-ray observations. These features collectively enable eROSITA to achieve its mission goals of mapping the X-ray sky with unparalleled sensitivity.

The primary goal of eROSITA is to map the large-scale structure of the universe through the detection of galaxy clusters via their X-ray emissions. By observing clusters of galaxies, eROSITA aims to study the distribution of dark matter and constrain cosmological parameters, including those governing the nature of dark energy. Additionally, eROSITA aims to:

- Detect millions of new X-ray sources, including active galactic nuclei (AGN), galaxy clusters, X-ray binaries, and supernova remnants.
- Study the variability and spectral properties of compact objects, such as black holes and neutron stars.
- Provide a legacy dataset for multi-wavelength follow-up studies [27].

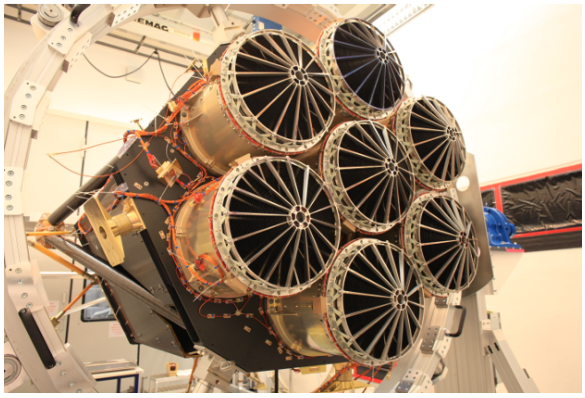


Figure 2.22: Front view of the telescope with all seven MAs installed. Each MA consists of a mirror module, an X-ray baffle in front, and a magnetic electron deflector behind. (from Predehl et al., 2021) [27]

The eROSITA features seven identical Wolter-I mirror modules, each paired with its own CCD camera, shown as in Figure 2.22. These mirror modules are designed to focus soft X-rays efficiently, providing a combined effective area of approximately 2,400 cm^2 at 1 keV. The cameras are equipped with framestore CCDs, which are optimized for X-ray detection and provide a high temporal resolution. Key design features include:

- A field of view of 1 degree in diameter, enabling wide-area surveys.
- High spectral resolution (70–80 eV at 1 keV), allowing detailed spectral analysis.
- An energy range of 0.2–8 keV, covering both soft and moderately hard X-rays [27].

Figure 2.23 highlights the results of the eROSITA all-sky survey, showcasing its remarkable capability in capturing X-ray data across the 0.6–2.3 keV band. The figure demonstrates eROSITA's effectiveness in conducting large-scale surveys and providing detailed insights into both Galactic and extragalactic phenomena, emphasizing its contributions to advancing X-ray astronomy.

It operates in a scanning mode, continuously surveying the sky in great detail. Over its planned 4-year survey period, the mission is expected to complete eight full-sky surveys, with a sensitivity 20–30 times better than ROSAT in the soft X-ray band [27].

Since its launch, eROSITA has made significant contributions to X-ray astronomy, including:

- **Detection of New X-ray Sources:** eROSITA has detected millions of X-ray sources, including AGN, galaxy clusters, and transient objects. These observations have expanded the known population of X-ray-emitting objects significantly.
- **Cosmological Studies:** By mapping galaxy clusters, eROSITA has provided valuable data for understanding the evolution of large-scale cosmic structures and probing the nature of dark energy.
- **Transient X-ray Events:** The mission has uncovered numerous transient phenomena, such as tidal disruption events (TDEs) where stars are shredded by supermassive black holes.

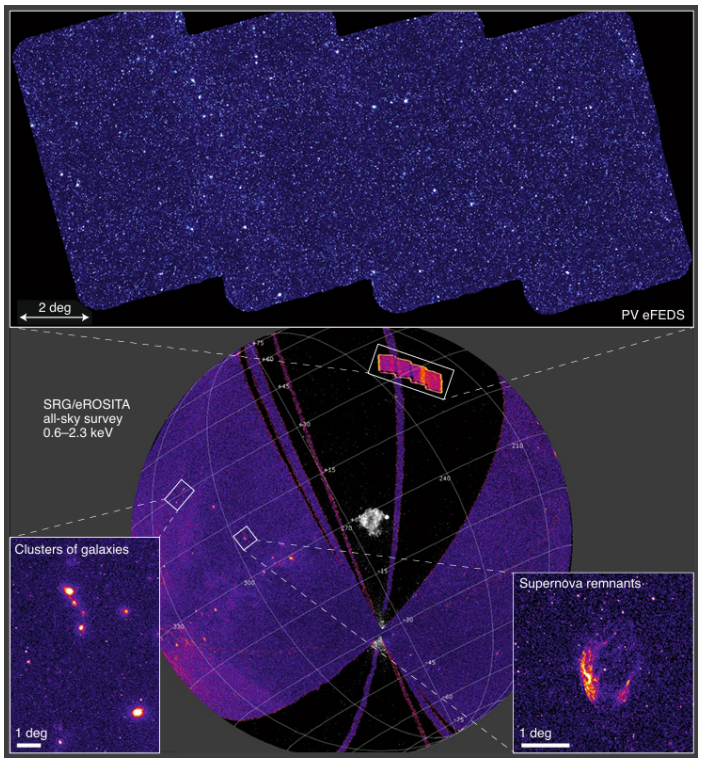


Figure 2.23: The eROSITA all-sky survey. Spherical projection of the eROSITA all-sky survey image in the 0.6–2.3 keV band (purple), taken with an average exposure of −200 s. In the background, a black and white image of the ROSAT all-sky survey (average exposure −300 s; `http://cade.irap.omp.eu/documents/Ancillary/4Aladin/RASS_IM2`). The top panel shows the exposure-corrected X-ray image of the entire SRG/eROSITA performance verification (PV) eFEDS field (−140 deg^2) in the 0.6˘2.3 keV band. The average exposure over the field (2.5 ks) is comparable to the final depth that will be achieved over the whole sky at the end of the survey phase of the mission (end of 2023). The two insets at the bottom show details of an extragalactic and a Galactic field, centred on the Shapley supercluster (left) and the supernova remnant PKS 1209-52 (right), respectively. Courtesy of A. Merloni and C. Maitra (MPE) (a,b); and M. Ramos (MPE) (c). (from Merloni et al., 2020) [99]

- **Detailed Spectral Studies:** The high spectral resolution of eROSITA has allowed for precise measurements of elemental abundances and ionization states in galaxy clusters and supernova remnants, providing insights into the chemical evolution of the universe [100].
- **X-ray Binaries and Compact Objects:** eROSITA has provided time-resolved and spectral data for studying the accretion processes in X-ray binaries, revealing variability patterns and spectral state transitions [27, 99].

The eROSITA mission is expected to produce a legacy dataset that will remain valuable for decades. Its all-sky survey data are being used in conjunction with multi-wavelength observatories, including radio, optical, and infrared telescopes, to enhance our understanding of the universe's high-energy phenomena. The cooperation between eROSITA and ground-based surveys like Sloan Digital Sky Survey (SDSS) and Legacy Survey of Space and Time, (now officially called Vera C. Rubin Observatory Legacy Survey of Space and Time) is expected to lead to numerous groundbreaking discoveries.

As the mission continues, its data will provide critical inputs for addressing some of the most pressing questions in astrophysics, from the physics of black holes to the large-scale structure of the universe.

The eROSITA represents a significant leap forward in X-ray astronomy, combining innovative instrumentation with ambitious scientific goals. Its contributions to understanding cosmic structures, compact objects, and transient phenomena highlight the importance of large-scale, high-sensitivity surveys in modern astrophysics. In this study, we utilized eROSITA data to analyze the quiescent black holes and the long-term behavior of neutron star SXP 726.

2.3 Advantages of Multi-Satellite Observations

In high-energy astrophysics, the complexity and variability of astronomical phenomena such as neutron stars and black holes often require a multi-faceted approach to fully understand their behavior. By combining data from multiple satellites with varying energy sensitivities, temporal resolutions, and observational capacities, researchers can obtain a more complete and robust picture of these systems. In this study, we utilized a suite of X-ray observatories—including XMM-Newton, eROSITA, Insight-HXMT, NuSTAR, and NICER—which together provide a complementary set of tools for investigating neutron stars and black holes. The advantages of such multi-satellite observations are discussed below.

1. Broad Energy Coverage

Different X-ray observatories specialize in distinct energy ranges, enabling detailed exploration of various emission processes:

- **XMM-Newton:** With an energy range of 0.2–12 keV, XMM-Newton is optimized for studying soft X-ray emissions, such as those from neutron star surfaces and accretion disks [26].
- **eROSITA:** Covering 0.2–10 keV, eROSITA excels at wide-field surveys and

long-term monitoring, providing a census of X-ray sources and population studies across the Galactic plane [27].

- **Insight-HXMT:** Extending into the hard X-ray band (up to 250 keV), Insight-HXMT is particularly suited for non-thermal processes and studying high-energy tails in black holes and neutron stars [95].
- **NuSTAR:** Covering 3–79 keV with high sensitivity, low background level, and spatial resolution in the hard X-ray band.
- **NICER:** With high sensitivity in the soft X-ray band (0.2–12 keV), NICER focuses on high-precision timing and the study of neutron star pulse profiles and spin dynamics [86].

By integrating these datasets, researchers achieve comprehensive spectral coverage, capturing both thermal and non-thermal components and allowing for detailed modeling of the physical processes at work.

2. Improved Temporal Resolution and Timing Precision

Timing analysis is critical for understanding spin evolution, pulsations, and variability in compact objects:

- **NICER:** Renowned for its microsecond timing precision, NICER provides unparalleled data for studying QPOs and neutron star spin dynamics.
- **Insight-HXMT:** With broad spectral and temporal capabilities, Insight-HXMT enables the study of high-energy variability and burst timing in hard X-ray bands.

Combining timing data across soft and hard X-ray bands enhances the precision of pulse period measurements and allows for the detection of rare events such as glitches or anti-glitches.

3. Long-Term Monitoring and Transient Event Detection

Observatories with large fields of view and long operational timelines, such as eROSITA and Insight-HXMT, provide unique capabilities for monitoring transient phenomena:

- **Transient Detection:** eROSITA's wide-field surveys allow for the discovery of new X-ray transients, while Insight-HXMT captures hard X-ray emissions from outbursts and bursts [27].
- **Long-Term Trends:** Combining long-term data with shorter, high-resolution observations from XMM-Newton and NICER enables the study of accretion rate changes and magnetic field evolution.

This dual capability allows for tracking the life cycles of neutron stars and black holes and understanding the variability across timescales. By combining short-term, high-resolution observations with long-term monitoring data, we can track the evolution of neutron stars and black holes over time. This is particularly useful for studying systems with periodic or semi-periodic behavior, where changes in accretion rates or

magnetic field configurations may only become apparent over extended observational timescales.

4. Comprehensive Analysis of Different Physical Processes

Each observatory is uniquely sensitive to different astrophysical processes:

- **Thermal Processes:** XMM-Newton and NICER excel in analyzing thermal emissions, such as those from neutron star surfaces or accretion disks.
- **Non-Thermal Emissions:** NuSTAR and Insight-HXMT focus on hard X-ray phenomena, including reflection and Compton scattering.
- **Population Studies:** eROSITA provides population-wide insights, identifying large numbers of faint sources across the Galactic and extragalactic fields [27].

In summary, the combination of data from multiple satellites offers a powerful advantage for studying neutron stars and black holes. By utilizing different energy ranges, timing resolutions, and observational strategies, we can achieve a more complete understanding of the physical processes at play. The complementary strengths of XMM-Newton, eROSITA, Insight-HXMT, NuSTAR, and NICER allow for robust cross-validation of results, comprehensive spectral and timing analysis, and the detection of both short-term and long-term variability in these fascinating astrophysical systems.

3 Data and Methods

3.1 Data Sources and Preprocessing

The observational data used in this thesis were collected from multiple X-ray observatories that provide high-quality observations of X-ray binaries and neutron stars. These data span various energy bands and offer complementary perspectives, enabling a comprehensive analysis of accretion processes and related phenomena in compact objects. The primary sources of data include:

3.1.1 eROSITA

The extended ROentgen Survey with an Imaging Telescope Array (eROSITA), onboard the Spectrum-Roentgen-Gamma (SRG) mission, has played a pivotal role in this research. eROSITA's capability to conduct all-sky surveys in the soft X-ray band (0.2–8.0 keV) enables systematic identification and monitoring of transient sources, including quiescent and outbursting X-ray binaries. Data products from eROSITA, including light curves and imaging data, were obtained through the mission's data archive and processed using standard analysis pipelines.

Members of the eROSITA mission can access the data through DATool (`https://erosita.mpe.mpg.de/internal/Datool`) and process them using the eROSITA Standard Analysis Software System (eSASS). The command `SRCTOOL` is utilized to extract light curves, spectra, response matrix files (RMF), and ancillary response files (ARF).

eROSITA data products follow a systematic naming convention to ensure proper management and analysis. For example, the file names are structured as follows:

`PQii_jjjjjj_klm_nnnnnn_rrr_Rooo.fits`

In this format, the placeholders represent the following: - `P, Q`: Observation mode and ownership, - `ii`: eRASS (eROSITA All-Sky Survey) number, - `jjjjjj`: Sky map number, - `k, l, m`: Telescope ID, filter wheel number, and energy band, - `nnnnnn`: Product type, - `rrr`: Dataset version, - `R`: Processing configuration, - `ooo`: Processing configuration number.

For the study of quiescent black holes, the following data files were used:

`all_e1_201008_poscorr_mpe_clean.fits`
`all_e2_201221_poscorr_mpe_clean.fits`
`all_e3_210426_poscorr_mpe_clean.fits`

These files correspond to the corrected eROSITA all-sky surveys 1, 2, and 3, with

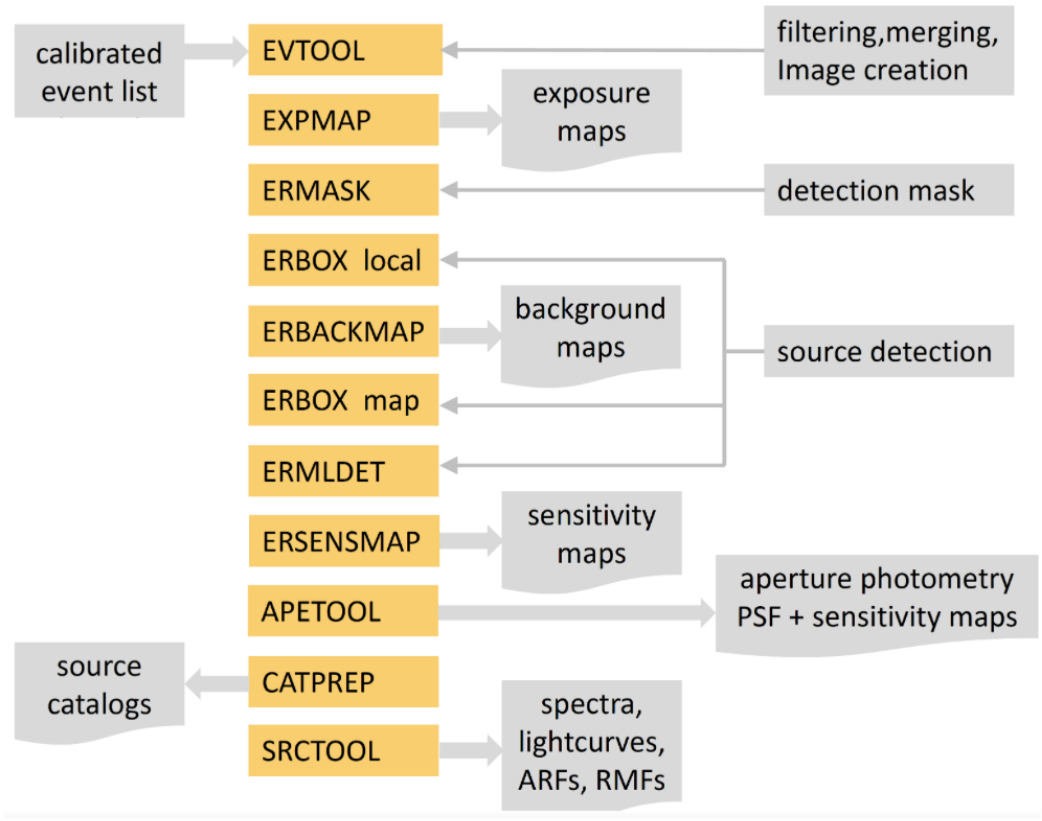


Figure 3.1: Overview of the eROSITA data reduction process, from calibrated event files to source catalogues (adapted from the eSASS Cookbook; Credits: MPE).

positional corrections applied by the Max Planck Institute for Extraterrestrial Physics (MPE).

Figure 3.1 provides an overview of the data reduction process, highlighting the main commands used. Further details and commands can be found in the eSASS Cookbook (`https://wiki.mpe.mpg.de/eRosita/CookBook`).

The data reduction pipeline involves the following steps: 1. Calibration of raw event files using `evtool`. 2. Extraction of light curves and spectra using `srctool`. 3. Generation of response files (RMF and ARF) for spectral analysis.

In this thesis, observational data corresponding to the neutron star SXP 726 and quiescent black holes were selected based on their exposure times and observational quality. These data span multiple observation epochs, enabling a detailed study of both timing and spectral variations over time.

3.1.2 NICER

The Neutron Star Interior Composition Explorer (NICER) onboard the International Space Station provides high temporal and spectral resolution data in the soft X-ray band (0.2–12 keV). NICER's primary contributions to this thesis involve time-resolved spectroscopy and pulsation studies, enabling detailed investigation of variability phenomena such as quasi-periodic oscillations (QPOs) and spectral transitions.

Data from NICER were processed using standard procedures to ensure high-quality analysis. The following steps outline the data reduction and analysis workflow:

1. **Software Setup**: Install the latest version of HEASoft, which includes NICER Data Analysis Software (NICERDAS). Ensure that the NICER Calibration Database (CALDB) is up to date.

2. **Data Retrieval**: Obtain NICER observation data from the HEASARC archive. For large datasets, consider using the SciServer platform to access and analyze public NICER data without local downloads.

3. **Initial Processing**: Use the `nicerl2` task to perform standard calibration and filtering, producing cleaned event files. This step applies calibration, removes unwanted events, and generates Level 2 data product, using `nicerl2 indir=/path/to/data clobber=YES detlist=‘‘launch,-14,-34’’`. Analysis of detector behavior on-orbit shows that, under certain conditions, two of the NICER focal plane modules, namely DETID 34 and DETID 14, exhibit episodes of increased detector noise. So, we exclude data from these detectors in our analysis.

4. **Light Curve and Spectrum Extraction**: Utilize the `nicerl3-lc` and `nicerl3-spect` scripts to create light curves and spectra, respectively.

5. **Background Estimation**: Apply the background model `nibackgen3C50` tool to estimate and subtract background contributions from the data, enhancing the accuracy of the analysis. This model is for both space environment and particle background and ensures that the extracted source data are free from significant background contamination.

6. **Timing Analysis**: For precise timing studies, perform barycentric corrections using the `barycorr` tool to account for Earth's motion. This correction is essential for phase-resolved spectroscopy and pulsation searches.

7. **Spectral Analysis**: Load the extracted spectra into XSPEC for modeling. Apply appropriate response files (RMF and ARF) and fit the data with suitable astrophysical models to derive physical parameters.

Figure 3.2 shows the workflow for NICER data processing follows a structured approach using high-level pipeline tasks. The primary steps include running `nicerl2` for standard calibration and data screening, followed by `nicerl3-spect` to generate spectral products. The overall processing is designed to streamline the creation of high-quality data products for timing and spectral analysis. Detailed information about NICER's data processing levels is available in the NICER Processing Levels thread (`https://heasarc.gsfc.nasa.gov/docs/nicer/analysis_threads/`).

The input to the `nicerl3-spect` task consists of the calibrated and screened event file ("cl" file) produced by `nicerl2`, along with auxiliary files such as the filter file (MKF file). For specific background modeling tasks, such as using the 3C50 model, unfiltered event files ("ufa" files) may also be required. The `nicerl3-spect` task is designed to recognize the standard NICER observation directory structure or handle outputs of `nicerl2` saved in alternate directories, offering flexibility for various data configurations.

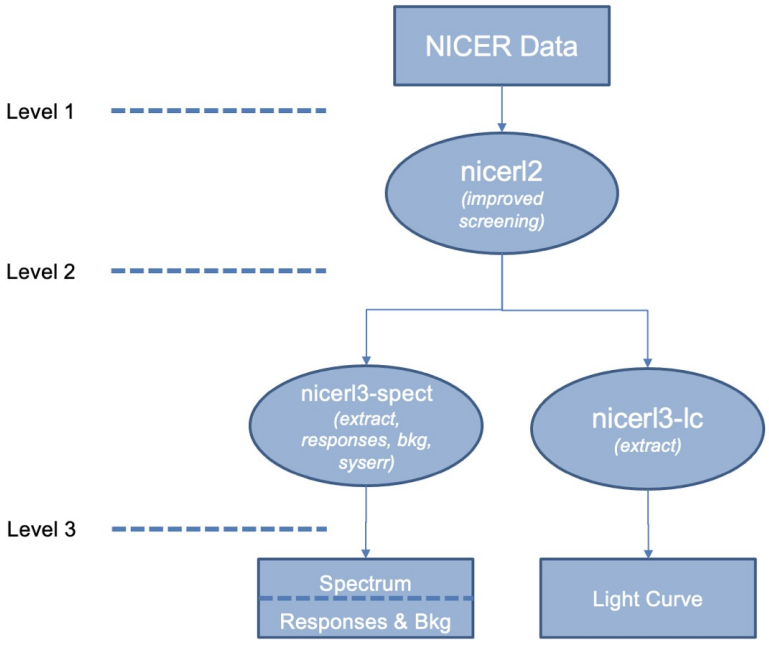


Figure 3.2: NICER Data Processing Workflow. (Credits: NASA).

This standardized processing pipeline ensures the reliability and reproducibility of NICER data analyses, facilitating robust scientific investigations.

3.1.3 NuSTAR

The Nuclear Spectroscopic Telescope Array (NuSTAR) observes in the hard X-ray band (3–79 keV) with high energy resolution. NuSTAR's unique capability to provide broadband coverage facilitates detailed spectral modeling, including the detection of reflection features and cyclotron resonance scattering features (CRSFs). These data were critical for understanding accretion physics in high-energy regimes.

Data from NuSTAR were processed using the following standard procedures:

1. **Software Setup**: Ensure the latest version of HEASoft, which includes the NuSTAR Data Analysis Software (NuSTARDAS), is installed. Verify that the NuSTAR CALDB is up to date. Detailed setup instructions are available in the NuSTAR Data Analysis Software Guide. (`https://heasarc.gsfc.nasa.gov/docs/nustar/analysis/nustar_swguide.pdf`)

2. **Data Retrieval**: Obtain the required observation data from the HEASARC archive. The data are organized in directories following NuSTAR's naming conventions, facilitating straightforward identification of files.

3. **Data Calibration**: Execute the `nupipeline` script to process Level 1 data into calibrated event files. This script performs tasks such as metrology processing, attitude correction, bad pixel flagging, hot pixel identification, and energy calibration.

4. **Event Screening**: Apply the `nupipeline` tool to filter events based on criteria like energy range, grade, and time intervals. This step ensures the selection of

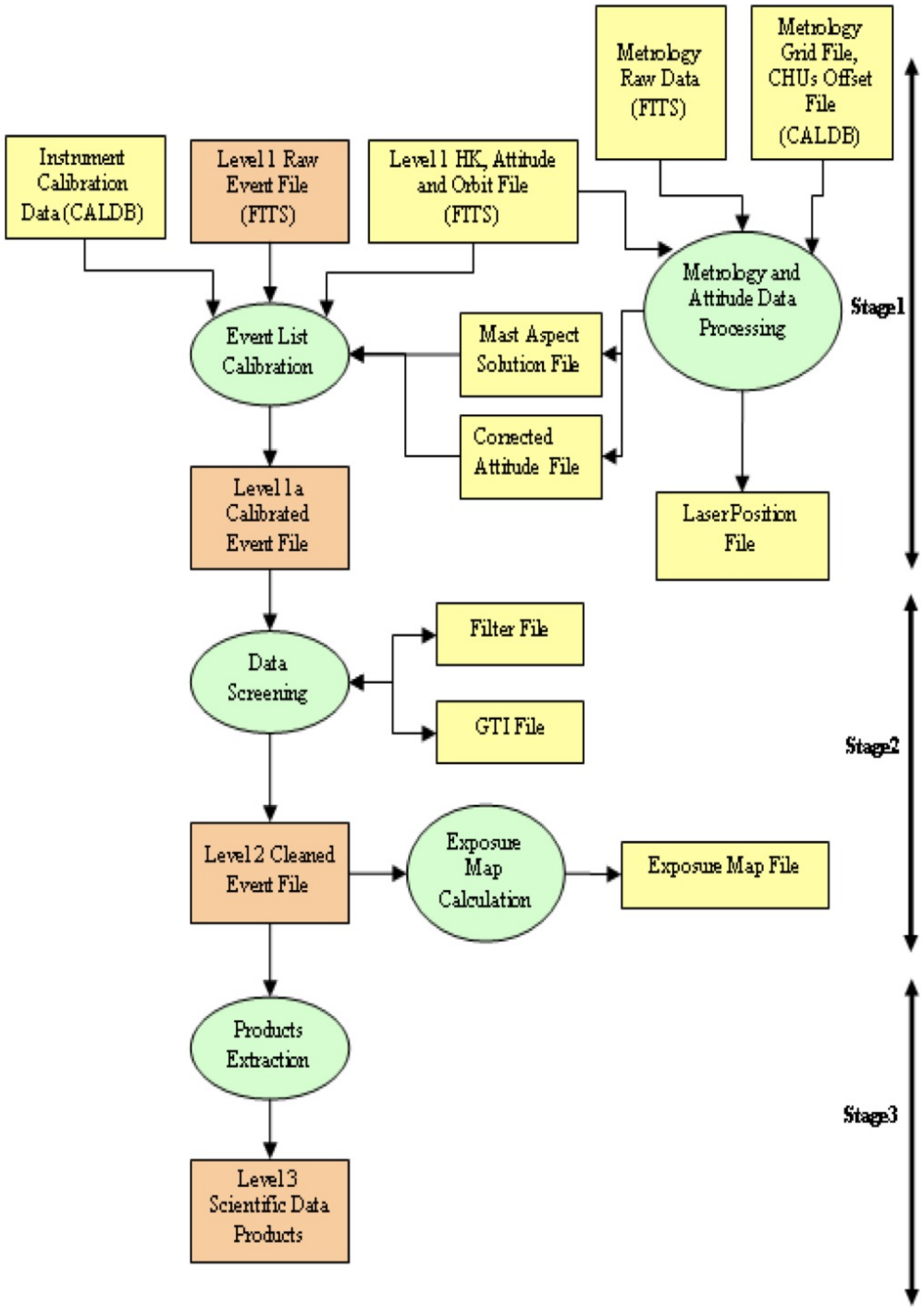


Figure 3.3: NuSTARDAS data reduction flow diagram. (Credits: NASA).

high-quality data for analysis.

5. **Product Generation**: Use the `nuproducts` task to create scientific products, including light curves, spectra, and response files (RMF and ARF). These products are essential for subsequent timing and spectral analyses.

Figure 3.3 illustrates the overall NuSTAR data reduction workflow, showing the progression from raw event files to scientific data products across the three stages. The Nuclear Spectroscopic Telescope Array (NuSTAR) generates data products that are organized in a systematic directory structure for each observation, named according to the observation ID. The structure facilitates data access and processing through three primary stages, as outlined below:

1. **Stage 1: Calibration and Housekeeping**
   This stage includes the calibration of raw event data and the preparation of auxiliary housekeeping files. The "auxil" directory contains files such as corrected star tracker attitude files and orbit data, while the "hk" directory stores essential housekeeping files like electronics box data and raw metrology files. The Level 1 science event files for both FPMA and FPMB detectors are stored in the "event_uf" directory.

2. **Stage 2: Event Screening and Filtering**
   During this stage, event screening and filtering processes are applied to produce cleaned and calibrated event files, which are stored in the "event_cl" directory. Additional products such as Good Time Interval (GTI) files, filter files, and exposure maps are generated to support further analysis. These outputs are critical for ensuring the quality of scientific results and provide the basis for subsequent data extraction.

3. **Stage 3: Scientific Data Products**
   In the final stage, Level 3 data products are generated, including source and background energy spectra, light curves, and response files (ARF and RMF). These files, stored in the "event_cl" directory, are essential for spectral and timing analysis. NuSTAR provides both FPMA and FPMB data for scientific use, enabling detailed studies of various astrophysical phenomena.

For detailed usage instructions and parameter settings for the NuSTAR pipeline, please refer to the official documentation available at `https://heasarc.gsfc.nasa.gov/docs/software/lheasoft/help/nupipeline.html`.

These steps ensure the data are processed consistently and accurately, providing a reliable foundation for scientific investigation.

3.1.4 XMM-Newton

The X-ray Multi-Mirror Mission (XMM-Newton) offers high sensitivity and spectral resolution in the 0.2–12 keV band. XMM-Newton data were primarily used to perform detailed spectral analysis of X-ray binaries during outburst states, contributing to the characterization of accretion disk properties and emission mechanisms.

Data from the XMM-Newton Observatory were processed using standard procedures to ensure reliable analysis. The data reduction was performed using the Science Analysis System (SAS), a comprehensive software package designed for processing and analyzing XMM-Newton data. The key steps for data processing are outlined below:

1. **Setup and Preparation**: Ensure that the latest version of SAS is installed and configured on user system. Update the Calibration Access and DataBase (CIF and CCF:current calibration files) using the `cifbuild` and `calindex` commands to ensure accurate calibration information is applied to the data. Further details about SAS installation and setup can be found at `https://www.cosmos.esa.int/web/xmm-newton/sas-installation`.

2. **Data Retrieval and Initial Calibration**: Download observation data files (ODFs) from the XMM-Newton Science Archive (XSA) and unpack them. Run the `odfingest` task to generate the necessary metadata files, which are required for subsequent processing steps. The output of this step includes a summary of the ODF content.

3. **Event File Creation and Screening**: Generate event files for the EPIC (MOS, PN) instruments using the `epchain` and `emchain` tasks. These tasks apply standard calibrations, such as bad pixel corrections and energy-scale calibration. Apply filtering criteria to remove high-background intervals using the `tabgtigen` task, creating a good time interval (GTI) file to ensure data quality. For GTI, we applied the following conditions during filtering:

   - Background Flares: High background levels due to soft proton flares were removed by extracting the high-energy light curve (typically 10–12 keV) and applying a count rate threshold.
   - PATTERN Selection: For EPIC-pn data, we selected events with `PATTERN <= 4` to include only single and double pixel events. For EPIC-MOS, we used `PATTERN <= 12`.
   - FLAG Selection: Only good events were retained by setting `FLAG == 0`.

4. **Light Curve and Spectral Extraction**: Use the `evselect` command to extract source and background light curves, spectra, and images from the cleaned event files. For spectral analysis, generate RMFs and ARFs using the `rmfgen` and `arfgen` tasks. Combine these products for further scientific analysis.

5. **Background Subtraction and Final Products**: For accurate background modeling, use the `especget` task to extract source and background spectra with appropriate scaling. Create exposure maps using the `eexpmap` task if required for extended source analysis.

The structure of XMM-Newton data and the sequence of processing tasks are summarized in `https://www.cosmos.esa.int/web/xmm-newton/sas-threads`, which provides a comprehensive overview of the data reduction workflow. Detailed instructions for each step are provided in the SAS User Guide, available at `https://www.cosmos.esa.int/web/xmm-newton/documentation`.

For a more straightforward approach to XMM-Newton data processing, users can utilize the interactive interface provided by the XMM-Newton Science Archive (XSA).

By searching for the source name on the XSA platform, users can easily access images of the area surrounding the target source.

The background can be extracted by defining circular regions around the source (point source) and drawing annular regions nearby to represent the background. The interactive tools allow users to select specific parameters and extract corresponding data products such as event files or light curve files directly.

This method provides a simplified and intuitive alternative to manual data reduction, reducing the complexity of traditional processing while maintaining accuracy and reliability. Further information and instructions can be found at `https://www.cosmos.esa.int/web/xmm-newton/xsa`.

3.1.5 Insight-HXMT

The Hard X-ray Modulation Telescope (Insight-HXMT) is China's first X-ray astronomy satellite, capable of observing in a wide energy range (1–250 keV). Insight-HXMT data were utilized for timing and spectral studies, particularly for investigating transient phenomena and the hard X-ray properties of X-ray binaries.

The data from Insight-HXMT were processed using the standard procedures provided by the HXMT Data Analysis Software (HXMTDAS). The following steps outline the workflow:

1. **Preparation**: Download the latest HXMTDAS version from the official website (`http://hxmtweb.ihep.ac.cn/software.jhtml`) and install it in a HEASoft-compatible environment. Ensure that the calibration database (CALDB) is up to date.

2. **Data Calibration**: Run the `he` and `me` pipelines for the high-energy (HE) and medium-energy (ME) telescopes, respectively. The commands apply standard calibration and filtering to the raw event files, generating cleaned event files suitable for analysis. The event screening criteria include the satellite elevation angle (`ELV`), geomagnetic rigidity (`COR`), and South Atlantic Anomaly (SAA) conditions.

3. **Good Time Interval (GTI) Screening**: The screening criteria are applied using commands like `screenhe` and `screenme`. These steps ensure that only valid observation periods are selected for further analysis. Parameters such as `ANG_DIST < 0.04` and `SAA_FLAG=0` are applied.

4. **Light Curve and Spectrum Extraction**: Generate light curves and spectra for both the source and the background using the `HXMTlcgen` and `HXMTspecgen` commands. Background estimation is crucial and involves specialized scripts for each energy band (HE, ME, and LE).

5. **Response Matrix Application**: Apply the RMF and ARF for spectral fitting. These files are required for accurate energy calibration and are provided in the CALDB.

6. **Advanced Analysis**: Perform timing and spectral analysis using tools such as `Xspec` for spectral fitting or Python-based libraries like `Stingray` for timing

studies. Generate power density spectra (PDS) and phase-resolved spectra if necessary.

For the Insight-HXMT satellite data processing, a well-structured workflow was adopted to ensure the quality and reliability of the scientific products. The analysis utilized the pipeline software developed by Professor Ji Long's team, which is based on Python and integrates various data processing modules. The software is available at `https://code.ihep.ac.cn/jldirac/insight-hxmt-code-collection`, with regular updates aligning with the Insight-HXMT team's requirements.

Data reduction primarily relied on the HXMT Data Analysis Software (HXMTDAS), which is downloadable from `http://hxmtweb.ihep.ac.cn/software.jhtml`. After downloading the raw observation data and installing the HXMTDAS, calibration files (CALDB) were applied to ensure accuracy. By running the pipeline, key scientific products such as light curves, energy spectra, and event files were generated without extensive manual intervention.

To improve data selection accuracy, specific Good Time Interval (GTI) criteria were considered during preprocessing. These criteria include adjustments for key parameters, as outlined below:

- **ELV**: Elevation angle greater than 10° was used to exclude periods where the satellite pointed too close to Earth's surface, reducing contamination from Earth's albedo radiation.
- **COR $>$ 8 GeV**: The cut-off rigidity threshold ensures that only observations with minimal charged-particle interference are included. For high-quality data, COR values above 8 GeV are generally preferred, and stability improves when COR exceeds 10 GeV, where the contamination rate drops below 20%.
- **ANG_DIST $<$ 0.04**: This parameter limits the offset between the telescope pointing and the source position, ensuring accurate source localization.
- **SAA Criteria**: Data within 300 seconds before or after crossing the South Atlantic Anomaly (SAA) were excluded due to excessive particle interference.

3.2 Data Analysis

After obtaining the satellite data products (light curves, spectra, etc.) through the pipeline, further analysis and processing can be performed based on the specific scientific goals. This section is divided into two main parts: analysis of X-ray timing and spectral data.

3.2.1 X-ray Timing Analysis

For X-ray timing analysis, we use tools available in the `HEASoft` software package, such as the `Xronos` sub-package. Detailed documentation for these tools can be found at the `Xronos` official website. The ftool `powspec` commonly used include tasks for periodicity searches, epoch folding, and power density spectra(PDS) analysis.

For more advanced timing analyses, we also leverage the `Stingray` Python package, which is specifically designed for variability analysis in astrophysical time series. More information about `Stingray` is available at https://docs.stingray.science/index.html. This package provides functionality for PDS estimation, cross-spectral analysis, and time-domain modeling, which are essential for studying temporal properties of X-ray sources.

3.2.2 X-ray Spectral Analysis

`XSPEC` is a versatile tool developed by NASA for modeling X-ray spectra. It provides excellent functionality for fitting and visualizing observed X-ray spectral data and offers a wide range of predefined physical models. XSPEC has been widely adopted by the high-energy astrophysics community for its reliability and flexibility in spectral analysis. XSPEC allows for complex multi-component model fitting, enabling users to analyze physical processes such as absorption, emission, and scattering. Details about XSPEC and its usage can be found on the XSPEC official manual. For users familiar with Python, `PyXspec` provides a Python interface for XSPEC, allowing seamless integration with Python-based workflows. Documentation for PyXspec is available at https://heasarc.gsfc.nasa.gov/xanadu/xspec/python/html/index.html. For spectral analysis, models such as `tbabs`, `powerlaw`, `nthComp` ,and `diskbb` are frequently employed to describe the observed X-ray spectra. These models allow for the determination of physical parameters such as the hydrogen column density, power-law photon index, temperature of seed photon and electron in Compton scattering process, and disk temperature. Advanced features, such as covariance analysis and Monte Carlo Markov Chain (MCMC) fitting, can also be utilized in XSPEC to refine parameter estimation. By combining the capabilities of `HEASoft`, `Stingray`, and `XSPEC`, we achieve a comprehensive approach to analyzing X-ray timing and spectral data, enabling robust interpretation of the physical properties of X-ray sources.

3.2.3 Spectral Fitting with XSPEC

This section focuses on the spectral analysis component, utilizing the *XSPEC* software within the HEASoft package (detailed documentation available at `https://heasarc.gsfc.nasa.gov/docs/xanadu/xspec/manual/manual.html`).

Spectral Modeling and Fitting Process

The observation data from satellites generally include three dimensions of information: time (T), energy channel (E), and photon counts (C). If the photon counts in a given time interval are accumulated across energy channels, the corresponding energy spectrum $C(I)$ can be obtained. However, to derive the actual energy spectrum of the source, $f(E)$, we must deconvolve the instrument response $R(E, I)$, which maps the source energy spectrum into the detected energy channels. Mathematically, this is expressed as:

$$C(I) = \int R(E, I) f(E) dE. \tag{3.1}$$

Here, $C(I)$ represents the observed counts in channel I, $R(E, I)$ is the response matrix of the instrument, and $f(E)$ is the source energy spectrum. To approximate $f(E)$, we adopt a model $M(E)$ and iterate by fitting the model-predicted counts, $C_m(I)$, to the observed counts $C(I)$. The goodness of fit is assessed by the reduced chi-squared statistic:

$$\chi^2_{\rm red} = \frac{\chi^2}{\rm d.o.f.} = \frac{1}{\rm d.o.f.} \sum_I \frac{[C(I) - C_m(I)]^2}{\sigma(I)^2}, \tag{3.2}$$

where $\sigma(I)$ is the statistical uncertainty in $C(I)$, and d.o.f. represents the degrees of freedom in the fit.

Workflow for XSPEC Spectral Fitting

The general workflow (HXMT data as an example) for spectral fitting in XSPEC is as follows:

1. Load the spectral data and associated files:

```
XSPEC> data 1:1 LErsp.pha 2:2 MEresp.pha 3:3 HEresp.pha
XSPEC> response 1 LErsp.rmf 2 MErsp.rmf 3 HErsp.rmf
XSPEC> back 1:1 LEbkg.pha 2:2 MEbkg.pha 3:3 HEbkg.pha
```

2. Set the energy range and fit parameters:

```
XSPEC> ignore **-1.0 10.0-**
XSPEC> model TBabs*(diskbb+cutoffpl)
```

   Here, `TBabs` represents the absorption model, and `diskbb` and `cutoffpl` correspond to the disk blackbody and cutoff power-law models, respectively.

3. Perform fitting and visualize results:

```
XSPEC> fit
XSPEC> plot ldata del
```

4. Refine the model using additional components, such as Gaussian lines, or modify fit parameters to optimize convergence.

Visualization and Parameter Error Estimation

To visualize the fit results, the following commands can be used:

```
PLT> plot ldata del
PLT> setplot energy
PLT> setplot rebin 3
PLT> time off
```

For error estimation, the `error` command or Markov Chain Monte Carlo (MCMC) techniques can be employed. The corresponding confidence intervals are typically set at the 90% level.

This methodology allows for precise spectral fitting and parameter estimation, forming the foundation for interpreting astrophysical phenomena. Detailed information about XSPEC functionalities can be found at `https://heasarc.gsfc.nasa.gov/xanadu/xspec/`.

3.3 Spin Measurement Methods

3.3.1 PDS and RMS Calculation

PDS Calculation Using Powspec

Powspec, a software in the Xronos package, is used to calculate the PDS. Below, we briefly describe its usage. First, the relevant time series files need to be prepared, and HEASOFT must be installed. By executing the Powspec command in an interactive mode, users can process the input data step by step.

```
>>> powspec cfile1=file1.lc window="-" dtnb=0.004 nbint=25000 nintfm=INDEF
     rebin=1.01 plot=yes plotdev="file1.gif/gif" outfile=default norm=2
```

In this command:

- **dtnb**: Controls the time resolution of the PDS. This parameter determines the Nyquist frequency $f_N = \frac{1}{2\text{dtnb}}$ and is critical in defining the upper frequency of the PDS.
- **nbint**: Sets the segment length for each PDS calculation.
- **rebin**: Rebins the PDS into logarithmic bins for better visualization, where > 1 represents logarithmic rebinning and $= 1$ performs no rebinning.
- **norm**: Specifies the normalization method. For RMS/Mean^2/Hz normalization, norm=2 is recommended [101].

Attention must be paid to white noise subtraction when using normalization values other than 2, as improper subtraction could lead to inaccuracies. For white noise removal, use norm=2.

RMS Calculation Using Xspec

The methodology proposed by Ingram et al. (2012)[102] is applied to calculate the RMS amplitude from the PDS. After generating the PDS using `powspec`, users can convert the power-frequency file into an energy spectrum file compatible with Xspec for further analysis.

```
>>> fplot infile=file1.fps xparm=frequency[yax_e] yparm=power[error]
    rows="-" device="/xw" pltcmd = "wdata file.dat"
>>> sed -i "1,3d" file.dat
>>> cat file.dat | awk "{print $1"-"$2" "$1+$2" "$3*$3" "$2*$4"$2}"
> file.txt
>>> flx2xsp file.txt file.pha file.rsp
```

After generating the PDS file, RMS can be calculated in Xspec by loading the flux-calibrated file. Additionally, we use multiple Lorenz functions to fit the PDS and compute RMS values using cpflux for the PDS model.

Python libraries, such as Stingray, can also assist in analyzing the time variability properties (e.g., PDS, phase lag). For more details, refer to `https://docs.stingray.science`.

3.3.2 Pulsar Period Analysis

The pulsar period search for this research primarily utilizes Stingray's pulsar timing analysis module. For further methodological details, refer to `https://docs.stingray.science/pulsar.html`.

3.3.3 Solar System Barycenter Correction

Since satellites orbit the Earth and the Earth orbits the Sun, it is necessary to transform observational data into the Solar System Barycenter (SSB) reference frame for further analysis. The relationship between the observed time at the barycenter $t_{\rm SSB}$ and the satellite's observational time $t_{\rm obs}$ can be expressed as:

$$t_{\rm SSB} = t_{\rm obs} + t_{\rm corr} - \Delta D/c^2 + \Delta R + \Delta S + \Delta E, \tag{3.3}$$

where:

- $t_{\rm corr}$: Time system correction,
- $\Delta D/c^2$: Gravitational delay,
- ΔR: Römer delay,
- ΔS: Shapiro delay,
- ΔE: Einstein delay.

The $t_{\rm corr}$ term accounts for differences in time systems. The Römer delay, ΔR, is due to the geometric difference between the satellite and the SSB, while the Shapiro delay, ΔS, accounts for the gravitational curvature of light paths near massive objects. The Einstein delay, ΔE, is due to the relativistic effects of the observer's motion and gravitational time dilation.

Among these terms, the Römer delay is the largest, as it reflects the light travel time difference between the satellite and the SSB. Calculations of these corrections

require accurate solar system ephemeris data, which are provided by the Jet Propulsion Laboratory (JPL). Current standards include the DE200 and DE405 models.

The Shapiro delay, on the other hand, is usually negligible except in cases involving massive stars. It is typically about 120 μs and may increase to 200 μs for X-ray binaries with neutron stars or black holes. These corrections ensure high precision in the timing analysis and minimize errors due to the Earth's motion relative to the SSB.

To correct observational data to the SSB, we use HXMTDAS and the `hxbary` tool. The command for performing the barycenter correction is as follows:

```
>>> hxbary eventfile=infile/eventfile orbitfile=orbit.fits ra=RA dec=DEC
eph=1 clobber=yes
```

The corrected file will include an updated time column labeled as TDB, which is ready for further analysis.

3.3.4 Binary Orbital Correction

After applying the Solar System Barycenter (SSB) correction, an additional binary orbital correction is required if the pulsar under study is part of a binary system. This correction accounts for the Doppler shift caused by the orbital motion of the neutron star within the binary system. The observed pulsar frequency, $P_{\rm obs}(A_T)$, can be expressed as:

$$P_{\rm obs}(A_T) = P_0 \left(1 + \frac{V(A_T)}{c}\right), \tag{3.4}$$

where P_0 is the intrinsic pulsar period, and $V(A_T)$ is the radial velocity of the pulsar due to its orbital motion, which is given by:

$$V(A_T) = \frac{2\pi}{P_{\rm orb}} \frac{a \sin i}{\sqrt{1-e^2}} \left(\cos(\omega + A_T) + e\cos\omega\right), \tag{3.5}$$

with the orbital true anomaly, $A_T(E)$, defined as:

$$A_T(E) = 2\arctan\sqrt{\frac{1+e}{1-e}}\tan\frac{E}{2}, \tag{3.6}$$

and the eccentric anomaly, E, expressed as:

$$E - e\sin E = \frac{2\pi}{P_{\rm orb}}(T - T_w). \tag{3.7}$$

Here:

- $P_{\rm orb}$: Orbital period of the binary system,
- $a\sin i$: Projected semi-major axis along the line of sight,

- e: Orbital eccentricity,
- ω: Longitude of the periastron,
- T_w: Time of periastron passage.

These orbital parameters can be obtained from publicly available databases such as Fermi/GBM's pulsar catalogs (`https://gammaray.msfc.nasa.gov/gbm/science/pulsars.html`). Note that parameters in these catalogs are often provided as times relative to the ascending node of the orbit, which is 90 degrees away from the periastron. Time conversions can be done accordingly.

To implement binary orbital corrections, the Python package `binaryCorr` is used. The steps for installation and correction are as follows:

1. Download the `binaryCorr` package from the HXMT Code Collection.
2. Install the package:

```
>>> python setup.py build_ext --inplace
```

3. Add the following to your `.bashrc` file:

```
export PYTHONPATH=\$PYTHONPATH:path-to-binaryCorr
```

4. Use the provided Python scripts to execute the binary orbital correction:

```
>>> binCor
```

This process ensures that the pulsar timing data are corrected for binary orbital motion, allowing for high-precision analysis in subsequent studies.

χ^2 Maximization Method

The χ^2 maximization method is used to identify a frequency range where periodic signals are likely to be present by testing different frequencies against the light curve data. This is particularly useful for searching for pulsar signals (coherent signals). The method applies the standard χ^2 statistic (commonly used for Gaussian distributed data) to evaluate how well a given frequency fits the observed data. The χ^2 statistic is calculated as follows:

$$\chi^2 = \sum_i \frac{(P_i - \text{Mean})^2}{\sigma^2}, \tag{3.8}$$

where P_i represents the data points, Mean is their average value, and σ^2 is the variance. For more details on the implementation, refer to the documentation provided by the Stingray library.

Z_n^2-Test

The Z_n^2-test is another effective method for periodic signal detection, especially when χ^2 maximization does not sufficiently highlight pulsar periodicity (Buccheri et al. 1983) [103]. Unlike χ^2, the Z_n^2-test is designed for the detection of periodic signals in sparse or noisy data. The Z_n^2 statistic is defined as:

$$Z_n^2(f) = \frac{2}{N} \sum_{k=1}^{n} \left[\left(\sum_{j=1}^{N} \cos(kft_j) \right)^2 + \left(\sum_{j=1}^{N} \sin(kft_j) \right)^2 \right], \tag{3.9}$$

where N is the number of data points, n is the number of harmonics, f is the frequency being tested, and t_j is the time of arrival of the j-th event. In general, $n = 2$ is chosen for most analyses to include fundamental and first-harmonic components. For detailed instructions, refer to the Stingray documentation: `https://docs.stingray.science/en/stable/#using-stingray`.

Software for Implementation

The periodic signal search and analysis described above can be performed using the `HENDRICS` software package, which is available at HENDRICS Documentation. This package is particularly suitable for analyzing data from NuSTAR and NICER, among other X-ray observatories. It offers powerful tools for time-domain analyses, such as pulsar signal searches, and ensures high precision in deriving pulsation parameters.

3.3.5 Pulse Folding and Phase Alignment

After determining the correct pulse frequency, the phase of photon arrival times can be calculated, and pulse folding can be performed using Python:

```
>>> import scipy.stats
>>> phase = f0 * (t - t[0])
```

Here, $t[0]$ represents the initial time of observation, `bins` specifies the number of phase bins, and `phase` is used to calculate the phases of photon arrival times. A `template` is a two-dimensional array, where `template[0]` corresponds to the pulse profile and `template[1]` represents the associated phase.

Due to variations in the start times and initial phases across different light curves, their phases may not be aligned. To address this, cross-correlation with a standard template or Fourier Transform Phase Fitting (FFTFIT) can be utilized to obtain the relative phase shifts [104]:

```
>>> from numpy import *
>>> from stingray.pulse import fftfit

>>> dphi, dphie = transpose(fftfit(profiles[0] / np.mean(profiles[0]),
>>> template = template[0] / np.mean(template[0])))
```

Here, `template` is the reference pulse profile template used for alignment. The outputs `dphi` and `dphie` represent the calculated phase shift and its associated uncertainty, respectively. Using the calculated phase shift, the times of arrival (TOAs) of pulses can be computed as follows:

```
>>> toa0 = toa0 + dphi * (1 / f0)  # Update pulse arrival time
>>> toa = toa0 / 86400 + mjdref  # Convert to Modified Julian Date (MJD)
```

Here, `mjdref` represents the reference time in Modified Julian Date (MJD). By folding photon arrival times at the computed pulse frequency and aligning their phases using `toa0`, the pulse profiles can be stacked for further analysis.

For additional details, please refer to the documentation of `PINT` (`https://nanograv-pint.readthedocs.io/en/latest/examples/time_a_pulsar.html`), which provides a comprehensive explanation of the methodology.

This approach primarily relies on fitting observed pulse profiles to model templates. For sources with rapidly varying pulse profiles, this method may not yield precise results. For rapidly evolving sources, continuous observations of periodic timing residuals (e.g., from Fermi/GBM) can help estimate frequency derivatives and better describe pulse evolution.

3.3.6 Phase-Resolved Spectroscopy

After determining the aligned phases, we can extract the energy spectra of interest from the `events` data within specified phase intervals. This process is referred to as phase-resolved spectroscopy. Due to the rotational motion of the pulsar, we observe emission originating from distinct regions of the emission geometry, leading to variations in phase. Therefore, phase-resolved spectroscopy serves as a powerful tool to investigate the accretion and emission mechanisms in X-ray binaries and pulsars.

The procedure for phase-resolved spectroscopy is straightforward. First, we utilize the `gti` file generated during the time interval selection process to extract the corresponding phase-resolved energy spectra. A Python script can be employed to automate this task. It is important to ensure that the aligned phases of the pulsar are properly corrected, especially if the pulsar exhibits strong phase evolution during the observation.

For implementation details and practical examples, refer to the Python script [1].

[1] `https://code.ihep.ac.cn/jldirac/insight-hxmt-code-collection/-/tree/master/version2.04`

4 Black Holes Research Results

This chapter presents the results of the detailed analysis of black hole X-ray binaries, focusing on their spectral and timing properties, particularly in their different states. The study investigates the complex interplay between accretion flows and relativistic jets, as well as the role of quasi-periodic oscillations (QPOs) in probing the inner regions of the accretion disk. We utilized data from multiple X-ray observatories, including NICER, NuSTAR, Insight-HXMT, and eROSITA, and aim to uncover the physical processes driving the variability in black hole systems and provide new insights into accretion and corona in the vicinity of black holes.

The works studied two representative black hole X-ray binaries that exhibit different states conditions during their reflare events. Accretion in the reflares is different from the accretion process of the corresponding main outburst, but it also shows certain similarities. For this study, we also showed how to find quiescent black holes in the sky survey. The published papers could be found in the appendix.

4.1 Summary: Evolution of Disc and Corona in MAXI J1348-630 During the 2019 Reflare (Dai et al., 2023 [1])

4.1.1 Aim of the Research

This study investigates the broadband spectral and timing evolution of the black hole X-ray binary (BHXRB) MAXI J1348-630 during its 2019 reflare, which occurred approximately four months after its main outburst. By utilizing NICER and Insight-HXMT observations, the research aims to explore the interplay between the accretion disc and corona at different luminosity levels and to identify the physical processes governing the reflare evolution.

Figure 4.1 shows the overall light curve of MAXI J1348-630 observed by MAXI in the 2-20 keV energy range, including the primary outburst phase and the subsequent reflare part. The reflare part, marked by the red rectangle, shows a distinct flux increase followed by a gradual decline, indicating renewed activity in the accretion process.

4.1.2 Conclusions

Our findings suggest the existence of a characteristic luminosity, $L_{\rm crit} \sim 0.002 L_{\rm Edd}$, below which the inner radius of the accretion disc remains stable, while above this

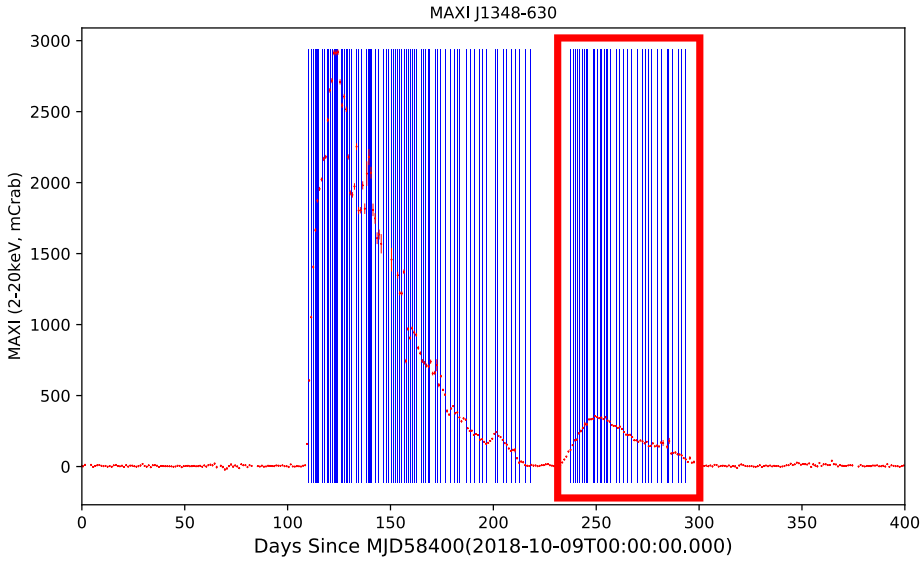


Figure 4.1: The MAXI (2–20 keV) light curve shows the main outburst and the first reflare of MAXI J1348-630. The blue areas indicate the Insight-HXMT's observations. The red rectangle displays the focused reflare part. (from Dai et al. 2023)

threshold, the inner disc radius moves inward.

We propose that below $L_{\rm crit}$, the evaporation process in the accretion disc dominates, preventing efficient angular momentum transfer and disc condensation. However, once the luminosity exceeds this critical value, the condensation process becomes dominant, leading to a more effective formation of the accretion disc and allowing for angular momentum redistribution. Additionally, our spectral modeling indicates significant variations in the spectral hardening factor, suggesting that the transition of the disc structure is accompanied by changes in the Comptonization properties of the corona.

Our timing analysis further reveals the presence of type-C QPOs with frequencies evolving in response to the increasing accretion rate. The QPO fractional RMS shows an energy-dependent behavior, remaining stable at higher energies while displaying variability at lower energies. Moreover, we detect an evolution in the hard lags, indicating a complex interplay between the disc, corona, and Comptonization processes.

Our results provide new insights into the disc-corona interaction in black hole X-ray binaries during reflaring episodes, offering further evidence for the role of accretion state transitions at low luminosities. Future observations with next-generation X-ray telescopes, such as *eXTP*, will be essential to further explore the mechanisms governing the reflare phenomenon and the disc-corona evolution in transient black hole binaries.

4.1.3 Creative Ideas and Novel Contributions

- **Identification of a Critical Luminosity ($L_{\rm crit}$)**: A key discovery is the existence of a critical luminosity threshold, $L_{\rm crit} \sim 2.5 \times 10^{36}$ erg s^{-1} ($\sim 0.002 L_{\rm Edd}$), beyond which the behavior of the inner accretion disc changes significantly. Below $L_{\rm crit}$, the inner disc radius remains stable, while above $L_{\rm crit}$, it moves inward as expected in standard accretion scenarios.

- **Hardening Factor Evolution and Corona Dynamics**: The study finds that at low luminosities, the hardening factor $T_{\rm col}/T_{\rm eff}$ deviates significantly from the canonical value of ~ 1.7, indicating that the accretion flow remains in a non-equilibrium state. This suggests that evaporation dominates below $L_{\rm crit}$, preventing effective angular momentum transport, whereas condensation dominates above $L_{\rm crit}$, facilitating inward motion of the disc.

- **QPO and Noise Properties During the Reflare**: The research provides a broadband study of type-C QPOs in a reflare, showing that their frequencies increase with luminosity but remain stable above 10 keV. The QPO root mean square (RMS) spectrum follows different evolutionary trends at different energy bands, suggesting that low-energy QPOs are disk-dominated, whereas high-energy QPOs may originate from a compact jet precession.

- **Energy-Dependent Time Lags and Spectral Evolution**: The study reveals a systematic increase in hard time lags at high energies (70–120 keV), particularly at low flux levels. This suggests that at lower luminosities, soft photons undergo more Comptonization, while at higher luminosities, the disk cooling effects become more dominant.

4.1.4 Main Results

- **Spectral Evolution of the Reflare**
  - The study confirms that the accretion disk remains truncated at a large radii ($\sim 34R_g$) when the luminosity is below $L_{\rm crit}$, while it gradually moves inward (down to $\sim 17R_g$) when the luminosity exceeds $L_{\rm crit}$.
  - The disk flux-temperature relation follows $F \propto T^4$ at low flux, but deviates from this scaling at higher luminosities, indicating a transition in accretion physics.

- **Timing Evolution of the Reflare**
  - QPOs are observed, with frequencies increasing from ~ 0.4 Hz to 0.9 Hz at peak luminosity.
  - QPO RMS remains at $\sim 5\%$ above 10 keV, significantly lower than in the soft X-ray band ($\sim$ 10–20%), suggesting different emission mechanisms.
  - The low-frequency break in the power spectrum remains stable at low luminosities, implying that the accretion flow is stable below $L_{\rm crit}$.

- **Interplay Between the Disc and Corona**
  - The covering fraction of the corona ($C_{\rm ovf}$) decreases as the flux increases, implying that at peak flux, fewer photons are Comptonized and the system relatively becomes disk-dominated.
  - The study supports the idea that at low luminosities, the corona remains geometrically thick, while at higher luminosities, it collapses into a more compact configuration.

This work demonstrates that the reflare in MAXI J1348-630 follows a distinct accretion evolution pattern, characterized by a transition between evaporation- and condensation-dominated states. The identification of a critical luminosity provides a new perspective on accretion physics in low-luminosity BHXRBs, with implications for understanding disk truncation, corona evolution, and reflare mechanisms.

4.2 Unveiling the Rebrightening Mechanism of GRS 1915+105: Insights from QPOs and Disk Winds (Dai et al., 2024 [2])

4.2.1 Aim of the Research

This study investigates the physical mechanisms driving the rebrightening event in the black hole X-ray binary (BHXRB) GRS 1915+105, which was observed in July 2021 using NICER and NuSTAR. The primary goal is to examine the interplay between quasi-periodic oscillations (QPOs) and disk winds during this rebrightening phase, providing new insights into magnetically-driven accretion-ejection processes.

4.2.2 Conclusion

In this study, we employed the Hilbert-Huang Transform (HHT) to decompose QPOs and performed a phase-resolved spectral analysis. Our results reveal a significant correlation between the QPO phase and the spectral parameters, particularly the iron absorption features and the continuum properties.

We find that the Fe XXV absorption edge exhibits strong phase-dependent variations, while the Fe XXV and Fe XXVI absorption lines show moderate changes. The electron temperature and optical depth of the Comptonized component are also modulated by the QPO phase. These findings suggest that the observed QPOs are driven by magnetic activity rather than precession, supporting the accretion-ejection instability (AEI) model. Our results indicate that during QPO cycles, the corona and disk wind undergo periodic structural transformations, likely influenced by the magnetic field.

The presence of QPOs in the soft state of GRS 1915+105, contrary to conventional expectations, highlights the complex interplay between accretion, magnetic processes, and disk winds. This study provides new insights into the accretion-ejection mechanism in black hole X-ray binaries. Future high-resolution observations and polarization studies will be crucial for further constraining the nature of these phenomena and advancing our understanding of magnetically regulated accretion flows.

4.2.3 Creative Ideas and Novel Contributions

- **Discovery of Low-Frequency QPOs (LFQPOs) in the Soft State**: Traditionally, LFQPOs are absent in the soft state of GRS 1915+105. This study identifies their presence during rebrightening, suggesting a magnetic origin rather than precession-based models.

- **Application of the Hilbert-Huang Transform (HHT) for QPO Decomposition**: By employing variational mode decomposition (VMD), the study extracts QPO components with enhanced accuracy, resolving mode-mixing issues commonly encountered in QPO analyses. (A more detailed description of the HHT method can be found in the Appendix (see Dai et al., 2024 [2]))

- **Phase-Resolved Spectral Analysis of QPO Evolution**: The research reveals systematic variations in Fe XXV and Fe XXVI absorption lines and a strong correlation between the photon index, seed photon temperature, and QPO phase, demonstrating a direct link between QPO activity and disk wind properties.

- **Magnetic-Driven Disk Winds and Failed Ejection Mechanism**: The study proposes that LFQPOs are generated by accretion-ejection instability (AEI), where the magnetic field induces a failed wind composed of highly ionized, low-velocity material, distinct from standard thermally-driven winds.

4.2.4 Main Results

- **Spectral and Timing Evolution of the Rebrightening Event**
  - The disk wind ionization degree increased during the rebrightening, indicating a shift in the accretion flow properties.
  - The Fe XXV absorption edge varies significantly with QPO phase, supporting a magnetic interaction between the corona and disk wind.
  - QPO phase-resolved analysis shows anticorrelation between electron temperature and QPO flux, implying that the corona contracts during high-flux QPO phases while the wind expands.

- **The Role of the Accretion-Ejection Instability (AEI) Model**
  - The findings challenge standard coronal precession models and suggest that QPOs are directly linked to magnetic field activity in the inner accretion flow.
  - Magnetic energy injection into the wind drives quasi-periodic heating and cooling processes, explaining the observed spectral and timing behavior.

- **Corona-Wind Interplay During the QPO Cycle**
  - At high QPO flux, the corona is more extended, whereas at low QPO flux, part of the corona collapses into the wind, leading to increased absorption strength.
  - A schematic model suggests a dynamic exchange between the corona and the wind, regulated by magnetic fields and LFQPOs.

This study provides the first direct evidence of magnetically-driven disk winds linked to QPOs in GRS 1915+105. The findings support the AEI framework, where a dynamically evolving corona interacts with a magnetized wind. These results offer a novel perspective on accretion physics, QPO generation, and black hole disk-wind interactions.

4.3 Search for Quiescent Black Holes with eROSITA

The quiescence state is one of the most common state observed in black hole X-ray binaries, yet it remains one of the least explored due to the challenges associated with detecting low-luminosity sources. Black holes in the quiescent state typically exhibit very low flux levels, making observations difficult and limiting the number of studies on their variability. The limited number of studies conducted so far suggest that quiescent spectra are often consistent with a power-law shape, with a photon index around 2. However, the absence of spectral variability and the faintness of the emission make it challenging to constrain models of accretion in this state.

It is generally believed that the emission from quiescent black holes is dominated by either advection-dominated accretion flows (ADAF) or jet-dominated accretion flows (JDAF). These models propose different mechanisms for extremely low accretion rates, where the accretion disk is far from the black hole. The ADAF model describes inefficiently radiating, whereas the JDAF model attributes the emission to synchrotron radiation from a relativistic jet. Distinguishing between these models requires detailed spectral and timing analyses, which remain challenging with current X-ray instruments.

With the launch of the eROSITA mission, we now have an unprecedented opportunity to systematically study black holes in the quiescent state. The eROSITA All-Sky Survey(eRASS) will accumulate the largest sample of quiescent black holes to date, allowing for a systematic investigation of their timing and spectral properties. This project aims to take advantage of the vast dataset provided by eRASS to search for variability and spectral features, such as the presence of fluorescent iron lines, which could help distinguish between different accretion models.

4.3.1 Cataloging of Quiescent Black Holes

Our work leverages the second data release (version 201008, based on the c946 data processing) from eRASS. Using the calibrated source catalog from 3 times of eRASS, named `all_e1_201008_poscorr_mpe_clean.fits`, `all_e2_201221_poscorr_mpe_clean.fits` and `all_e3_20210426_poscorr_mpe_clean.fits`, we performed a systematic search for quiescent black holes. We note that an official eFEDS X-ray source list was made public in the data release related to the journal of Astronomy & Astrophysics special issue with eRosita data, which may be different from our results. The initial steps involved constructing a pipeline to search for sources by matching precise coordinates with a tolerance of 0.1 degrees, which was further refined to 0.001 degrees to maximize accuracy.

The initial phase of this research involved constructing a pipeline to identify potential sources by matching precise coordinates from the SIMBAD database with data from eROSITA surveys. In November 2020, the SIMBAD database listed 195 black holes and black hole candidates, each with precise coordinates (RA, DEC). Coordinate units are in equatorial coordinates. We used these coordinates as a reference point for our search.

At first, we employed a tolerance of 0.1 degrees, where each source's coordinate from the SIMBAD catalog was used as the center of a circular search region. With this tolerance, we identified 61 corresponding sources in the three eROSITA surveys (eSASS1, eSASS2, and eSASS3). These 61 sources are in Table 4.1, which shows the

detailed results of this matching process.

However, this low precision resulted in overlapping regions, leading to multiple sources being detected within the same area, significantly increasing the ambiguity and decreasing the accuracy of the matches. To resolve this, we gradually increased the search precision, eventually narrowing it down to 0.001 degrees. While this high precision reduced the number of detected sources, it also posed the risk of missing out on relevant sources due to too small a search region.

After experimenting with various levels of precision, we determined that a search tolerance of 15 arcseconds (0.004167 degrees) provided the optimal balance. At this level of precision, the majority of black holes and black hole candidates in the eROSITA data were found to have fewer than four corresponding sources within this region. The 15 arcseconds tolerance is also suitable for defining the radius of the region to calculate flux from a single point source, which is critical for estimating the luminosity of compact objects such as black holes. Despite this refinement, a few cases remained where multiple sources were detected within the 15 arcseconds region. For those, we manually examined the sources and excluded those that were not in quiescent states or those with excessively high flux (luminosity on the order of 10^{-9} or brighter).

Once the sources were filtered, we processed the data using Python scripts, which generated tables detailing the properties of each matched source, including their name, RA, DEC, observation times (Tstart, Tstop), and flux (ML_FLUX_0). This process was repeated for each of the three eSASS surveys. Out of the 195 black hole and black hole candidates from the SIMBAD catalog, 78 fell within the eROSITA Image Tot. Due to data access restrictions, we were able to analyze only certain sky tiles, which yielded a total of 43 matched sources across the three eSASS surveys.

Table 4.3 shows the situation of 43 black holes and black hole candidates in 3 eSASS successively.

After identifying potential quiescent black hole candidates, we used the website `https://www2.mpia-hd.mpg.de/~calj/gdr2_distances/main.html` to query the distances to each source. This allowed us to distinguish between isolated black holes and BHXRBs. Additionally, we classified each source as either a low-mass X-ray binary (LMXB) or a high-mass X-ray binary (HMXB) and determined whether they were persistent or transient sources.

In our analysis, we matched 43 sources from the eROSITA surveys, categorized into different types of astrophysical objects based on their characteristics. Below is a detailed classification of the types of sources and their specific features:

LMXBs: these systems consist of a low-mass companion star and compact star. The material from the star is accreted onto the compact object, producing X-rays.

- **4 sources with uncertain distances**:
  - **X Nor X-1 (4U 1630-472)**: Detected in eSASS1. This is an LMXB, and due to its variability, it is considered an excellent candidate for further study.
  - **NAME Great Annihilator (2E 3938)**: Detected in all three eSASS surveys. This is a strong LMXB candidate, and the source is known for its historical significance as a potential black hole candidate.

Table 4.1: Possible BHs & BHCs in eSASS1, eSASS2 and eSASS3

Name	**RA**	**DEC**	**eROSITA[a]**
X Nor X-1	248.5067	-47.393	100
V* V1228 Sco	259.9958	-31.7503	010
2E 3238	214.7659	-13.17910583	111
ICRF J230343.5-680737	345.9315	-68.1270675	110
QSO B0403-132A	61.3917	-13.13713639	111
ICRF J045608.9-215909	74.0372	-21.98594444	111
Ton 469	149.5873	32.40061361	110
ICRF J130533.0-103319	196.3876	-10.55539722	111
RX J1749.8-3312	267.4539	-33.20322222	101
V* V381 Nor	237.7444	-56.47647472	100
[SBC2007] NGC 3201 12560	154.4045	-46.41535306	110
[GHE2001b] U97	265.183	-53.66830556	111
PKS 0405-123	61.9518	-12.19351667	111
PG 0953+414	149.2183	41.25617	110
EWS 2006-BLG-44	268.7926	-30.44105556	110
QSO B1228+077	187.8357	7.431288889	111
LBQS 1340-0038	205.715	-0.895941389	111
ICRF J110715.0+162802	166.8127	16.46729	110
ICRF J145427.4-374733	223.6142	-37.79254	111
LBQS 1230+0947	188.3574	9.523157222	110
MAXI J1543-564	235.8222	-56.41343056	011
LBQS 1132-0302	173.7705	-3.314318333	110
7C 1028+3118	157.7462	31.04881167	110
2E 962	64.3199	-5.896002222	111
V* V4134 Sgr	269.6667	-33.8075	111
PG 1216+069	184.8372	6.644018611	110
NAME Great Annihilator265.9785	-29.74516667	111	
V* GU Mus	171.6108	-68.67580222	110
QSO B1104-181	166.63912	-18.35661111	110
PB 4007	204.0084	17.42030278	111
Ton 28	151.0109	28.92648056	110
QSO J0441-4313	70.3222	-43.22930194	111
NAME CO-0.40-0.22	266.3858	-29.3925	110
2E 2584	181.1755	27.90329639	110
2MASSI J1159262+210655	179.8592	21.11552139	110
ICRF J074541.6+314256	116.4236	31.71572611	111
CRTS J135716.8-093238	209.3201	-9.544109167	011
[KB2007] J110631.8+005253.4	166.6325	0.881388889	010
2E 3174	211.0441	9.6292525	111
[KB2007] J105151.5+005118.1	162.9646	0.855	100
PB 3894	183.5736	14.05366167	111
SWIFT J1539.2-6227	234.7998	-62.46730556	001
V* BW Cir	209.5404	-64.73494444	010
X LMC X-1	84.9118	-69.74320361	111
[LB2005] NGC 4472 X3	187.4155	7.891833333	111
LBQS 1317-0142	199.9598	-1.967731111	111

Table 4.2: Continued

Ton 1388	169.7862	21.32166278	110
LBQS 1138+0204	175.3407	1.800987222	110
QSO J2355-3357	358.8575	-33.96533694	110
V* V821 Ara	255.7058	-48.7897675	111
LBQS 1144-0115	176.8253	-1.535291667	110
V* IL Lup	236.7845	-47.66952333	100
2MASX J04523006-2953353	73.1253	-29.89311833	111
ESO 113-45	20.9409	-58.80578083	110
CXOU J122941.0+075744	187.4208	7.962222222	111
2MASS J03512857-1429082	57.869	-14.48562722	111
ICRF J084047.5+131223	130.1983	13.20654556	110
1A 0620-00	95.6856	-0.345635833	100
V* MM Vel	153.4017	-45.07570972	110
2MASX J09504838+3926503	147.7016	39.44735083	110
2E 2978	197.446	8.330059722	111

[a] A value of 1 or 0 indicates whether the source was detected by eROSITA using eSASS1 (left), eSASS2 (middle), and eSASS3 (right), respectively.

Table 4.3: Possible BHs & BHCs in eSASS1, eSASS2 and eSASS3

	Total	**ImageTot**	**eSASS**	**eSASS1**	**eSASS2**	**eSASS3**
Number	195	78	43	41	40	20

  - **V* V821 Ara (4U 1658-48)**: Detected in all three eSASS surveys. This source's classification between LMXB and HMXB is uncertain, making it a valuable subject for future analysis.
  - **X LMC X-1 (4U 0540-69)**: Detected in eSASS1 and eSASS2. This is classified as a high-mass X-ray binary (HMXB).

HMXBs: These systems are similar to LMXBs but involve a high-mass star, usually an O or B-type star, accreting material onto the compact object.

- **1 HMXB with uncertain distance**:
  - **1A 0620-00 (3A 0620-003)**: This HMXB was only detected in eSASS1 but not in eSASS2 or eSASS3, indicating variability or periods of quiescence.
- **2 confirmed sources**:
  - **V4134 Sgr (4U 1755-338)**: Detected in all three eSASS surveys. This is a well-known LMXB with persistent emission.
  - **V* GU Mus (2RE J112617-684044)**: Detected only in eSASS2, and absent in eSASS1 and eSASS3. This source is notable for its variable nature and may require more precise analysis.

Active Galactic Nuclei (AGN): AGNs are galaxies with supermassive black holes at their centers. These black holes actively accrete material, producing significant X-ray emissions.

- **25 AGN Seyfert 1**: Seyfert 1 galaxies are a subclass of AGN that show both broad and narrow optical emission lines. They are characterized by highly variable X-ray emission and have been observed consistently across eROSITA.

Blazars (BL Lac Objects): These are a specific type of AGN where the jet of relativistic particles is pointed almost directly at Earth, leading to intense variability and emission across the electromagnetic spectrum, including X-rays.

- **2 BL Lac Objects**: These objects are highly variable in X-rays and are known for their significant contribution to the cosmic X-ray background.

Quasars: Quasars are a highly energetic type of AGN, with supermassive black holes actively accreting material at their centers. Quasars are the most luminous objects in the universe, producing massive amounts of energy in X-rays.

- **9 Quasars**: These quasars were detected across multiple eSASS surveys, and they represent some of the most distant and energetic objects observed.

In conclusion, the 43 sources detected in the eROSITA and eSASS surveys span a wide range of astrophysical phenomena. These sources include:

- 4 LMXBs and 1 HMXB with uncertain distances
- 2 confirmed LMXB/HMXB in multiple eSASS surveys
- 25 AGNs of the Seyfert 1 type
- 2 Blazars (BL Lac Objects)
- 9 Quasars

Each type of source presents unique characteristics:

- **LMXBs and HMXBs** are critical for studying accretion processes and the evolution of compact objects.
- **AGN and Quasars** provide insights into supermassive black hole activity and the large-scale structure of the universe.
- **Blazars** are significant for their extreme variability and emission mechanisms, providing a direct look into relativistic jet activity.

These findings contribute to our understanding of both stellar-mass and supermassive black holes, offering a rich dataset for further astrophysical investigation. In this study, we focused on transient sources, as they are more likely to be in a quiescent state between outbursts. Based on our classification, we narrowed down the candidate list to seven quiescent black holes which are LMXBs or HMXBs.

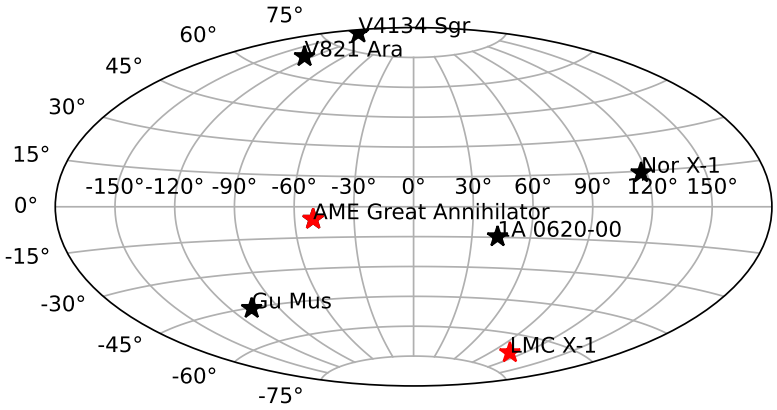


Figure 4.2: The positions of seven black holes in quiescent state searched from eSASS

4.3.2 Observation Results of Luminosity Changes

We studied the seven sources.For two sources with certain distance, we found it their luminosity with different observations, shown in table 4.4

Name	D (kpc)	XMM	Chandra	XRT	eROSITA
V* GU Mus	2.3(4.8)	$9.42e^{-15}$	-	-	$3.50e^{-14}$
1A 0620-00	1.6 (1.5)	$1.72e^{-14}$	$1.70e^{-14}$	$7.79e^{-14}$	$1.89e^{-13}$

Table 4.4: Comparison of flux values from different observatories.

Note: In the 'D' column, means the distance in units of kpc. The first value is the distance obtained from the Gaia satellite, and the second value (the value in brackets) is from the literature. The satellite column shows the luminosity of the source as observed by the satellite, in units of $\mathrm{erg\,s^{-1}\,cm^{-2}}$.

V* GU Mus was in quiescent in eSASS2, which was observed once in 3 times eSASS. **V* V821 Ara** was in quiescent state in eSASS2, but was in outburst in eSASS1 and eSASS3. **1A 0620-00** was in quiescent state in eSASS1, then cannot be found in eSASS2 or eSASS3. We found that these processes were so faint when they were in quiescent state that we could not to get the effective spectral and temporal analysis. Therefore, we checked their flux one by one. The flux values were mostly in the range of single-digit counts, and no significant fluctuations were detected over the observation periods. This lack of variability and low photon flux suggests that these sources remained in a stable quiescent state throughout the eROSITA observations. Here we show the position of the seven sources are in figure 4.2, the sources in red stars are persistent sources. Our initial goal, as outlined in the research proposal, was to systematically investigate the timing and spectral variability of quiescent black holes and to search for fluorescent iron lines. Unfortunately, the low photon counts made it difficult to perform detailed variability studies or detect any significant spectral

features, such as the Fe Kα line, which is often used to probe the inner regions of the accretion disk. Besides that, we purpose the results of this investigation will offer a comprehensive view of quiescent black holes detected in the eROSITA survey. After the completion of eRASS8, we could anticipate publishing a summary paper that will consolidate our findings on the quiescent state of black holes, providing a critical reference for future studies of low-accretion-rate systems. These results will not only enhance our understanding of quiescent black holes but also contribute to broader discussions on accretion physics and the nature of black hole emission at low luminosities. However, the current findings are not sufficient to support the expected findings.

Although the data collected from eROSITA did not reveal the expected variability or spectral features, the systematic approach used in this study demonstrates the potential of eROSITA to detect and catalog quiescent black holes. Future data releases, particularly eRASS8, are expected to provide a larger sample size and potentially higher photon counts, allowing for more detailed studies. The results of this project lay the groundwork for future investigations, including the potential publication of a summary paper that consolidates the properties of quiescent black holes detected in eRASS. The limitations encountered in this study emphasize the importance of deeper observations with more sensitive instruments. Despite not achieving the initial goals of the proposal, this work contributes to the broader understanding of black hole accretion at low luminosities, offering insights into the challenges of detecting and characterizing quiescent states in BHXRBs.

5 Neutron Star Research Results

In this chapter, we present the results of our comprehensive study on pulsars, focusing on various aspects such as spin measurements and anti-glitch searching. Each subsection includes specific observations and analyses performed using data from different satellite missions. These results advance our understanding of neutron star behavior.

5.1 Spin Measurement and Evolution Analysis of SXP726(Haberl et al.,2022 [3])

This chapter is based on one part of the following publication: "eROSITA calibration and performance verification phase: High-mass X-ray binaries in the Magellanic Clouds", published in Astronomy and Astrophysics in 2022 [3].

The spin evolution of neutron stars provides crucial insights into their magnetic field structure and accretion dynamics. We utilized data from XMM-Newton and eROSITA to conduct a detailed spin measurement and evolution analysis of the neutron star RX J1015.9-7203 (SXP 726), which is a single bright and likely a Be/X-ray object in Small Magellanic Cloud [105]. The region surrounding the supernova remnant (SNR) 1E0102.2-7219 has been a focal point of multiple observations using the XMM-Newton telescope since its launch, primarily for the calibration of the EPIC-MOS and EPIC-PN cameras. This area is ideal for calibration due to its well-studied nature and the stability of the source. In addition to XMM-Newton, eROSITA has also conducted observations of this region. The Small Magellanic Cloud (SMC) mosaic, as captured by eROSITA observations, is shown in Figure 5.1, providing a detailed view of the area. These observations play a crucial role in calibrating instruments and expanding our knowledge of the SMC and related astrophysical phenomena, particularly the dynamic processes associated with SNR 1E0102.2-7219. In Figure 5.1, the source SXP 726 is marked near the lower-left region of the image, identified with a pulse period of 726.0 seconds. This source is relatively stable and stands out in the image as it allows for a well-defined measurement of its pulse period, making it a reliable object for further analysis. Compared to other sources in the image, SXP 726 is distinct due to its stability in terms of pulse period, which contrasts with the variability observed in other sources. For instance, some other sources marked in the figure show either no clear pulse periods or highly variable characteristics. Additionally, while other sources may show changes in luminosity or more complex behaviors, SXP 726 remains consistent, making it an important reference point in the study of the region.

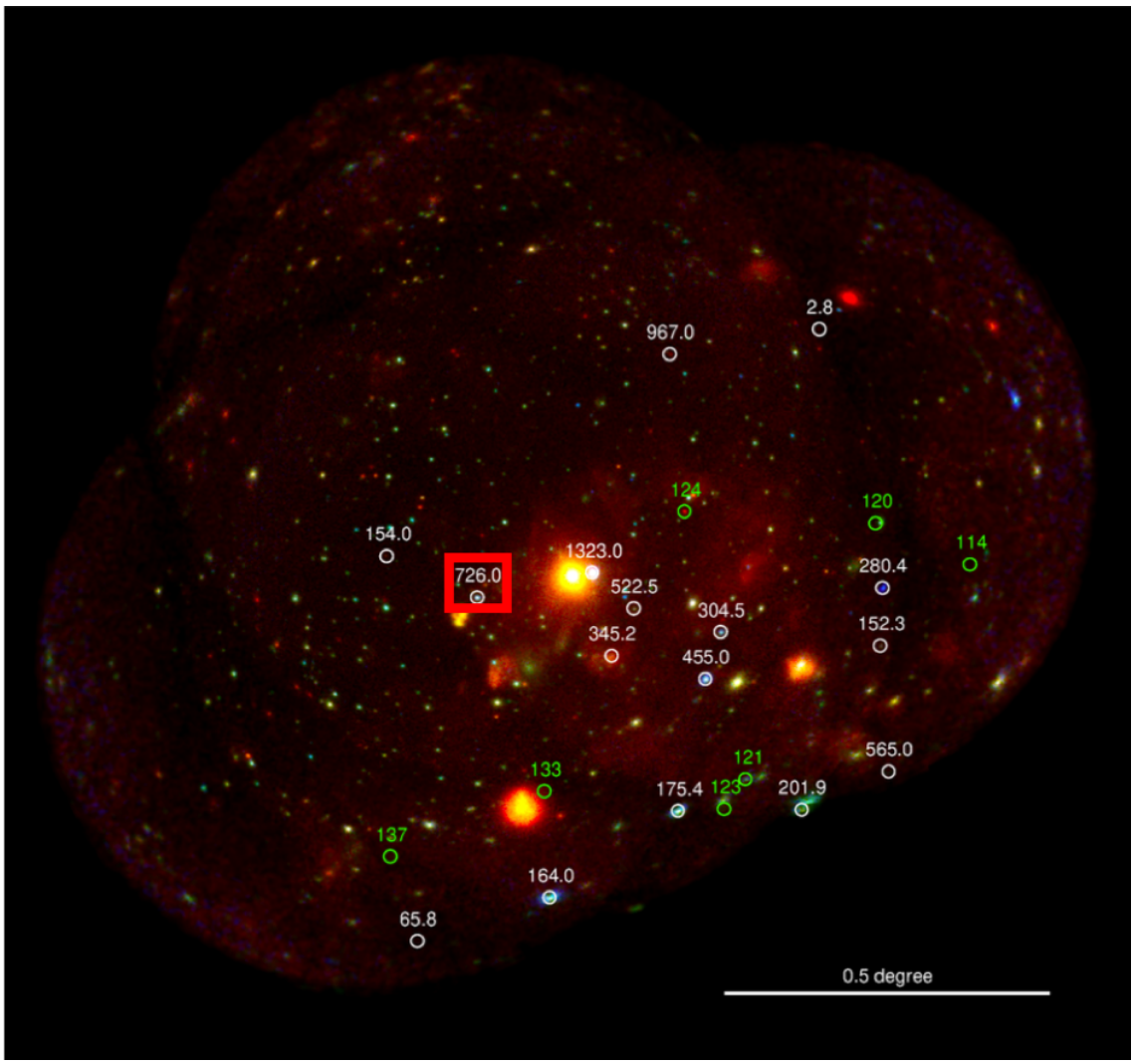


Figure 5.1: SMC mosaic from eROSITA observations around the supernova remnant 1E 0102.2-7219, the brightest source near the image centre. HMXBs without known pulse period are indicated by green circles. The red box outlines the location of the source. (from Haberl et al., 2022[3])

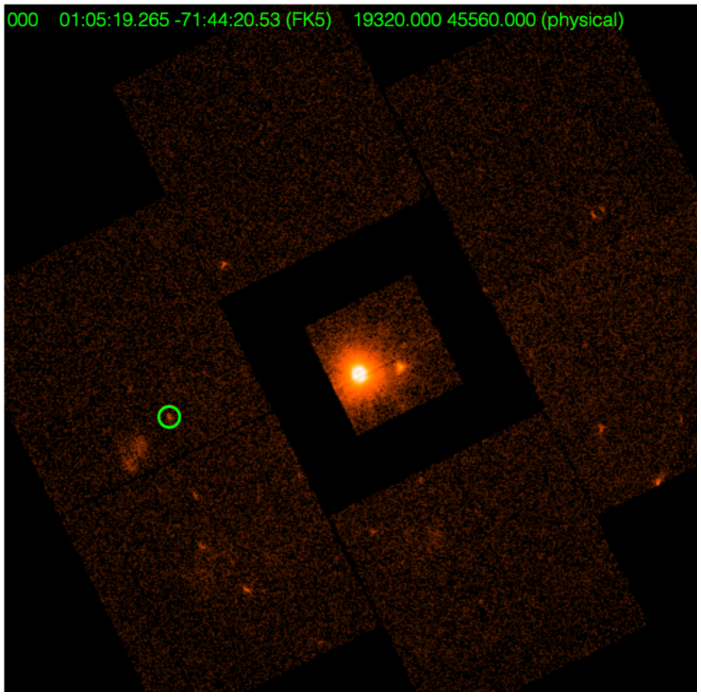


Figure 5.2: SXP 726 spectral extraction position from XMM archive.

5.1.1 XMM-Newton Data Analysis

In this study, we conducted a detailed analysis of the X-ray emissions and timing properties of SXP 726, utilizing data from XMM-Newton. The observations included 31 datasets, with a focus on counting statistics sufficient for period detection. To extract and analyze the data, we used the **XMM-Newton Science Analysis System (SAS)** version **19.0.0**, combined with tools from the **FTOOLS** package and **XSPEC** version **12.11.0** for spectral modeling.

The position of the source was set to RX J0105.9-7203, as reported by Eger & Haberl in 2008 [106], with coordinates RA=01 05 55.31 and Dec=-72 03 50.2 (J2000.0). Source photons were extracted from the 0.2–10 keV energy band within a source-centered region with a radius of 30 arcsec. We applied standard screening criteria to filter the data, correcting photon arrival times to the Solar System barycenter. Figure 5.2 presents the spectral extration position from XMM archive. Specific steps for XMM observations are as follows: For the analysis of the X-ray spectra we extracted pulse-phase averaged EPIC spectra for PN (PATTERN 0-4) and MOS (PATTERN 0-12) disregarding the bad CCD pixels and columns (FLAG=0). We applied a background screen for source detection spectral and timing analyses. All data can be found from the website "`https://www.cosmos.esa.int/web/xmm-newton/xsa`". The standard screening criteria are described in the documentation from "`https://www.cosmos.esa.int/web/xmm-newton/sas-threads`". We repeated the results in the reference from Eger & Haberl in 2008[106]. Of the 22 observations included in the reference study, seven had timing periods available in the literature. While our spectral analysis largely aligns with previous findings, our timing analysis differed slightly. For instance, we did not detect timing periods for the observations on April 14, 2001, and November 16, 2003. Additionally, for the April 16, 2000 observation, we identified a spin period of 721.5 s, which was not previously reported. In other cases, our findings were within the margin of error.

5.1.2 Spin evolution combined with eROSITA

To determine the spin evolution of SXP 726, we used data obtained from the XMM-Newton and eROSITA, and applied the Z^2 test and Lomb-Scargle (LS) periodogram for period searching. The following steps outline the procedure we employed: First, we extracted the source events from the observational data, ensuring that all relevant photon events were included for accurate analysis. To account for timing corrections, we applied a barycentric correction, aligning the photon arrival times with the Solar System barycenter. The barycentric correction was performed in the same way as for the spectral fitting procedure. Next, we utilized the Z^2 test, a standard method for searching for periodic signals in photon arrival times. This test calculates the Z^2 statistic over a range of trial periods, identifying the most likely spin period based on the peak of the Z^2 distribution. We searched for periods between 650 and 850 seconds. The errors in the detected period were estimated using the "threshold" method, ensuring that the confidence range was within 1σ. For instance, using observation ObsID 0810880601 from XMM, the Z^2 test successfully identified a spin period of 802.78 s for SXP 726, with an error of $\pm$5.95 s, as shown in Figure 5.3. In addition to the period detection, we constructed the pulse profile of SXP 726. This periodic signal confirms the detection of the pulsar's spin period, showing clear modulations over the detected cycle. The spin evolution result is consistent with previous XMM-Newton observations, which indicated a long-term spin-down rate of approximately 3.2 s yr^{-1} between April 2001 and November 2003.

We also analyzed the spin period of SXP 726 using observations from eROSITA taken in November 2019. The observations were captured under observation ObsIDs 700001–700005. During these observations, the pulsar exhibited a consistent count rate, allowing us to precisely determine the spin periods by combining five observations. The Lomb-Scargle (LS) periodogram identified a strong periodic signal with a fundamental period of approximately 799 seconds, which is consistant with the Z^2 test, indicating a significant spin-down of nearly 80 seconds since the initial discovery of the pulsar's spin period. Figure 5.4 shows the light curve from eROSITA data and LS periodogram. The LS periodogram referred to "`https://docs.astropy.org/en/stable/timeseries/lombscargle.html`". We also conducted a detailed analysis of the spin periods from each observation. The periods were determined to be 798.8 $\pm$ 4.0 s, 800.0 $\pm$ 3.8 s, 797.6 $\pm$ 6.6 s, 801.5 $\pm$ 4.4 s, and 799.9 $\pm$ 3.2 s, respectively, with 1σ errors. These results were derived from the November 2019 eROSITA observations (ObsIDs 700001, 700003, 700004, 700005), demonstrating consistency across the data. A subsequent observation (ObsID: 710000) taken in June 2020 indicated a further increase in the spin period to 803.0 $\pm$ 5.5 seconds, showing that the spin-down trend continued. Our analysis demonstrates the continuous spin-down behavior of SXP 726, with the spin evolution results illustrated in Figure 5.5. The consistent spin-down over time provides valuable insights into the pulsar's accretion dynamics and its interaction with the surrounding environment.

The pulse profile analysis showed no significant change in the pulse shape between the November 2019 observations, as evidenced by the combined pulse profile, which was single-peaked with a pulsed fraction of 30 $\pm$ 8% in the energy range of 0.2–8 keV. However, the pulse profile from the June 2020 observation exhibited a narrower peak with a pulsed fraction of 35 $\pm$ 5%, suggesting changes in the pulsar's emission characteristics, as shown in Figure 5.6.

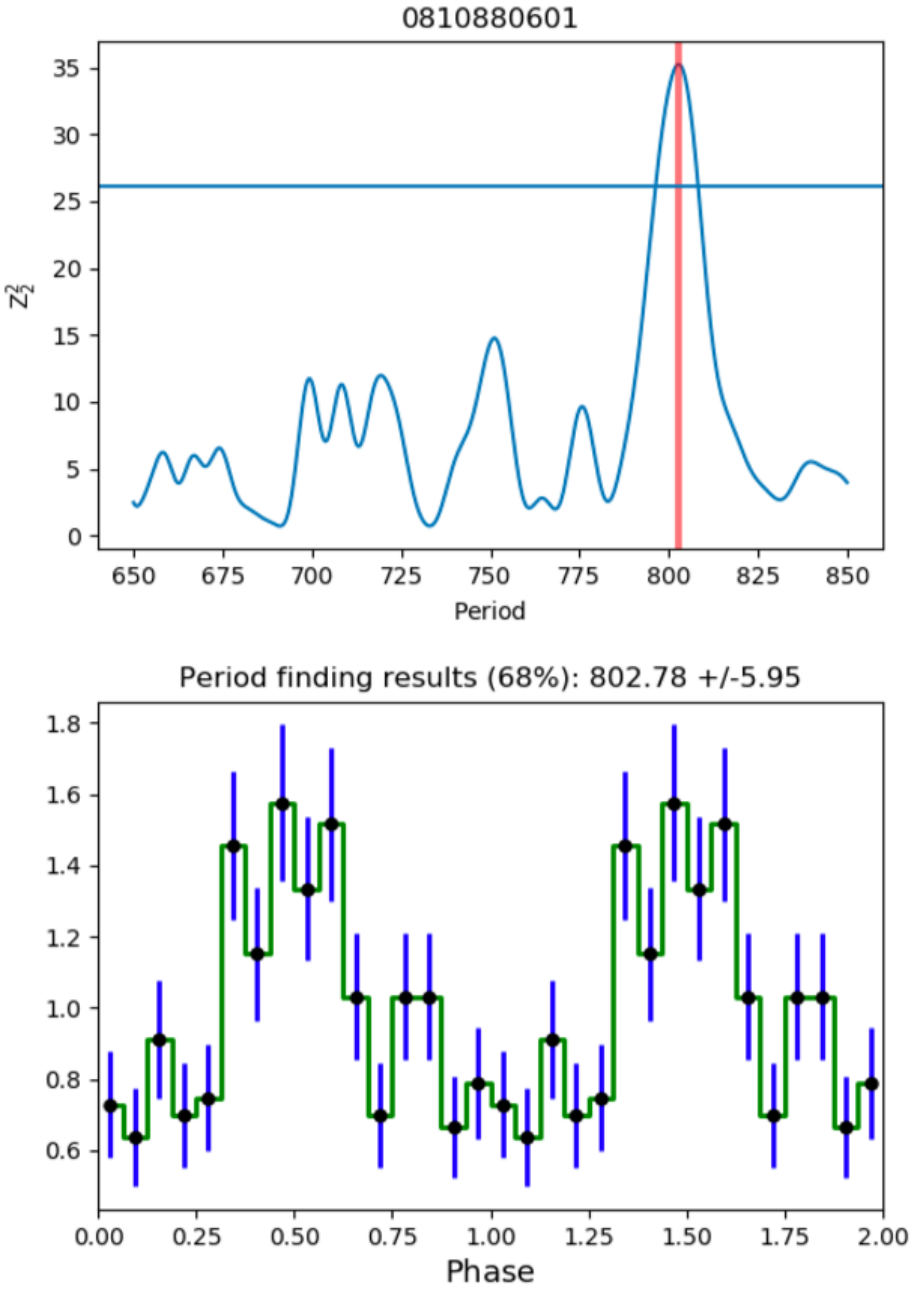


Figure 5.3: Z^2 test results for the period search of SXP 726 based on the XMM-Newton observation ID 0810880601. The top panel shows the Z_2^2 periodogram, with the highest peak indicating a detected spin period of 802.78 s with a 68% confidence interval of ± 5.95 s. The number of harmonics was set to 2. The blue horizontal line represents the significance threshold. The bottom panel displays the corresponding pulse profile as a function of phase, illustrating the periodic signal detected with error bars indicating the uncertainties for each phase bin. The green curve represents the best-fit model, and the black dots are the data points with 1σ errors (blue bars).

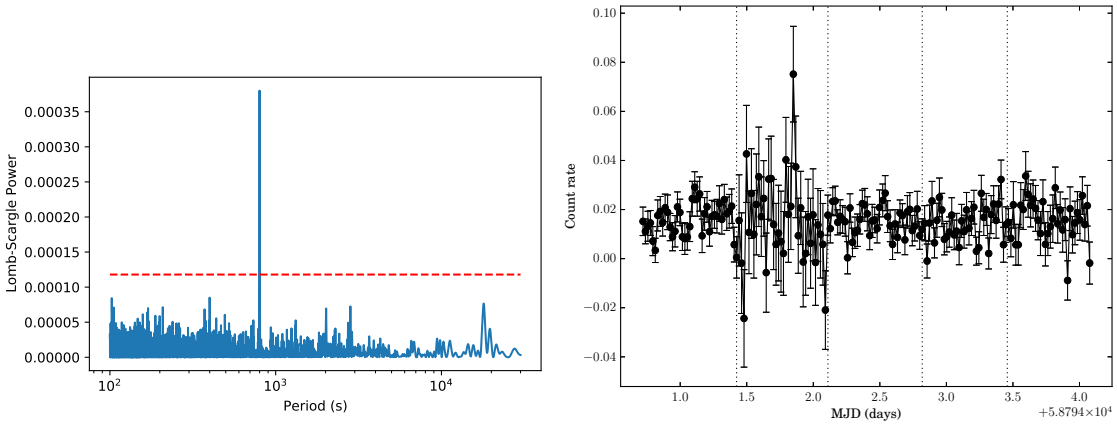


Figure 5.4: Left panel: LS periodogram obtained from the combined light curve of SXP726 shown below. The dashed red line indicates the 99% confidence level. Right panel: Background-subtracted and vignetting-corrected light curve of SXP726 (binned at twice the pulse period) in the energy band of 0.2-8.0 keV. (from Haberl et al, 2022[3])

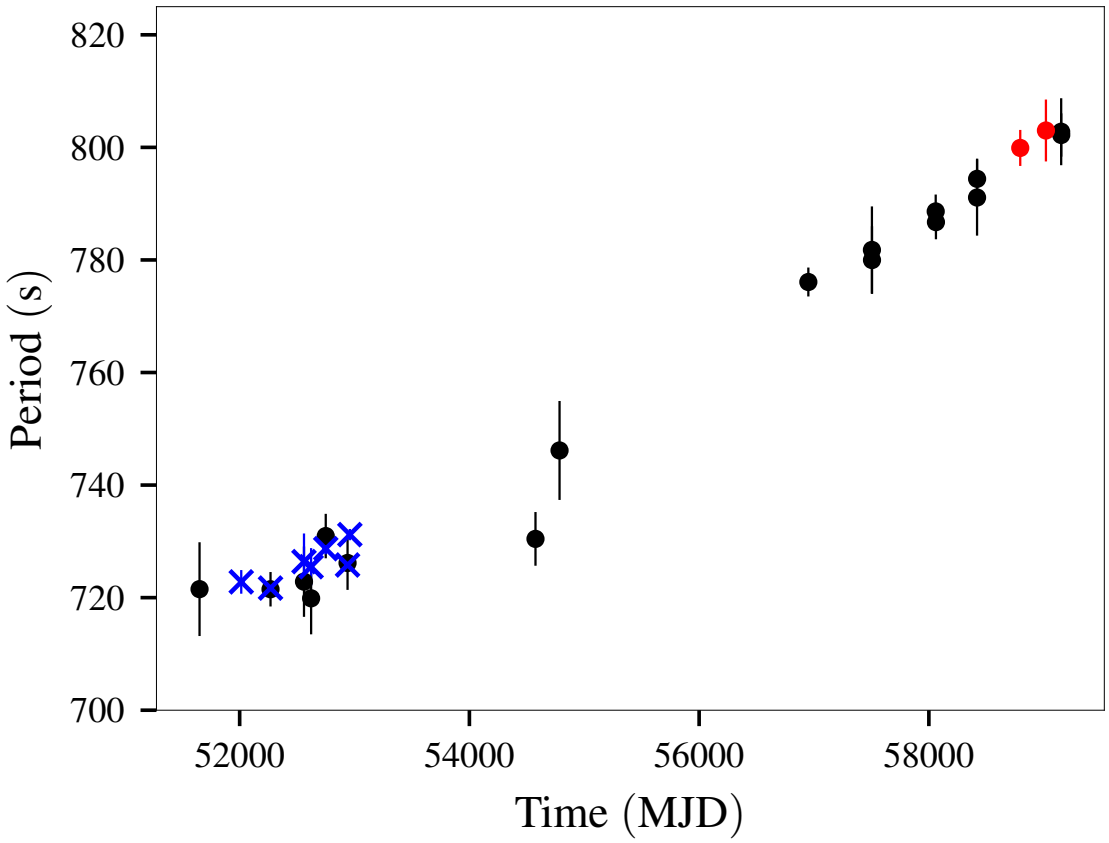


Figure 5.5: Spin period evolution of SXP726 measured in this work using the XMM-Newton (black) and eROSITA (red) data. The values reported by [106] for some of the XMM-Newton observations are also plotted for reference (blue crosses). (from Haberl et al, 2022[3])

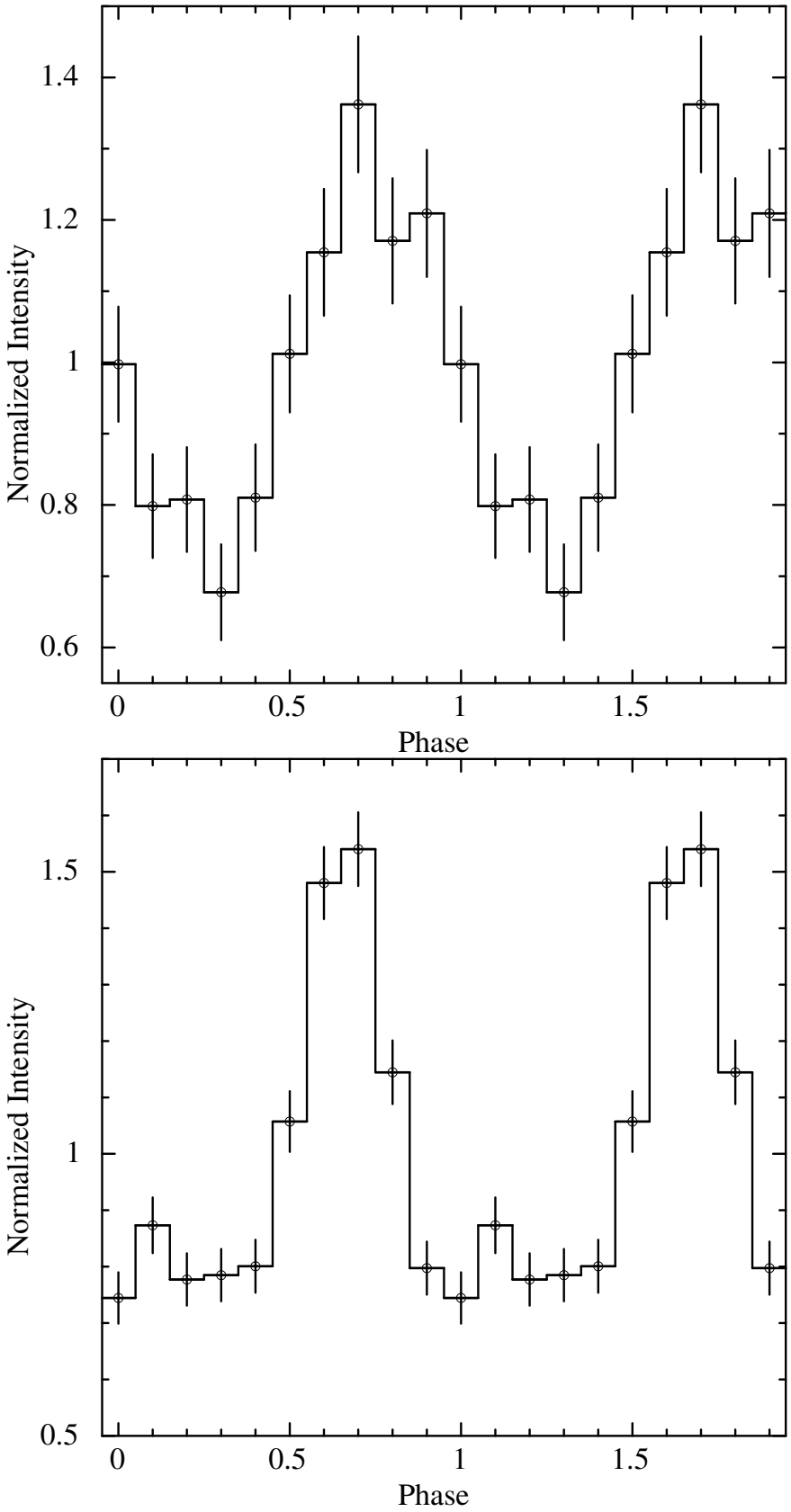


Figure 5.6: Background-subtracted pulse profile of SXP726 in the energy range of 0.2-8 keV averaged over all the observations in which pulsations were detected (top) and for ObsID 710000 (bottom) (from Haberl et al, 2022[3])

In conclusion, the spin-down behavior of SXP 726 has been consistently observed over several years, and the results from eROSITA align with measurements from XMM-Newton. A linear fit applied to all data points, including both XMM-Newton and eROSITA observations, confirms the overall spin-down trend, with a more precise determination of the spin-down rate (see Figure 5.5). The calculated rate is approximately 0.01178(6) s day^{-1}, corresponding to a spin-down rate of about 4.3 s yr^{-1}, which is slightly higher than previous estimates. This increase indicates a significant change in the pulsar's spin evolution, providing new insights into the long-term behavior of the system.

5.1.3 Flux evolution combined with eROSITA

For XMM observations, spectral modeling was performed using an absorbed power-law model with two absorption components: one accounting for the Galactic foreground (with a fixed hydrogen column density of 6×10^{20} cm^{-2}) and another for the SMC absorption, where the column density was allowed to vary and with metal abundances reduced to 0.2 as typical for the SMC. When necessary, we fixed certain parameters, such as the hydrogen column density ($N_H = 4.6 \times 10^{21}$ cm^{-2}) and photon index ($\Gamma = 0.71$), to account for high background or low source counts. The fluxes were then translated into intrinsic luminosities using a known SMC distance of 60 kpc. We modeled the eROSITA data using an absorbed power-law model, incorporating both Galactic foreground absorption and the appropriate parameters for the Small Magellanic Cloud (SMC). No additional absorption was required beyond the Galactic foreground, and the hydrogen column density was fixed at 6×10^{20} cm^{-2}. The power-law index was determined to be 0.63 ± 0.13, and the observed flux in the 0.2–10 keV band was $1.14 \pm 0.21 \times 10^{-13}$ erg cm^{-2} s^{-1}, corresponding to a luminosity of 5.2×10^{34} erg s^{-1}. These results demonstrate the reliability of the spectral model and provide valuable measurements of the source's energy output during the observation period. In the subsequent observation from June 2020, the source showed a flux of $7.5^{+0.61}_{-0.56} \times 10^{-13}$ erg cm^{-2} s^{-1}, indicating a substantial increase in luminosity to 3.3×10^{35} erg s^{-1}. The power-law index was consistent with the previous observations at 0.70 ± 0.06. This consistency reinforces the robustness of the spectral analysis, with minimal deviation in key parameters between observations.

We calculated the unabsorbed flux for SXP 726 using the cflux tool within the XSPEC software package. The flux measurements were derived for a distance of 60 kpc, which corresponds to the known distance of the SMC using the function as followed:

$$L = 4\pi d^2 \times \text{Flux} \tag{5.1}$$

The energy range used for the flux calculations was 0.2-10.0 keV. By applying this method, we were able to determine the X-ray luminosity over time, which is plotted in Figure 5.7. The blue data points in the figure represent flux values reported by Eger & Haberl (2008)[106], while the black points correspond to new flux measurements derived from XMM-Newton observations. The red point indicates the flux from eROSITA observations. The green arrows highlight upper limits for instances where the source was not detected. The variability in X-ray luminosity reveals significant changes over time, particularly between the earlier XMM-Newton observations and the more recent data. This analysis allows for a better understanding of the pulsar's behavior, especially in terms of spin evolution and changes in its accretion processes over extended periods.

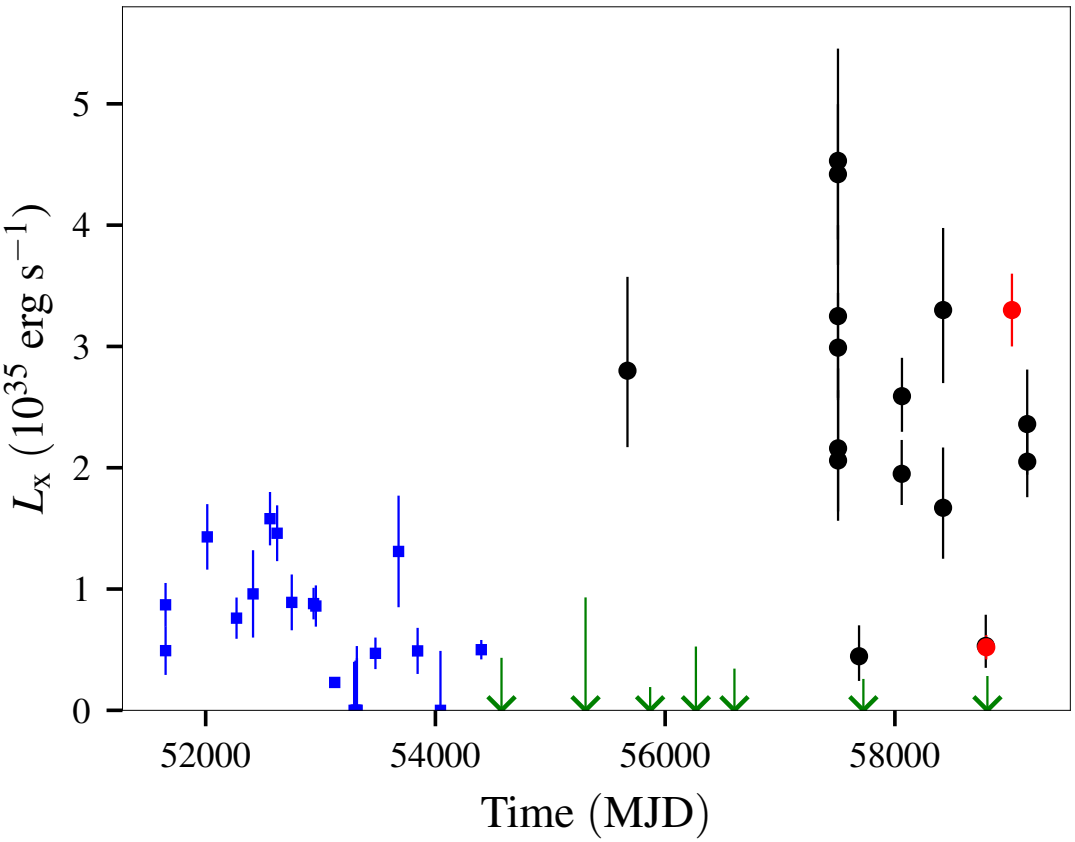


Figure 5.7: Variability of SXP726 as observed by XMM-Newton and eROSITA (red). The blue points correspond to flux values reported by Eger & Haberl (2008)[106], whereas black points are reported here for the first time. The upper limits for observations when the source was not detected are also indicated (green arrows). (from Haberl et al, 2022[3])

During the November 2019 eROSITA observations (ObsID: 700001–700005), SXP 726 was detected at a flux level consistent with previous observations. However, in a subsequent observation taken approximately six months later, the source exhibited a significant increase in brightness, with the flux rising by a factor of approximately 7. The spectral analysis of these observations was conducted using the same methods as in earlier studies, ensuring consistency in the processing and comparison of results. These flux findings underscore the variability of SXP 726 and provide further evidence for the dynamic processes occurring in this Be/X-ray binary system.

These findings contribute to a more comprehensive understanding of the long-term evolution of SXP 726. The observed spin-down trend and the variability in the X-ray flux suggest complex interactions between the pulsar and its environment, likely driven by changes in the accretion process. The combined analysis of eROSITA and XMM-Newton data provides a clearer picture of the dynamic processes at play and highlights the importance of continued monitoring to fully unravel the pulsar's behavior.

5.2 Anomalies in Swift J0243.6+6124

The study of glitches and anti-glitches in pulsars provides insights into the complex internal structure and dynamic processes occurring within these extreme dense objects.

While a glitch typically refers to a sudden increase in the rotational frequency of a pulsar, an anti-glitch (spin-down glitch) is characterized by a rapid and unexpected decrease in the frequency. This phenomenon is rare and has only been observed in a handful of magnetars and accreting pulsars, making it a subject of significant interest in astrophysics [107, 108].

Swift J0243.6+6124 is an intriguing accreting pulsar for studying anti-glitches, as it is the first Galactic ULX Be/X-ray pulsar with an extremely high magnetic field ($\geq 10^{13}$ G), possibly including an additional non-dipole field component [109], which makes it a bridge between magnetars and accreting pulsars. This source has been observed to undergo dramatic changes in its X-ray flux, spin behavior and spectral evolution, making it a prime candidate for investigating both typical glitches and potential anti-glitches. Understanding these events in Swift J0243.6+6124 could provide new insights into the interaction between the accretion disk, the magnetic field, and the neutron star's crust.

In this section, we detail our search for anti-glitch events in the X-ray emissions of Swift J0243.6+6124. The primary objective of this study is to search for evidence of anti-glitches in the archival data of Swift J0243.6+6124. Given the source's complex behavior and high variability, detecting an anti-glitch would be significant for several reasons:

- **Probing Internal Neutron Star Dynamics:** An anti-glitch would suggest complex internal processes, such as superfluid vortex unpinning or crustal movements.

- **Magnetospheric Interactions:** It could indicate a sudden change in the magnetospheric environment, potentially related to magnetic field restructuring or accretion dynamics.

- **Accretion Disk Influence:** The presence of an anti-glitch in an accreting neutron star like Swift J0243.6+6124 could reveal new information about the interaction between the neutron star's magnetic field and the surrounding accretion disk.

5.2.1 Search for Anti-glitch

An anti-glitch is the opposite of a typical glitch event, where the pulsar's rotation slows down rather than speeding up. Such events are unusual because they suggest the release of a substantial amount of angular momentum or a reconfiguration of the star's internal structure. The mechanisms that can lead to an anti-glitch are not yet fully understood, but several theories have been proposed. For example, it is speculated that an anti-glitch could be caused by a sudden shift in the superfluid core of the neutron star or a rapid reconfiguration of the magnetic field.

To date, anti-glitches have been reported in only a few instances [110]. The most notable case is the 2013 observation of an anti-glitch in the magnetar 1E 2259+586, which exhibited a sudden spin-down event along with a burst of X-ray emission but radio quiet [111]. This discovery challenged the existing models of pulsar dynamics

and suggested that alternative mechanisms, such as magnetospheric interactions or crustal deformations, could play a role. The rarity of anti-glitches makes them a unique opportunity to probe the physical conditions inside neutron stars, which are otherwise inaccessible.

To systematically search for the pulsar's profile using NICER data, the following methodology was employed:

1. Data Processing using `nicerl2`: The NICER data was processed using the `nicerl2` command with appropriate directory paths. This command handles data calibration and initial filtering, ensuring that the observations are properly prepared for analysis. The command used is shown below:

   ```
   nicerl2 indir=../1050390101 cldir=1050390101 clobber=YES
   ```

2. Extraction of Light Curve and Spectrum using `xselect`: The tool `xselect` was employed to extract the light curve and spectrum of the source. A bin size of 0.001 was chosen, and different energy ranges (1–10 keV, 1–5 keV, and 5–10 keV) were explored. This allowed us to analyze the source behavior in various energy bands.

3. Barycentric and Binary Corrections: Barycentric corrections (`barycorr`) were applied to account for the motion of the NICER observatory relative to the Solar System's barycenter, ensuring that the timing information is accurate. Binary corrections were also applied using the parameters listed in Figure 5.8, such as orbital period, eccentricity, and semi-major axis of the orbit. The parameters used for Swift 0243.9+6124 are from GBM epoch-folding monitor, which is part of the Fermi Gamma-ray Burst Monitor (GBM) and used for tracking and analyzing pulsar data.

4. Z^2 Search and χ^2 Search: A Z^2 and a χ^2 search were conducted to determine the pulsation period accurately. This statistical method helps identify periodic signals within the data. The pulse profile was then folded over the determined period, resulting in the final pulse profile plots.

The Z^2 results and χ^2 results are shown in the Figure 5.9. The Chi-squared Search (χ^2) for Pulsation Period Detection is a statistical method used to detect periodic signals in time-series data, such as pulsations from pulsars or variable stars. This method involves folding the data over trial periods and calculating a chi-squared value to test how well the data fits a periodic model compared to a constant, non-periodic model. By minimizing the chi-squared statistic across a range of trial periods, it identifies the period with the best fit to the observed data, which is often corroborated with additional statistical tests like the Z^2. The χ^2 process referred to "`https://fermi.gsfc.nasa.gov/ssc/data/analysis/scitools/period_search_tutorial.html`". In the Figure 5.9, the X-axis represents the period in seconds, while the Y-axis shows the corresponding Z^2 value (left). A prominent peak is observed at a period of approximately 9.854 seconds, indicating the most likely pulsation period of the source. The χ^2 search is another statistical method (right) for detecting pulsations, where the X-axis represents the period in seconds and the Y-axis indicates the χ^2 value. The peak near

Swift J0243.6+6124

The parameters below are used for this source in the GBM epoch-folding monitor

Source Monitor Parameters	
RA	40.9180 deg
Decl	61.4341 deg
Orbital Parameters	
Orbital Period	27.698899 days
Period Deriv.	0.0000E+00 days/day
$T_{\pi/2}$	2458116.09700 (JED)
axsin(i)	115.531 light-sec
Long. of periastron	-74.05 deg
Eccentricity	0.1029

Figure 5.8: The binary parameters of Swift J0243.6+6124 (from GBM epoch-folding monitor)

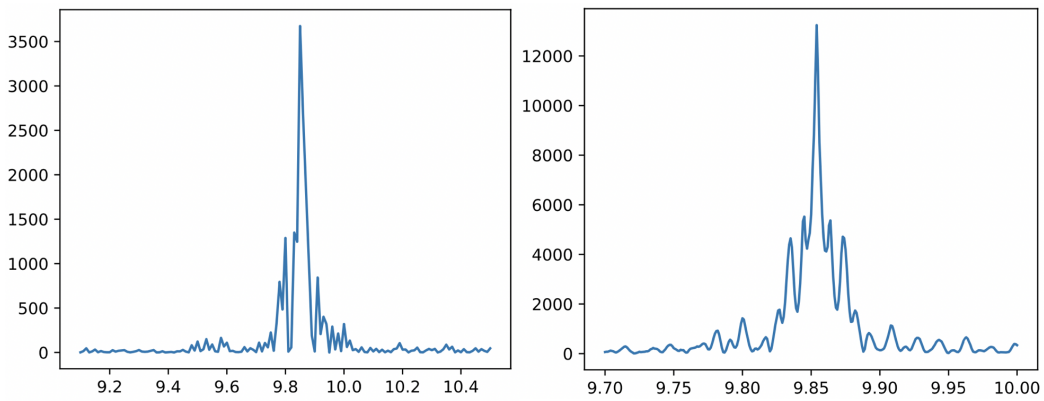


Figure 5.9: Z-squared and Chi-squared Search for Pulsation Period Detection: the results of the Z^2 search (left) and χ^2 search (right) conducted to identify the pulsation period of the source Swift J0243.6+6124. The analysis was performed using NICER observational data with the specific observation ID `ni1050390101`. The horizontal axis is the period and the vertical axis is the intensity.

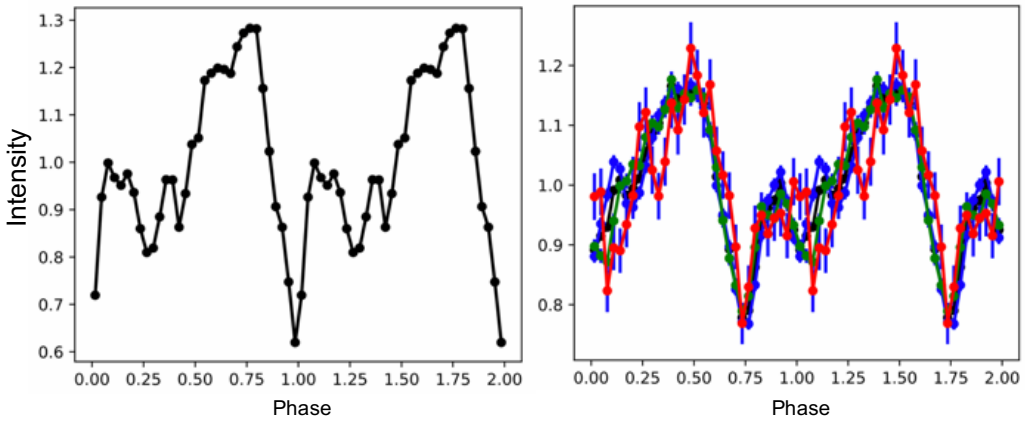


Figure 5.10: Left: Pulse profile in the 1-10 keV energy band. Right: Black, blue, green, and red lines represent pulse profiles in the 1-10 keV, 1-3 keV, 3-7 keV, and 7-10 keV energy bands, respectively.

9.854 seconds confirms the pulsation period detected by the Z^2 search. Both plots demonstrate a strong peak at a period of around 9.854 seconds, which corresponds to a frequency of approximately 0.101482 Hz. This consistency between the two methods validates the detection of the pulsation period for Swift J0243.6+6124. In subsequent studies, we adopted the Z^2 method and got the period evolution with time.

We present the pulse profiles of the X-ray pulsar Swift J0243.6+6124 in the Figure 5.10, observed using the NICER instrument. The left panel shows the Z^2 search results, which indicate the periodic variation in the pulsar's intensity. The plot on the right compares the pulse profiles across four different energy ranges: 1-10 keV (black), 1-3 keV (blue), 3-7 keV (green) and 7-10 keV (red). Each profile is normalized to unity to facilitate comparison, highlighting how the pulse shape and amplitude vary across different energy bands. The changes in pulse profile shape with energy suggest different emission regions or processes dominating at different energies. The parameters of the pulse profile shown in the Fig 5.10 are from the Observation ID (`ni1050390101`), exposure time (3074.0 seconds), pulse fraction (34.856892), period (9.854000 seconds) and frequency (0.101482 Hz).

The spin frequency evolution of Swift J0243.6+612 is shown in Figure 5.11 from swift/GBM. As seen in the top panel, the spin frequency, measured in millihertz (mHz), increases rapidly during the outburst, reaching a plateau after the outburst. This sharp increase in spin frequency corresponds to the enhanced accretion rate during the outburst, which exerts additional torque on the pulsar, causing it to spin up. The bottom panel of Figure 5.11 presents the 12-50 keV pulsed flux, which also demonstrates a rapid rise followed by a decay, further correlating the pulsar's spin evolution with the overall intensity of the outburst.

The primary focus is on understanding the evolution of the spin frequency, particularly the sharp increase observed during the outburst phase. This investigation is crucial for studying the accretion-induced spin-up processes in Swift J0243.6+612 and other similar X-ray binaries. The correlation between the spin frequency and pulsed flux provides valuable information for constraining the physical mechanisms driving these processes. We focus on the rapid spin-up of Swift J0243.6+6124 and the corresponding fast changes in its pulse profile. Using NICER data, we obtained pulse profiles at

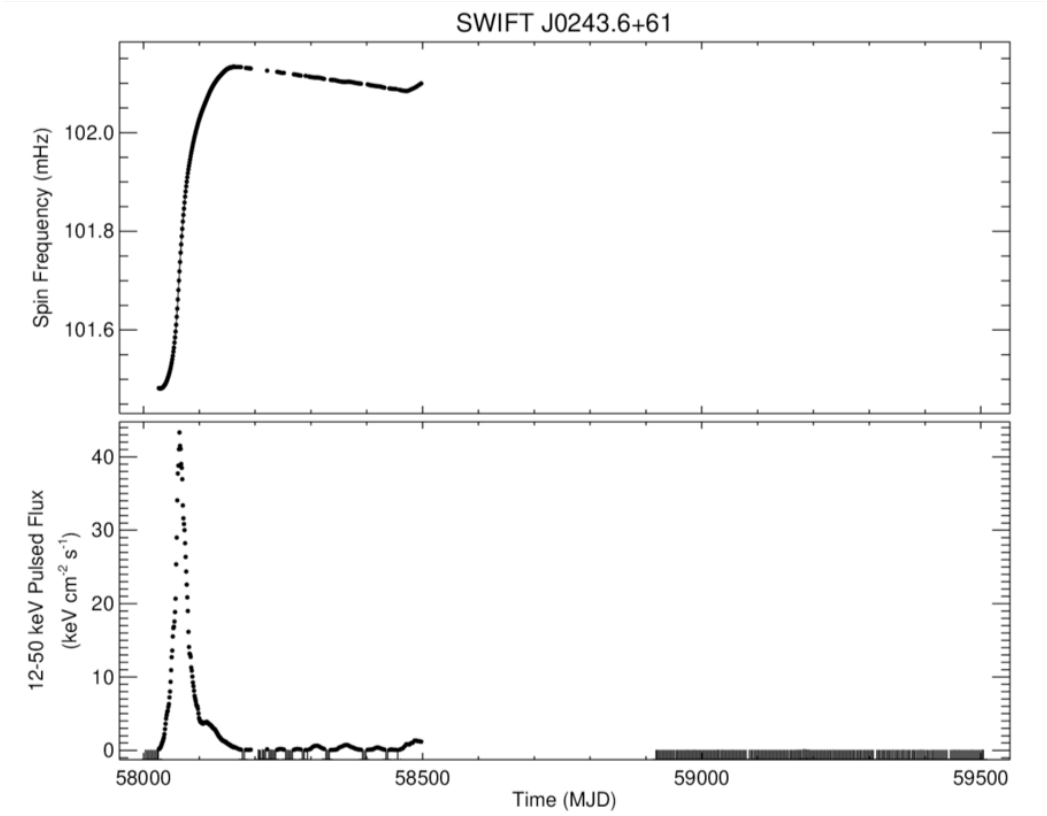


Figure 5.11: Spin frequency (top) and 12–50 keV pulsed flux (bottom) of Swift J0243.6+6124 observed with Swift/GBM. The top panel shows the evolution of the spin frequency in millihertz (mHz), revealing a rapid increase during the outburst around MJD 58000, followed by a plateau phase. The bottom panel displays the pulsed flux in the 12–50 keV energy band, which exhibits a sharp rise and subsequent decay, indicating the intensity of the outburst and the pulsar's corresponding response. Credit: NASA/Swift/GBM.

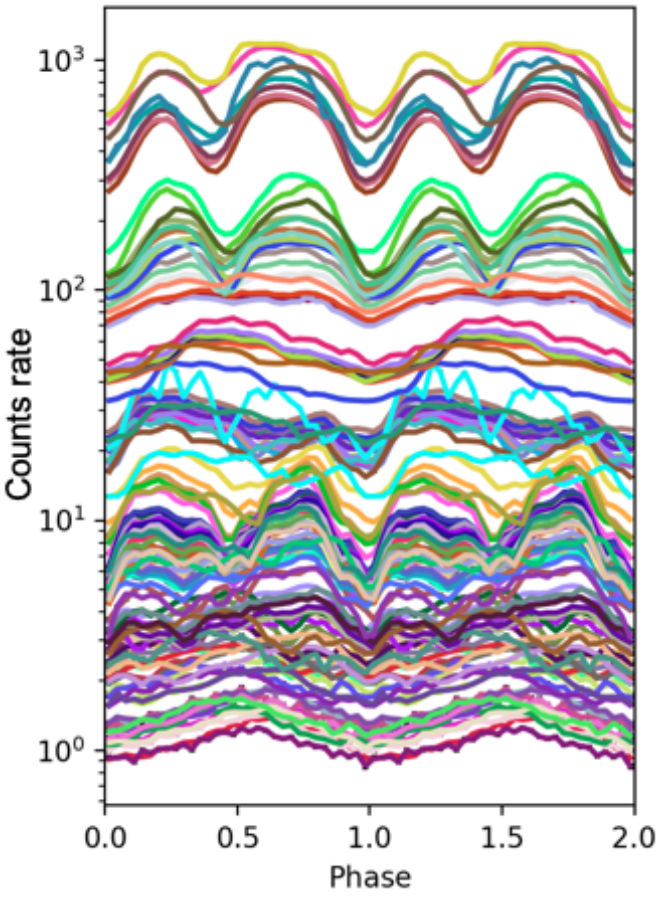


Figure 5.12: Pulse profiles of Swift J0243.6+612 in different time as observed with NICER, plotted as a function of phase. The profiles show significant structural evolution, with each line (shown in different colors) representing pulse profiles at different count rates across the outburst with a logarithmic scale for the y-axis. The diverse patterns observed in the profiles illustrate the rapid changes in the emission structure, correlating with the source's high accretion rates during the outburst phase.

different count rates, allowing us to track the evolution of the pulse shape throughout the outburst. The pulse profiles, as shown in Figure 5.12, are plotted as a function of phase, with the y-axis representing the count rate in logarithmic scale. Each line corresponds to a specific count rate, capturing the changes in pulse shape and intensity over time. The variation in the pulse profile structure is evident, particularly at different count rates, where the profiles display greater complexity. This complexity reflects the impact of the increased accretion rate on the pulsar's emission pattern during its outburst.

The NICER data has indeed revealed the complex structure of the pulse profiles, along with the evolution of the spin frequency. Despite the rapid spin-up and notable changes in the pulse profile, no evidence of glitches or anti-glitches has been observed during this phase of the outburst. The time scale of this analysis is nearly larger than one day and makes difficulties to find tiny structure. This absence of such events in the NICER data leads us to consider alternative datasets to further investigate the possibility of detecting anti-glitches. One such dataset is from Insight-HXMT (HXMT), which observed Swift J0243.6+6124 during the same outburst with long exposures and extensive photometric coverage. The prolonged and detailed observations provided by

HXMT are advantageous for searching for anti-glitches, as the increased exposure time enhances the likelihood of detecting subtle changes in the spin frequency. Moreover, HXMT's wider energy coverage, spanning a broader energy range than NICER, allows for a more comprehensive analysis of the source's behavior across different energy bands. This broader spectral coverage is one of the main reasons we turn to HXMT data to further our investigation into potential anti-glitch events and to better understand the accretion-induced spin-up process in Swift J0243.6+6124.

Using different energy band data from HXMT's LE, ME, and HE detectors, we constructed pulse profile maps across various energy bands. These pulse profiles were folded and processed to obtain the time of arrival (TOA) and analyzed with the tools **Pint** and **Tempo2**. Considering the variability of the source phase, after obtaining the pulse profile, we manually aligned the phase by using the cross-correlation method. Figure 5.13 illustrates the pulse profile maps for different energy bands. While we initially included data from all three detectors, some considerations led us to focus primarily on the ME energy band. Due to the characteristics of the HXMT satellite, the HE energy band suffers from high background noise, which complicates the search for subtle changes such as anti-glitches. Similarly, the LE data may be less stable for the required level of precision due to numerous time gaps. As a result, the ME energy band was determined to provide more continuous and reliable data for our investigation.

In our search for anti-glitches, we analyzed the TOAs of pulses by dividing the light curve of each exposure into several segments, each approximately 50 pulses long. The TOA method allows us to track the precise timing of each pulse and detect any sudden shifts in spin frequency, which would indicate the presence of a glitch or anti-glitch event. However, despite the detailed analysis, no clear anti-glitch was detected in the HXMT data. The long exposure time and wide energy coverage provided by HXMT offer significant advantages for identifying such events, yet the absence of an anti-glitch may suggest that either no such event occurred during this outburst. Further research may involve refining the search techniques or combining data from other missions to enhance the sensitivity of anti-glitch detection. Nevertheless, the detailed pulse profile evolution across different energy bands, as shown in the pulse profile map, provides critical insights into the pulsar's behavior throughout the outburst.

5.2.2 Finding and Analysis of Slight glitches

In our search for anti-glitches in Swift J0243.6+612, while no definitive anti-glitch events were identified, we observed some intriguing results. We identified and analyzed several possible slight glitch events in Swift J0243.6+612. Figure 5.14 displays the post-fit timing residuals obtained through a TOA (Time of Arrival) fitting method. For most observations, including this one in Figure 5.14 is from October 7, 2017 and those observations in this outburst, the residuals fall within a reasonable distribution, indicating stable timing behavior across these periods. However, there are a few instances where linear deviations appear in the residuals, suggesting potential slight glitches or other timing anomalies [112, 113]. As shown in Figure 5.15, we noted significant linear residual trends on three specific dates: November 3, 2017; November 20, 2017; and November 22, 2017. These deviations indicate a departure from the otherwise stable timing, which may suggest minor glitches or variations in the pulsar's

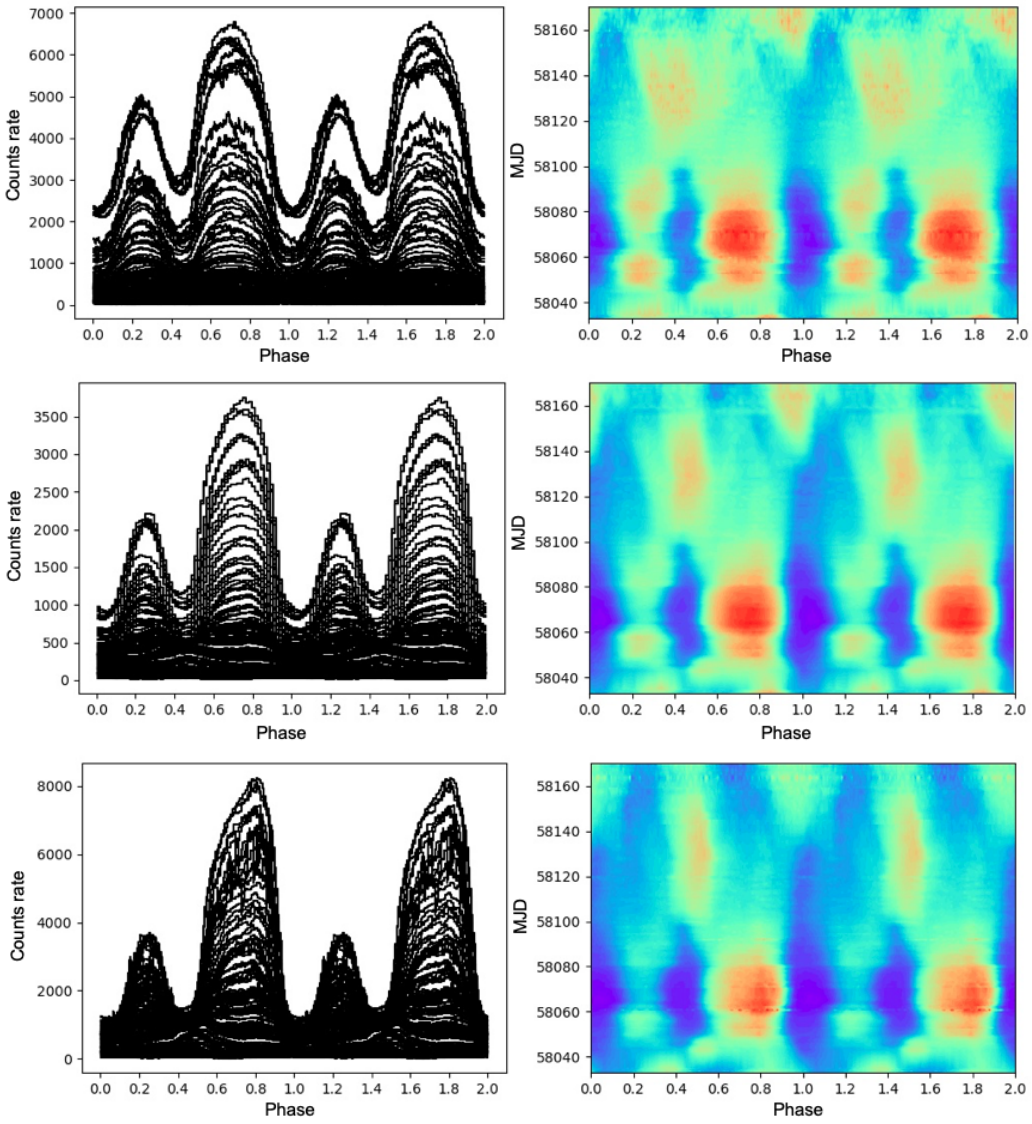


Figure 5.13: Pulse profile maps of Swift J0243.6+612 in different energy bands as observed with HXMT. The left column shows pulse profiles with the counts rate, and the right column displays the corresponding phase-resolved intensity maps over time (MJD). From top to bottom, the rows represent data from the LE (Low Energy: 2-10 keV) band, ME (Medium Energy: 10-30 keV) band, and HE (High Energy: 25-80 keV) band. Each profile reveals distinct variations in pulse shape across phases and energy bands, highlighting the source's dynamic behavior during the outburst. Notably, the ME data exhibits the most stable pulse profiles with lower background interference, making it ideal for detecting potential anti-glitch events.

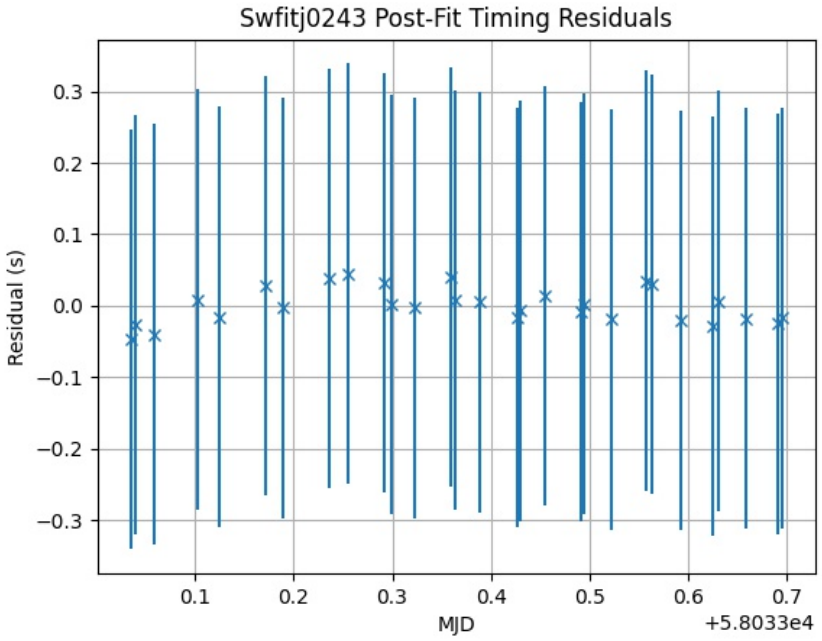


Figure 5.14: Post-fit timing residuals of Swift J0243.6+612 observed on October 7, 2017, in the ME energy band. The residuals are plotted against MJD, showing a stable distribution around zero with minimal deviations, indicating a consistent timing solution on this date. The limited scatter of residuals suggests no significant timing anomalies or glitches, supporting the stability of the source during this observation period.

rotational behavior. The linear trend in the post-fit timing residuals observed on November 3, 2017, for both the ME and LE energy bands of Swift J0243.6+612, as shown in Figure 5.15 suggests a timing anomaly that may be indicative of a slight glitch or rotational irregularity in the pulsar. This phenomenon is unusual, as a stable pulsar typically displays residuals randomly distributed around zero. The presence of such a clear linear trend hints at a gradual drift or phase shift in the pulsar's timing, possibly due to changes in its rotational behavior. Several factors could contribute to this effect: 1) Accretion Torque Fluctuations: During periods of high accretion, the pulsar's spin frequency may experience additional torque, causing slight shifts in the timing residuals. Swift J0243.6+612, being an accreting X-ray pulsar, is susceptible to accretion-driven changes that can manifest as timing irregularities. The observed linear trend in residuals could reflect this torque-induced drift in spin frequency. 2) Magnetic Field Interactions: The pulsar's magnetic field interacts with the accretion disk, potentially causing disruptions or instabilities in its rotation. These interactions can lead to timing anomalies, such as small glitches or phase shifts, as the magnetic field adapts to changes in the accretion rate or structure. 3) Instrumental or Data Processing Effects: While the HXMT ME and LE detectors are calibrated for timing observations, slight differences in sensitivity or processing artifacts could amplify certain residual trends. However, the fact that both the ME and LE bands exhibit a similar linear trend suggests that this is more likely an intrinsic feature of the source rather than an artifact.

The presence of this phenomenon in both the ME and LE bands strengthens the case for an intrinsic timing anomaly. If it were limited to a single energy band, it might be

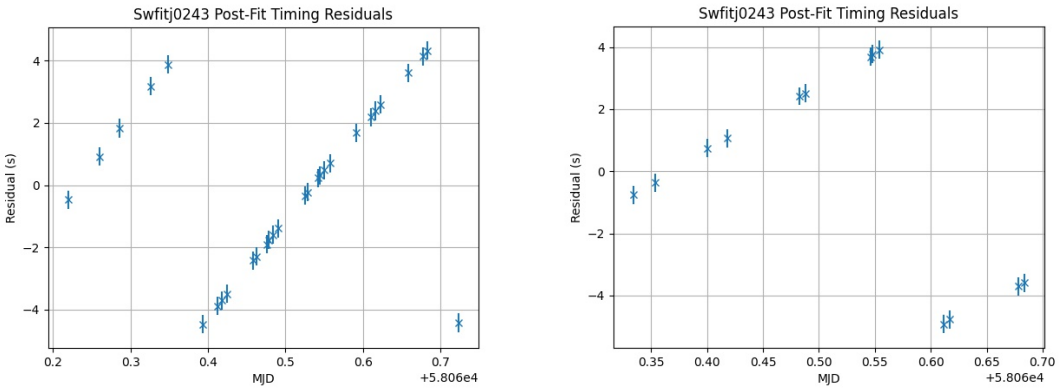


Figure 5.15: Post-fit timing residuals observed on November 3, 2017, in the ME (left) and LE (right) energy bands. The residuals are plotted as a function of MJD, showing a noticeable linear trend, particularly in the ME band. This pattern indicates a deviation from the expected timing solution, potentially suggesting a slight glitch or timing irregularity on this date. The linear residuals observed in both energy bands highlight an interesting anomaly that warrants further investigation.

dismissed as an instrumental or statistical fluctuation. The consistency across multiple bands points to a genuine irregularity in the pulsar's timing behavior on this specific date, potentially offering new insights into the mechanisms governing accretion-induced spin changes in Swift J0243.6+612. Further investigation, potentially with additional observations or a comparative analysis with other accreting pulsars, could provide a more comprehensive understanding of the cause of these timing anomalies. In Figure 5.16, we highlight these three instances with red circles, marking the points where the linear deviations were observed. These specific dates coincide with moments of notable change in the spin frequency curve, as plotted over time. The existence of such slight glitches, while not as prominent as typical glitch events, is nonetheless fascinating, as it suggests subtle variations in the pulsar's spin behavior that may relate to underlying accretion processes or magnetic field interactions.

In comparing our findings with the Swift/GBM results, we observe several similarities and distinctions regarding the spin frequency evolution of Swift J0243.6+612 during its outburst. The Swift/GBM data, as shown in Figure 5.11, reveals a rapid increase in spin frequency, reaching a plateau after the initial rise. This behavior is consistent with our findings, where the pulsar experiences significant spin-up due to high accretion torque, a common characteristic in accreting X-ray pulsars. Both our analysis and the GBM data demonstrate the influence of accretion-induced torque on the pulsar's spin frequency during the peak of the outburst. However, our analysis using post-fit timing residuals and TOA fits identified subtle, yet significant, anomalies on specific dates—November 3, 2017; November 20, 2017; and November 22, 2017—that are not explicitly highlighted in the GBM data. These slight timing irregularities, manifested as linear deviations in the residuals, suggest potential minor glitches or phase shifts, which could be attributed to fluctuations in the accretion rate or magnetic field interactions. The GBM data, while providing an overview of the overall spin frequency trend, may lack the precision to detect these finer anomalies, which our high-resolution timing analysis has revealed. This may come from an interesting physical phenomenon, but at present it may still be due to data deviation, which need to be double checked with more databases. Nevertheless, these findings still contribute valuable insight into

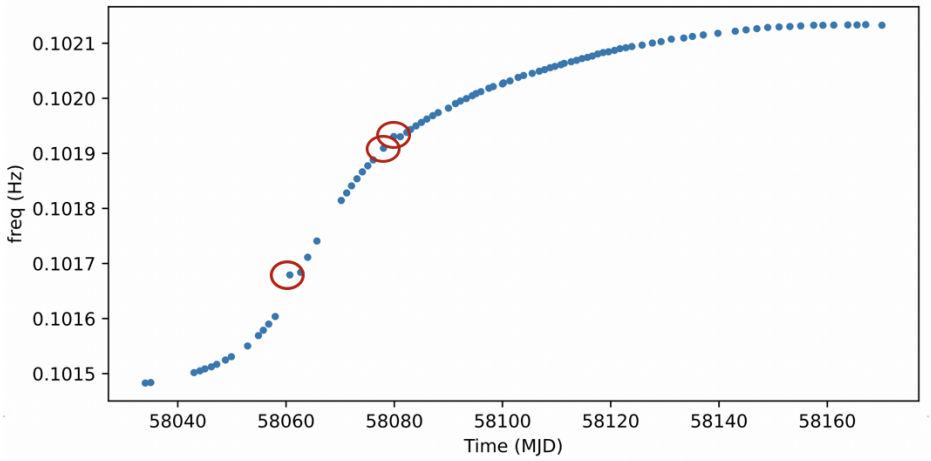


Figure 5.16: Spin frequency evolution of Swift J0243.6+612 over time, plotted as a function of MJD. The red circles highlight specific dates: November 3, 2017, November 20, 2017, and November 22, 2017, where slight timing anomalies were observed in the post-fit residuals. The rapid increase in spin frequency during the outburst is evident, with these highlighted points potentially indicating subtle irregularities or adjustments in the pulsar's rotation, possibly due to accretion torque fluctuations or magnetic field interactions.

the timing characteristics of Swift J0243.6+612, revealing minor, possibly notable, deviations that might reflect complex internal or environmental factors affecting the pulsar's rotation.

In summary, our findings align with the Swift/GBM data in terms of the general trend of spin-up associated with the outburst in Swift J0243.6+612. However, our analysis provides additional insights into slight timing anomalies that may be indicative of complex internal processes in the pulsar's rotation. These subtle deviations could reflect interactions between the pulsar's magnetic field and accretion flow, highlighting the advantage of high-resolution timing observations in capturing detailed timing behaviors. These findings emphasize the need for further observational and theoretical studies to fully understand the mechanisms driving the observed timing anomalies in Swift J0243.6+612. Additional high-resolution timing data from future outbursts, combined with data from other X-ray missions, could provide critical insights into the interplay between accretion dynamics and spin evolution in accreting pulsars. A deeper theoretical framework will also be essential to explain the minor glitches and potential magnetic interactions observed in this and similar sources.

6 Discussion and Conclusion

6.1 Summary of Work

This dissertation has presented a comprehensive investigation of X-ray binaries, focusing on both black hole and neutron star systems. By utilizing multi-satellite observations from eROSITA, NICER, NuSTAR, XMM-Newton, and Insight-HXMT, the study has explored key physical processes governing accretion, variability, and emission mechanisms in these systems. The work summarized here is based on three published articles (see the appendix). Further details of which are provided in the thesis. Additionally, this research includes descriptions of as yet unpublished studies on quiescent black holes using eROSITA and the search for glitches or anti-glitches in Swift J0243.6+612 and other timing irregularities. The major findings of this work include:

- Identification of critical luminosity thresholds in black hole MAXI J1348-630, marking the transition between different accretion regimes.
- Detailed analysis of quasi-periodic oscillations (QPOs) and their correlation with accretion disk and corona evolution.
- Detection and characterization of disk winds, establishing their link with magnetic fields.
- Investigation of spectral state transitions and their implications for accretion-ejection coupling.
- Study of quiescent black holes using eROSITA surveys, revealing previously undetected sources and refining constraints on the X-ray emission properties of non-active black holes.
- Spin evolution and pulse timing analysis of neutron stars, revealing insights into slight anomalous timing residuals.

The results presented in this thesis contribute to the broader understanding of compact objects and their accretion physics, offering new perspectives on the interaction between accretion flows, magnetic fields, and relativistic outflows.

6.2 Comprehensive Discussion of Research Results

The research results discussed in Chapters 4 and 5 highlight the complex interplay between accretion processes and variability in X-ray binaries. Key findings include:

6.2.1 Black Hole X-ray Binaries

- **MAXI J1348-630:** The study of the 2019 reflare revealed the presence of a critical luminosity ($L_{\rm crit} \sim 2.5 \times 10^{36}$ erg s^{-1}), beyond which the inner accretion disk began to move inward. This transition marks a shift from an evaporation-dominated to a condensation-dominated state, influencing disk-corona interactions.
- **GRS 1915+105:** The analysis of QPOs during the 2021 rebrightening event demonstrated a correlation between QPO phase evolution and Fe XXV/Fe XXVI absorption lines, indicating a strong connection between disk winds and accretion-ejection instability (AEI).
- **Quiescent Black Holes:** The search for quiescent black holes using eROSITA data led to the identification of new candidates, revealing low-luminosity states of black hole X-ray binaries. These findings refine the theoretical models of quiescent accretion and the faint-end population of black holes.

6.2.2 Neutron Star X-ray Binaries

- **Swift J0243.6+612:** Timing analysis revealed the presence of slight glitches and the lack of anti-glitches, possibly linked to magnetospheric changes during accretion events.
- **SXP 726:** The spin evolution of the neutron star SXP 726 was analyzed using XMM-Newton and eROSITA, revealing long-term variations in spin period and torque behavior. These results provide insights into accretion torque theory and the interaction between the magnetosphere and the surrounding accretion disk.

The discussion of these findings in the context of theoretical models supports the role of magnetic fields in shaping variability in both black hole and neutron star systems.

6.3 Future Work

Future research directions will build upon the findings presented in this dissertation and address open questions related to accretion physics and variability in compact objects:

- **Advanced Timing Analysis:** Future studies will employ higher-resolution timing data to further investigate QPO phase dependence and its connection to inner disk structure.
- **Exploring AEI in Other Systems:** The link between accretion-ejection instability and disk winds should be tested in additional X-ray binaries to assess its universality.
- **Further Investigation of Quiescent Black Holes:** Follow-up studies on candidate quiescent black holes identified by eROSITA will clarify the nature of their emission and refine the models of low-luminosity accretion.

- **Detailed Study of Neutron Star Spin Evolution:** Long-term pulse timing observations of SXP 726 and similar systems will help constrain neutron star magnetic field evolution and accretion torque models. Searching for timing irregularities for other sources is also available and then do a focused study on the theoretical aspects that could explain them.

By addressing these challenges, future studies will enhance our understanding of the physical mechanisms driving variability in X-ray binaries and contribute to a more unified picture of compact object accretion.

6.4 Conclusion

This thesis has provided significant insights into the spectral and timing properties of X-ray binaries through multi-mission observations and advanced analytical techniques.

The following are the papers I published during my doctoral studies:

1, **Dai Xiaohang**, et al., 2024, Astronomy & Astrophysics, title: *Unveiling the rebrightening mechanism of GRS 1915+105: Insights from a change in the quasi-periodic oscillations and from a wind analysis*

2, **Dai Xiaohang**; Kong L, Bu Q, et al., 2023, Monthly Notices of the Royal Astronomical Society, title: *Evolution of disc and corona in MAXI J1348-630 during the 2019 reflare: NICER and Insight-HXMT view*

3, Haberl F, Maitra C, Carpano S, **Dai Xiaohang**, et al., 2022, Astronomy & Astrophysics, title: *eROSITA calibration and performance verification phase: High-mass X-ray binaries in the Magellanic Clouds*

Acknowledgements

The pursuit of physics is like chasing the fleeting glimmers of the universe, a quest for the essence of reality—a journey of purity, curiosity, and boundless joy. Despite the winding roads, the uncertainties, and the countless nights of contemplation, the process of seeking, questioning, and uncovering has filled my heart with an incomparable sense of fulfillment.

Looking back, these years have been a treasure—an era when I could immerse myself in the beauty of knowledge, when the flames of youthful passion burned bright, when perseverance turned struggles into triumphs. Such moments of pure devotion to one's pursuit may become scarce in the years to come, but they will forever shine as the most cherished memories of my life. For this, I am profoundly grateful.

More than anything, I want to express my deepest gratitude to those who have accompanied me on this journey. To my supervisor, Prof. Andrea Santangelo, whose vibrant personality and unwavering enthusiasm for research have been a guiding force in my academic path. His dedication, his belief in his students, and his constant encouragement have been invaluable gifts, and I shall always hold immense appreciation for his support.

I would also like to express my sincere gratitude to Dr. Victor Doroshenko, whose patience and willingness to share his knowledge were invaluable in my early research days. His scientific intuition and expertise have been inspiring, and I am fortunate to have learned from him.

My sincerest gratitude belongs to Dr. Kong Lingda, who, through my most difficult times in research, has been like a lighthouse in the storm—steady, warm, and unwavering. His immense knowledge, gentle humility, kindness, and fearless perseverance remind me to never lose sight of my passion. In both research and life, he has given me the most support, and for that, I am forever indebted.

I am also deeply thankful to my colleagues Charles Thorpe-Morgan, Camille Diez and Nhan Nguyen. Their kindness and their cheerful laughter have made my days in academia so much more delightful. And to my Chinese colleagues Du Yujia, Zhou Menglei, Xiong Hao, Wang Pengju, Liu Qi, Wang Xianqi, and Dou Wanchao, who have shared with me the warmth of home, the joy of companionship, and countless delicious meals that made distant lands feel familiar again. I am equally grateful to my senior peers Bu Qingcui, Ji Long, and Bi Baiyang, whose guidance and advice have been invaluable in shaping my research path.

Outside of research, I have been blessed with the kindness of my landlady, Ms. Anne Röhm, and my neighbors, whose warmth and optimism, and especially Ms. Röhm's kindness and meticulous care, have eased my journey in this foreign land.

I am also fortunate to have met an incredible group of friends from across China, bound not only by our studies but by shared dreams and aspirations. Xia Shuning, Yang Xuefeng, Xu Ying, Jiang Qingjun, Zhang Ying, Li Gaopeng, and many others—their generosity, their perseverance, their unremitting pursuit of truth and excellence inspire me beyond words. The road of knowledge is never smooth, but I hope we will all forge ahead with courage, hold fast to our dreams, and walk this path to its fullest. May we always support and encourage one another.

Finally, my most profound gratitude belongs to my beloved homeland and my family. They have stood behind me with confirmed faith, providing the unshakable foundation upon which I have built my aspirations. I also extend my heartfelt thanks to the China Scholarship Council (CSC) for its generous support. Without the strength of my homeland and the love of my family, none of this would have been possible. Words are too pale to express the depth of my gratitude, and repaying their kindness may be beyond measure. The only way I can truly honor their love is to remain sincere, to approach life with an open heart, and to strive forward with unalterable determination. No matter where the road ahead leads, I will hold onto my passion, stand by my values, and march forward with courage—doing what is right, without fear of what the future holds.

References

[1] Xiaohang Dai, Lingda Kong, Qingcui Bu, Andrea Santangelo, Shu Zhang, Long Ji, Shuangnan Zhang, and Emre Seyit Yorgancioglu. Evolution of disc and corona in MAXI J1348-630 during the 2019 reflare: NICER and Insight-HXMT view. *Monthly Notices of the Royal Astronomical Society*, 521(2):2692–2703, 03 2023. ISSN 0035-8711. doi: 10.1093/mnras/stad714. URL `https://doi.org/10.1093/mnras/stad714`.

[2] Xiaohang Dai, Lingda Kong, Long Ji, Menglei Zhou, Qingcang Shui, Pengju Wang, Shu Zhang, and Andrea Santangelo. Unveiling the rebrightening mechanism of GRS 1915+105: Insights from a change in the quasi-periodic oscillations and from a wind analysis. *A&A*, 692:A117, December 2024. doi: 10.1051/0004-6361/202452132.

[3] F Haberl, C Maitra, S Carpano, X Dai, V Doroshenko, K Dennerl, MJ Freyberg, M Sasaki, A Udalski, KA Postnov, et al. erosita calibration and performance verification phase: High-mass x-ray binaries in the magellanic clouds. *Astronomy & Astrophysics*, 661:A25, 2022.

[4] Stuart L Shapiro and Saul A Teukolsky. *Black holes, white dwarfs, and neutron stars: The physics of compact objects*. John Wiley & Sons, 2008.

[5] R. A. Remillard and J. E. McClintock. X-ray properties of black-hole binaries. *Annual Review of Astronomy and Astrophysics*, 44:49–92, 2006.

[6] Stephen W Hawking. Black hole explosions? *Nature*, 248(5443):30–31, 1974.

[7] John Kormendy and Luis C Ho. Coevolution (or not) of supermassive black holes and host galaxies. *Annual Review of Astronomy and Astrophysics*, 51(1): 511–653, 2013.

[8] Paweł Haensel, Aleksander Yu Potekhin, and Dmitry G Yakovlev. *Neutron stars 1*. Springer, 2007.

[9] S. E. Motta, J. Rodriguez, E. Jourdain, M. Del Santo, G. Belanger, F. Cangemi, V. Grinberg, J. J. E. Kajava, E. Kuulkers, J. Malzac, K. Pottschmidt, J. P. Roques, C. Sánchez-Fernández, and J. Wilms. The INTEGRAL view on black hole X-ray binaries. *New A Rev.*, 93:101618, December 2021. doi: 10.1016/j.newar.2021.101618.

[10] Dipankar Bhattacharya and Edeard Peter Jacobus van den Heuvel. Formation and evolution of binary and millisecond radio pulsars. *Physics Reports*, 203(1-2): 1–124, 1991.

[11] Alexander Mushtukov and Sergey Tsygankov. Accreting strongly magnetised neutron stars: X-ray Pulsars. *arXiv e-prints*, art. arXiv:2204.14185, April 2022. doi: 10.48550/arXiv.2204.14185.

[12] Pablo Reig. Be/X-ray binaries. *Ap&SS*, 332(1):1–29, March 2011. doi: 10.1007/s10509-010-0575-8.

[13] Shuang-Nan Zhang, TiPei Li, FangJun Lu, LiMing Song, YuPeng Xu, CongZhan Liu, Yong Chen, XueLei Cao, QingCui Bu, Zhi Chang, et al. Overview to the hard x-ray modulation telescope (insight-hxmt) satellite. *Science China Physics, Mechanics & Astronomy*, 63:1–18, 2020.

[14] Z Arzoumanian, KC Gendreau, CL Baker, T Cazeau, P Hestnes, JW Kellogg, SJ Kenyon, RP Kozon, K-C Liu, SS Manthripragada, et al. The neutron star interior composition explorer (nicer): mission definition. In *Space Telescopes and Instrumentation 2014: Ultraviolet to Gamma Ray*, volume 9144, pages 579–587. SPIE, 2014.

[15] Fiona A. Harrison, William W. Craig, Finn E. Christensen, Charles J. Hailey, William W. Zhang, Steven E. Boggs, Daniel Stern, W. Rick Cook, Karl Forster, Paolo Giommi, Brian W. Grefenstette, Yunjin Kim, Takao Kitaguchi, Jason E. Koglin, Kristin K. Madsen, Peter H. Mao, Hiromasa Miyasaka, Kaya Mori, Matteo Perri, Michael J. Pivovaroff, Simonetta Puccetti, Vikram R. Rana, Niels J. Westergaard, Jason Willis, Andreas Zoglauer, Hongjun An, Matteo Bachetti, Nicolas M. Barrière, Eric C. Bellm, Varun Bhalerao, Nicolai F. Brejnholt, Felix Fuerst, Carl C. Liebe, Craig B. Markwardt, Melania Nynka, Julia K. Vogel, Dominic J. Walton, Daniel R. Wik, David M. Alexander, Lynn R. Cominsky, Ann E. Hornschemeier, Allan Hornstrup, Victoria M. Kaspi, Greg M. Madejski, Giorgio Matt, Silvano Molendi, David M. Smith, John A. Tomsick, Marco Ajello, David R. Ballantyne, Mislav Baloković, Didier Barret, Franz E. Bauer, Roger D. Blandford, W. Niel Brandt, Laura W. Brenneman, James Chiang, Deepto Chakrabarty, Jerome Chenevez, Andrea Comastri, Francois Dufour, Martin Elvis, Andrew C. Fabian, Duncan Farrah, Chris L. Fryer, Eric V. Gotthelf, Jonathan E. Grindlay, David J. Helfand, Roman Krivonos, David L. Meier, Jon M. Miller, Lorenzo Natalucci, Patrick Ogle, Eran O. Ofek, Andrew Ptak, Stephen P. Reynolds, Jane R. Rigby, Gianpiero Tagliaferri, Stephen E. Thorsett, Ezequiel Treister, and C. Megan Urry. The Nuclear Spectroscopic Telescope Array (NuSTAR) High-energy X-Ray Mission. *ApJ*, 770(2):103, June 2013. doi: 10.1088/0004-637X/770/2/103.

[16] Andrea Santangelo, Rosalia Madonia, and Santina Piraino. A chronological history of x-ray astronomy missions. In *Handbook of X-ray and Gamma-ray Astrophysics*, pages 1–68. Springer, 2023.

[17] Riccardo Giacconi, Herbert Gursky, Frank R Paolini, and Bruno B Rossi. Evidence for x rays from sources outside the solar system. *Physical Review Letters*, 9(11):439, 1962.

[18] Riccardo Giacconi. *Secrets of the Hoary Deep: A Personal History of Modern Astronomy*. Johns Hopkins University Press, 2005.

[19] R Giacconi, H Gursky, E Kellogg, E Schreier, and H Tananbaum. Discovery of periodic x-ray pulsations in centaurus x-3 from uhuru. *Astrophysical Journal, vol. 167, p. L67*, 167:L67, 1971.

[20] Charles Thomas Bolton. Identification of cygnus x-1 with hde 226868. *Nature*, 235(5336):271–273, 1972.

[21] B. G. Taylor, R. D. Andresen, A. Peacock, and R. Zobl. The EXOSAT Mission. *Space Sci. Rev.*, 30(1-4):479–494, March 1981. doi: 10.1007/BF01246069.

[22] J. H. Swank. The Rossi X-Ray Timing Explorer. *Nuclear Physics B Proceedings Supplements*, 69(1-3):12–19, January 1999. doi: 10.1016/S0920-5632(98)00175-3.

[23] M Van der Klis. Fourier techniques in x-ray timing. In *Timing neutron stars*, pages 27–69. Springer, 1989.

[24] Adam R. Ingram and Sara E. Motta. A review of quasi-periodic oscillations from black hole X-ray binaries: Observation and theory. *New A Rev.*, 85:101524, September 2019. doi: 10.1016/j.newar.2020.101524.

[25] Rudy Wijnands and Michiel Van Der Klis. A millisecond pulsar in an x-ray binary system. *nature*, 394(6691):344–346, 1998.

[26] F Jansen, D Lumb, B Altieri, J Clavel, M Ehle, C Erd, C Gabriel, M Guainazzi, P Gondoin, R Much, et al. Xmm-newton observatory. i. the spacecraft and operations. *Astronomy & Astrophysics*, 365(1):L1–L6, 2001.

[27] Peter Predehl, R Andritschke, V Arefiev, V Babyshkin, O Batanov, W Becker, H Böhringer, A Bogomolov, T Boller, K Borm, et al. The erosita x-ray telescope on srg. *Astronomy & Astrophysics*, 647:A1, 2021.

[28] Ti-Pei Li. HXMT: A Chinese High-Energy Astrophysics Mission. *Nuclear Physics B Proceedings Supplements*, 166:131–139, April 2007. doi: 10.1016/j.nuclphysbps.2006.12.070.

[29] S Zhang, SN Zhang, FJ Lu, TP Li, LM Song, YP Xu, HY Wang, JL Qu, CZ Liu, Y Chen, et al. The insight-hxmt mission and its recent progresses. In *Space Telescopes and Instrumentation 2018: Ultraviolet to Gamma Ray*, volume 10699, pages 434–455. SPIE, 2018.

[30] Robert F Archibald, VM Kaspi, C-Y Ng, KN Gourgouliatos, D Tsang, P Scholz, AP Beardmore, N Gehrels, and JA Kennea. An anti-glitch in a magnetar. *Nature*, 497(7451):591–593, 2013.

[31] Tomaso M Belloni and Sara E Motta. Transient black hole binaries. *Astrophysics of Black Holes: From Fundamental Aspects to Latest Developments*, pages 61–97, 2016.

[32] Liang Zhang, Mariano Méndez, Diego Altamirano, Jinlu Qu, Li Chen, Konstantinos Karpouzas, Tomaso M. Belloni, Qingcui Bu, Yue Huang, Xiang Ma, Lian Tao, and Yanan Wang. A systematic analysis of the phase lags associated with the type-C quasi-periodic oscillation in GRS 1915+105. *MNRAS*, 494(1): 1375–1386, May 2020. doi: 10.1093/mnras/staa797.

[33] Daniela Huppenkothen, Matteo Bachetti, Abigail Stevens, Simone Migliari, Paul Balm, Omar Hammad, Usman Mahmood Khan, Himanshu Mishra, Haroon Rashid, Swapnil Sharma, Evandro Martinez Ribeiro, and Ricardo Valles Blanco. stingray: A modern python library for spectral timing. *Journal of Open Source Software*, 4(38):1393, 2019. doi: 10.21105/joss.01393. URL `https://doi.org/10.21105/joss.01393`.

[34] H Gursky, P Gorenstein, and R Giacconi. The distribution of galactic x-ray sources from scorpio to cygnus. *Astrophysical Journal, vol. 150, p. L75*, 150:L75, 1967.

[35] Thomas M Tauris and Edward PJ van den Heuvel. *Physics of Binary Star Evolution: From Stars to X-ray Binaries and Gravitational Wave Sources*, volume 42. Princeton University Press, 2023.

[36] Juhan Frank, Andrew R King, and Derek Raine. *Accretion power in astrophysics*. Cambridge university press, 2002.

[37] Luciano Rezzolla and Olindo Zanotti. *Relativistic hydrodynamics*. Oxford University Press, USA, 2013.

[38] Kip Thorne. *Black Holes & Time Warps: Einstein's Outrageous Legacy (Commonwealth Fund Book Program)*. WW Norton & Company, 1995.

[39] R Penrose. Gravitational collapse: The role of general relativity. 1969.

[40] Roger D Blandford and Roman L Znajek. Electromagnetic extraction of energy from kerr black holes. *Monthly Notices of the Royal Astronomical Society*, 179 (3):433–456, 1977.

[41] Ramesh Narayan. Black holes in astrophysics. *New Journal of Physics*, 7(1):199, 2005.

[42] AC Fabian, K Iwasawa, CS Reynolds, and AJ Young. Broad iron lines in active galactic nuclei. *Publications of the Astronomical Society of the Pacific*, 112(775): 1145, 2000.

[43] MM Basko and Rashid Alievich Sunyaev. The limiting luminosity of accreting neutron stars with magnetic fields. *Monthly Notices of the Royal Astronomical Society*, 175(2):395–417, 1976.

[44] Alexander A Mushtukov, Valery F Suleimanov, Sergey S Tsygankov, and Juri Poutanen. The critical accretion luminosity for magnetized neutron stars. *Monthly Notices of the Royal Astronomical Society*, 447(2):1847–1856, 2015.

[45] PA Becker, D Klochkov, G Schönherr, O Nishimura, C Ferrigno, I Caballero, P Kretschmar, MT Wolff, J Wilms, and R Staubert. Spectral formation in accreting x-ray pulsars: bimodal variation of the cyclotron energy with luminosity. *Astronomy & Astrophysics*, 544:A123, 2012.

[46] Chris Done, Marek Gierliński, and Aya Kubota. Modelling the behaviour of accretion flows in X-ray binaries. Everything you always wanted to know about accretion but were afraid to ask. *A&A Rev.*, 15(1):1–66, December 2007. doi: 10.1007/s00159-007-0006-1.

[47] N. I. Shakura and R. A. Sunyaev. Black holes in binary systems. Observational appearance. *A&A*, 24:337–355, January 1973.

[48] S. Motta, T. Muñoz-Darias, P. Casella, T. Belloni, and J. Homan. Low-frequency oscillations in black holes: a spectral-timing approach to the case of GX 339-4. *MNRAS*, 418(4):2292–2307, December 2011. doi: 10.1111/j.1365-2966.2011.19566.x.

[49] Ann A. Esin, Jeffrey E. McClintock, and Ramesh Narayan. Advection-Dominated Accretion and the Spectral States of Black Hole X-Ray Binaries: Application to Nova Muscae 1991. *ApJ*, 489(2):865–889, November 1997. doi: 10.1086/304829.

[50] T. M. Belloni. States and Transitions in Black Hole Binaries. In Tomaso Belloni, editor, *Lecture Notes in Physics, Berlin Springer Verlag*, volume 794, page 53. 2010. doi: 10.1007/978-3-540-76937-8_3.

[51] S. Motta, T. Belloni, and J. Homan. The evolution of the high-energy cut-off in the X-ray spectrum of GX 339-4 across a hard-to-soft transition. *MNRAS*, 400 (3):1603–1612, December 2009. doi: 10.1111/j.1365-2966.2009.15566.x.

[52] Ramesh Narayan and Insu Yi. Advection-dominated Accretion: Underfed Black Holes and Neutron Stars. *ApJ*, 452:710, October 1995. doi: 10.1086/176343.

[53] Marek A. Abramowicz, Xingming Chen, Shoji Kato, Jean-Pierre Lasota, and Oded Regev. Thermal Equilibria of Accretion Disks. *ApJ*, 438:L37, January 1995. doi: 10.1086/187709.

[54] N. D. Kylafis and T. M. Belloni. Accretion and ejection in black-hole X-ray transients. *aap*, 574:A133, February 2015. doi: 10.1051/0004-6361/201425106.

[55] Adam Ingram, Chris Done, and P. Chris Fragile. Low-frequency quasi-periodic oscillations spectra and Lense-Thirring precession. *MNRAS*, 397(1):L101–L105, July 2009. doi: 10.1111/j.1745-3933.2009.00693.x.

[56] Rudy Wijnands and Michiel van der Klis. The Broadband Power Spectra of X-Ray Binaries. *apj*, 514(2):939–944, April 1999. doi: 10.1086/306993.

[57] Rob Fender and Tomaso Belloni. GRS 1915+105 and the Disc-Jet Coupling in Accreting Black Hole Systems. *ARA&A*, 42(1):317–364, September 2004. doi: 10.1146/annurev.astro.42.053102.134031.

[58] Abigail L. Stevens and Phil Uttley. Phase-resolved spectroscopy of Type B quasi-periodic oscillations in GX 339-4. *mnras*, 460(3):2796–2810, August 2016. doi: 10.1093/mnras/stw1093.

[59] M. Tagger and R. Pellat. An accretion-ejection instability in magnetized disks. *A&A*, 349:1003–1016, September 1999. doi: 10.48550/arXiv.astro-ph/9907267.

[60] Lev Titarchuk, Vladimir Osherovich, and Sergey Kuznetsov. Timing Spectroscopy of Quasi-Periodic Oscillations in the Low-Mass X-Ray Neutron Star Binaries. *apjl*, 525(2):L129–L132, November 1999. doi: 10.1086/312341.

[61] Frederick K. Lamb and M. Coleman Miller. Changing Frequency Separation of Kilohertz Quasi-periodic Oscillations in the Sonic-Point Beat-Frequency Model. *apj*, 554(2):1210–1215, June 2001. doi: 10.1086/323148.

[62] Luigi Stella, Mario Vietri, and Sharon M. Morsink. Correlations in the Quasi-periodic Oscillation Frequencies of Low-Mass X-Ray Binaries and the Relativistic Precession Model. *ApJ*, 524(1):L63–L66, October 1999. doi: 10.1086/312291.

[63] S. E. Motta, P. Casella, M. Henze, T. Muñoz-Darias, A. Sanna, R. Fender, and T. Belloni. Geometrical constraints on the origin of timing signals from black holes. *MNRAS*, 447(2):2059–2072, February 2015. doi: 10.1093/mnras/stu2579.

[64] Xiang Ma, Lian Tao, Shuang-Nan Zhang, Liang Zhang, Qing-Cui Bu, Ming-Yu Ge, Yu-Peng Chen, Jin-Lu Qu, Shu Zhang, Fang-Jun Lu, Li-Ming Song, Yi-Jung Yang, Feng Yuan, Ce Cai, Xue-Lei Cao, Zhi Chang, Gang Chen, Li Chen, Tian-Xiang Chen, Yi-Bao Chen, Yong Chen, Wei Cui, Wei-Wei Cui, Jing-Kang Deng, Yong-Wei Dong, Yuan-Yuan Du, Min-Xue Fu, Guan-Hua Gao, He Gao, Min Gao, Yu-Dong Gu, Ju Guan, Cheng-Cheng Guo, Da-Wei Han, Yue Huang, Jia Huo, Long Ji, Shu-Mei Jia, Lu-Hua Jiang, Wei-Chun Jiang, Jing Jin, Yong-Jie Jin, Ling-Da Kong, Bing Li, Cheng-Kui Li, Gang Li, Mao-Shun Li, Ti-Pei Li, Wei Li, Xian Li, Xiao-Bo Li, Xu-Fang Li, Yan-Guo Li, Zheng-Wei Li, Xiao-Hua Liang, Jin-Yuan Liao, Bai-Sheng Liu, Cong-Zhan Liu, Guo-Qing Liu, Hong-Wei Liu, Xiao-Jing Liu, Yi-Nong Liu, Bo Lu, Xue-Feng Lu, Qi Luo, Tao Luo, Bin Meng, Yi Nang, Jian-Yin Nie, Ge Ou, Na Sai, Ren-Cheng Shang, Xin-Ying Song, Liang Sun, Ying Tan, Yuo-Li Tuo, Chen Wang, Guo-Feng Wang, Juan Wang, Ling-Jun Wang, Wen-Shuai Wang, Yu-Sa Wang, Xiang-Yang Wen, Bai-Yang Wu, Bo-Bing Wu, Mei Wu, Guang-Cheng Xiao, Shuo Xiao, Fu-Guo Xie, Shao-Lin Xiong, He Xu, Yu-Peng Xu, Jia-Wei Yang, Sheng Yang, Yan-Ji Yang, Qi-Bin Yi, Qian-Qing Yin, Yuan You, Ai-Mei Zhang, Cheng-Mo Zhang, Fan Zhang, Hong-Mei Zhang, Juan Zhang, Tong Zhang, Wan-Chang Zhang, Wei Zhang, Wen-Zhao Zhang, Yi Zhang, Yi-Fei Zhang, Yong-Jie Zhang, Yue Zhang, Zhao Zhang, Zhi Zhang, Zi-Liang Zhang, Hai-Sheng Zhao, Xiao-Fan Zhao, Shi-Jie Zheng, Deng-Ke Zhou, Jian-Feng Zhou, Yu-Xuan Zhu, Yue Zhu, and Ren-Lin Zhuang. Discovery of oscillations above 200 keV in a black hole X-ray binary with Insight-HXMT. *Nature Astronomy*, 5:94–102, January 2021. doi: 10.1038/s41550-020-1192-2.

[65] M. A. Sobolewska and P. T. Życki. Spectral and Fourier analyses of X-ray quasi-periodic oscillations in accreting black holes. *MNRAS*, 370(1):405–414, July 2006. doi: 10.1111/j.1365-2966.2006.10489.x.

[66] G. Ponti, R. P. Fender, M. C. Begelman, R. J. H. Dunn, J. Neilsen, and M. Coriat. Ubiquitous equatorial accretion disc winds in black hole soft states. *MNRAS*, 422(1):L11–L15, May 2012. doi: 10.1111/j.1745-3933.2012.01224.x.

[67] M. C. Begelman, C. F. McKee, and G. A. Shields. Compton heated winds and coronae above accretion disks. I. Dynamics. *ApJ*, 271:70–88, August 1983. doi: 10.1086/161178.

[68] M. C. Begelman and C. F. McKee. Compton heated winds and coronae above accretion disks. II. Radiativetransfer and observable consequences. *ApJ*, 271: 89–112, August 1983. doi: 10.1086/161179.

[69] Christopher S. Reynolds. Constraints on Compton-thick Winds from Black Hole Accretion Disks: Can We See the Inner Disk? *apjl*, 759(1):L15, November 2012. doi: 10.1088/2041-8205/759/1/L15.

[70] R. D. Blandford and D. G. Payne. Hydromagnetic flows from accretion disks and the production of radio jets. *MNRAS*, 199:883–903, June 1982. doi: 10.1093/mnras/199.4.883.

[71] R. E. Pudritz, R. Ouyed, Ch. Fendt, and A. Brandenburg. Disk Winds, Jets, and Outflows: Theoretical and Computational Foundations. In Bo Reipurth, David Jewitt, and Klaus Keil, editors, *Protostars and Planets V*, page 277, January 2007.

[72] L. D. Kong, S. Zhang, Y. P. Chen, S. N. Zhang, L. Ji, P. J. Wang, L. Tao, M. Y. Ge, C. Z. Liu, L. M. Song, F. J. Lu, J. L. Qu, T. P. Li, Y. P. Xu, X. L. Cao, Y. Chen, Q. C. Bu, C. Cai, Z. Chang, G. Chen, L. Chen, T. X. Chen, W. W. Cui, Y. Y. Du, G. H. Gao, H. Gao, M. Gao, Y. D. Gu, J. Guan, C. C. Guo, D. W. Han, Y. Huang, J. Huo, S. M. Jia, W. C. Jiang, J. Jin, B. Li, C. K. Li, G. Li, W. Li, X. Li, X. B. Li, X. F. Li, Z. W. Li, X. H. Liang, J. Y. Liao, B. S. Liu, H. W. Liu, H. X. Liu, X. J. Liu, X. F. Lu, Q. Luo, T. Luo, R. C. Ma, X. Ma, B. Meng, Y. Nang, J. Y. Nie, G. Ou, X. Q. Ren, N. Sai, X. Y. Song, L. Sun, Y. Tan, Y. L. Tuo, C. Wang, L. J. Wang, W. S. Wang, Y. S. Wang, X. Y. Wen, B. B. Wu, B. Y. Wu, M. Wu, G. C. Xiao, S. Xiao, S. L. Xiong, R. J. Yang, S. Yang, Y. J. Yang, Y. J. Yang, Q. B. Yi, Q. Q. Yin, Y. You, F. Zhang, H. M. Zhang, J. Zhang, P. Zhang, W. C. Zhang, W. Zhang, Y. F. Zhang, Y. H. Zhang, H. S. Zhao, X. F. Zhao, S. J. Zheng, Y. G. Zheng, and D. K. Zhou. Insight-HXMT Observations of a Possible Fast Transition from the Jet- to Wind-dominated State during a Huge Flare of GRS 1915+105. *ApJ*, 906 (1):L2, January 2021. doi: 10.3847/2041-8213/abd03d.

[73] LG Schulz. A direct method of determining preferred orientation of a flat reflection sample using a geiger counter x-ray spectrometer. *Journal of Applied Physics*, 20(11):1030–1033, 1949.

[74] GW Fraser, AF Abbey, A Holland, K McCarthy, A Owens, and A Wells. The x-ray energy response of silicon part a. theory. *Nuclear Instruments and Methods in Physics Research Section A: Accelerators, Spectrometers, Detectors and Associated Equipment*, 350(1-2):368–378, 1994.

[75] Joachim E Trümper and Günther Hasinger. *The Universe in X-rays*. Springer Science & Business Media, 2008.

[76] G Boella, L Chiappetti, G Conti, G Cusumano, S Del Sordo, G La Rosa, MC Maccarone, T Mineo, S Molendi, S Re, et al. The medium-energy concentrator spectrometer on board the bepposax x-ray astronomy satellite. *Astronomy and Astrophysics Supplement Series*, 122(2):327–340, 1997.

[77] PN Burrows. A ccd vertex detector for a high-energy linear e+ e- collider. *Nuclear Instruments and Methods in Physics Research Section A: Accelerators, Spectrometers, Detectors and Associated Equipment*, 447(1-2):194–201, 2000.

[78] Keith Arnaud, Randall Smith, and Aneta Siemiginowska. *Handbook of X-ray Astronomy*, volume 7. Cambridge University Press, 2011.

[79] L Strüder, U Briel, K Dennerl, R Hartmann, E Kendziorra, N Meidinger, E Pfeffermann, C Reppin, B Aschenbach, W Bornemann, et al. The european

photon imaging camera on xmm-newton: the pn-ccd camera. *Astronomy & Astrophysics*, 365(1):L18–L26, 2001.

[80] Norbert Meidinger, Robert Andritschke, Robert Hartmann, Sven Herrmann, Peter Holl, Gerhard Lutz, and Lothar Strüder. pnccd for photon detection from near-infrared to x-rays. *Nuclear Instruments and Methods in Physics Research Section A: Accelerators, Spectrometers, Detectors and Associated Equipment*, 565(1):251–257, 2006.

[81] Paolo Soffitta, Luca Baldini, Ronaldo Bellazzini, Enrico Costa, Luca Latronico, Fabio Muleri, Ettore Del Monte, Sergio Fabiani, Massimo Minuti, Michele Pinchera, et al. The instrument of the imaging x-ray polarimetry explorer. *The Astronomical Journal*, 162(5):208, 2021.

[82] HV Bradt, RE Rothschild, and JH Swank. X-ray timing explorer mission. In *Non-accelerator Particle Physics: Proceedings Of The International Conference*, page 281. World Scientific, 1995.

[83] MC Weisskopf, B Brinkman, C Canizares, G Garmire, S Murray, and LP Van Speybroeck. An overview of the performance and scientific results from the chandra x-ray observatory. *Publications of the Astronomical Society of the Pacific*, 114(791):1, 2002.

[84] Katsuji Koyama, Hiroshi Tsunemi, Tadayasu Dotani, Mark W Bautz, Kiyoshi Hayashida, Takeshi Go Tsuru, Hironori Matsumoto, Yoshiaki Ogawara, George R Ricker, John Doty, et al. X-ray imaging spectrometer (xis) on board suzaku. *Publications of the Astronomical Society of Japan*, 59(sp1):S23–S33, 2007.

[85] Neil Gehrels, Guido Chincarini, PE Giommi, KO Mason, JA Nousek, AA Wells, NE White, SD Barthelmy, David N Burrows, Lynn R Cominsky, et al. The swift gamma-ray burst mission. *The Astrophysical Journal*, 611(2):1005, 2004.

[86] Keith C. Gendreau, Zaven Arzoumanian, Phillip W. Adkins, Cheryl L. Albert, John F. Anders, Andrew T. Aylward, Charles L. Baker, Erin R. Balsamo, William A. Bamford, Suyog S. Benegalrao, Daniel L. Berry, Shiraz Bhalwani, J. Kevin Black, Carl Blaurock, Ginger M. Bronke, Gary L. Brown, Jason G. Budinoff, Jeffrey D. Cantwell, Thoniel Cazeau, Philip T. Chen, Thomas G. Clement, Andrew T. Colangelo, Jerry S. Coleman, Jonathan D. Coopersmith, William E. Dehaven, John P. Doty, Mark D. Egan, Teruaki Enoto, Terry W. Fan, Deneen M. Ferro, Richard Foster, Nicholas M. Galassi, Luis D. Gallo, Chris M. Green, Dave Grosh, Kong Q. Ha, Monther A. Hasouneh, Kristofer B. Heefner, Phyllis Hestnes, Lisa J. Hoge, Tawanda M. Jacobs, John L. Jørgensen, Michael A. Kaiser, James W. Kellogg, Steven J. Kenyon, Richard G. Koenecke, Robert P. Kozon, Beverly LaMarr, Mike D. Lambertson, Anne M. Larson, Steven Lentine, Jesse H. Lewis, Michael G. Lilly, Kuochia Alice Liu, Andrew Malonis, Sridhar S. Manthripragada, Craig B. Markwardt, Bryan D. Matonak, Isaac E. Mcginnis, Roger L. Miller, Alissa L. Mitchell, Jason W. Mitchell, Jelila S. Mohammed, Charles A. Monroe, Kristina M. Montt de Garcia, Peter D. Mulé, Louis T. Nagao, Son N. Ngo, Eric D. Norris, Dwight A. Norwood, Joseph Novotka, Takashi Okajima, Lawrence G. Olsen, Chimaobi O. Onyeachu, Henry Y. Orosco, Jacqualine R. Peterson, Kristina N. Pevear, Karen K. Pham, Sue E. Pollard, John S. Pope, Daniel F. Powers, Charles E. Powers, Samuel R. Price, Gregory Y. Prigozhin,

Julian B. Ramirez, Winston J. Reid, Ronald A. Remillard, Eric M. Rogstad, Glenn P. Rosecrans, John N. Rowe, Jennifer A. Sager, Claude A. Sanders, Bruce Savadkin, Maxine R. Saylor, Alexander F. Schaeffer, Nancy S. Schweiss, Sean R. Semper, Peter J. Serlemitsos, Larry V. Shackelford, Yang Soong, Jonathan Struebel, Michael L. Vezie, Joel S. Villasenor, Luke B. Winternitz, George I. Wofford, Michael R. Wright, Mike Y. Yang, and Wayne H. Yu. The Neutron star Interior Composition Explorer (NICER): design and development. In Jan-Willem A. den Herder, Tadayuki Takahashi, and Marshall Bautz, editors, *Space Telescopes and Instrumentation 2016: Ultraviolet to Gamma Ray*, volume 9905 of *Society of Photo-Optical Instrumentation Engineers (SPIE) Conference Series*, page 99051H, July 2016. doi: 10.1117/12.2231304.

[87] Jiawen Li and Xinwu Cao. The large-scale magnetic field of a thin accretion disk with outflows. *The Astrophysical Journal*, 872(2):149, feb 2019. doi: 10.3847/1538-4357/ab0207. URL `https://doi.org/10.3847%2F1538-4357%2Fab0207`.

[88] W Niel Brandt and G Hasinger. Deep extragalactic x-ray surveys. *Annu. Rev. Astron. Astrophys.*, 43(1):827–859, 2005.

[89] George B Lansbury, D Stern, James Aird, David M Alexander, Cesar Fuentes, Fiona A Harrison, Ezequiel Treister, Franz E Bauer, John A Tomsick, Mislav Baloković, et al. The nustar serendipitous survey: the 40-month catalog and the properties of the distant high-energy x-ray source population. *The Astrophysical Journal*, 836(1):99, 2017.

[90] Slavko Bogdanov, Frederick K Lamb, Simin Mahmoodifar, M Coleman Miller, Sharon M Morsink, Thomas E Riley, Tod E Strohmayer, Albert K Tung, Anna L Watts, Alexander J Dittmann, et al. Constraining the neutron star mass–radius relation and dense matter equation of state with nicer. ii. emission from hot spots on a rapidly rotating neutron star. *The Astrophysical Journal Letters*, 887 (1):L26, 2019.

[91] MC Miller, Frederick K Lamb, AJ Dittmann, Slavko Bogdanov, Zaven Arzoumanian, Keith C Gendreau, S Guillot, AK Harding, WCG Ho, JM Lattimer, et al. Psr j0030+ 0451 mass and radius from nicer data and implications for the properties of neutron star matter. *The Astrophysical Journal Letters*, 887(1): L24, 2019.

[92] Thomas E Riley, Anna L Watts, Slavko Bogdanov, Paul S Ray, Renee M Ludlam, Sebastien Guillot, Zaven Arzoumanian, Charles L Baker, Anna V Bilous, Deepto Chakrabarty, et al. A nicer view of psr j0030+ 0451: millisecond pulsar parameter estimation. *The Astrophysical Journal Letters*, 887(1):L21, 2019.

[93] Benjamin P Abbott. Multi-messenger observations of a binary neutron star merger. 2017.

[94] Keith C Gendreau, Zaven Arzoumanian, and Takashi Okajima. The neutron star interior composition explorer (nicer): an explorer mission of opportunity for soft x-ray timing spectroscopy. In *Space Telescopes and Instrumentation 2012: Ultraviolet to Gamma Ray*, volume 8443, pages 322–329. SPIE, 2012.

[95] Shuang-Nan Zhang, TiPei Li, FangJun Lu, LiMing Song, YuPeng Xu, CongZhan Liu, Yong Chen, XueLei Cao, QingCui Bu, Zhi Chang, Gang Chen, Li Chen, TianXiang Chen, YiBao Chen, YuPeng Chen, Wei Cui, WeiWei Cui, JingKang Deng, YongWei Dong, YuanYuan Du, MinXue Fu, GuanHua Gao, He Gao, Min Gao, MingYu Ge, YuDong Gu, Ju Guan, Can Gungor, ChengCheng Guo, DaWei Han, Wei Hu, Yue Huang, Jia Huo, ShuMei Jia, LuHua Jiang, WeiChun Jiang, Jing Jin, YongJie Jin, Bing Li, ChengKui Li, Gang Li, MaoShun Li, Wei Li, Xian Li, XiaoBo Li, XuFang Li, YanGuo Li, ZiJian Li, ZhengWei Li, XiaoHua Liang, JinYuan Liao, GuoQing Liu, HongWei Liu, ShaoZhen Liu, XiaoJing Liu, Yuan Liu, YiNong Liu, Bo Lu, XueFeng Lu, Tao Luo, Xiang Ma, Bin Meng, Yi Nang, JianYin Nie, Ge Ou, JinLu Qu, Na Sai, RenCheng Shang, GuoHong Shen, Liang Sun, Ying Tan, Lian Tao, YouLi Tuo, Chen Wang, ChunQin Wang, GuoFeng Wang, HuanYu Wang, Juan Wang, WenShuai Wang, YuSa Wang, XiangYang Wen, BaiYang Wu, BoBing Wu, Mei Wu, GuangCheng Xiao, ShaoLin Xiong, LinLi Yan, JiaWei Yang, Sheng Yang, YanJi Yang, QiBin Yi, Bin Yuan, AiMei Zhang, ChunLei Zhang, ChengMo Zhang, Fan Zhang, HongMei Zhang, Juan Zhang, Qiang Zhang, ShenYi Zhang, Shu Zhang, Tong Zhang, WanChang Zhang, Wei Zhang, WenZhao Zhang, Yi Zhang, YiFei Zhang, YongJie Zhang, Yue Zhang, Zhao Zhang, Zhi Zhang, ZiLiang Zhang, HaiSheng Zhao, XiaoFan Zhao, ShiJie Zheng, JianFeng Zhou, YuXuan Zhu, Yue Zhu, RenLin Zhuang, and Insight-HXMT team. Overview to the Hard X-ray Modulation Telescope (Insight-HXMT) Satellite. *Science China Physics, Mechanics, and Astronomy*, 63(4):249502, February 2020. doi: 10.1007/s11433-019-1432-6.

[96] CongZhan Liu, YiFei Zhang, XuFang Li, XueFeng Lu, Zhi Chang, ZhengWei Li, AiMei Zhang, YongJie Jin, HuiMing Yu, Zhao Zhang, et al. The high energy x-ray telescope (he) onboard the insight-hxmt astronomy satellite. *Science China Physics, Mechanics & Astronomy*, 63:1–15, 2020.

[97] ShuangNan Zhang, Andrea Santangelo, Marco Feroci, YuPeng Xu, FangJun Lu, Yong Chen, Hua Feng, Shu Zhang, Søren Brandt, Margarita Hernanz, Luca Baldini, Enrico Bozzo, Riccardo Campana, Alessandra De Rosa, YongWei Dong, Yuri Evangelista, Vladimir Karas, Norbert Meidinger, Aline Meuris, Kirpal Nandra, Teng Pan, Giovanni Pareschi, Piotr Orleanski, QiuShi Huang, Stephane Schanne, Giorgia Sironi, Daniele Spiga, Jiri Svoboda, Gianpiero Tagliaferri, Christoph Tenzer, Andrea Vacchi, Silvia Zane, Dave Walton, ZhanShan Wang, Berend Winter, Xin Wu, Jean J. M. in't Zand, Mahdi Ahangarianabhari, Giovanni Ambrosi, Filippo Ambrosino, Marco Barbera, Stefano Basso, Jörg Bayer, Ronaldo Bellazzini, Pierluigi Bellutti, Bruna Bertucci, Giuseppe Bertuccio, Giacomo Borghi, XueLei Cao, Franck Cadoux, Riccardo Campana, Francesco Ceraudo, TianXiang Chen, YuPeng Chen, Jerome Chevenez, Marta Civitani, Wei Cui, WeiWei Cui, Thomas Dauser, Ettore Del Monte, Sergio Di Cosimo, Sebastian Diebold, Victor Doroshenko, Michal Dovciak, YuanYuan Du, Lorenzo Ducci, QingMei Fan, Yannick Favre, Fabio Fuschino, José Luis Gálvez, Min Gao, MingYu Ge, Olivier Gevin, Marco Grassi, QuanYing Gu, YuDong Gu, DaWei Han, Bin Hong, Wei Hu, Long Ji, ShuMei Jia, WeiChun Jiang, Thomas Kennedy, Ingo Kreykenbohm, Irfan Kuvvetli, Claudio Labanti, Luca Latronico, Gang Li, MaoShun Li, Xian Li, Wei Li, ZhengWei Li, Olivier Limousin, HongWei Liu, XiaoJing Liu, Bo Lu, Tao Luo, Daniele Macera, Piero Malcovati, Adrian Martindale, Malgorzata Michalska, Bin Meng, Massimo Minuti, Alfredo

Morbidini, Fabio Muleri, Stephane Paltani, Emanuele Perinati, Antonino Picciotto, Claudio Piemonte, JinLu Qu, Alexandre Rachevski, Irina Rashevskaya, Jerome Rodriguez, Thomas Schanz, ZhengXiang Shen, LiZhi Sheng, JiangBo Song, LiMing Song, Carmelo Sgro, Liang Sun, Ying Tan, Phil Uttley, Bo Wang, DianLong Wang, GuoFeng Wang, Juan Wang, LangPing Wang, YuSa Wang, Anna L. Watts, XiangYang Wen, Jörn Wilms, ShaoLin Xiong, JiaWei Yang, Sheng Yang, YanJi Yang, Nian Yu, WenDa Zhang, Gianluigi Zampa, Nicola Zampa, Andrzej A. Zdziarski, AiMei Zhang, ChengMo Zhang, Fan Zhang, Long Zhang, Tong Zhang, Yi Zhang, XiaoLi Zhang, ZiLiang Zhang, BaoSheng Zhao, ShiJie Zheng, YuPeng Zhou, Nicola Zorzi, and J. Frans Zwart. The enhanced X-ray Timing and Polarimetry mission—eXTP. *Science China Physics, Mechanics, and Astronomy*, 62(2):29502, February 2019. doi: 10.1007/s11433-018-9309-2.

[98] Bei You, Yuoli Tuo, Chengzhe Li, Wei Wang, Shuang-Nan Zhang, Shu Zhang, Mingyu Ge, Chong Luo, Bifang Liu, Weimin Yuan, et al. Insight-hxmt observations of jet-like corona in a black hole x-ray binary maxi j1820+ 070. *Nature Communications*, 12(1):1025, 2021.

[99] Andrea Merloni, Kirpal Nandra, and Peter Predehl. erosita's x-ray eyes on the universe. *Nature Astronomy*, 4(7):634–636, 2020.

[100] Johan Comparat, Dominique Eckert, Alexis Finoguenov, Robert Schmidt, Jeremy Sanders, Daisuke Nagai, Erwin T Lau, Florian Kaefer, Florian Pacaud, Nicolas Clerc, et al. Full-sky photon simulation of clusters and active galactic nuclei in the soft x-rays for erosita. *arXiv preprint arXiv:2008.08404*, 2020.

[101] Sigenori Miyamoto, Kazuhiro Kimura, Shunji Kitamoto, Tadayasu Dotani, and Ken Ebisawa. X-Ray Variability of GX 339-4 in Its Very High State. *apj*, 383: 784, December 1991. doi: 10.1086/170837.

[102] A. Ingram and C. Done. A physical model for the continuum variability and quasi-periodic oscillations in accreting black holes. *Monthly Notices of the Royal Astronomical Society*, 419(3):2369–2374, 2012.

[103] R Buccheri, K Bennett, GF Bignami, JBGM Bloemen, V Boriakoff, PA Caraveo, W Hermsen, G Kanbach, RN Manchester, JL Masnou, et al. Search for pulsed gamma-ray emission from radio pulsars in the cos-b data. *Astronomy and Astrophysics (ISSN 0004-6361), vol. 128, no. 1, Nov. 1983, p. 245-251.*, 128: 245–251, 1983.

[104] J. H. Taylor. Pulsar Timing and Relativistic Gravity. *Philosophical Transactions of the Royal Society of London Series A*, 341(1660):117–134, October 1992. doi: 10.1098/rsta.1992.0088.

[105] F. Haberl and M. Sasaki. Doubling the number of be/x-ray binaries in the smc, 2000. URL `https://arxiv.org/abs/astro-ph/0005226`.

[106] P Eger and F Haberl. Xmm-newton observations of the small magellanic cloud: Rx j0105. 9-7203, a 726 s be/x-ray binary pulsar. *Astronomy & Astrophysics*, 485(3):807–811, 2008.

[107] Victoria M. Kaspi and Andrei M. Beloborodov. Magnetars. *ARA&A*, 55(1): 261–301, August 2017. doi: 10.1146/annurev-astro-081915-023329.

[108] Paul S. Ray, Sebastien Guillot, Wynn C. G. Ho, Matthew Kerr, Teruaki Enoto, Keith C. Gendreau, Zaven Arzoumanian, Diego Altamirano, Slavko Bogdanov, Robert Campion, Deepto Chakrabarty, Julia S. Deneva, Gaurava K. Jaisawal, Robert Kozon, Christian Malacaria, Tod E. Strohmayer, and Michael T. Wolff. Anti-glitches in the Ultraluminous Accreting Pulsar NGC 300 ULX-1 Observed with NICER. *ApJ*, 879(2):130, July 2019. doi: 10.3847/1538-4357/ab24d8.

[109] Ling-Da Kong, Shu Zhang, Shuang-Nan Zhang, Long Ji, Victor Doroshenko, Andrea Santangelo, Yu-Peng Chen, Fang-Jun Lu, Ming-Yu Ge, Peng-Ju Wang, Lian Tao, Jin-Lu Qu, Ti-Pei Li, Cong-Zhan Liu, Jin-Yuan Liao, Zhi Chang, Jing-Qiang Peng, and Qing-Cang Shui. Insight-HXMT Discovery of the Highest-energy CRSF from the First Galactic Ultraluminous X-Ray Pulsar Swift J0243.6+6124. *ApJ*, 933(1):L3, July 2022. doi: 10.3847/2041-8213/ac7711.

[110] Youli Tuo, Muhammed Miraç Serim, Marco Antonelli, Lorenzo Ducci, Armin Vahdat, Mingyu Ge, Andrea Santangelo, and Fei Xie. Discovery of the first antiglitch event in the rotation-powered pulsar psr b0540-69. *The Astrophysical Journal Letters*, 967(1):L13, 2024.

[111] George Younes, Paul S. Ray, Matthew G. Baring, Chryssa Kouveliotou, Corinne Fletcher, Zorawar Wadiasingh, Alice K. Harding, and Adam Goldstein. A Radiatively Quiet Glitch and Anti-glitch in the Magnetar 1E 2259+586. *ApJ*, 896(2):L42, June 2020. doi: 10.3847/2041-8213/ab9a48.

[112] CM Espinoza, D Antonopoulou, R Dodson, M Stepanova, and A Scherer. Small glitches and other rotational irregularities of the vela pulsar. *Astronomy & Astrophysics*, 647:A25, 2021.

[113] Shiqi Zhou, Erbil Gügercinoğlu, Jianping Yuan, Mingyu Ge, and Cong Yu. Pulsar glitches: A review. *Universe*, 8(12):641, 2022.

Appendix

Manuscript 1

Monthly Notices of the ROYAL ASTRONOMICAL SOCIETY

MNRAS **521,** 2692–2703 (2023) https://doi.org/10.1093/mnras/stad714
Advance Access publication 2023 March 9

Evolution of disc and corona in MAXI J1348−630 during the 2019 reflare: *NICER* and *Insight-HXMT* view

Xiaohang Dai [1]★ Lingda Kong,[1,2]★ Qingcui Bu,[1] Andrea Santangelo,[1] Shu Zhang,[2] Long Ji [3] Shuangnan Zhang[2,4] and Emre Seyit Yorgancioglu[1]

[1]*Institut für Astronomie und Astrophysik, Kepler Center for Astro and Particle Physics, Eberhard Karls, Universität, Sand 1, D-72076 Tübingen, Germany*
[2]*Key Laboratory for Particle Astrophysics, Institute of High Energy Physics, Chinese Academy of Sciences, 19B Yuquan Road, Beijing 100049, China*
[3]*School of Physics and Astronomy, Sun Yat-Sen University, Zhuhai, 519082, China*
[4]*University of Chinese Academy of Sciences, Chinese Academy of Sciences, Beijing 100049, China*

Accepted 2023 March 4. Received 2023 February 13; in original form 2022 November 29

ABSTRACT

In this work, using *Neutron star Interior Composition Explorer* and *Insight-Hard X-ray Modulation Telescope* observations, we present a study of the broad-band spectral and timing evolution of the source throughout the first reflare, which occurred about 4-month after the major outburst. Our findings suggest that during the reflare, below a critical luminosity $L_{\rm crit} \sim 2.5 \times 10^{36}$ (D/2.2 kpc)^2 erg s^{-1}, the scale of the corona shrinks in the radial direction, whereas the inner radius of the disc does not change considerably; however, the inner radius of the disc starts to move inward when the source exceeds the critical luminosity. We conclude that at low luminosity the increase in accretion rate only heats up the inner zone of the accretion disc without the transfer of angular momentum which occurs above a certain luminosity.

Key words: accretion, accretion discs – black hole physics – X-ray: binaries.

1 INTRODUCTION

X-ray binaries (XRBs) consist of a black hole (BH) or neutron star (NS) gravitationally bound to a normal companion star. Depending on the mass of the donor stars, XRBs are classified as high-mass X-ray binaries (HMXBs: $M \gtrsim 5\,{\rm M}_\odot$) and low-mass X-ray binaries (LMXBs: $M \lesssim 1\,{\rm M}_\odot$). In HMXBs, the compact objects accrete mainly through the stellar wind from the companion stars, whereas in LMXBs, accretion is in the form of Roche-lobe overflow (Shakura & Sunyaev 1973; Reig 2011) of the companion. Four stable accretion flow structures can exist: a geometrically thin, optically thick, cold accretion disc (Shakura & Sunyaev 1973); a geometrically thick, optically thin, hot corona (Gilfanov 2010); an advection-dominated accreting flow (ADAF) (Abramowicz et al. 1995; Narayan & Yi 1995); and an optically thick ADAF, often called 'slim disc', which is expected when the mass accretion rate is very high (Kawaguchi 2003).

Some BH transients spend virtually all of their lives in a fairly faint state in the X-ray band, but they occasionally experience unpredictable and irregular active X-ray outbursts that last from a few days to several months (Belloni, Motta & Muñoz-Darias 2011). In contrast, some BH binary systems remain active in the X-ray band for rather long periods of time, such as GRS 1915+105 (Belloni et al. 2000) and Cyg X-1 (Liang & Nolan 1984). Low-mass black hole X-ray binaries (LM-BHXRBs) in outbursts are characterized by the rapid evolution of their spectral and timing properties, which can be studied in terms of different states (Homan & Belloni 2005; Remillard & McClintock 2006). A classical BH binary outburst may cycle through many different states and follow a 'q' shape in the hardness–intensity diagram (HID), which quickly and clearly displays the relationship between the distribution of soft and hard photons in the energy spectrum and the source intensity. Furthermore, in different branches of the HID, the quasi-periodic and aperiodic signals in the light curve can produce intriguing different power-density spectrum (PDS) in the frequency domain.

According to these properties, LM-BHXRBs are typically classified according to different states (Remillard & McClintock 2006; Motta, Belloni & Homan 2009; Belloni 2010). At the beginning of an outburst, the flux rises rapidly, the majority of emitted photons are in the hard X-ray range, and the spectra are dominated by a hard power-law component in the X-ray band (power-law photon index Γ between approximately 1.5 and 1.7) in what is known as the hard state (HS). A PDS in the HS normally has a strong band-limited noise (30 per cent–40 per cent RMS) component accompanied by a low-frequency quasi-periodical oscillation (QPO). Following the HS, the outburst switches to the intermediate state (IMS) which can further be classified into a hard-intermediate state (HIMS) and soft-intermediate state (SIMS). In this transition state, the emission gradually changes from power law to thermal. Inverse-Compton photons scattering in a hot corona or the jet base, which originated from a geometrically thick, optically thin region near the compact object determine the power-law component in the energy spectrum. The band-limited noise decreases with increasing flux, and the total RMS of HIMS (10 per cent–20 per cent) is lower than that in the HS. Compared to the HIMS where type-C QPOs are normally present, a PDS in the SIMS has a RMS lower than 10 per cent and a weak power-law component with the occasional presence of type-A or -B QPOs. After the IMS, photons mainly originate from the disc,

★ E-mail: dai@astro.uni-tuebingen.de (XD); lingda.kong@mnf.uni-tuebingen.de (LK)

© 2023 The Author(s)
Published by Oxford University Press on behalf of Royal Astronomical Society

Downloaded from https://academic.oup.com/mnras/article/521/2/2692/7074565 by guest on 06 February 2025

Manuscript 1

which displays a thermal component in the energy spectrum. Then, the transient switches into a soft state (SS), where the spectrum is the softest and dominated by thermal emission. The spectrum can be described by a strong multicolour blackbody component with a weak power-law tail, and the PDS shows a further weakened power-law noise component. Generally, it is assumed that the disc-truncated radius gets to the innermost stable circular orbit (ISCO) during the SS. This is consistent with observations showing that the disc component gradually gets larger during this period. After the SS, the source once again begins to harden and returns to the IMS. The IMS this time is SS-to-HS switches. Finally, the outburst enters HS again, and it quenches after a few days, completing the hysteresis cycle in the HID.

The truncated accretion disc and hot corona cooling are successfully used to illustrate spectro-temporal variability, jet emission, and disc wind in the vicinity of accreting BH transients (Esin, McClintock & Narayan 1997; Done, Gierliński & Kubota 2007; Meyer-Hofmeister, Liu & Meyer 2009; Ponti et al. 2012). The Lense-Thirring (L-T) precession model of the hot corona seems consistent with observations showing increasing QPO with frequency decreasing inner disc radius and increased QPO fractional RMS with higher energies (Ingram, Done & Fragile 2009). However, some recent new observational pieces of evidence do not fit the truncated disc model. In MAXI J1820+070, Kara et al. (2019) found that the broadened iron K emission line keeps constant profiles in the HS, while the time-scale of the reverberation lags shortens by an order of magnitude over a period of weeks. This suggests that in the HS, there is a reduction in the spatial extent of the corona, rather than a change in the inner edge of the accretion disc. Later, in the same source, You et al. (2021) found that the Compton hump arises from disc reflection, indicating a jet-like corona outflowing faster, and Ma et al. (2021) found a QPO with large RMS and soft lag up to 200 keV suggesting that the QPO probably originates from the precession of a small-scale jet. Therefore, up to now, the nature of the disc-corona-jet is still unclear.

Sometimes, after their main outburst, the sources' flux shows several re-brightening episodes, reaching a level of a few orders of magnitude lower than the peak flux of the main outburst. This phenomenon is called a 'reflare' or 'mini-outburst' (Patruno et al. 2016; Cúneo et al. 2020; Zhang et al. 2020b). In these reflares, the flux is at least approximately one to two orders of magnitude fainter than that of the main outburst, but the whole process has a similar behaviour in HS and IMS. In GRS 1739–278 and MAXI J1535−571, Yan & Yu (2017) and Cúneo et al. (2020) found that some reflares also showed hysteresis loops in the HID. Yan & Yu (2017) found that the luminosity in the HS-to-SS and HS of the mini-outbursts also follows the correlation that can be previously found in main outbursts. The similarities between the main outbursts and followed 'nesting dolls-like' reflares point out the same physical origin for both phenomena. But, how the ignition of reflares occurs after the main outburst runs out of accumulated matter at the outer accretion disc is still an unsolved question.

MAXI J1348−630 is a BH candidate that was discovered with the Monitor of an All-sky X-ray Image (MAXI) gas slit camera at the start of its outburst on 2019 January 26 (Yatabe et al. 2019; Negoro et al. 2020; Tominaga et al. 2020), and was subsequently observed by the Neil Gehrels Swift Observatory (*Swift*; D'Elia, Lien & Page 2019), *INTEGRAL* (Cangemi et al. 2019; Lepingwell et al. 2019), and the *Neutron Star Interior Composition Explorer* (*NICER*; Sanna et al. 2019). *Insight-Hard X-ray Modulation Telescope* (*Insight-HXMT*; Chen et al. 2019) observed both the main outburst and mini outburst in the X-ray bands. Such outburst encouraged multiwavelength observations, i.e. the 50-cm *T31* telescope (Denisenko et al. 2019), the Las Cumbres Observatory 2-m and 1-m robotic telescopes, and the *Southern African Large Telescope* in the optical bands; the Australia Telescope Compact Array (Russell et al. 2019), MeerKAT, and the Murchison Widefield Array in the radio bands. A distance of ∼2.2 kpc was estimated from the H I absorption (Chauhan et al. 2021) or of ∼3.39 kpc from the dust-scattering ring around the source which was calculated by data combination from SRG/eROSITA, *XMM–Newton*, MAXI, and *Gaia* (Lamer et al. 2021). Following its main outburst, the system underwent several reflares before returning to the quiescent state.

In this paper, we illustrate and discuss the broad-band spectral evolution and timing properties of the first reflare of MAXI J1348−630 immediately after its main outburst. With the large effective area of *NICER* and *Insight-HXMT* at low and high energies, respectively, and their continuous coverage of the burst, we can study the spectral and timing properties of the disc and corona during the reflare. We report the observations and the data reduction in Section 2, the reflare evolution results in Section 3, and discuss the implication of the results in Section 4. The summary and conclusions are presented in Section 5.

2 OBSERVATIONS AND DATA REDUCTION

2.1 *Insight-HXMT*

The *HXMT* (Zhang et al. 2014, 2020a), named *Insight-HXMT*, was launched on 2017 June 15. It has three primary payloads with high temporal resolutions and sizable effective areas: the low-energy X-ray telescope (*LE*: 384 cm^2 at 1–10 keV; Chen et al. 2020); the medium-energy X-ray telescope (*ME*: 952 cm^2 at 5–30 keV; Cao et al. 2020); and the high-energy X-ray telescope (*HE*: 5000 cm^2/20–250 keV; Liu et al. 2020). The fields-of-view are 1.6° × 6°, 1° × 4°, and 1.1° × 5.7° for *LE*, *ME*, and *HE*, respectively. Due to its broad-band capacity (1–250 keV) and large collection area at high energies, *Insight-HXMT* is well suited to study the timing and spectral properties of non-thermal emission from X-ray sources.

Insight-HXMT was triggered to observe MAXI J1348−630 from 2019 January 27 (MJD 58510) to 2019 July 29 (MJD 58693), starting 1 d after its discovery and included both its first and the second outbursts (or first reflare). The main outburst lasted for 108 d from MJD 58 509 to MJD 58 617 (a count rate of 2 counts per second). Then, the second outburst lasted for 56 d, between MJD 58 637 to MJD 58693. We obtained 32 observations from *Insight-HXMT* (a total of 73 exposures), with 20 observations having more than one exposure.

We screen the event data and extract the light curves and spectra with the *Insight-HXMT* Data Analysis Software (HXMTDAS) v2.04 and the calibration model v2.05.[1] For observations with more than one exposure in 1 d, we combine their spectra to one spectrum by ftools *addspec*, *addrmf*, and *addarf*. The energy bands considered for spectral analysis are 2–10 keV for *LE*, 10–30 keV for *ME*, and 30–200 keV for *HE*. The background spectra and response files are created with LEBKGMAP, MEBKGMAP, and HEBKGMAP tasks and LERSPGEN, MERSPGEN, and HERSPGEN, respectively, based on the latest standard *Insight-HXMT* background models and calibration (Guo et al. 2020; Liao et al. 2020a, b).

[1] http://hxmtweb.ihep.ac.cn/software.jhtml

Downloaded from https://academic.oup.com/mnras/article/521/2/2692/7074565 by guest on 06 February 2025

Manuscript 1

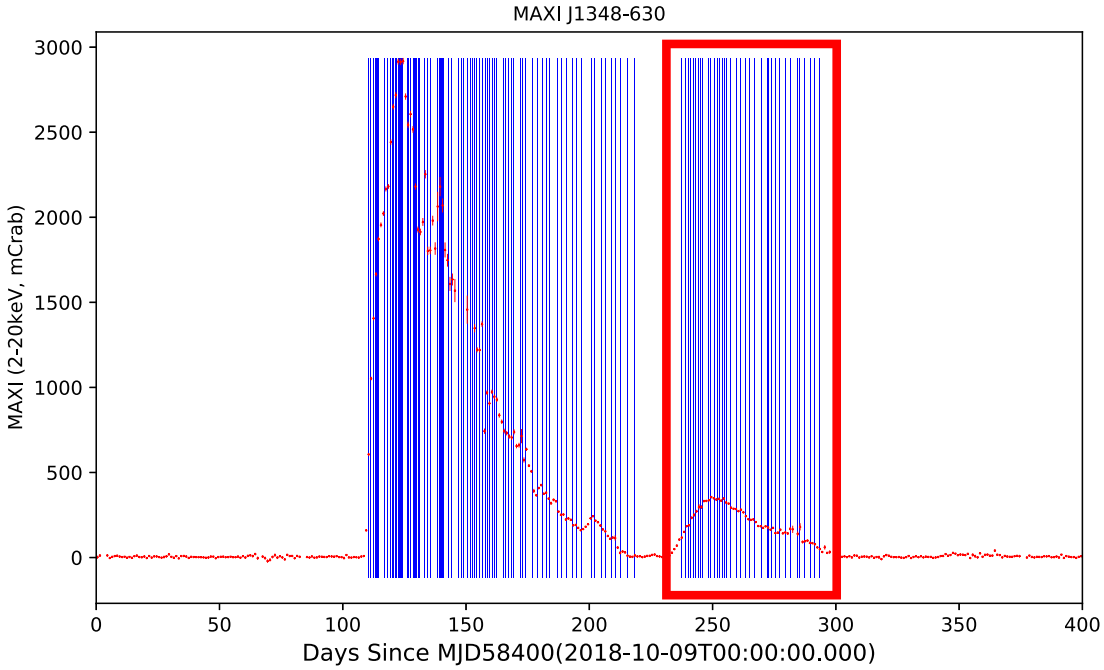


Figure 1. The MAXI (2–20)-keV light curve shows the main outburst and the first reflare of MAXI J1348−630. The blue areas indicate the *Insight-HXMT*'s observations. The red rectangle displays the focused reflare part.

2.2 *NICER*

The X-ray Timing Instrument of the *NICER* was launched aboard a SpaceX Falcon 9 rocket on 2017 June 3. It comprises an aligned collection of 56 X-ray 'concentrator' optics and silicon drift detector pairs. It provides high-signal-to-noise-ratio photon-counting capability within the (0.2–12)-keV X-ray band with a peak effective area of ∼1900 cm^2 at 1.5 keV, which is perfectly matched to blackbody component in low temperatures, such as surface radiation from the NS or accretion disc radiation from the BH.

NICER started to observe MAXI J1348−630 after its discovery several hours later. We use *NICER* data between MJD 58 637 to MJD 58693, which are on nearly identical days of *Insight-HXMT* observations. We apply *NICER* Level2 standard calibration and filtering to process data by *NICERl2*, and we get the spectral response files by *NICERRMF* and *NICERARF*. We use the 'nibackgen3C50' model to estimate the background for the spectral analysis. We remove data from detectors 14 and 34 to escape occasional episodes of increased electronic noise.

Other analyses are processed using heasoft version 6.29. We extract light curves using xselect with 0.001 s bin size in (1–10)-keV energy band. We also extract the light curve in 2–4 and 4–7 keV to calculate the hardness ratio (HR).

2.3 Spectral and timing analysis

We jointly fit *NICER* spectra, with *ME HE* of *Insight-HXMT* spectra for each data segment for spectral analysis. We produce an average PDS for timing analysis in the (10–30)- and (25–80)-keV energy band for each data segment from *HXMT*. Time resolution and time intervals are 0.004 and 100 s, respectively, corresponding to the frequency range 0.01–125 Hz. The Miyamoto normalization is used in PDS, and we use xspec v12.12.0 (Arnaud 1996) to fit PDS and estimate the RMS with a sum of Lorentzian components for red noise and QPO. An additional power-law component, with zero index, is used to model the white noise. We use the cross-correlation method in the Stingray[2] package to get the time lag in different frequency and energy bands (Huppenkothen et al. 2019a, b; Bachetti et al. 2022).

For spectral fitting in xspec, the parameter uncertainties are reported at the 90-per cent confidence interval. Considering the current accuracy of the instrument calibration and appropriate χ^2, we add the 3-per cent system error for *NICER* 0.3–1.5 keV, 0.5 per cent for *NICER* 1.5–10 keV, 1 per cent for *ME* 8–40 keV, and 1 per cent for *HE* 30–150 keV during spectral fittings. We use *ftgrouppha* from ftools based on Kaastra & Bleeker (2016) with the signal-to-noise ratio ≥5 to group and improve the spectrum quality for *NICER* (grouptype=optsnmin groupscale = 5.0) and *Insight-HXMT* (grouptype=snmin groupscale = 5.0).

3 RESULTS

3.1 Light curve of the reflare

Fig. 1 shows the light curve of both the main outburst and second outburst from the MAXI (2–20 keV) all-sky monitoring of MAXI J1348−630. After the main outburst, the source remained in quiescence for 20 d, which is less than one-fifth of the main outburst duration and nearly one-third of the second outburst duration. The second outburst lasted for 56 d from MJD 58 637 to MJD 58 693 and was one order of magnitude fainter than the peak luminosity of the main outburst. Hence, it has all the features of a 'reflare'. Fig. 2 shows the light of the reflare in detail, and the trends of (1–10)-keV light curves from *Insight-HXMT/LE* and *NICER* are consistent.

[2]https://docs.stingray.science

Downloaded from https://academic.oup.com/mnras/article/521/2/2692/7074565 by guest on 06 February 2025

Manuscript 1

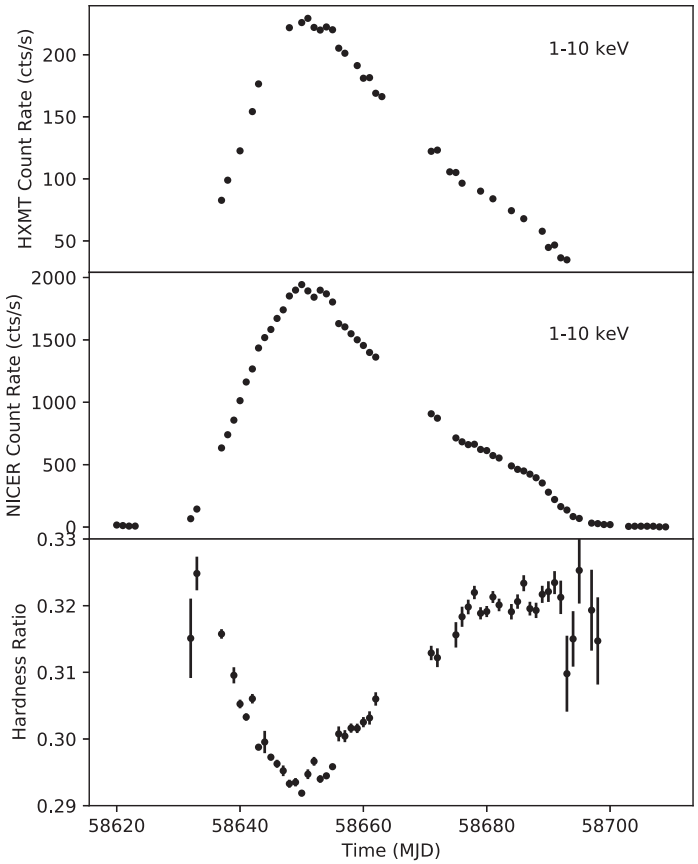


Figure 2. Upper panel: *HXMT* (1–10)-keV light curve. Medium panel: *NICER* (1–10)-keV light curve. Bottom panel: The HR of 4–7 keV/2–4 keV from *NICER*'s observations.

The flux of the reflare rapidly rises and slowly decays like other BH sources. To confirm its characteristics, we use *NICER* observations to define the HR from the (4–7)- to (2–4)-keV count rates, since *NICER* performed much more observations than *Insight-HXMT*. The HR during the reflare reaches lower values, in general evolves with the reflare and ranges in the window $\sim$0.29–0.33, as shown in the bottom panel in Fig. 2. The HR shows an anticorrelation with the flux, which means a softening process of spectra during the outburst.

3.2 Spectral analysis

When performing the spectral analysis, we combined *NICER* and *Insight-HXMT* observations, using *NICER* observations between 0.3 and 10 keV to better constrain the column density, and *Insight-HXMT* observations between 8 and 150 keV to constrain the physical characteristics of non-thermal emission throughout the reflare epoch (MJD 58637–MJD 58693). Because of the narrow allowed energy (2–7 keV) band and lower effective area than *NICER*, and for some observations (on MJD 58640, 58642, 58645, and 58646), due to the lack of Good Time Interval (GTI), *Insight-HXMT* cannot provide the low-energy band below 10 keV, though this is compensated with *NICER*'s observations. Therefore, we only use *NICER* observations for our spectral analysis in the lower energy band. In general, the spectrum from the BH binaries can be typically fitted by a multicolour blackbody *DISKBB* from the accreting disc (Shakura & Sunyaev 1973), the non-thermal component from the Comptonization in a corona (Sunyaev & Titarchuk 1980, 1985), which can be described by a phenomenological *cutoffpl* model, or physical models such as *compTT* (Titarchuk 1994) and *thcomp* (Zdziarski, Johnson & Magdziarz 1996; Zdziarski et al. 2020a), and, sometimes, an additional relativistic reflection spectrum from an illuminated accretion disc (Fabian 2016). Firstly, we fit the spectra with the model *TBabs*$\times$*(Gaussian+Gaussian + thcomp*$\times$*DISKBB)*, where *thcomp* is a much better physical self-consistent model of the continuum shape from thermal Comptonization than an exponential cutoff power-law but has similar corresponding free parameters, such as the spectral index Γ, and the electron temperature (kT_e; Zdziarski et al. 2020b). The model also provides an accurate description of the Comptonization process at energies comparable to those of seed photons from the accretion disc; hence it can afford a reasonable disc temperature kT_{in} and normalization N_{bb}. The Tuebingen–Boulder interstellar medium (ISM) absorption model *TBabs* is used (Wilms, Allen & McCray 2000), and the equivalent hydrogen column density n_H is first set as a freely varying parameter during the fit. A *Gaussian* line is fixed at 6.4 keV to reproduce the Fe-K line; the width of the Fe-K line has been fixed at 0.3 keV, which is the average value from fittings. Additional residuals are observed around 1 keV, which is possibly due to instrumental effects (Zhang et al. 2020b; Kumar et al. 2022). Hence, we take the same approach as Zhang et al. (2020b) and add another *Gaussian* component to account for these residuals; the

Downloaded from https://academic.oup.com/mnras/article/521/2/2692/7074565 by guest on 06 February 2025

Manuscript 1

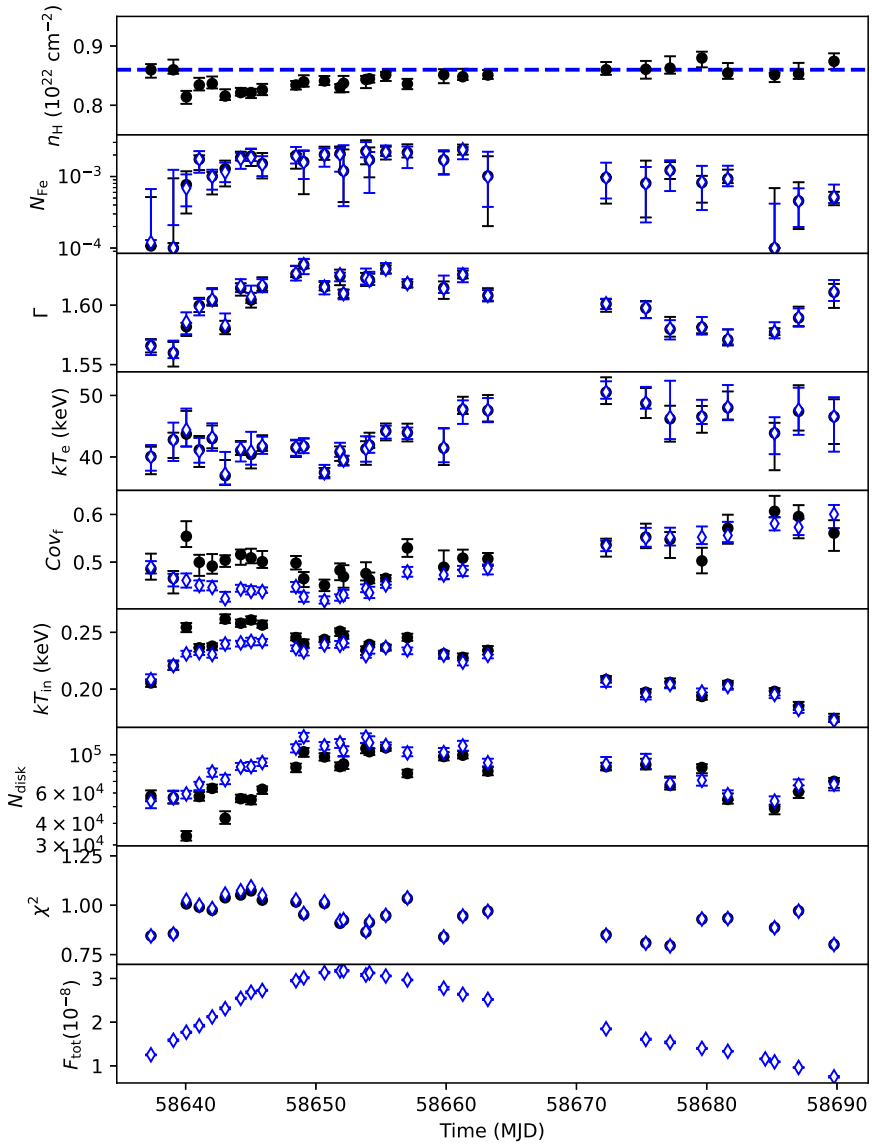


Figure 3. Spectral parameter evolution with time. The panel shows the fitting result of *TBabs×(Gaussian+Gaussian + thcomp×DISKBB)*, and the black and blue points are on behalf of the free n_H and fixed n_H, respectively. F_{tot} is the total unabsorption flux in 0.1–150 keV.

centroid energy of the line was fixed at 1 keV, and the width of the line was fixed at 0.9 keV, which is the average value from fittings. These additional *Gaussian* components have a significant effect on the *DISKBB* normalization N_{disc} but have little effect on the evolution of kT_{in} and photon index Γ. The black points in Fig. 3 show the results of the best fits. The column density n_H basically remains stable around $\sim 0.86 \times 10^{22}$ cm^{-2}, except near the peak of the outbreak. We use the n_H value from the average value of the spectral fitting, and it is also consistent with *Swift*/XRT results during the main outburst (Tominaga et al. 2020; Carotenuto et al. 2021a, b). Since the n_H can easily affect the measurement of kT_{in}, we keep it fixed at this value in the following analysis processes; the results are shown in Fig. 3 with blue hollow points. N_{Fe}, Γ, kT_{in}, and the *DISKBB* normalization N_{bb} increases with the flux, while the trends of the covering fraction Cov_f decrease with the flux. The multicolour blackbody component *DISKBB* describes emission arising from the accretion disc with the defined normalization parameter $N_{disc} = (R_{in}/D_{10})^2 \cos\theta$, where R_{in} is an apparent inner disc radius. According to our results, the disc recedes at the peak flux, which is similar to the results in Zhang et al. (2020b). We observe here that although the 1-keV Gaussian component can indeed affect the value of the N_{disc}, it will not significantly change the trend. Therefore, it would exist that a scenario in which the disc is further away from the compact object during the outburst, is not consistent with the canonical scenario. As the flux increases, the Cov_f drops from 0.5 to 0.4, indicating that at the peak of the outburst, fewer photons scatter with the high-temperature electrons in the corona. At the same time, Γ increases with the flux from ∼1.55 to 1.65 consisting of the variation of the HR in HID. At

Downloaded from https://academic.oup.com/mnras/article/521/2/2692/7074565 by guest on 06 February 2025

Manuscript 1

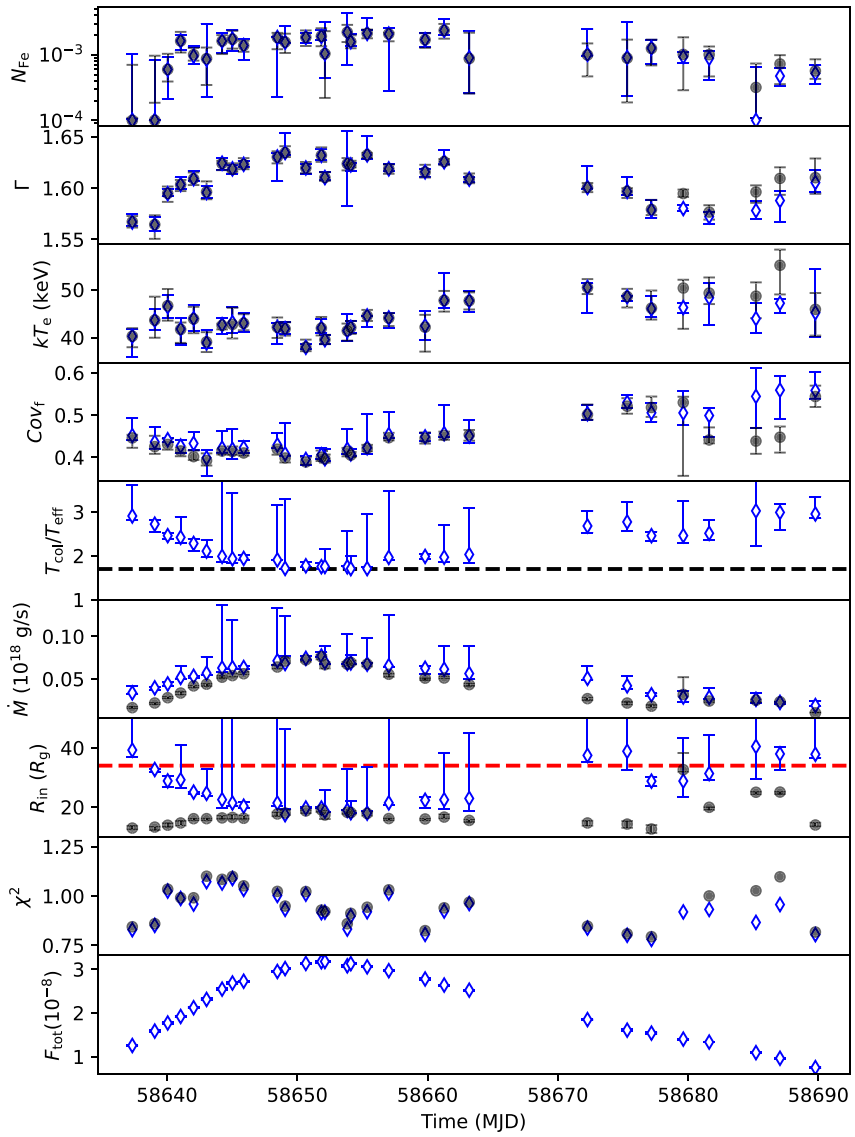


Figure 4. Spectral parameter evolution with the model *TBabs×(Gaussian+Gaussian + thcomp×kerrd)* with fixed $n_H = 0.86 \times 10^{22}$ cm^{-2}. The blue and black points are on behalf of a free harden factor T_{col}/T_{eff} and fixed harden factor $T_{col}/T_{eff} = 1.7$, respectively (shown in black dashed line). The red dashed line represents the $R_{in} = 34\ R_g$. The time range of stable R_{in} is consistent with the time range with the disc flux below $3.3 \pm 0.2 \times 10^{-9}$ erg cm^{-2} s^{-1} in Fig. 6.

the end of the reflare, there is an insignificant upward trend of the kT_e.

In Fig. 4, we show the fitting results from another model *TBabs×(Gaussian+Gaussian + thcomp×kerrd)*, where *kerrd* describes the thermal emission from the optically thick accretion disc around a Kerr BH (Laor 1991; Ebisawa et al. 2003); MAXI J1348−630 is a high-spin system with $a = 0.80 \pm 0.02$ (Kumar et al. 2022). We fix the disc-inclination angle at 36.5°, the mass of the central object at 8.7 ± 0.3 M$_\odot$ (Kumar et al. 2022), and the distance at 2.2 kpc (Chauhan et al. 2021). Firstly, we fix the spectral hardening factor, T_{col}/T_{eff} at 1.7 for a typical accretion disc with high values of the accretion rate and low values of the viscosity parameter (Shimura & Takahara 1995; Ebisawa et al. 2003), where T_{eff} is the effective temperature of the accretion disc and the T_{col} is the colour temperature of the accretion disc. Because of the Comptonization in the disc atmosphere, the colour temperature of the local emission becomes higher than the effective temperature. And we left the inner radius R_{in} and mass accretion rate $\dot{M}$ as free parameters during the fittings. The parameters are shown in Fig. 4 with black points. N_{Fe}, Γ, kT_e, and Cov_f follow similar trends and values as in the previous model. R_{in} follows a similar trend as N_{disc} when the accretion rate increases, moving outward from ∼10 R_g to ∼17 R_g. Considering that the change of T_{col}/T_{eff} itself may affect the evolutionary trend and measurements of R_{in}, we further set T_{col}/T_{eff} free to change and plot the results in Fig. 4 with blue points. We found that the values of $\dot{M}$ are higher, but the evolutionary trend is unchanged. The estimates of

Downloaded from https://academic.oup.com/mnras/article/521/2/2692/7074565 by guest on 06 February 2025

Manuscript 1

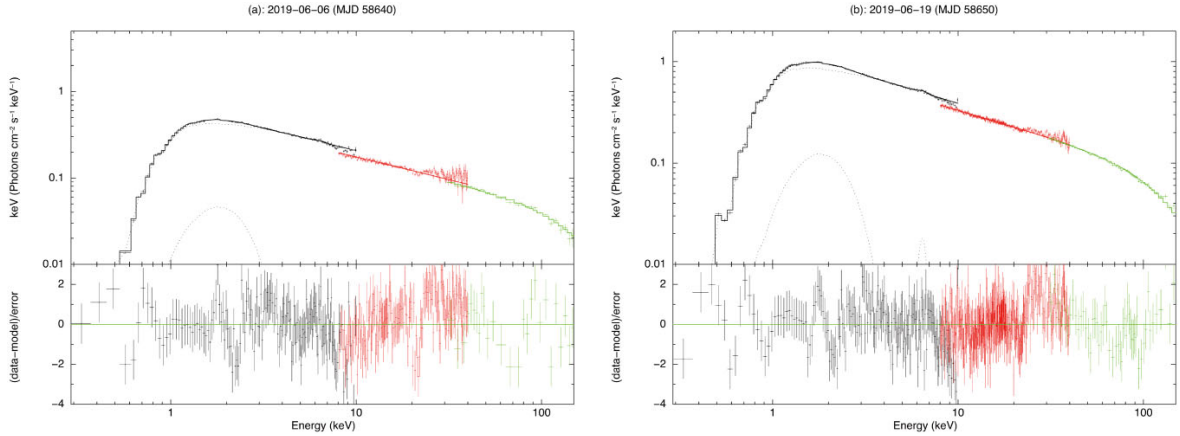


Figure 5. (a) Presents the spectrum on MJD 58 640 with the model *TBabs×(Gaussian+Gaussian + thcomp×kerrd)* with the fixed $n_{\rm H} = 0.86 \times 10^{22}$ cm^{-2} and free harden factor, respectively. (b) Presents the spectrum on MJD 58 650 from *Insight-HXMT* with the model *TBabs×(Gaussian+Gaussian + thcomp×kerrd)* with the fixed $n_{\rm H} = 0.86 \times 10^{22}$ cm^{-2} and free harden factor, respectively. The black, red, and green points mark the spectrum of *NICER* (0.3–10 keV), *ME* (8–40 keV), and *HE* (30–150) keV.

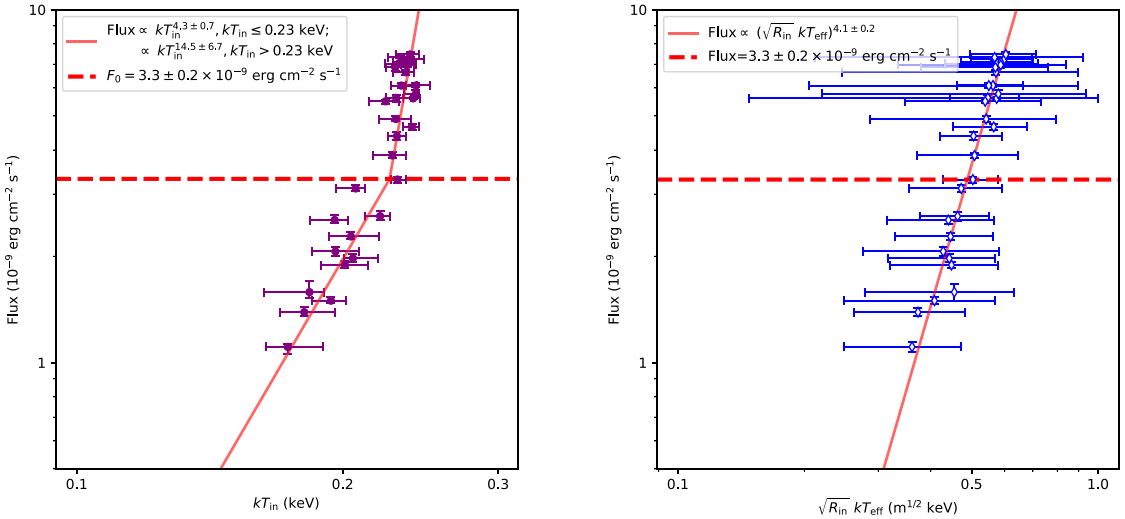


Figure 6. Left-hand panel: Evolution of unabsorbed disc flux with disc temperature. The unabsorbed disc flux is obtained from the cflux model calculated between 0.1 and 150 keV. We use a broken power-law model to fit the data. And we find that the points follow the $F \propto kT_{\rm in}^{4.3\pm0.7}$ (the fluxes obey the $kT_{\rm in}^4$ law assuming $R_{\rm in}$ is not change) when the $kT_{\rm in} \le 0.23$ (the flux below $3.3 \pm 0.2 \times 10^{-9}$ erg cm^{-2} s^{-1}). While, when $kT_{\rm in} > 0.23$, the fluxes do not obey the $kT_{\rm in}^4$ law. Right-hand panel: Evolution of unabsorbed disc flux with $\sqrt{R_{\rm in}}\, kT_{\rm eff}$. The $kT_{\rm eff}$ is $kT_{\rm in}/f_{\rm colour}$, where the hardening factor $f_{\rm colour} = T_{\rm col}/T_{\rm eff}$ and the inner radius $R_{\rm in}$ are get from the *kerrd* model. After taking into account changes in $R_{\rm in}$ and hardening factor, all points complied with the $F \propto R_{\rm in}^2\, T_{\rm eff}^4$.

$T_{\rm col}/T_{\rm eff}$ and $R_{\rm in}$ are greatly different from those before. The $R_{\rm in}$ stays stable at ∼34 $R_{\rm g}$ in the low-flux level from MJD 58670, while the $R_{\rm in}$ goes inward to ∼17 $R_{\rm g}$ near the reflare peak. And the values of $T_{\rm col}/T_{\rm eff}$ also show a significant deviation, except around the reflare peak; $T_{\rm col}/T_{\rm eff}$ decreases from 3 to 1.7 to reach again ∼3 at the end of reflare.

Figs 5(a) and (b) show the fitting results at the peak flux (on MJD 58650) with the model *TBabs×(Gaussian+Gaussian + thcomp×diskbb)* and *TBabs×(Gaussian+Gaussian + thcomp×kerrd)*, respectively. For spectral fitting with the fixed $n_{\rm H}$, fitting errors χ^2 are constrained in compatible values ∼ 1.2. The additional dips ∼ 0.56 keV and ∼ 0.87 keV are caused by known features of *NICER* around the O-K edge and the Ne-K edge. The peak at ∼ 1.84 keV is due to the Si-K edge. These systematic features are more visible only in few observations where the count rate is relatively high and do not affect the measurement results of the continuum components.

We further investigate the relationship between the disc flux and the inner disc colour temperature ($kT_{\rm in}$) during the reflare, as shown in the left-hand panel of Fig. 6. We use the orthogonal distance regression in the scipy.odr package in result fitting (https://docs.scipy.org/doc/scipy/reference/odr.html). The disc flux is obtained from the integral of *DISKBB* in 0.1–150 keV. For fitting these relations, we use the relation flux $\propto kT_{\rm in}^{\alpha}$ to measure whether the inner radius of the disc has changed during the reflare. Obviously, we find that it is not possible to describe all observations with one power-law

Downloaded from https://academic.oup.com/mnras/article/521/2/2692/7074565 by guest on 06 February 2025

Manuscript 1

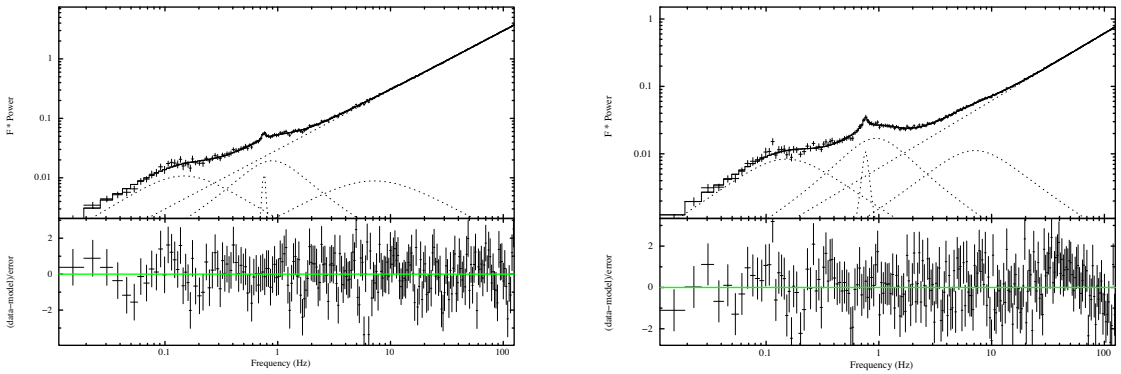


Figure 7. PDS fitting results for *ME* (right-hand panel: 10–30 keV) and *HE* (left-hand panel: 25–80 keV). Here, we just choose a PDS on MJD 58 657 with a relatively high confidence level, which shows the noise and QPO components clearly.

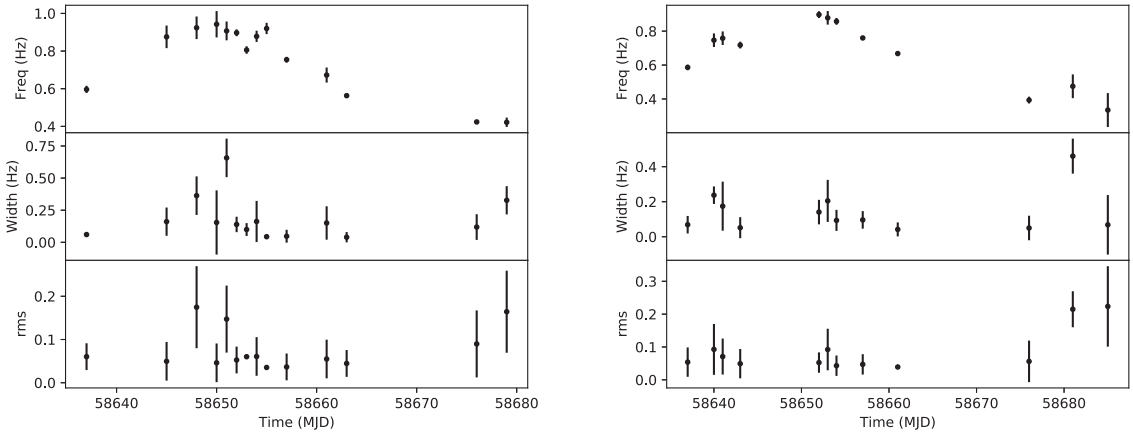


Figure 8. C-QPO frequency, width, and RMS as a function of time for *ME* (10–30 keV) and *HE* (25–80 keV).

function. And then, we try to use a broken power-law model to fit all points. We find the parameter α deviates far from 4 when the flux above $3.3 \pm 0.2 \times 10^{-9}$ erg cm^{-2} s^{-1} and the disc temperature >0.23 keV. Below this flux, we find the remaining points follow flux $\propto kT_{\rm in}^{4.3\pm0.7}$ well. We also give an unabsorbed X-ray luminosity of $\sim 2.5 \times 10^{36}$ (D/2.2 kpc)^2 erg s^{-1}. Deviating from this relationship means that the $R_{\rm in}$ and hardening factor change significantly along the flux. Therefore, using the fitting results of $R_{\rm in}$ and hardening factor $f_{\rm colour} = T_{\rm col}/T_{\rm eff}$ from the *kerrd* model, we can study the relation of the disc flux and the $R_{\rm in}^2 T_{\rm eff}^4$, where $T_{\rm eff} = T_{\rm in}/f_{\rm col}$ is the effective disc temperature. In the right-hand panel of Fig. 6, we find all points follow the flux $\propto (\sqrt{R_{\rm in}} T_{\rm eff})^{4.1\pm0.2}$, which is consistent with the blackbody emission from the inner region of the accretion disc.

3.3 Timing analysis

We study the fast X-ray variability in different energy bands and produce the PDS for each observation used for spectral analysis. The PDS is applied to Miyamoto normalization. Observations in MJD 58657, 3-d after the peak flux are shown in Fig. 7. It shows the noise and QPO components clearly with a relatively high confidence level. We use multiple Lorentzian components to fit the PDS, where one component can fit a type-C QPO with a quality factor (Q ≡ QPO's central frequency/full width at half-maximum) above 2. We take into account the white noise in the PDS and model it by a power-law component with zero indexes.

Based on the data quality, only the combined observations consisting of multiple *Insight-HXMT* exposures provided clearer PDS results. Meanwhile, only a few observations displayed obvious QPO structures. We obtained the QPO frequency, and the QPO width, and calculated the QPO fractional RMS throughout the reflare. Fig. 8 shows the evolution of these three parameters with time in the *ME* (10–30 keV) and *HE* (25–80 keV) energy bands. As for *Insight-HXMT*, the *ME*, and *HE* energy band offers much more photon counts than the *LE* energy band, and considering the limited number of QPOs we find at the same time, we ignore the related evolution in the *LE* energy band. Also, we note that the QPOs in *NICER* were reported in Alabarta et al. (2022). In Fig. 8, although the number of QPOs is limited, the QPO frequency evolution with the flux is evident. The type-C QPO has increased from ∼0.4 Hz, at the beginning and end of the reflare, to 0.9 Hz at the reflare peak. And the QPO width and the QPO RMS do not vary with flux. Except for some large error intervals due to low statistical observations, the RMS nearly contains all values within 5 per cent in the *ME* and the *HE* band, which is lower than RMS ∼15 per cent–20 per cent in the (2.5–5.0)-keV energy range in Alabarta et al. (2022). Hence, our results show that the QPO RMS decreases to a lower value and then remains stable in the higher energy band.

Downloaded from https://academic.oup.com/mnras/article/521/2/2692/7074565 by guest on 06 February 2025

Manuscript 1

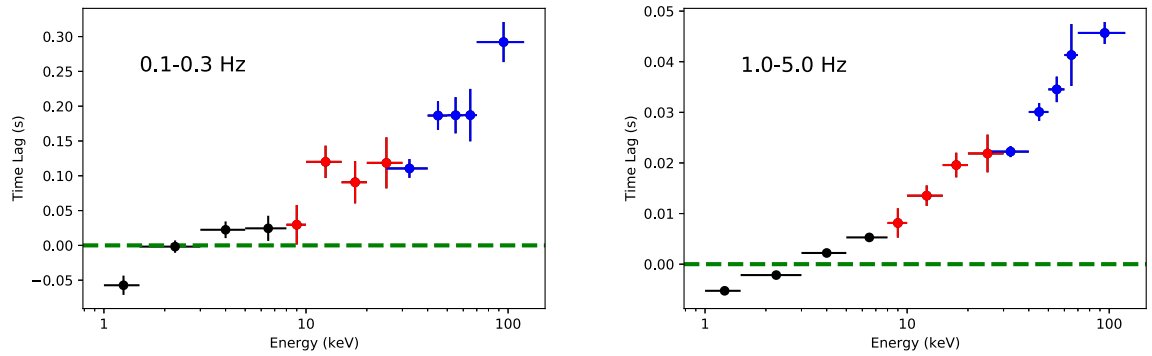


Figure 9. Time lags in different energy bands (reference energy band 1–10 keV): black for *LE* (1.0–1.5, 1.5–3.0, 3.0–5.0, and 5.0–8.0 keV), red for *ME* (8.0–10.0, 10.0–15.0, 15.0–20.0, and 20.0–30.0 keV), and blue for *HE* (25.0–40.0, 40.0–50.0, 50.0–60.0, 60.0–70.0, and 70.0–120.0 keV) in the disparate frequency range from *HXMT* observations on MJD 58657. Left-hand panel: 0.1–0.3 Hz; right-hand panel: 1.0–5.0 Hz.

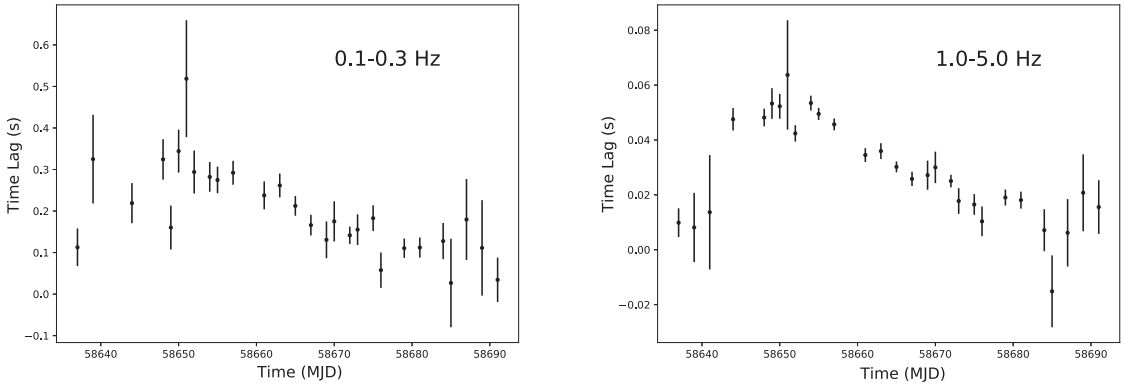


Figure 10. Time lag evolution in high-energy band 70.0–120.0 keV for two frequency ranges. Left-hand panel: 0.1–0.3 Hz; right-hand panel: 1.0–5.0 Hz.

We also study the energy-dependent time lags in two different frequency ranges (0.1–0.3 Hz and 1.0–5.0 Hz, respectively, away from the QPO frequency), from 1.0 to 120 keV with respect to the (1.0–10.0)-keV band (reference band). Results are shown in Fig. 9. The black points, red points, and blue points correspond to *LE* (1.0–1.5, 1.5–3.0, 3.0–5.0, and 5.0–8.0 keV), *ME* (8.0–10.0, 10.0–15.0, 15.0–20.0, and 20.0–30.0 keV), and *HE* (25.0–40.0, 40.0–50.0, 50.0–60.0, 60.0–70.0, and 70.0–120.0 keV), respectively (see again Fig. 9). A hard lag (hard photons delay soft photons) occurs, and the time lags increase with the energy band. In 0.1–0.3 Hz, the time lag in the high-energy band between 70 and 120 keV is $\sim$0.29 s, and the time lag in 1.0–5.0 Hz between 70 and 120 keV is $\sim$0.05 s.

Time lags are also time-dependent. The evolution of time lags in 70–120 keV with the largest time lag, is shown in Fig. 10. When frequency is lower or higher than QPO frequency (i.e. 0.1–0.3 Hz and 1.0–5.0 Hz), the evolution of time lags is not affected by QPO components. As seen in left- and right-hand panels of Fig. 10, in 0.1–0.3 Hz, along with increasing flux, the time lags increase from 0.1 to 0.4 s. Also, compared with low frequency, we find that the time lags at 1.0–5.0 Hz evolve from 0 to 0.06 s. Here, we notice that although different frequency ranges are selected, the phase delays are similar. So this suggests that the physical reason for this delay at different time-scales could be same.

For further analysis, in Fig. 11, we show the evolution of the break frequency or characteristic frequency for the different noise components in Fig. 7. The left- and right-hand panels show the lowest characteristic frequency (low-frequency break) and highest characteristic frequency (high-frequency break) in the high-energy band (25–80 keV), respectively. We find that the high-energy band shows pronounced evolutionary trends, i.e. the characteristic frequency increases as the flux increases, and we also find that the characteristic frequency of the high-frequency noise has the same evolutionary trend as the low-frequency noise.

4 DISCUSSION

4.1 Spectrum evolution

In this paper, we focus on the first reflare after the main outburst of the LM-BHXRB MAXI J1348−630 in 2019, and in particular on the spectral and timing evolution throughout the reflare. This is the first time that the reflare properties are studied in a broad energy band (0.3–150 keV) by joint *NICER* and *Insight-HXMT* observations.

In all our observations, thermal emission from an accretion disc is required by the fitting residual observed using a non-thermal model only. When the non-thermal component dominates, the scattering of soft photons in the corona dominates. To avoid underestimating the soft photons from the disc, we use the convolution model *thcomp* to fit the non-thermal components and their internal scattering processes. In Fig. 3, the column density $n_{\rm H}$ stays at $\sim 0.86 \times 10^{22}$ cm^{-2} during the reflare, except for some observations around the peak.

Downloaded from https://academic.oup.com/mnras/article/521/2/2692/7074565 by guest on 06 February 2025

Manuscript 1

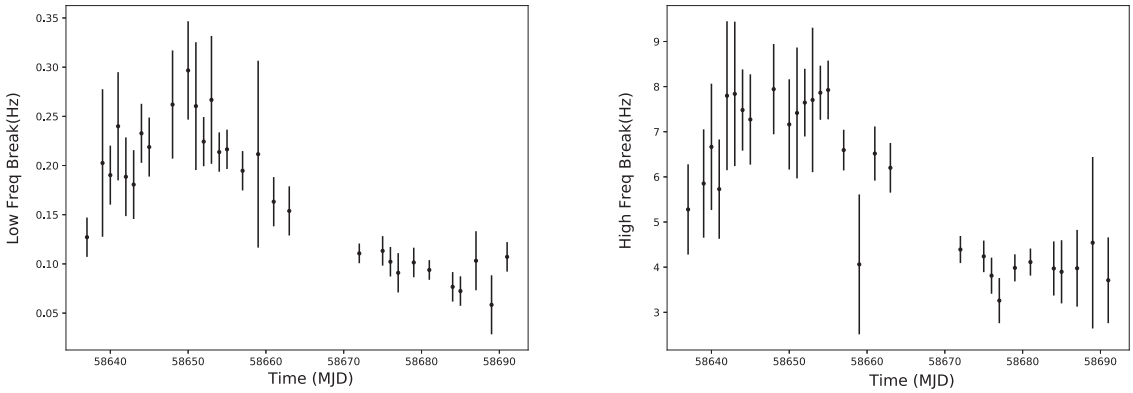


Figure 11. Left- and right-hand panels present the evolution of the low-frequency break in high energy and high-frequency break in high energy, respectively.

Considering that the residual below 2.1 keV from *NICER*, can be affected by the high flux changing apparently the absorption parameter $n_{\rm H}$, we fix its value to that of $n_{\rm H}$ during the SS estimated by *Swift*/XRT (Tominaga et al. 2020), and the average $n_{\rm H}$ during the whole main outburst (Zhang et al. 2022). We note that the $N_{\rm disc}$ is correlated with the $kT_{\rm in}$, while the cover factor $Cov_{\rm f}$ shows slight anticorrelation with flux. The $N_{\rm disc}$ trend indicates that the inner radius of the accretion disc recedes as the accretion rate increases, which is clearly inconsistent with the expected evolution of the canonical accretion disc: The inner radius should become smaller, or keep stable at the ISCO when the accretion rate increases. We note that such a peculiar trend was also reported in Zhang et al. (2020b), who used only *NICER* observations. Through the joint analysis of *NICER* and *Insight-HXMT*, we find that this trend is not due to the narrow energy band used for the fitting. Meanwhile, in Zhang et al. (2022), an outward trend of the inner radius was also found during the HS of the main outburst of MAXI J1348−630, even using self-consistent Comptonization models, which take into account the upscattering of photons from the disc emission into the corona region. They suggested that at the beginning of the outburst, the hardening factor for the inner disc emission could be larger than the canonical value ∼1.7 of the standard disc (Shimura & Takahara 1993; Shafee et al. 2006). Dunn et al. (2011) found that the hardening factors can reach a value as high as ∼3 in the initial phase of an outburst, which can be used to explain the anomalously low values of $R_{\rm in}$ in some BH transients. We suggest that the same process occurs in the reflare; the detected trend of increasing $N_{\rm disc}$ is caused by the hardening factor deviating far from 1.7 from a sufficiently high effective optical thickness of the standard Shakura–Sunyaev disc (Shakura & Sunyaev 1973). We note that MAXI J1348−630 is a Kerr BH because of its high spin parameter $a = 0.8$–0.998 (Jia et al. 2022; Kumar et al. 2022). So, we replace the *DISKBB* model with *kerrd* model which describes the thermal emission from the optically thick accretion disc around a Kerr BH. The model incorporates the spectral hardening factor, $T_{\rm col}/T_{\rm eff}$ and $R_{\rm in}$ for a given distance (fixed at 2.2 kpc), inclination angle (fixed at 36.5°), and BH mass (fixed at 8.7 $M_{\odot}$). In Fig. 4, if we fix the $T_{\rm col}/T_{\rm eff}$ at 1.7, we get the $R_{\rm in}$ increase as the accretion rate becomes larger, which is similar to the trend of $N_{\rm disc}$ in Fig. 3. If we free $T_{\rm col}/T_{\rm eff}$, the evolutionary trend of $R_{\rm in}$ changes significantly. The $R_{\rm in}$ decreases from 34 $R_{\rm g}$ to 17 $R_{\rm g}$ with the increasing accretion rate within MJD 58637−58673, while at a lower accretion rate the increased accretion rate does not lead to a significant change of $R_{\rm in}$ and it stays at 34 $R_{\rm g}$. The $R_{\rm in}$ estimated from the *kerrd* model is similar to the $R_{\rm in}$ estimated from the reflection model (Kumar et al. 2022). As discussed earlier, the change in $R_{\rm in}$ is due to the evolution of the $T_{\rm col}/T_{\rm eff}$ from ∼3 to ∼1.7, and similar to the $R_{\rm in}$, there is a clear decline for the $T_{\rm col}/T_{\rm eff}$ only in MJD 58640−59673, while it is stable at ∼3 at other times.

In Fig. 6, we plot the variation in the disc flux with the disc temperature $kT_{\rm in}$, and we also plot the disc flux with $\sqrt{R_{\rm in}}kT_{\rm eff}$. In the left-hand panel, we find that the overall evolutionary trend is not consistent with the flux $\propto kT_{\rm in}^4$. However, the points below the red dashed line can be fitted by flux $\propto kT_{\rm in}^{4.3\pm0.7}$. For observations with flux above $3.3 \pm 0.2 \times 10^{-9}$ erg cm^{-2} s^{-1}, as disc flux increases, the $kT_{\rm in}$ stays nearly stable at 0.23 keV. Based on these results, we find that for observations with low fluxes (flux below the red dashed line in Fig. 6), the disc does not change significantly. In the right-hand panel, we consider the effect of the hardening factor (colour correction factor) $f_{\rm colour} = T_{\rm col}/T_{\rm eff}$ on disc temperature and the evolution of the inner radius $R_{\rm in}$. So, it shows the true physical temperature versus flux evolution of the accretion disc, following the flux $\propto R_{\rm in}^2 T_{\rm eff}^4$. In Fig. 4, we note that the purple points in the left-hand panel of Fig. 6 correspond to observations where the hardening factor is stable at ∼3 and the inner radius is stable at 34 $R_{\rm g}$.

From the spectral analysis, we find that the evolution of the inner radius of the accretion disc with the accretion rate is not a continuously decreasing process, but can be divided into two different regions according to a critical luminosity $L_{\rm crit}$. In the region below the $L_{\rm crit}$, the inner radius of the disc does not change significantly and is truncated at a relatively far distance from the BH. In the region above the $L_{\rm crit}$, on the other hand, the disc evolves with the usual expected HS, with the inner radius gradually approaching the $R_{\rm ISCO}$ as the accretion rate increases. The studied reflare only goes through a HS. Therefore, although the inner disc moves inward, it does not reach the ISCO. From the luminosity of the source at the red dashed line in Fig. 6, this characteristic luminosity can be obtained as $L_{\rm crit} \sim 2.5 \times 10^{36}$ erg s^{-1} $\approx 0.002\,L_{\rm Edd}$ (calculated in 1–10 keV), and the $L_{\rm Edd} = 1.3 \times 10^{38}(M/{\rm M}_{\odot})$ erg s^{-1}, where $M = 8.7$ $M_{\odot}$. In Shakura & Sunyaev (1973), from the standard disc solution, the hardening factor $f \sim (\alpha^{es}/\alpha^{ff})^{1/8} \propto n_{\rm e}^{-1/8}$, where $\alpha^{\rm es}$ is the electron-scattering coefficient, $\alpha^{\rm ff}$ is the free–free absorption coefficient, and $n_{\rm e}$ is the electron density. During the reflare, except for the peak with $f \sim 1.7$ which is the same as the characteristic value of a standard disc, in most observations the inner region of the accretion disc might still be in a non-equilibrium state, i.e. it is still in the process of condensing from the hot corona (Liu et al. 2007; Taam et al. 2008; Meyer-Hofmeister et al. 2009; Liu, Done & Taam 2011; Qiao & Liu 2017). Combined with Figs 4 and 6, we speculate that,

Downloaded from https://academic.oup.com/mnras/article/521/2/2692/7074565 by guest on 06 February 2025

Manuscript 1

for the luminosity above the $L_{\rm crit}$, the cooling of the corona becomes more dominant, and the inner disc gradually becomes a standard disc; for the luminosity below the $L_{\rm crit}$, the evaporation process of the disc might be more dominant, resulting in the inability of the accretion material in the inner region of the disc to form an effective inner flow of material and transfer the angular momentum outward. The hardening factor f can also be determined by the Comptonization in the corona near or covering the accretion disc (Shimura & Takahara 1993), and such process can be described by the cover factor $Cov_{\rm f}$ in the *thcomp* model.

In Fig. 4, at the end of the reflare, we find that the $Covf_{\rm f}$ recovers simultaneously with the f. This suggests that there is indeed a connection between the cover factor and hardening factor, but $Cov_{\rm f}$ is clearly not the only reason affecting the f, since $Cov_{\rm f}$ begins at a lower value, suggesting that f is also influenced by other factors.

4.2 QPO evolution

In Fig. 8, we firstly show the type-C QPO evolution in the higher energy band during a reflare. The frequencies of the QPO are consistent with the *NICER* observations (Alabarta et al. 2022). Compared to their results (fig. 9 in Alabarta et al. 2022), our results show that the QPO RMS keeps at $\sim$5 per cent, and it does not evolve significantly with energy and flux above 10 keV. Combined with the *NICER* results in Alabarta et al. (2022), we find that the shape of the QPO RMS spectrum evolves during the reflare. In Alabarta et al. (2022), for higher flux observations, the RMS spectrum increased with energy below 2.5 keV and stayed at the maximum value $\sim$10 per cent$-$15 per cent between 2.5 and 7 keV. Then we find that it decreases to 5 per cent above 7 keV. For lower flux observations, the RMS spectrum stabilized at $\sim$20 per cent below 7 keV and decreased sharply to 5 per cent above 7 keV. The trends above 2.5 keV are similar to the results of the failed-transition outburst of H 1743$-$322 (Wang et al. 2022) and the first outburst of MAXI J1820+070 (Ma et al. 2021). These findings suggest that the trend is typical for sources that have been in an HS for a long time during an outburst. While the trends below the 2.5 keV were similar to the trends below 10 keV of the IMS of the canonical BH outburst.

For the shape of QPO's RMS with energy, we speculate that it is determined by two aspects: On the one hand, it is related to the flux ratio of the spectrum components contributing RMS to the total energy spectrum at different energy bands, and on the other hand, it is determined by the intrinsic properties of QPO itself (Gierliński & Zdziarski 2005; Sobolewska & Życki 2006; Kong et al. 2020; Shui et al. 2021). If the QPO originates from the L-T precession of the corona, disc does not contribute to the QPO RMS (Kong et al. 2020). Based on the above description, we can interpret the QPO RMS spectrum. Firstly, for energies above 2.5 keV, the flux ratio of the non-thermal component to the total energy spectrum does not change with energy because the flux of the disc is weak, and the geometric properties of the corona determine the RMS size. For non-thermal radiation, we assume that the high-energy photons arise from the inner region of the corona, while the low-energy photons arise from the outer region of the corona. If the geometry of the corona is considered to be more similar to the flat shape of a disc in the outer region, and a more spherical shape in the inner region, then the projection effect is larger in the outer region, which would naturally explain the observed QPO RMS spectra. We also note that the higher energy band of RMS spectra could also originate from the small-scale jets procession (Ma et al. 2021), so a low-speed stable jet could also explain the high-energy part of the RMS energy spectrum. Secondly, for energies below 2.5 keV, the QPO RMS decreases with higher flux. Because the inner radius of the inward accretion disc can contribute to a higher disc flux and disc temperature, the flux ratio of the non-thermal component to total spectral will decrease in the low-energy band, hence lowering the QPO RMS. For low flux, the far truncated non-standard disc dominated by the evaporation allowed the QPO RMS to be dominated by the corona in all energy bands.

4.3 Noise evolution

Further analyses of the noise time lag among high-energy photons (70–120 keV) with reference to low-energy photons (1–10 keV) in the low- and high-frequency ranges are shown in Fig. 10. For low- and high-frequency ranges, the hard lag evolution shows significant evolution between MJD 58 640 and MJD 58670. We find that this time range corresponds exactly to period of $R_{\rm in}$ evolution in Fig. 4, when the inner radius of the disc moves significantly inward. For the rest of the time, the hard lag remains stable. Therefore, the hard lag reflects the Compton upscattering process of low-energy photons in the corona. For low-flux range, the small delay might indicate that both low- and high-energy photons experience sufficient Compton scattering before they leave the corona, which is consistent with the high coverage in Fig. 4. Also, if the disc is considered to deviate from the standard disc in low flux, the small delay indicates that photons radiating from inside the disc or corona are difficult to distinguish. In contrast, for the high-flux range, a low-coverage corona with a cooling-/condensing-dominated standard optical thick disc will be able to effectively distinguish between photons from the disc or the corona, producing a significant hard delay. At this point, the larger hard delay with increasing flux may indicate that more scattering time is required for the photons to scatter from low energy (1–10 keV) to high energy (70–120 keV), which may be related to the effective cooling of the corona by the disc. This is consistent with the results in Fig. 4 where the electron temperature is lower at high accretion rates.

The low- and high-characteristic frequencies of two noise components are shown in Fig. 11. We find that, similar to the time lag in Fig. 10, the characteristic frequencies can also be divided into two different regions because the characteristic low-frequency break can be associated with the viscous time-scale ($t_{\rm visc}$) at the truncation radius of the accretion disc (Done et al. 2007; Husain, Misra & Sen 2022). Meanwhile, the $t_{\rm visc} \propto R_{\rm in}^{3/2}$, so the constant viscous time-scale means that $R_{\rm in}$ does not change. The characteristic high-frequency break might be associated with the dynamical time-scale (t_ϕ) at the truncation radius. Because of $t_\phi \sim \alpha(H/R)^2 t_{\rm visc}$, in Fig. 11 the right-hand panel also shows a similar trend to the left-hand panel.

5 CONCLUSIONS

In this paper, we discussed the spectral and timing characteristics of the LM-BHXRB MAXI J1348$-$630 during its second outburst, or reflare. Our results support the existence of a characteristic luminosity, $L_{\rm crit} \sim 0.002\,L_{\rm Edd}$ that makes the inner radius of the disc exhibit different properties as the accretion rate increases. The inner radius of the disc far from the BH is kept constant below the $L_{\rm crit}$, which might be related to the dominant evaporation process in the accretion disc. When the condensing process dominates above the $L_{\rm crit}$, the disc formation will be very effective, and angular momentum transfer can occur. Further confirmation for this scenario requires future X-ray telescopes with large areas and high sensitivity at both

Downloaded from https://academic.oup.com/mnras/article/521/2/2692/7074565 by guest on 06 February 2025

Manuscript 1

low- and high-energy bands simultaneously, such as the enhanced X-ray Timing and Polarimetry mission (eXTP).

ACKNOWLEDGEMENTS

This work is supported by the National Key R&D Program of China (2021YFA0718500), the National Natural Science Foundation of China under Grant No. U1838201, U2038102, and Guangdong Major Project of Basic and Applied Basic Research (Grant No. 2019B030302001). This work was partially supported by International Partnership Program of Chinese Academy of Sciences (Grant No. 113111KYSB20190020). This work is supported by China Scholarship Council (CSC) at Eberhard Karls Universität of Tübingen.

DATA AVAILABILITY

This work made use of data from the *Insight-HXMT* mission (http://hxmtweb.ihep.ac.cn/), a project funded by China National Space Administration (CNSA) and the Chinese Academy of Sciences (CAS). The data of *NICER* were obtained through the High Energy Astrophysics Science Archive Research Center (HEASARC, https://heasarc.gsfc.nasa.gov/).

REFERENCES

Abramowicz M. A., Chen X., Kato S., Lasota J.-P., Regev O., 1995, ApJ, 438, L37
Alabarta K., Méndez M., García F., Peirano V., Altamirano D., Zhang L., Karpouzas K., 2022, MNRAS, 514, 2839
Arnaud K. A., 1996, in Jacoby G. H., Barnes J., eds, ASP Conf. Ser. Vol. 101, Astronomical Data Analysis Software and Systems V. Astron. Soc. Pac., San Francisco, p. 17
Bachetti M. et al., 2022, StingraySoftware/stingray: v1.0-beta. Zenodo. https://doi.org/10.5281/zenodo.6290078
Belloni T. M., 2010, in Belloni T., ed., The Jet Paradigm, Lecture Notes in Physics, Vol. 794. Springer, Berlin, p. 53
Belloni T., Klein-Wolt M., Méndez M., van der Klis M., van Paradijs J., 2000, A&A, 355, 271
Belloni T. M., Motta S. E., Muñoz-Darias T., 2011, Bull. Astron. Soc. India, 39, 409
Cangemi F., Rodriguez J., Belloni T., Clavel M., Grinberg V., 2019, Astron. Telegram, 12457, 1
Cao X. et al., 2020, Sci. Chin. Phys. Mech. Astron., 63, 249504
Carotenuto F. et al., 2021a, MNRAS, 504, 444
Carotenuto F. et al., 2021b, MNRAS, 505, L58
Chauhan J. et al., 2021, MNRAS, 501, L60
Chen Y. P. et al., 2019, Astron. Telegram, 12470, 1
Chen Y. et al., 2020, Sci. Chin. Phys. Mech. Astron., 63, 249505
Cúneo V. A. et al., 2020, MNRAS, 496, 1001
D'Elia V., Lien A. Y., Page K. L., 2019, GCN Circ., 23795, 1
Denisenko D. et al., 2019, Astron. Telegram, 12430, 1
Done C., Gierliński M., Kubota A., 2007, A&AR, 15, 1
Dunn R. J. H., Fender R. P., Körding E. G., Belloni T., Merloni A., 2011, MNRAS, 411, 337
Ebisawa K., Życki P., Kubota A., Mizuno T., Watarai K.-y., 2003, ApJ, 597, 780
Esin A. A., McClintock J. E., Narayan R., 1997, ApJ, 489, 865
Fabian A. C., 2016, Astron. Nach., 337, 375
Gierliński M., Zdziarski A. A., 2005, MNRAS, 363, 1349
Gilfanov M., 2010, in Belloni T., ed., The Jet Paradigm, Lecture Notes in Physics, Vol. 794. Springer, Berlin, p. 17
Guo C.-C. et al., 2020, J. High Energy Astrophys., 27, 44
Homan J., Belloni T., 2005, Ap&SS, 300, 107
Huppenkothen D. et al., 2019a, J. Open Source Softw., 4, 1393
Huppenkothen D. et al., 2019b, ApJ, 881, 39
Husain N., Misra R., Sen S., 2022, MNRAS, 510, 4040
Ingram A., Done C., Fragile P. C., 2009, MNRAS, 397, L101
Jia N. et al., 2022, MNRAS, 511, 3125
Kaastra J. S., Bleeker J. A. M., 2016, A&A, 587, A151
Kara E. et al., 2019, Nature, 565, 198
Kawaguchi T., 2003, ApJ, 593, 69
Kong L. D. et al., 2020, J. High Energy Astrophys., 25, 29
Kumar R., Bhattacharyya S., Bhatt N., Misra R., 2022, MNRAS, 513, 4869
Lamer G., Schwope A. D., Predehl P., Traulsen I., Wilms J., Freyberg M., 2021, A&A, 647, A7
Laor A., 1991, ApJ, 376, 90
Lepingwell A. V. et al., 2019, Astron. Telegram, 12441, 1
Liang E. P., Nolan P. L., 1984, Space Sci. Rev., 38, 353
Liao J.-Y. et al., 2020a, J. High Energy Astrophys., 27, 24
Liao J.-Y. et al., 2020b, J. High Energy Astrophys., 27, 14
Liu B. F., Taam R. E., Meyer-Hofmeister E., Meyer F., 2007, ApJ, 671, 695
Liu B. F., Done C., Taam R. E., 2011, ApJ, 726, 10
Liu C. et al., 2020, Sci. Chin. Phys. Mech. Astron., 63, 249503
Ma X. et al., 2021, Nature Astron., 5, 94
Meyer-Hofmeister E., Liu B. F., Meyer F., 2009, A&A, 508, 329
Motta S., Belloni T., Homan J., 2009, MNRAS, 400, 1603
Narayan R., Yi I., 1995, ApJ, 452, 710
Negoro H. et al., 2020, Astron. Telegram, 13994, 1
Patruno A., Maitra D., Curran P. A., D'Angelo C., Fridriksson J. K., Russell D. M., Middleton M., Wijnands R., 2016, ApJ, 817, 100
Ponti G., Fender R. P., Begelman M. C., Dunn R. J. H., Neilsen J., Coriat M., 2012, MNRAS, 422, L11
Qiao E., Liu B. F., 2017, MNRAS, 467, 898
Reig P., 2011, Ap&SS, 332, 1
Remillard R. A., McClintock J. E., 2006, ARA&A, 44, 49
Russell T., Anderson G., Miller-Jones J., Degenaar N., Eijnden J. v. d., Sivakoff G. R., Tetarenko A., 2019, Astron. Telegram, 12456, 1
Sanna A. et al., 2019, Astron. Telegram, 12447, 1
Shafee R., McClintock J. E., Narayan R., Davis S. W., Li L.-X., Remillard R. A., 2006, ApJ, 636, L113
Shakura N. I., Sunyaev R. A., 1973, A&A, 24, 337
Shimura T., Takahara F., 1993, ApJ, 419, 78
Shimura T., Takahara F., 1995, ApJ, 445, 780
Shui Q. C. et al., 2021, MNRAS, 508, 287
Sobolewska M. A., Życki P. T., 2006, MNRAS, 370, 405
Sunyaev R. A., Titarchuk L. G., 1980, A&A, 86, 121
Sunyaev R. A., Titarchuk L. G., 1985, A&A, 143, 374
Taam R. E., Liu B. F., Meyer F., Meyer-Hofmeister E., 2008, ApJ, 688, 527
Titarchuk L., 1994, ApJ, 434, 570
Tominaga M. et al., 2020, ApJ, 899, L20
Wang P. J. et al., 2022, MNRAS, 512, 4541
Wilms J., Allen A., McCray R., 2000, ApJ, 542, 914
Yan Z., Yu W., 2017, MNRAS, 470, 4298
Yatabe F. et al., 2019, Astron. Telegram, 12425, 1
You B. et al., 2021, Nat. Commun., 12, 1025
Zdziarski A. A., Johnson W. N., Magdziarz P., 1996, MNRAS, 283, 193
Zdziarski A. A., Szanecki M., Poutanen J., Gierliński M., Biernacki P., 2020a, MNRAS, 492, 5234
Zdziarski A. A., Szanecki M., Poutanen J., Gierliński M., Biernacki P., 2020b, MNRAS, 492, 5234
Zhang S., Lu F. J., Zhang S. N., Li T. P., 2014, Proc. SPIE Conf. Ser. Vol. 9144, Space Telescopes and Instrumentation 2014: Ultraviolet to Gamma Ray. SPIE, Bellingham, p. 914421
Zhang S.-N. et al., 2020a, Sci. Chin. Phys. Mech. Astron., 63, 249502
Zhang L. et al., 2020b, MNRAS, 499, 851
Zhang W. et al., 2022, ApJ, 927, 210

This paper has been typeset from a TEX/LATEX file prepared by the author.

Downloaded from https://academic.oup.com/mnras/article/521/2/2692/7074565 by guest on 06 February 2025

Manuscript 2

A&A, 692, A117 (2024)
https://doi.org/10.1051/0004-6361/202452132
© The Authors 2024

Astronomy & Astrophysics

Unveiling the rebrightening mechanism of GRS 1915+105: Insights from a change in the quasi-periodic oscillations and from a wind analysis

Xiaohang Dai[1,⋆], Lingda Kong[1,⋆], Long Ji[2], Menglei Zhou[1], Qingcang Shui[3,4], Pengju Wang[1], Shu Zhang[3], and Andrea Santangelo[1]

[1] Institut für Astronomie und Astrophysik, Kepler Center for Astro and Particle Physics, Eberhard Karls, Universität, Sand 1, D-72076 Tübingen, Germany
[2] School of Physics and Astronomy, Sun Yat-Sen University, Zhuhai 519082, China
[3] Key Laboratory for Particle Astrophysics, Institute of High Energy Physics, Chinese Academy of Sciences, 19B Yuquan Road, Beijing 100049, China
[4] University of Chinese Academy of Sciences, Chinese Academy of Sciences, Beijing 100049, China

Received 5 September 2024 / Accepted 30 October 2024

ABSTRACT

We report a significant rebrightening event in the microquasar GRS 1915+105 that was observed in July 2021 with NICER and NuSTAR. This event was characterized by quasi-periodic oscillations (QPOs) in the soft state, but is typically free of these oscillations. It was also marked by an increase in the disk wind ionization degree. By employing the Hilbert-Huang transform (HHT), we decomposed the stable low-frequency QPO from the light curves using data from NICER and NuSTAR. Our spectral analysis shows a weak change in the Fe XXV absorption lines and a strong change in the Fe XXV absorption edge with QPO phase. Other spectral parameters, including the photon index and the seed photon temperature, correlate positively with the QPO phase, but the electron temperature is inversely correlated. Based on our findings we propose that the observed QPOs were caused by magnetic activity and not by precession. The magnetic field drove a failed disk wind of high-ionization low-velocity material. These results support the accretion ejection instability model and provide deeper insights into the dynamics of accretion-ejection processes that are magnetized by a black hole.

Key words. accretion, accretion disks – stars: black holes – stars: winds, outflows

1. Introduction

The microquasar GRS 1915+105 (Castro-Tirado et al. 1992) is a well-studied black hole X-ray binary system (Rodriguez et al. 2008; Belloni et al. 2000; Fender & Belloni 2012). Its 26 years of extensive activity were characterized by frequent transitions between different spectral states and light-curve types, which sets this source apart from others. The extensive documentation of the behavior of this system has revealed phenomena such as low- and high-frequency quasi-periodic oscillations (QPOs) (Morgan et al. 1997; Zhang et al. 2020; Motta & Belloni 2024), jet ejections (Fuchs et al. 2003), and disk wind (Lee et al. 2002; Neilsen & Lee 2009). Therefore, it is key to understanding the interactions and connections between accretion disks, jets, and the disk wind, which are central themes in high-energy astrophysics (Mirabel & Rodríguez 1999; Klein-Wolt et al. 2002; Remillard & McClintock 2006; Done et al. 2007).

GRS 1915+105 underwent exponential decay from April to July in 2018 (MJD 58230−58330) and a linear decay between July 2018 and Jan. 2019 (MJD 58330−58500). It then entered a low X-ray state (Koljonen & Tomsick 2020; Koljonen & Hovatta 2021) while remaining radio bright (Motta et al. 2021). In July 2021, the system exhibited a notable soft rebrightening event, marking the second such rebrightening since 2018. This event was first detected by the Monitor of All-sky X-ray Image/Gas Slit Camera (MAXI/GSC) all-sky monitor, the Neutron Star Interior Composition Explorer (NICER), and AstroSat (Neilsen et al. 2021; Ravishankar et al. 2021), and it was later subjected to a detailed analysis using data from AstroSat, NICER, and Nuclear Spectroscopic Telescope Array (NuSTAR) (Athulya & Nandi 2023; Kong et al. 2024). This rebrightening is particularly intriguing because it included low-frequency quasi-periodic oscillations (LFQPOs) in the soft state, which are typically absent under these conditions (Belloni et al. 2000; Zhang et al. 2020). Additionally, there was a marked increase in the disk wind ionization (Ueda et al. 2009; Neilsen & Lee 2009; Ponti et al. 2012). Notably, Belloni et al. (2000) conducted a comprehensive analysis of the variability patterns in GRS 1915+105. The authors emphasized that QPOs are usually not observed in the soft state, which makes their appearance during this event particularly significant. Furthermore, Ueda et al. (2009) and Neilsen & Lee (2009) identified significant changes in the disk wind temperature that indicated a complex interaction between the accretion disk and wind dynamics. More recent studies used AstroSat observations and identified high-frequency QPOs (68−72 Hz) within the softer variability classes of GRS 1915+105. This adds further complexity to these oscillations (Majumder et al. 2022). Collectively, these observations offer a valuable opportunity to explore the mechanisms that drive the QPO generation and the dynamics of disk winds in this unique system.

⋆ Corresponding authors; dai@astro.uni-tuebingen.de, lingda.kong@mnf.uni-tuebingen.de

Open Access article, published by EDP Sciences, under the terms of the Creative Commons Attribution License (https://creativecommons.org/licenses/by/4.0), which permits unrestricted use, distribution, and reproduction in any medium, provided the original work is properly cited.
This article is published in open access under the Subscribe to Open model. Subscribe to A&A to support open access publication.

Manuscript 2

Previous studies have emphasized the critical role of magnetic fields in shaping the behavior of GRS 1915+105. Miller et al. (2006) explored the magnetic nature of disk accretion onto black holes. They highlighted its importance for understanding the associated magnetic process in an accretion disk. Similarly, Fender & Belloni (2004) proposed a unified model for black hole X-ray binary jets and underscored the role of magnetic fields and their interactions with accretion disks. Research has extensively investigated LFQPOs in hard states, and several theories proposed that magnetic fields are a driving factor (Titarchuk & Fiorito 2004; Cabanac et al. 2010; Tagger & Pellat 1999). Titarchuk & Fiorito (2004) proposed the transition layer model and suggested that type-C QPOs arise from viscous magnetoacoustic oscillations in a spherical transition layer, where matter from the accretion disk adjusts to sub-Keplerian boundary conditions near the central compact object. Cabanac et al. (2010) proposed a model in which magnetoacoustic waves that propagate within the corona cause oscillations that modulate the Comptonization process and that they simultaneously produce type-C QPOs through resonance effects and the associated broadband noise. In contrast to the magnetoacoustic models, Tagger & Pellat (1999) proposed a model based on the accretion-ejection instability (AEI), in which a spiral density wave in the disk, driven by magnetic stresses, becomes unstable by exchanging angular momentum with a Rossby vortex. This instability creates standing spiral patterns with low azimuthal wavenumbers, which are thought to be the origin of LFQPOs. Building on a series of subsequent studies, this model was expanded to explain the three types of LFQPOs (A, B, and C), and the root mean square (rms) of the QPOs is larger in highly inclined systems (Varnière & Tagger 2002; Varnière & Blackman 2005; Varnière et al. 2012). For the former two models, the LFQPOs arise from the corona, which naturally aligns with the nonthermal origin of the QPOs (Huang et al. 2018; Kong et al. 2020). However, these models predict that both QPOs and their associated noise are independent of the inclination, which cannot explain the geometric dependence of the QPO rms (Motta et al. 2015). Because the latter model originates from a magnetized disk, the QPO signal should still be observed even when the corona is weak in the soft state. However, we cannot currently explain the absence of QPOs in the soft state.

The soft rebrightening of GRS 1915+105 in 2021 offers a unique opportunity to study LFQPOs in conditions in which they are typically absent. This expands on the findings regarding the role of magnetic activity. Through the study of long-term spectral-timing evolution, Kong et al. (2024) found that the presence and absence of QPO signals correspond to a transition from a more highly ionized magnetically driven wind to a lower-ionization thermally driven wind. This result suggests that in a state with an active magnetic field, the LFQPO signal may have a magnetic origin. This phenomenon is very different from the LFQPOs observed in the hard state (Zhang et al. 2020). Therefore, a more detailed study of the correlation between the wind properties and the QPO signal would be beneficial for exploring the origin of this new QPO phenomenon. In this study, using NICER and NuSTAR observations, we leverage advanced analytical techniques such as the Hilbert-Huang transform (HHT) to decompose them and perform a QPO phase-resolved analysis. This provides new insights into the interplay between accretion processes and magnetic activity.

The following sections describe the observations and data reduction techniques in Sect. 2. We present our spectral analysis and other results in Sect. 3, and we discuss the implications of our findings for understanding QPO mechanisms and disk wind interactions in black hole systems in Sect. 4. We conclude with a summary of our results and suggestions for future research in Sect. 5.

2. Observation and data reduction

2.1. Data selection of NICER

The Neutron Star Interior Composition Explorer (NICER), an X-ray astronomy mission launched on June 3, 2017, is equipped with the X-ray Timing Instrument (XTI). This instrument comprises 56 coaligned concentrator optics and silicon drift detectors that cover an energy range of 0.2−12 keV. It provides a field of view of approximately 30 arcmin, with a high time and spectral resolution, a short dead time, and a large effective area (Gendreau et al. 2016).

For this study, we analyzed NICER observations of GRS 1915+105 that were conducted between July 9, 2021 (MJD 59404), and July 31, 2021 (MJD 59425). They coincided with a QPO epoch, as reported by Kong et al. (2024). The dataset includes 20 observations in Fig. 6 in Kong et al. (2024) with a cumulative exposure time of approximately 75 ks. The data processing followed the NICER standard pipeline tasks `nicerl2` and `nicerl3`[1], which are embedded in `HEASOFT v6.32.1` with the calibration database `xti20221001`. These tasks apply the necessary calibrations and screening to generate clean event files and spectra.

2.2. Data selection of NuSTAR

The Nuclear Spectroscopic Telescope Array (NuSTAR), launched on June 13, 2012, provides high-energy X-ray imaging in the 3−79 keV range with an excellent spatial resolution. It uses two coaligned X-ray telescopes, each equipped with CdZnTe pixel detectors, to achieve this imaging capability. These telescopes offer a field of view of 12 arcmin (Harrison et al. 2013). Additionally, NuSTAR has a larger effective area and a good spectral resolution above 7 keV. During the observation period, NuSTAR captured a single observation of GRS 1915+105 on MJD 59409, with an exposure time of approximately 20 ks (ObsID: 90701323002). The data reduction used the NuSTAR Data Analysis Software (NuSTARDAS) with the `nupipeline v0.4.9` and `nuproducts`[2].

3. Results

The Hilbert-Huang transform (HHT) was employed, and we used the Python package `vmdpy` to decompose the QPO components from the light curves into ten phases (Carvalho et al. 2020). The phase intervals ranged from 0.0−0.1 for the lowest phase point to 0.5−0.6 for the highest phase point. Using the phase information, we performed the QPO phase-resolved analysis.

The timing analysis was conducted using the Python package `Stingray` (Huppenkothen et al. 2019a,b) and the `Xronos 6.0` task `powspec` (Stella & Angelini 1992). The power density was generated in the frequency range from 1/256 Hz to 0.5 Hz for the subsequent analysis.

The spectra were grouped using the `ftgrouppha` task with the optimal binning scheme proposed by Kaastra & Bleeker (2016), ensuring a minimum of 25 counts per bin. The spectral

[1] https://heasarc.gsfc.nasa.gov/docs/nicer/nicer_analysis.html
[2] https://heasarc.gsfc.nasa.gov/docs/nustar/analysis/

Manuscript 2

Dai, X., et al.: A&A, 692, A117 (2024)

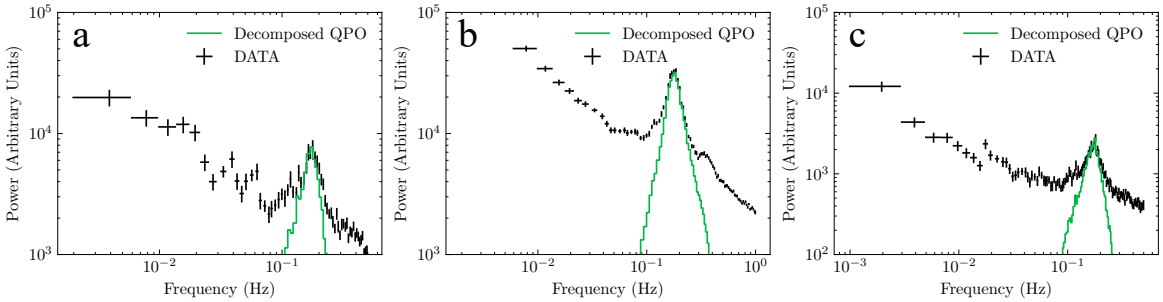


Fig. 1. Power density spectrum and QPO analysis results. Panels a–c display the PDS in black and the HHT decomposed QPO in green from (a) a single NICER observation, (b) combined NICER observation data, and (c) a single NuSTAR observation. The prominent peak at 0.2 Hz in these panels confirms the stability of the QPO signal for different observations.

analysis was performed with XSPEC v12.14.0h (Arnaud 1996), and we focused on the energy range of 2−10 keV for NICER and on 4−25 keV for NuSTAR. During the spectral analysis, we combined the NICER observations with the QPO signals to enhance the statistical significance. Additionally, we used a single NuSTAR spectrum to constrain the broadband spectral shape. This ensured a more robust and accurate analysis. The uncertainties for each spectral parameter were estimated at the 90% confidence level. This incorporated a systematic error of 1%. The parameter errors were calculated using a Markov chain Monte Carlo (MCMC; Taylor 2003) method with a chain length of 10 000.

3.1. HHT decomposed QPO component

The Hilbert-Huang transform (HHT) is an advanced method for analyzing nolinear and non-stationary signals. Traditionally, the HHT employs empirical mode decomposition (EMD) to break a signal down into intrinsic mode functions (IMFs). However, the EMD has several limitations: The number of extreme and zero crossings in a data segment must either be equal to or differ by no more than one, and the average value of the upper and lower envelopes formed by local maxima and minima must be zero to ensure local symmetry around the time axis. Furthermore, the EMD is empirical and lacks a strong physical foundation (Huang et al. 1998; Huang & Wu 2008).

To address these limitations, we used a variational mode decomposition (VMD) instead of the EMD. The VMD decomposes the signal into a sum of IMFs with analytically defined center frequencies and bandwidths. This effectively resolves mode-mixing issues (Dragomiretskiy & Zosso 2014).

Using VMD, we extracted the QPO component from the NICER and NuSTAR light curves (see details in the appendix). In Fig. 1, the power density spectrum (PDS) that we derived from the light curve is depicted in black, while the QPO component decomposed using the HHT is shown in green. This representation highlights a strong peak at approximately 0.2 Hz and accurately describes the broad peak components. Figure 1 consists of three panels: (a) a single NICER observation, (b) 20 combined NICER observations between MJD 59404 and MJD 59425 with a Q factor larger than 2 (see the observation points in Fig. 6 of Kong et al. 2024), and (c) a single NuSTAR observation. The combined PDS from multiple NICER observations consistently shows the QPO characteristics, and the prominent peak at 0.2 Hz confirms the stability of the QPO signal in different observations. Similarly, the PDS from the single NuSTAR observation also reveals a QPO at approximately 0.2 Hz. Although they are based on a single observation, the NuSTAR data corroborate the findings from NICER.

3.2. Spectral analysis

The single spectrum from NuSTAR was used to constrain the broadband spectral shape in the combined spectra, and combined NICER data were used to focus on the spectral properties. Based on Fig. 11 in Kong et al. (2024), we assumed that combining the spectra is reasonable because the shape of the spectra remains stable over the period of the 20 observations, with a photon index Γ around 3.5 and $kT_{\rm bb}$ around 1.1 keV, except for the drop at the beginning. On the other hand, the absorption properties are also stable, with $n_{\rm H}$ around 40 and the $\log \xi$ around 4.

Following Kong et al. (2024), we considered the disk in the rebrightening event, which might extend far beyond the standard thin disk and be encased in a warm layer (Zhang et al. 2000; Gronkiewicz & Różańska 2020). This warm layer is stronger for higher accretion rates and greater magnetic field strengths (Gronkiewicz & Różańska 2020). Following Zhang et al. (2000), Pszota & Cui (2007), we replaced `diskbb` to `comptt` to model the disk emission with saturated Compton scattering (Titarchuk 1994). The kT_0 value for the `comptt` model was linked to $kT/2.7f_{\rm col}$ during the fitting, where the color factor $f_{\rm col} = 1.7$, representing a standard disk (see Pszota & Cui 2007 for more details). From model 2 in Table 1 of Kong et al. (2024), the optical depth of the `comptt` τ_0 is higher than 50. This means that the seed photons with a temperature $kT \simeq 1$ keV that escape the warm layer as blackbody emission can be Comptonized to higher energies as they pass through the corona. Therefore, we used the thermally Comptonized model `thcomp` (Zdziarski et al. 2020) convolved with `comptt` to fit the continuum. The absorption by the interstellar medium (ISM) was accounted for using the Tuebingen-Boulder ISM absorption model `TBabs`, with abundances as in Wilms et al. (2000), and with the photoelectric cross sections given in Verner et al. (1996). The equivalent hydrogen column density $n_{\rm H}$ was fixed at 4.9 based on the results from Kong et al. (2024). The cross-calibration between NICER and NuSTAR was performed using the `Crabcorr(plabs)` model rather than a simple `constant` (Steiner et al. 2010; Wang et al. 2020). This model multiplies each spectrum by a power law with an index and coefficient parameters, and corrections were applied to both the slope and normalization. Because of this, the continuum model can be written as `plabs` × `TBabs` × `thcomp` ⊗ `comptt`. This approach

Manuscript 2

Dai, X., et al.: A&A, 692, A117 (2024)

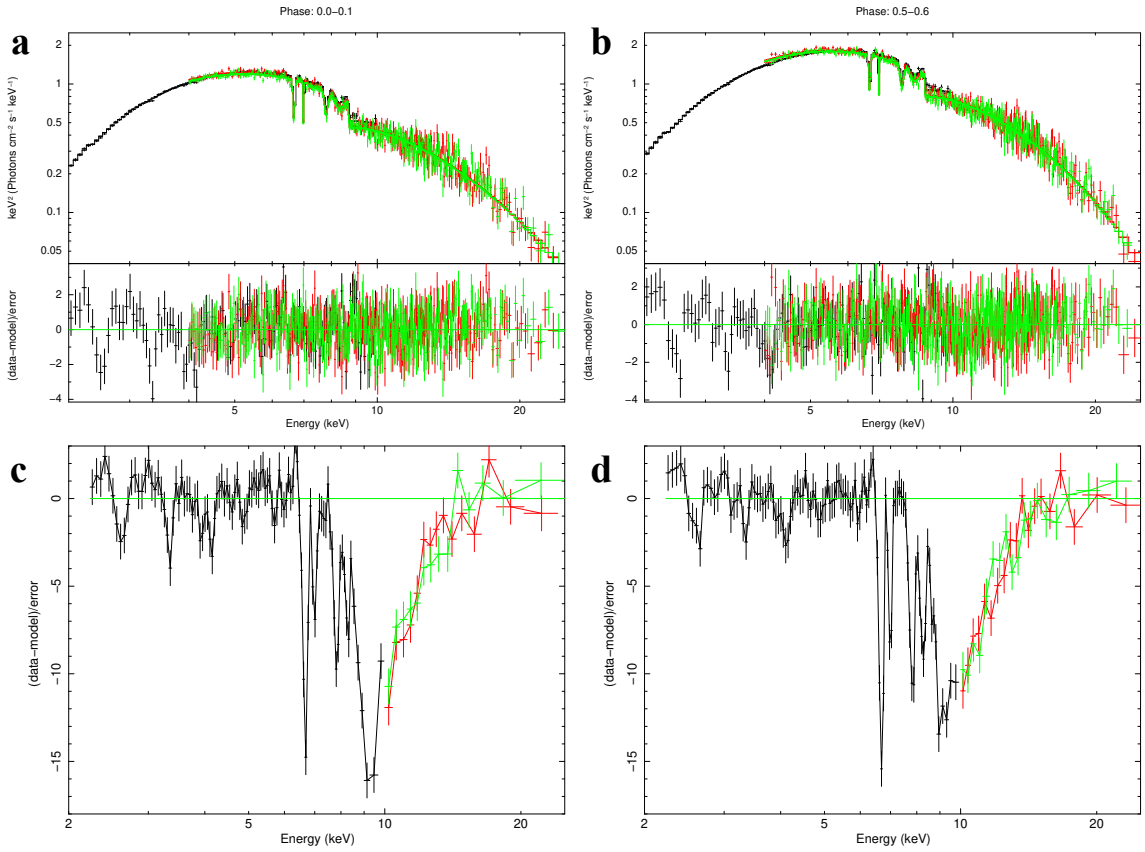


Fig. 2. Spectral fitting and residual analysis for NICER and NuSTAR observations. Panels a and b: Spectral fit using the model `TBabs` × (4 × `gabs`) × `edge` × `thcomp` × `comptt`. The black lines represent the NICER data in the energy range of 1−10 keV. The red and green lines correspond to the NuSTAR data from the FPMA and FPMB mirrors, respectively, covering the energy range of 4−25 keV. Panels c and d: Residuals of the spectral fit without the `gabs` and `edge` components. The black lines indicate the NICER data, and the red and green lines represent the FPMA and FPMB data from NuSTAR. The depicted energy ranges are 2−10 keV for NICER and 10−25 keV for NuSTAR.

allowed us to account for the energy-dependent response differences between the detectors and to normalize the data to the Crab nebula, ensuring a consistent calibration across the different instruments. Specifically, the model adjusts for the known slope differences between the NICER and NuSTAR energy ranges and aligns the spectra to a common reference. This is essential because NICER and NuSTAR cover different energy bands and have varying sensitivities.

The fit that only considered the continuum spectrum yielded a large reduced χ^2 that left at least seven narrow absorption features below 9 keV and one broad dip around 7−15 keV (see panels c and d in Fig. 2). We used four `gabs` components to fit the narrow absorption features at approximately 6.7 keV, 6.97 keV, 7.8 keV, and 8.27 keV, which correspond to the Fe XXV He-α, Fe XXVI Ly-α, Fe XXV He-β, and Fe XXVI Ly-β lines, respectively. Although there are some other structures below 4 keV (see Fig. 2), we ignored them because only iron is the most abundant element, which provides a better illustration for the study. The broad dip was fit with an absorption edge at $\simeq$8.7 keV, which resembles the Fe XXV K-edge. Our new model can produce good residuals. Therefore, the fitting model we used for panels (a) in 0.0−0.1 QPO phase and (b) in 0.5−0.6 QPO phase is represented as `plabs`×`TBabs`×(4×`gabs`)×`edge`×`thcomp`⊗`comptt`. In this model, `gabs` denotes the absorption lines, and `edge` refers to the absorption edge. In Table 1, we show the fitting results of the phase average, 0.0−0.1, and 0.5−0.6 QPO phase. For the phase-resolved analysis, the energy and width of four absorption lines and the optical depth (τ_0) of the `comptt` were fixed during the fitting.

We combined NICER data to obtain a long-exposure spectral fit. The result is shown in Fig. 2. NuSTAR data cover the energy range of 4−25 keV, ensuring a comprehensive coverage of the spectral features and allowing for a detailed comparison between the NICER and NuSTAR data. Panels c and d focus on the residuals without `gabs` and `edge` from the fittings. This is shown for the energy range of 2−25 keV. We deliberately excluded the NuSTAR data below 10 keV when we plotted the residuals for clarity. The residuals are better visible, and this allows a clearer assessment of the model performance with the NICER data.

Figure 3 presents the results of the QPO phase-resolved spectral fitting analysis. The QPO phase obtained from NICER data in 1−10 keV and derived from a single NuSTAR observation in 3−79 keV. It shows variations in the iron absorption components and continuum parameters across different QPO phase. Because

Manuscript 2

Dai, X., et al.: A&A, 692, A117 (2024)

Table 1. Joint fitting results of NICER (20 combined observations) and NuSTAR.

Component	Parameters	Phase-average	0.0–0.1	0.5–0.6
TBabs	$n_{\rm H}$ (10^{22} cm^{-2})	$4.78^{+0.09}_{-0.11}$	4.78 (fixed)	4.78 (fixed)
gabs (Fe XXV He-α)	LineE (keV)	$6.662^{+0.005}_{-0.006}$	6.7 (fixed)	6.7 (fixed)
	Sigma (keV)	$0.039^{+0.007}_{-0.009}$	0.03 (fixed)	0.03 (fixed)
	Strength (keV)	$0.055^{+0.002}_{-0.001}$	$0.060^{+0.008}_{-0.003}$	$0.054^{+0.005}_{-0.004}$
gabs (Fe XXVI Ly-α)	LineE (keV)	$6.977^{+0.007}_{-0.008}$	6.97 (fixed)	6.97 (fixed)
	Sigma (keV)	$0.007^{+0.002}_{-0.002}$	0.01 (fixed)	0.01 (fixed)
	Strength (keV)	$0.046^{+0.016}_{-0.016}$	$0.034^{+0.008}_{-0.003}$	$0.032^{+0.010}_{-0.007}$
gabs (Fe XXV He-β)	LineE (keV)	$7.797^{+0.016}_{-0.016}$	7.80 (fixed)	7.80 (fixed)
	Sigma (keV)	$0.070^{+0.016}_{-0.013}$	0.06 (fixed)	0.06 (fixed)
	Strength (keV)	$0.062^{+0.006}_{-0.007}$	$0.066^{+0.009}_{-0.006}$	$0.060^{+0.006}_{-0.006}$
gabs (Fe XXVI Ly-β)	LineE (keV)	$8.31^{+0.023}_{-0.025}$	8.27 (fixed)	8.27 (fixed)
	Sigma (keV)	$0.20^{+0.02}_{-0.03}$	0.19 (fixed)	0.19 (fixed)
	Strength (keV)	$0.11^{+0.01}_{-0.01}$	$0.11^{+0.01}_{-0.01}$	$0.10^{+0.01}_{-0.01}$
edge (Fe XXV K-edge)	edgeE (keV)	$8.73^{+0.01}_{-0.02}$	$8.70^{+0.03}_{-0.02}$	$8.72^{+0.02}_{-0.01}$
	MaxTau	$0.44^{+0.01}_{-0.01}$	$0.49^{+0.03}_{-0.02}$	$0.41^{+0.02}_{-0.01}$
comptt (seed photon)	T_0 (keV)	0.24 [(a)]	0.23 [(a)]	0.24 [(a)]
	kT (keV)	$1.09^{+0.01}_{-0.01}$	$1.05^{+0.01}_{-0.01}$	$1.12^{+0.01}_{-0.01}$
	τ_0	49^{+2}_{-3}	50 (fixed)	50 (fixed)
	norm	$0.66^{+0.01}_{-0.02}$	$0.59^{+0.01}_{-0.01}$	$0.73^{+0.01}_{-0.01}$
thcomp	τ	$5.0^{+0.3}_{-0.2}$	$4.4^{+0.3}_{-0.3}$	$6.0^{+0.2}_{-0.6}$
	$kT_{\rm e}$ (keV)	$3.8^{+0.2}_{-0.1}$	$4.3^{+0.2}_{-0.3}$	$3.3^{+0.1}_{-0.2}$
	$f_{\rm cov}$	$1.00^{+0.01}_{-0.01}$	1 (fixed)	1 (fixed)
Crabcorr	$\Delta\Gamma_{\rm FPMA}$	$0.23^{+0.01}_{-0.01}$	$0.19^{+0.03}_{-0.03}$	$0.25^{+0.03}_{-0.01}$
(plabs)	$K_{\rm FPMA}$	$1.53^{+0.03}_{-0.04}$	$1.39^{+0.08}_{-0.07}$	$1.58^{+0.09}_{-0.04}$
	$\Delta\Gamma_{\rm FPMB}$	$0.22^{+0.01}_{-0.02}$	$0.18^{+0.03}_{-0.03}$	$0.25^{+0.02}_{-0.02}$
	$K_{\rm FPMB}$	$1.62^{+0.04}_{-0.05}$	$1.34^{+0.08}_{-0.08}$	$1.54^{+0.07}_{-0.07}$
Fitting (System error 1%)	$\chi^2_{\rm red}$/d.o.f.	1.04/1027	1.12/685	1.06/740

Notes. Uncertainties are reported at the 90% confidence interval and were computed using a MCMC with a length of 10 000. [(a)]T_0 is linked to $kT/2.7f_{\rm col}$, where $f_{\rm col} = 1.7$.

we focused on the variation in the absorption and because the energy of the lines does not vary with phases, we froze the line energies in accordance with physical scenarios. The four `gabs` components for the iron lines were fixed to specific energy. Notably, the two absorption lines of Fe XXV vary slightly with QPO phase, as observed from the fitting results. The variation in the absorption edge with the QPO phase is more pronounced. To calculate the significance, we employed a nonlinear least-squares method to fit a sinusoidal model to the data in one period. We took the measurement errors into account. The fitting process involved minimizing the χ^2 statistic. Based on an f-test, we compared the fits from the sinusoidal and the constant model. Our calculations and fitting in Fig. 4 show that the p value of the f-test is 2.7×10^{-3}, and the confidence level of this variation is approximately 3σ, indicating a significant variation. This variation underscores the dynamic nature of the absorption edge in response to the changes in QPO phase.

Beyond the variation in the absorption lines and edges, other spectral parameters also change significantly with QPO phase. Specifically, the optical depth τ, the seed photon temperature kT, and the seed photon normalization show a positive correlation with the QPO phase. In contrast, the electron temperature $kT_{\rm e}$ is anticorrelated with the flux of the QPO phase. This highlights the complex interplay between these parameters and the QPO phenomena. To further validate the spectrum fitting results, we constructed a multiparameter correlation diagram (Fig. A.1). This diagram reveals that the absorption K-edge of Fe XXV and the absorption lines are not affected by other parameters. This confirms their independence. However, the parameters of the continuous spectrum are strongly correlated, in particular, between those of the `comptt` and `thcomp` models. This strong interparameter correlation emphasizes that when the parameters of the continuum model are discussed, we should be mindful of the competing relation between this correlation trend and their broader tendency to vary with QPO phase.

The spectral fitting results in Fig. 3 delineate the modulation patterns of various spectral features with QPO phase and provide a strong statistical significance about the Fe XXV K-edge absorption component. The correlation analysis further corroborates the independence and interdependence of key spectral parameters, which ensures that the modulation results with QPO phase are reliable.

Manuscript 2

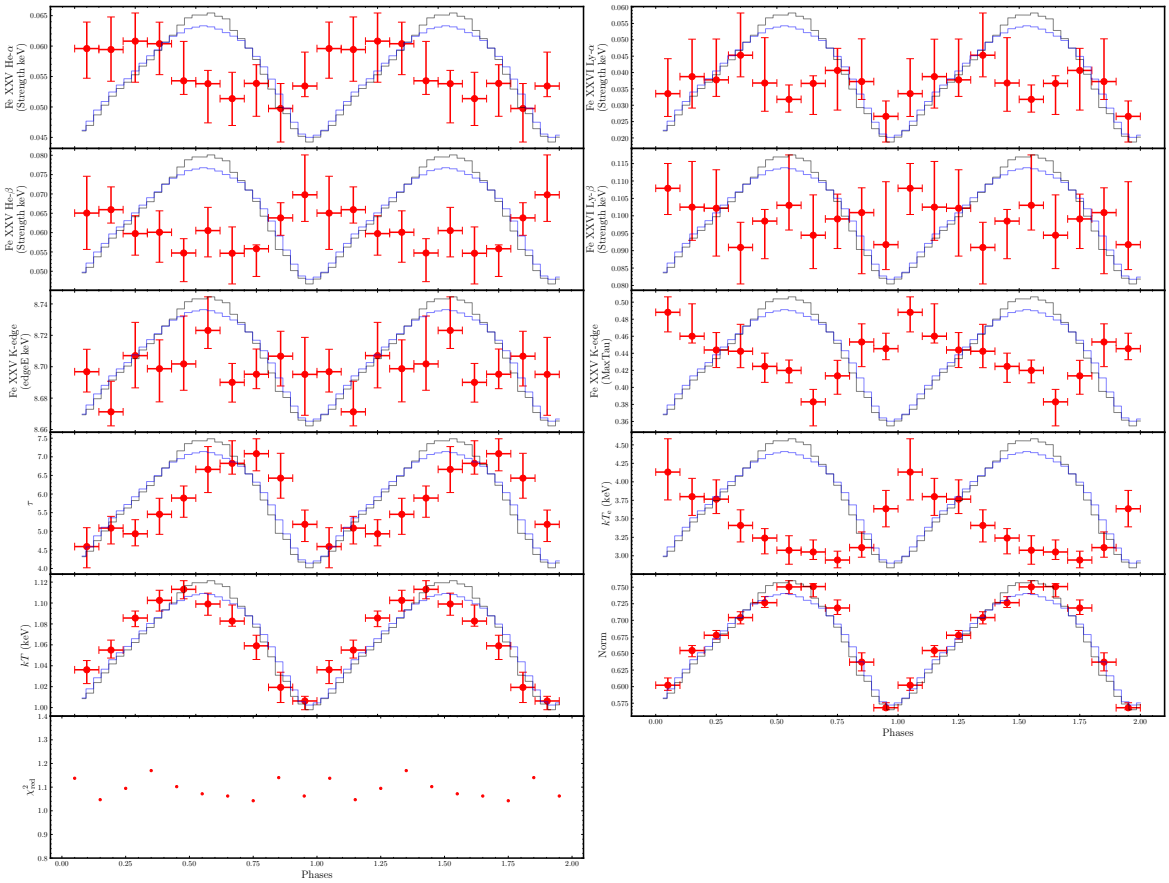


Fig. 3. QPO phase derived from combined NICER data (blue line) and a single NuSTAR observation (black line). The first four panels illustrate the strength of the iron absorption lines: Fe XXV He-α at ≃6.7 keV, Fe XXVI Ly-α at ≃6.97 keV, Fe XXV He-β at ≃7.8 keV, and Fe XXVI Ly-β at ≃8.27 keV, each shown with respect to the QPO phase. The fifth and sixth panels in the third row depict the edge threshold energy (edgeE) and absorption depth (MaxTau) of the Fe XXV K-edge. The fourth and fifth rows show the change in the continuum parameters with QPO phase. Finally, the last panel displays the spectral fitting residuals.

4. Discussions

Our spectral fitting results, in conjunction with previous findings in Kong et al. (2024), provide significant insights into the nature of the X-ray emissions and their variation with QPO phase. The soft X-ray rebrightening observed in 2021 suggests that the radiation predominantly stems from Compton-thick ($\tau \simeq 5.5$) low-temperature electrons ($kT_e \simeq 3.5$ keV) in the corona, with the seed photons ($kT \simeq 1.06$ keV) arising from the disk emission, diluted by the optically thick warm layer, accompanied by a QPO signal that is characterized by high column densities and a wind with a high ionization degree.

For the canonical low-mass black hole binaries (LMBHs), the occurrence of type-C low-frequency QPOs (LFQPOs) at ≃0.2 Hz is more prevalent in hard states than in the soft state (Motta et al. 2011), and the frequency of the LFQPOs is positively correlated to the photon index (Vignarca et al. 2003). In addition, in combination with the tendency of QPO properties to vary with inclination angle, coronal or jet precession models are currently preferred to explain the origin of QPOs (Ingram et al. 2016; Ma et al. 2021). However, (Kong et al. 2024) posited that the establishment and elimination of these QPOs largely depends not on the evolution of the spectral shape, such as the photon index and the electron temperature, but on the properties of the disk wind, including the ionization degree and the column density. Our results show a positive correlation between the optical depth τ and the QPO flux, however, which is opposite to the behavior observed in H1743−322, MAXI J1820+070, and Swift J1727.8−1613, where an anticorrelation (or a positive correlation between the photon index Γ and the QPO flux) was observed (Ingram et al. 2016; Shui et al. 2023). More importantly, we have discovered for the first time that the wind properties vary with QPO phase. We would like to emphasize that this observation contradicts models that rely on coronal precession to explain the observed phenomena, because the disk wind is always generated on the disk and is produced farther away from the black hole, regardless of the driving mechanism. This makes the Lense-Thirring precession weak. The highly ionized winds that accompany LFQPOs imply that the energy of the black hole activity is injected into the wind through quasi-periodic dynamical processes, which cause it to be heated. This behavior of

Manuscript 2

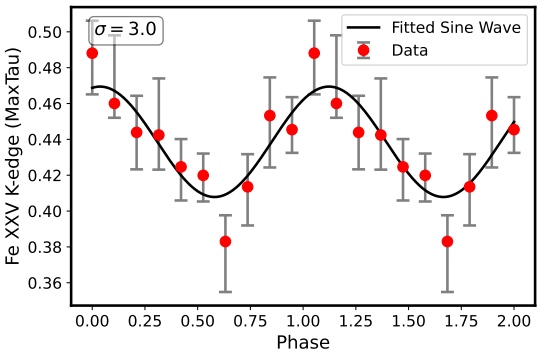


Fig. 4. Confidence level of the variation between the absorption depth (MaxTau) of Fe XXV K-edge and the QPO phase (3σ). The black line represents the fitted sine wave based on the simulation results, and the red points indicate the actual observational data, complete with error bars.

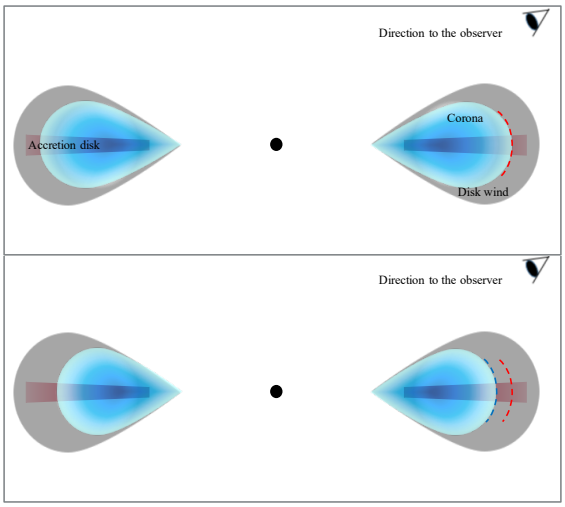


Fig. 5. Simplified schematic diagram of the transformation from the corona (blue area) to the wind (gray area) during the QPO phases. We show the change in a region of gas with a hot electron above the disk, referred to as the corona, in response to QPO phases. The diagram shows that the variation in the corona is anticorrelated with the ejection of ionized material through the disk wind during different QPO phases. The top and bottom panels show the situations of the QPO peak at 0.5−0.6 phase and the QPO trough at 0.0−0.1 phase. The dashed red and blue lines indicate the corona size at the highest and lowest points of the QPO phase, respectively.

the energy transfer also occurs in the usual QPO phenomena of GRS 1915+105, such as in the transformation into the relativistic jet or the accreting corona (Méndez et al. 2022). However, the sudden drop in the radio flux during the rebrightening is evidence of suppressed jet activity (Sánchez-Sierras et al. 2023), which implies that energy can only be fed into the Compton-thick low-temperature corona or into the highly ionized wind. The established facts above demonstrate that the LFQPO that was observed during the rebrightening is distinctly different from the usual LFQPO phenomenon in GRS 1915+105.

In Fig. 3, the positive correlation of the optical depth τ, the seed photon temperature kT, and the normalization factor with QPO phase is reasonable. When we generally accept that the flux of photons is determined by the optical depth and the normalization of the seed photon, which controls the Comptonization, then the high QPO intensity implies a relatively high optical depth τ and norm (see Fig. 3). This increases the scattering times, however, and results in lower electron temperatures, which is also consistent with a colder and larger corona. Our results also indicate that the strength of the iron absorption is anticorrelated with the QPO flux. This suggests that fewer materials are ejected as wind during a high QPO flux, but they instead cool and fall back to the corona, leading to a thicker corona with a higher optical depth and a thinner wind with a weaker absorption strength, as indicated by the continuum spectral fit parameters. Consequently, the increase in the thickness of the absorbing wind occurs simultaneously with the contraction of the corona scale, or vice versa. This interpretation was obtained from the results of our energy spectrum fit. This suggests that there might be other plausible explanations. During the rebrightening phase, the energies of the absorption lines do not show a significant mismatch (see Table 1). This indicates minimal red- and blueshifts. Without considering limitations from the detector resolution, we suggest based on the low-velocity winds that the driving force creates a dynamic equilibrium with gravitational forces, resulting in failed winds (Miller et al. 2020). In this case, we assume that the energy injection that carries the oscillatory signal can be retained in the failed wind, which causes the variation. Because the change with QPO phase occurs on short timescales, we speculate that this type of variation is highly likely to be related to magnetic processes.

These phenomena can be explained by the accretion ejection instability (AEI) model (Tagger & Pellat 1999), which attributes them to processes driven by the magnetic field, which play an important role in generating both QPOs and ejections, such as wind (Kong et al. 2024). The AEI model offers a plausible explanation for the change in the iron absorption lines and in the continuum spectrum with QPO phase. This model posits that the instabilities in the inner regions of the accretion disk, where magnetic field lines are twisted and sheared, can drive periodic ejections of material from the disk. This is observed as QPOs. When the magnetic field on the disk is strong enough, the magnetic pressure created by these twisted field lines, combined with differential rotation, launches material from the disk surface into a wind. Based on the comprehensive analysis and the robust statistical significance of our findings, it is evident that the observed modulations are consistent with the predictions of the AEI model. This model not only explains the occurrence of low-frequency QPOs in soft states, but also accounts for the variation in the iron absorption lines and continuum spectral parameters with QPO phase. Furthermore, our results suggest that the potential conversion of the corona into disk winds during magnetism-driven processes is a plausible scenario that indicates a complex interplay between these components.

Figure 5 presents a schematic that illustrates the transformation of the corona into wind during a QPO phase. The accretion disk is far from the black hole and is overlaid by the inner corona layer and the outer wind layer, which are both influenced by magnetic fields. During a QPO phase with high flux (upper panel in Fig. 5), the size of corona is largest, as indicated by the dashed red line. As the flux decreases, the corona scale shrinks, resulting in an increase in ejected material, which is further converted into disk wind. Our results in Fig. 3 show significant change in the spectral features with QPO phase. In the interface area (the dashed lines shown in Fig. 5), the contraction (dashed blue line) and expansion (dashed red line) of the corona during different QPO phases indicates a dynamic interaction between the

Manuscript 2

magnetic fields and the ionized gas that results in the periodic ejection of material from the corona into the wind and the cooling of material from the wind back to the corona. Furthermore, we note that the nature of the disk during this event may extend beyond the simple geometric thin disk. It might be enveloped in a warm layer that is stronger in cases of higher accretion rates and greater magnetic field strengths (Zhang et al. 2000; Gronkiewicz & Różańska 2020). This is self-consistent with the assumption of a strong magnetic field in the model.

Because this QPO phenomenon has not been captured in large numbers and in more sources, and considering the unique nature of GRS 1915+105 during its reflare process as well as the limited observational data available during this period, additional explanations are possible. These limitations may allow room for different interpretations of the observed phenomena. We expect that subsequent larger samples of observations as well as more observed polarization events will make it possible to constrain the model better. The capabilities of the future enhanced X-ray Timing and Polarimetry mission (eXTP) will provide huge advantages for these observations (Zhang et al. 2019). Our findings underscore overall the new intricate relation between QPOs, disk winds, and the magnetic dynamics within the accretion process of the black hole binary system. This contributes to a deeper understanding of the physical processes driving these phenomena.

5. Conclusions

This study has provided a comprehensive analysis of the spectral fitting results from NICER and NuSTAR observations of the X-ray source GRS 1915+105, with a focus on the variation in the spectral features with QPO phase. Our findings revealed significant variation in the iron absorption lines and edge with QPO phase, indicating dynamic changes in the source environment. The strong variation in the iron absorption edge that we reported with high confidence highlights substantial physical variations in the wind near the source during different QPO phases. We also observed that the continuum spectral parameters are (anti-)correlated with the QPO phase. These findings agree better with the AEI model than with the geometric precession model. The former attributes the QPO generation to instabilities in the inner accretion disk, caused by twisted magnetic fields, which naturally give rise to a periodically varying magnetically driven disk wind. Additionally, the disk nature during this event may involve a warm layer. This would affect the radiation dilution and provide further context for the magnetic accretion disk structure in GRS 1915+105.

In summary, this study advances our understanding of QPOs and the related radiation dynamics by revealing the intricate interplay between disk winds, magnetic fields, and the corona. Future research should extend these findings to other QPO sources and refine the theoretical models for a deeper understanding of these dynamic systems.

Acknowledgements. This work made use of data from the the High Energy Astrophysics Science Archive Research Center (HEASARC), provided by NASA's Goddard Space Flight Center. Xiaohang Dai is grateful for the financial supported provided by the China Scholarship Council (CSC) at Eberhard Karls Universität of Tübingen. Lingda Kong is grateful for the financial support provided by the Sino-German (CSC-DAAD) Postdoc Scholarship Program (57607866).

References

Arnaud, K. A. 1996, ASP Conf. Ser., 101, 17
Athulya, M. P., & Nandi, A. 2023, MNRAS, 525, 489
Belloni, T., Klein-Wolt, M., Méndez, M., van der Klis, M., & van Paradijs, J. 2000, A&A, 355, 271
Cabanac, C., Henri, G., Petrucci, P. O., et al. 2010, MNRAS, 404, 738
Carvalho, V. R., Moraes, M. F., Braga, A. P., & Mendes, E. M. 2020, Biomed. Signal Process. Control, 62, 102073
Castro-Tirado, A. J., Brandt, S., & Lund, N. 1992, IAU Circ., 5590, 2
Done, C., Gierliński, M., & Kubota, A. 2007, A&ARv, 15, 1
Dragomiretskiy, K., & Zosso, D. 2014, IEEE Trans. Signal Process., 62, 531
Fender, R., & Belloni, T. 2004, ARA&A, 42, 317
Fender, R. P., & Belloni, T. M. 2012, Science, 337, 540
Fuchs, Y., Rodriguez, J., Mirabel, I. F., et al. 2003, A&A, 409, L35
Gendreau, K. C., Arzoumanian, Z., Adkins, P. W., et al. 2016, SPIE Conf. Ser., 9905, 99051H
Gronkiewicz, D., & Różańska, A. 2020, A&A, 633, A35
Harrison, F. A., Craig, W. W., Christensen, F. E., et al. 2013, ApJ, 770, 103
Huang, N. E., & Wu, Z. 2008, Rev. Geophys., 46, RG2006
Huang, N. E., Shen, Z., Long, S. R., et al. 1998, Proc. Roy. Soc. London Ser. A, 454, 903
Huang, Y., Qu, J. L., Zhang, S. N., et al. 2018, ApJ, 866, 122
Huppenkothen, D., Bachetti, M., Stevens, A. L., et al. 2019a, ApJ, 881, 39
Huppenkothen, D., Bachetti, M., Stevens, A., et al. 2019b, J. Open Source Softw., 4, 1393
Ingram, A., van der Klis, M., Middleton, M., et al. 2016, MNRAS, 461, 1967
Kaastra, J. S., & Bleeker, J. A. M. 2016, A&A, 587, A151
Klein-Wolt, M., Fender, R. P., Pooley, G. G., et al. 2002, MNRAS, 331, 745
Koljonen, K. I. I., & Hovatta, T. 2021, A&A, 647, A173
Koljonen, K. I. I., & Tomsick, J. A. 2020, A&A, 639, A13
Kong, L. D., Zhang, S., Chen, Y. P., et al. 2020, J. High Energy Astrophys., 25, 29
Kong, L.-D., Ji, L., Santangelo, A., et al. 2024, A&A, 686, A211
Lee, J. C., Reynolds, C. S., Remillard, R., et al. 2002, ApJ, 567, 1102
Ma, X., Tao, L., Zhang, S.-N., et al. 2021, Nat. Astron., 5, 94
Majumder, S., Sreehari, H., Aftab, N., et al. 2022, MNRAS, 512, 2508
Méndez, M., Karpouzas, K., García, F., et al. 2022, Nat. Astron., 6, 577
Miller, J. M., Raymond, J., Fabian, A., et al. 2006, Nature, 441, 953
Miller, J. M., Zoghbi, A., Raymond, J., et al. 2020, ApJ, 904, 30
Mirabel, I. F., & Rodríguez, L. F. 1999, ARA&A, 37, 409
Morgan, E. H., Remillard, R. A., & Greiner, J. 1997, ApJ, 482, 993
Motta, S. E., & Belloni, T. M. 2024, A&A, 684, A209
Motta, S., Muñoz-Darias, T., Casella, P., Belloni, T., & Homan, J. 2011, MNRAS, 418, 2292
Motta, S. E., Casella, P., Henze, M., et al. 2015, MNRAS, 447, 2059
Motta, S. E., Kajava, J. J. E., Giustini, M., et al. 2021, MNRAS, 503, 152
Neilsen, J., & Lee, J. C. 2009, Nature, 458, 481
Neilsen, J., Altamirano, D., Homan, J., et al. 2021, ATel, 14792, 1
Ponti, G., Fender, R. P., Begelman, M. C., et al. 2012, MNRAS, 422, L11
Pszota, G., & Cui, W. 2007, ApJ, 663, 1201
Ravishankar, B. T., Tilak, K., Athulya, M. P., et al. 2021, ATel, 14811, 1
Remillard, R. A., & McClintock, J. E. 2006, ARA&A, 44, 49
Rodriguez, J., Shaw, S. E., Hannikainen, D. C., et al. 2008, ApJ, 675, 1449
Sánchez-Sierras, J., Muñoz-Darias, T., Motta, S. E., et al. 2023, A&A, 680, L16
Shui, Q. C., Zhang, S., Zhang, S. N., et al. 2023, ApJ, 957, 84
Shui, Q. C., Zhang, S., Zhang, S. N., et al. 2024, ApJ, 965, L7
Steiner, J. F., McClintock, J. E., Remillard, R. A., et al. 2010, ApJ, 718, L117
Stella, L., & Angelini, L. 1992, Data Anal. Astron., 59
Tagger, M., & Pellat, R. 1999, A&A, 349, 1003
Taylor, J. E. 2003, MNRAS, 341, 823
Titarchuk, L. 1994, ApJ, 434, 570
Titarchuk, L., & Fiorito, R. 2004, ApJ, 612, 988
Ueda, Y., Yamaoka, K., & Remillard, R. 2009, ApJ, 695, 888
Varnière, P., & Blackman, E. G. 2005, New Astron., 11, 43
Varnière, P., & Tagger, M. 2002, A&A, 394, 329
Varnière, P., Tagger, M., & Rodriguez, J. 2012, A&A, 545, A40
Verner, D. A., Ferland, G. J., Korista, K. T., & Yakovlev, D. G. 1996, ApJ, 465, 487
Vignarca, F., Migliari, S., Belloni, T., Psaltis, D., & van der Klis, M. 2003, A&A, 397, 729
Wang, J., Kara, E., Steiner, J. F., et al. 2020, ApJ, 899, 44
Wilms, J., Allen, A., & McCray, R. 2000, ApJ, 542, 914
Zdziarski, A. A., Szanecki, M., Poutanen, J., Gierliński, M., & Biernacki, P. 2020, MNRAS, 492, 5234
Zhang, S. N., Cui, W., Chen, W., et al. 2000, Science, 287, 1239
Zhang, S., Santangelo, A., Feroci, M., et al. 2019, Sci. China Phys. Mech. Astron., 62, 29502
Zhang, L., Méndez, M., Altamirano, D., et al. 2020, MNRAS, 494, 1375

Manuscript 2

Dai, X., et al.: A&A, 692, A117 (2024)

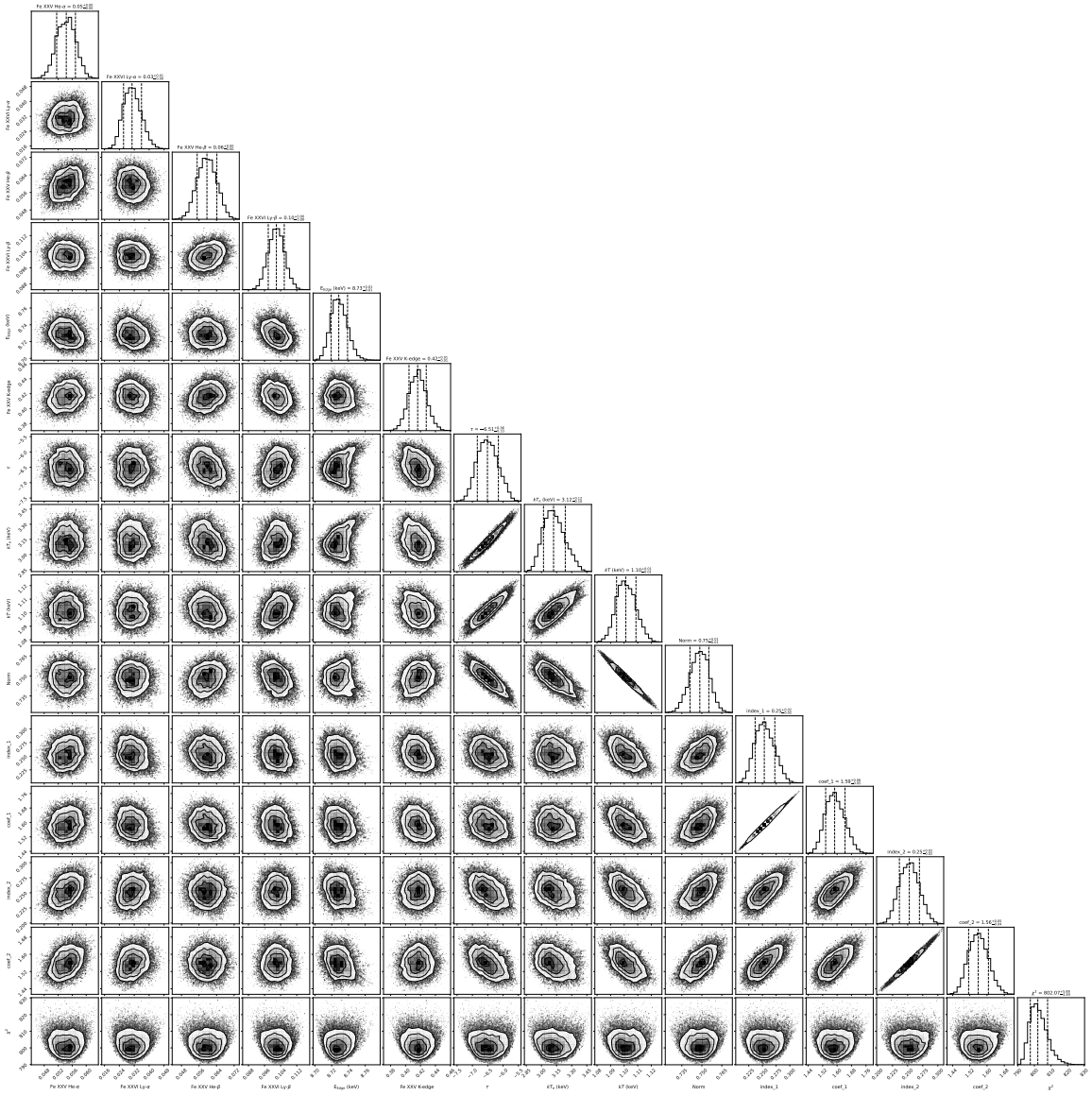


Fig. A.1. Distribution of the parameters from the 100,000 chain of MCMC results of the spectral fittings on the QPO phase 0.5-0.6 (for visualization purposes). The multi-parameter correlations indicate that only the continuum parameters, kT_e and τ from the `thcomp`, and kT and Norm from the `comptt` components exhibit strong correlations. In contrast, the strength of the absorption lines and edge show no significant correlation with other parameters.

Appendix A: Parameter correction

Appendix B: HHT functions

The VMD process involves solving a constrained optimization problem. Firstly, a single-sided band analytic signal is constructed:

$$s_k(t) = \left[\delta(t) + \frac{j}{\pi t}\right] * u_k(t),$$

where $\delta(t)$ is the Dirac delta function, $u_k(t)$ is the k-th mode, and $*$ denotes convolution. Each mode's spectrum is shifted to the baseband by complex modulation:

$$u_k(t) \cdot e^{-j\omega_k t},$$

Manuscript 2

Dai, X., et al.: A&A, 692, A117 (2024)

where ω_k is the center frequency of the k-th mode. Finally, the bandwidth of each mode is minimized:

$$\min_{\{u_k\},\{\omega_k\}} \left\{ \sum_{k=1}^{K} \left\| \partial_t \left[\left(\delta(t) + \frac{j}{\pi t} \right) * u_k(t) \right] e^{-j\omega_k t} \right\|_2^2 \right\},$$

where ∂_t denotes the time derivative. By introducing a quadratic penalty term and Lagrange multipliers, this constrained optimization problem is converted into an unconstrained problem:

$$L(u_k, \omega_k, \lambda) = \alpha \sum_{k=1}^{K} \left\| \partial_t \left[\left(\delta(t) + \frac{j}{\pi t} \right) * u_k(t) \right] e^{-j\omega_k t} \right\|_2^2 + \left\| f(t) - \sum_{k=1}^{K} u_k(t) \right\|_2^2 + \left\langle \lambda(t), f(t) - \sum_{k=1}^{K} u_k(t) \right\rangle,$$

where λ is the Lagrange multiplier, $f(t)$ is the original signal, and α controls the bandwidth of each mode. Solving this Lagrangian problem using the alternating direction method of multipliers, we can obtain each mode and their center frequencies. α and K are two parameters that need to be considered for introduction. Here, we determine them manually by matching the QPO component of the IMF to the shape of the power spectrum (see Fig. 1). In our analysis, the bandwidth of each mode is controlled by a parameter α, which we set to 100. We chose to decompose the signal into 3 modes ($K = 3$), capturing the QPO characteristics effectively (see Fig. 1). A larger α above 500 and K above 3 will cause the narrow QPO component (the second IMF) and the band-limited noise (the first IMF) to mismatch with the PDS. After obtaining the IMFs using VMD, we applied the Hilbert transform to each IMF to compute the instantaneous frequency:

$$H[IMF_i(t)] = \frac{1}{\pi} P \int \frac{IMF_i(\tau)}{t - \tau} d\tau,$$

where P denotes the Cauchy principal value. The analytic signal is then constructed as

$$z_i(t) = IMF_i(t) + jH[IMF_i(t)] = a_i(t) e^{j\theta_i(t)},$$

where $a_i(t)$ is the instantaneous amplitude, and $\theta_i(t)$ is the instantaneous phase. The instantaneous frequency is given by

$$\omega_i(t) = \frac{d\theta_i(t)}{dt}.$$

Appendix C: Simulation analysis

To ensure the reliability and validity of the QPO phase-folding analysis results, we conducted a comprehensive simulation analysis to test the robustness of our HHT-based method. Our simulation follows these steps (Shui et al. 2024): (1) Fit the PDS of real observations with a multi-Lorentz line profile; (2) Use the fitting parameters of the QPO and noise components to simulate total light curves, which are the sum of the QPO light curve and noise light curve, based on the Python package `Stingray.simulator` (Huppenkothen et al. 2019a); (3) Test the ability of the VMD algorithm to decompose the signal into QPO and low-frequency noise components accurately by comparing the simulated signals with the HHT-decomposed signals.

We select the original signal and use `powspec` to generate the PDS. The total model is plotted as a green line in the right panel of Fig. C.1. The parameters of the QPO are $f_{\rm QPO}$=0.178 Hz, FWHM$_{\rm QPO}$=0.047 Hz and RMS$_{\rm QPO}$ = 0.077. The parameters of the low-break-frequency noise are $f_{\rm N1}$=0 Hz, FWHM$_{\rm N1}$=0.021 Hz and RMS$_{\rm N1}$ = 0.005. The parameters of the high-break-frequency noise are $f_{\rm N2}$=0 Hz, FWHM$_{\rm N2}$=0.74 Hz and RMS$_{\rm N1}$ = 0.0149. The simulations of the light curves were performed using `Stingray.simulator`. The total light curve, with an average count rate of 249 cts/s, includes both red noise and the QPO, and is shown as black points in the left panel of Fig. C.1. The PDS of the simulated light curve is plotted as black points in the right panel of Fig. C.1, while the gray points represent the QPO and noise components in the PDS from the simulation. We find that these components fit the original PDS well.

After obtaining the simulated data, we performed the VMD-HHT analysis. The IMF components from the VMD of the simulated light curve are shown in Fig. C.2. The blue line and red line represent the low-frequency noise and QPO, respectively. The PDS of these two components is plotted as blue and red lines in the right panel of Fig. C.1. The VMD components show good alignment with the simulated components.In Fig. C.3, we assess the reliability of this method by showing the correlations between the simulated results and the decomposed results, including the QPO count rate and QPO phases in the top panels. The bottom panels show histograms of the count rate difference and phase difference between the simulated QPO and decomposed QPO signals, respectively. The red dashed lines in both the top and bottom panels represent perfect alignment between the two signals. We find that the structure of the decomposed QPO is highly consistent with that of the simulated QPO signal, though with local fluctuations, possibly due to mode mixing between the QPO and noise components, or statistical fluctuations. Specifically, in the right top panel of Fig. C.3, a small number of data points are distributed in the upper left and lower right of the plot, corresponding to the phase difference distributed around -2π and 2π in the right bottom panel. Since the QPO phase varies from $-\pi$ and $-\pi$, this phenomenon reflects local phase shifts between the simulated and decomposed QPO signals in a small portion of time bins.

Manuscript 2

Dai, X., et al.: A&A, 692, A117 (2024)

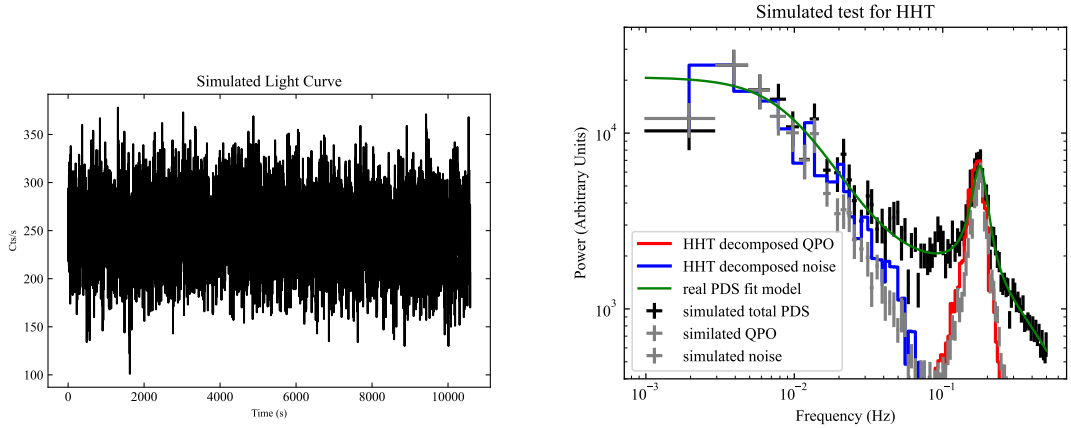


Fig. C.1. Simulated light curve and power density spectrum (PDS) analysis. Left panel: Simulated light curve with two broadband noise components at different break frequencies and one QPO signal at ~ 0.18 Hz. Right panel: PDS of the simulated light curve (black points) and the fitting model of the real PDS (green line). The gray lines represent the simulated low-frequency noise and QPO components in the PDS. The blue and red lines represent the VMD components of noise and the QPO signal in the PDS.

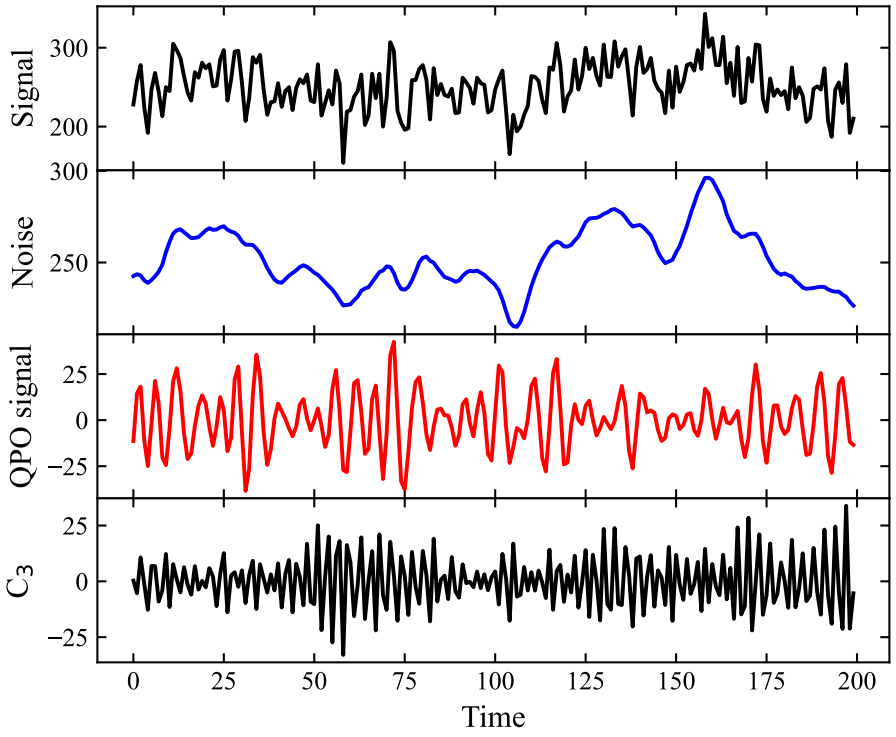


Fig. C.2. IMFs obtained from the VMD of the simulated light curve. The blue and red lines represent the low-frequency noise and QPO signals, respectively.

Manuscript 2

Dai, X., et al.: A&A, 692, A117 (2024)

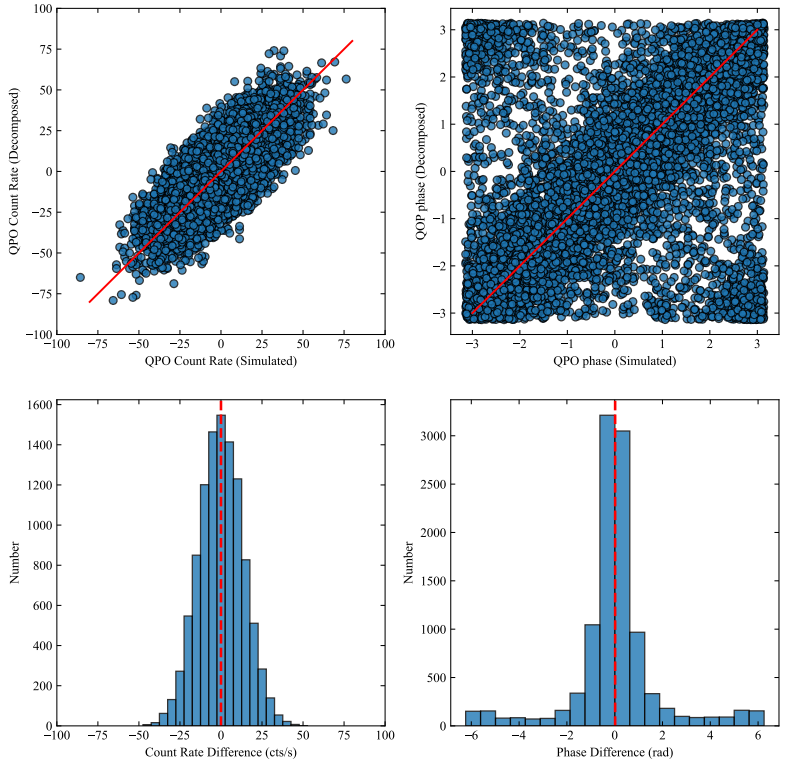


Fig. C.3. Comparison between simulated and decomposed QPO signals. Top panels: Correlations between the simulated results and decomposed results, including the QPO count rate and QPO phases. Bottom panels: Histograms of the count rate difference and phase difference between the simulated QPO and decomposed QPO signals. The dashed red lines in both the top and bottom panels represent the case where the two signals are in perfect alignment.

Manuscript 3

A&A 661, A25 (2022)
https://doi.org/10.1051/0004-6361/202141878
© F. Haberl et al. 2022

Astronomy & Astrophysics

The Early Data Release of eROSITA and Mikhail Pavlinsky ART-XC on the SRG mission

Special issue

eROSITA calibration and performance verification phase: High-mass X-ray binaries in the Magellanic Clouds

F. Haberl[1], C. Maitra[1], S. Carpano[1], X. Dai[2], V. Doroshenko[2], K. Dennerl[1], M. J. Freyberg[1], M. Sasaki[3], A. Udalski[4], K. A. Postnov[5,6], and N. I. Shakura[5,6]

[1] Max-Planck-Institut für extraterrestrische Physik, Gießenbachstraße 1, 85748 Garching, Germany
e-mail: fwh@mpe.mpg.de
[2] Institut für Astronomie und Astrophysik, Sand 1, 72076 Tübingen, Germany
[3] Dr. Karl-Remeis-Sternwarte und ECAP, Universität Erlangen-Nürnberg, Sternwartstraße 7, 96049 Bamberg, Germany
[4] Astronomical Observatory, University of Warsaw, Al. Ujazdowskie 4, 00-478 Warszawa, Poland
[5] Moscow State University, Sternberg Astronomical Institute, 119234 Moscow, Russia
[6] Kazan Federal University, Department of Astronomy and Space Geodesy, 420008 Kazan, Russia

Received 26 July 2021 / Accepted 25 August 2021

ABSTRACT

Context. During its performance verification phase, the soft X-ray instrument eROSITA on board the Spektrum-Roentgen-Gamma (SRG) spacecraft observed large regions in the Magellanic Clouds in which almost 40 known high-mass X-ray binaries (HMXBs, including candidates) are located.
Aims. We looked for new HMXBs in the eROSITA data, searched for pulsations in HMXB candidates, and investigated the long-term behaviour of the full sample using archival X-ray and optical data.
Methods. For sufficiently bright sources, we performed a detailed spectral and temporal analysis of their eROSITA data. A source detection analysis of the eROSITA images in different energy bands provided count rates and upper limits for the remaining sources.
Results. We report the discovery of a new Be/X-ray binary in the Large Magellanic Cloud. The transient SRGEt J052829.5−690345 was detected with a 0.2–8.0 keV luminosity of $\sim 10^{35}$ erg s^{-1}. It exhibits a hard X-ray spectrum, typical for this class of HMXBs. The OGLE *I*-band light curve of the $V \sim 15.7$ mag counterpart shows large variations up to 0.75 mag, which occur with a quasi-period of ∼511 days. The eROSITA observations of the Small Magellanic Cloud covered 16 Be/X-ray binary pulsars, 5 of which were bright enough for an accurate determination of their current pulse period. The pulse periods for SXP 726 and SXP 1323 measured from eROSITA data are ∼800 s and ∼1006 s, respectively, which is very different from their discovery periods. Including archival *XMM-Newton* observations, we update the spin-period history of the two long-period pulsars, which have shown nearly linear trends in their period evolution for more than 15 yr. The corresponding average spin-down rate for SXP 726 is 4.3 s yr^{-1}, while SXP 1323 has a spin-up rate of −23.2 s yr^{-1}. We discuss the spin evolution of the two pulsars in the framework of quasi-spherical accretion.

Key words. stars: emission-line, Be – stars: neutron – X-rays: binaries – galaxies: clusters: individual: LMC – galaxies: clusters: individual: SMC

1. Introduction

The Magellanic Clouds (MCs) are ideal laboratories for studying X-ray source populations in star-forming galaxies. They are relatively nearby with accurately known distances (50 kpc for the Large Magellanic Cloud, LMC, and 62 kpc for the Small Magellanic Cloud, SMC; Pietrzyński et al. 2019; Graczyk et al. 2014), and X-ray observations are little affected by Galactic foreground absorption. However, it should be noted that in particular the SMC is significantly extended along the line of sight (Tatton et al. 2021; Subramanian & Subramaniam 2009). While the SMC was largely covered by a mosaic of pointed observations with *XMM-Newton* (Sturm et al. 2013b; Haberl et al. 2012), the large extent of the LMC on the sky allowed only partial mapping (Maggi et al. 2016).

The *XMM-Newton* surveys of the MCs enlarged the number of known high-mass X-ray binaries, which are binary systems with a massive early-type star and a compact object that in most cases is a neutron star. The majority of the HMXBs in the MCs forms the subgroup of Be/X-ray binaries, in which a neutron star accretes matter from the circum-stellar disc of a Be star (BeXRBs; see Reig 2011, for a review). On the other hand, supergiant systems (SgXRBs), powered by accretion from the strong stellar wind, are less abundant. This is particularly true for the SMC, in which only one SgXRB (SMC X-1) but about 120 BeXRBs are known, half of which are confirmed X-ray pulsars (Haberl & Sturm 2016). On the other hand, ∼60 HMXB candidates were identified in the LMC, with detected pulsations in about 20 of them. The fraction of SgXRBs is somewhat higher in the LMC than in the SMC (Maitra et al. 2021, 2019a; van Jaarsveld et al. 2018; Vasilopoulos et al. 2018), which is probably related to the different star formation histories of the two clouds (Antoniou & Zezas 2016; Antoniou et al. 2010).

2. eROSITA observations

eROSITA, the soft X-ray instrument on board the Spektrum-Roentgen-Gamma (SRG) mission (Predehl et al. 2021), was successfully launched from Baikonur on July 13, 2019. After the instruments were commissioned, first-light observations, including an observation pointed at SN 1987A in the LMC

Open Access article, published by EDP Sciences, under the terms of the Creative Commons Attribution License (https://creativecommons.org/licenses/by/4.0), which permits unrestricted use, distribution, and reproduction in any medium, provided the original work is properly cited.
Open Access funding provided by Max Planck Society.

Manuscript 3

A&A 661, A25 (2022)

Table 1. Observation details.

ObsID [a]	TM [b]	Time UT	Exposure [c] (ks)	Pointing RA, Dec	Target
700016	3,4	2019-09-15 09:28:20 – 2019-09-16 21:30:00	25 002	83.83637,-69.31139	SN 1987A
700161	1-7	2019-10-18 16:54:34 – 2019-10-19 15:07:54	71 544	83.83638,-69.31139	SN 1987A FL
700156	5-7	2019-10-10 01:58:14 – 2019-10-10 15:18:14	19 349	81.25917,-69.64417	N 132D
700179	1-7	2019-11-22 15:44:11 – 2019-11-23 08:24:11	59 549	81.25917,-69.64417	N 132D
700184 [d]	1-7	2019-11-23 21:04:51 – 2019-11-24 08:11:31	34 702	80.68758,-69.37765	N 132D off-axis
700185 [d]	1-7	2019-11-25 08:03:01 – 2019-11-25 19:09:41	20 594	81.90048,-69.89292	N 132D off-axis
700183 [d]	1-7	2019-11-25 19:13:51 – 2019-11-26 06:20:31	33805	81.9935,-69.43154	N 132D off-axis
700182	1-7	2019-11-27 06:11:41 – 2019-11-27 17:18:21	31 483	80.51012,-69.85367	N 132D off-axis
700205	1-7	2019-12-07 13:00:00 – 2019-12-07 21:14:00	18 839	84.44442,-69.17140	PSR J0537−6910
700206	1-7	2019-12-07 21:20:00 – 2019-12-08 02:50:00	15 344	85.04515,-69.33173	PSR J0540−6919
700207	1-7	2019-12-08 02:56:00 – 2019-12-08 13:00:00	22 255	84.74217,-69.25035	PSR J0540 and J0537
700001	1-7	2019-11-07 17:13:18 – 2019-11-08 09:53:18	54 610	16.00833,-72.03194	1E 0102.2−7219
700002	1-7	2019-11-08 09:57:18 – 2019-11-09 02:37:18	58714	15.03687,-71.88838	1E 0102.2−7219 off-axis
700003	1-7	2019-11-09 02:41:38 – 2019-11-09 19:21:38	59 931	16.99466,-72.17060	1E 0102.2−7219 off-axis
700004	1-7	2019-11-09 19:25:38 – 2019-11-10 10:42:18	55 594	16.28235,-71.85088	1E 0102.2−7219 off-axis
700005	1-7	2019-11-10 10:45:48 – 2019-11-11 02:02:28	55 672	16.41901,-71.76044	1E 0102.2−7219 off-axis
710000 [e]	1-7	2020-06-18 20:00:00 – 2020-06-19 06:00:00	37 056	16.00833,-72.03194	1E 0102.2−7219

Notes. [a]eROSITA observation ID. [b]Active telescope modules. [c]Maximum exposure from vignetting-corrected exposure map normalised to one TM, i.e. total exposure divided by 7. In this way, the resulting count rates in the source detection lists are for the total of seven TMs even when not all TMs were active. [d]During part of these observations, the electronic chopper was set to 2, which was not handled correctly by the pipeline processing. We corrected this in the event files (see Appendix A). [e]Calibration observation near the end of the first eROSITA all-sky survey (eRASS1).

(Maitra et al. 2022) were performed, followed by a calibration and performance verification phase when pointed observations of selected targets were conducted. Henceforth, we call this phase of pointed observations before the start of the all-sky survey on December 13, 2019, the CalPV phase. A summary of the CalPV observations performed in the direction of LMC and SMC can be found in Table 1. The current publication focuses on the analysis of these observations and reports first results obtained by eROSITA for the LMC and the SMC.

To analyse the CalPV data, we used the eROSITA Standard Analysis Software System (`eSASS` version `eSASSusers_201009`, Brunner et al. 2022). The `eSASS` pipeline processing provides energy-calibrated event files that were used to create images, detect point sources, and extract spectra and light curves of the detected objects. While for images and light curves we used data from all seven telescope modules (Predehl et al. 2021), only telescope modules with on-chip optical blocking filter (TM1–TM4 and TM6) were used for spectroscopy because no reliable energy calibration is available for TM5 and TM7 so far because an optical light leak was discovered soon after the start of the CalPV phase (Predehl et al. 2021).

We extracted eROSITA light curves and spectra using the `eSASS` task `srctool` from circular or (at larger off-axis angles) elliptical regions around the source position and a nearby source-free background region. Events from all valid pixel patterns (PATTERN = 15) were selected. For the spectral analysis, we combined the data from the five on-chip filter cameras into a single spectrum. The spectra were binned to achieve a minimum of 20 counts per spectral bin to allow the use of χ^2-statistic. Corresponding response files were created by `srctool`.

Spectral analysis was performed using `XSPEC` v12.11.0k (Arnaud 1996). To account for the photo-electric absorption by the Galactic interstellar gas, we used `tbabs` in `XSPEC` with solar abundances following Wilms et al. (2000) with atomic cross sections from Verner et al. (1996). The Galactic column density was taken from Dickey & Lockman (1990) and was fixed in the fits. For the absorption along the line of sight through the LMC/SMC and local to the source, we included a second absorption component when required, with elemental abundances fixed at 0.49/0.20 solar (Rolleston et al. 2002; Luck et al. 1998), respectively, and left the column density free in the fit. Errors were estimated at 90% confidence intervals. To compute the X-ray luminosity, distances of 50 and 60 kpc were assumed for the LMC and SMC, respectively. Throughout the paper, we provide observed fluxes and absorption-corrected luminosities.

3. HMXBs covered by the eROSITA CalPV observations

The large (∼1° diameter) field of view (FoV) of the eROSITA telescopes implies that CalPV observations pointed towards the LMC around SN 1987A and N 132D overlap and cover a contiguous area of 4.4 square degrees. Therefore we produced mosaic images from the merged calibrated event file (combining data from all available cameras and observations) in three energy bands (red: 0.2–1.0 keV, green: 1.0–2.0 keV, and blue: 2.0–4.5 keV). The images were adaptively smoothed and divided by vignetting-corrected exposure maps to obtain count-rate images. The corresponding RGB mosaic image is shown in Fig. 1. The detector background was not yet subtracted from the images because more data with the filter wheel closed are still to be collected to construct a reliable background model. This leads to a slight over-correction of the detector-background component in the images towards the edges of the FoV, but does not affect our analysis of point sources where a local full background subtraction is applied. Similarly, the observations of the SMC

Manuscript 3

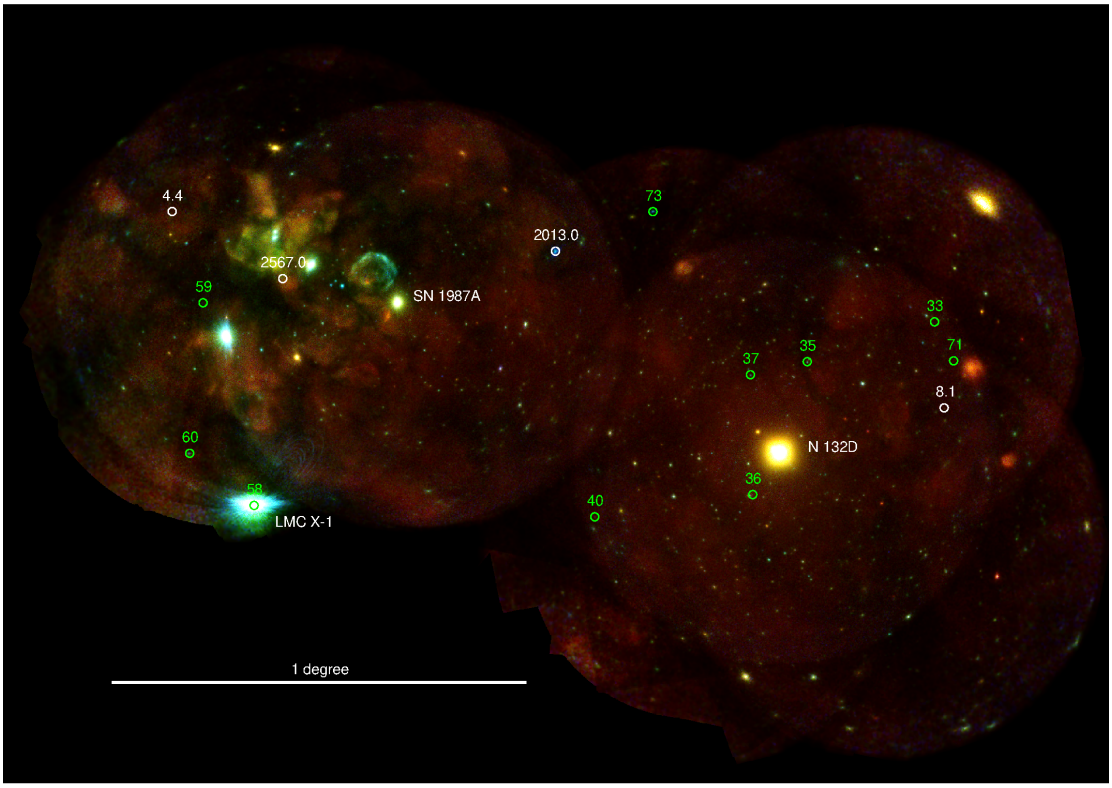


Fig. 1. LMC mosaic from eROSITA observations around SN 1987A and N 132D. Red, green, and blue represent X-ray energies in the bands 0.2–1.0 keV, 1.0–2.0 keV, and 2.0–4.5 keV, respectively. The HMXB pulsars are marked with white circles and labelled with their pulse period measured near the time of their discovery. HMXBs and candidates without known pulse period are indicated by green circles and the entry number from Table 2.

supernova remnant 1E 0102.2−7219 (placed at different off-axis angles) cover an area of 2.5 square degrees, and the RGB image is presented in Fig. 2.

For each observation, the eROSITA pipeline system perf orms source detection, based on a maximum likelihood point spread function (PSF) fitting algorithm, simultaneously on the images from the available TMs in the three energy bands 0.2–0.6 keV, 0.6–2.3 keV, and 2.3–5.0 keV (Brunner et al. 2022). We correlated the source detection lists with the catalogues of HMXBs (see below) with a matching radius of 10″ to determine which of the known HMXBs were detected at which brightness. Upper limits were derived for the non-detections from the sensitivity maps using the `eSASS` task `apetool`. Tables 3 and 5 summarise the detections and upper limits for all HMXBs observed in the LMC and SMC, respectively. Count rates are reported for the 0.2–5 keV energy band and all rates given in subsections describing the sources refer to this band, unless otherwise noted.

The available data cover several epochs, which also allows investigating the variability of the detected sources on several timescales. The observations of the LMC were irregularly distributed in time over nearly three months, whereas five of the SMC observations were performed consecutively, followed by an observation centred on 1E 0102.2−7219 about seven months later, providing two epochs for the HMXBs located within 0.5° of the supernova remnant.

4. LMC field

The CalPV observations of the LMC cover 14 (candidate) HMXBs that include 9 well-confirmed cases (4 X-ray pulsars). These objects are listed in Table 2 and marked in the image presented in Fig. 1. We used the numbering scheme from an HMXB catalogue of the LMC in preparation, similar to that of the SMC (Haberl & Sturm 2016). For 2 cases, the identification of the optical counterpart is still uncertain (cases 37 and 60), while the 3 remaining candidates for BeXRBs (candidates 33, 35, and 36) did not show significant Hα emission during optical spectroscopy, as reported by van Jaarsveld et al. (2018). The image shows that except for the persistently bright black hole system LMC X-1, only one source was sufficiently bright for a detailed spectroscopic and temporal analysis. This is the supergiant fast X-ray transient (SFXT) XMMU J053108.3−690923 (marked with its pulse period of 2013 s in the image), for which the eROSITA results have been presented in Maitra et al. (2021). One new BeXRB was discovered in this work (SRGEt J052829.5−690345, source 73 in Table 2 and Fig. 1). It is described in detail in the following section.

4.1. SRGEt J052829.5−690345, a new BeXRB in the LMC

Source position and optical counterpart. The faint transient SRGEt J052829.5−690345 was discovered in the eROSITA

Manuscript 3

A&A 661, A25 (2022)

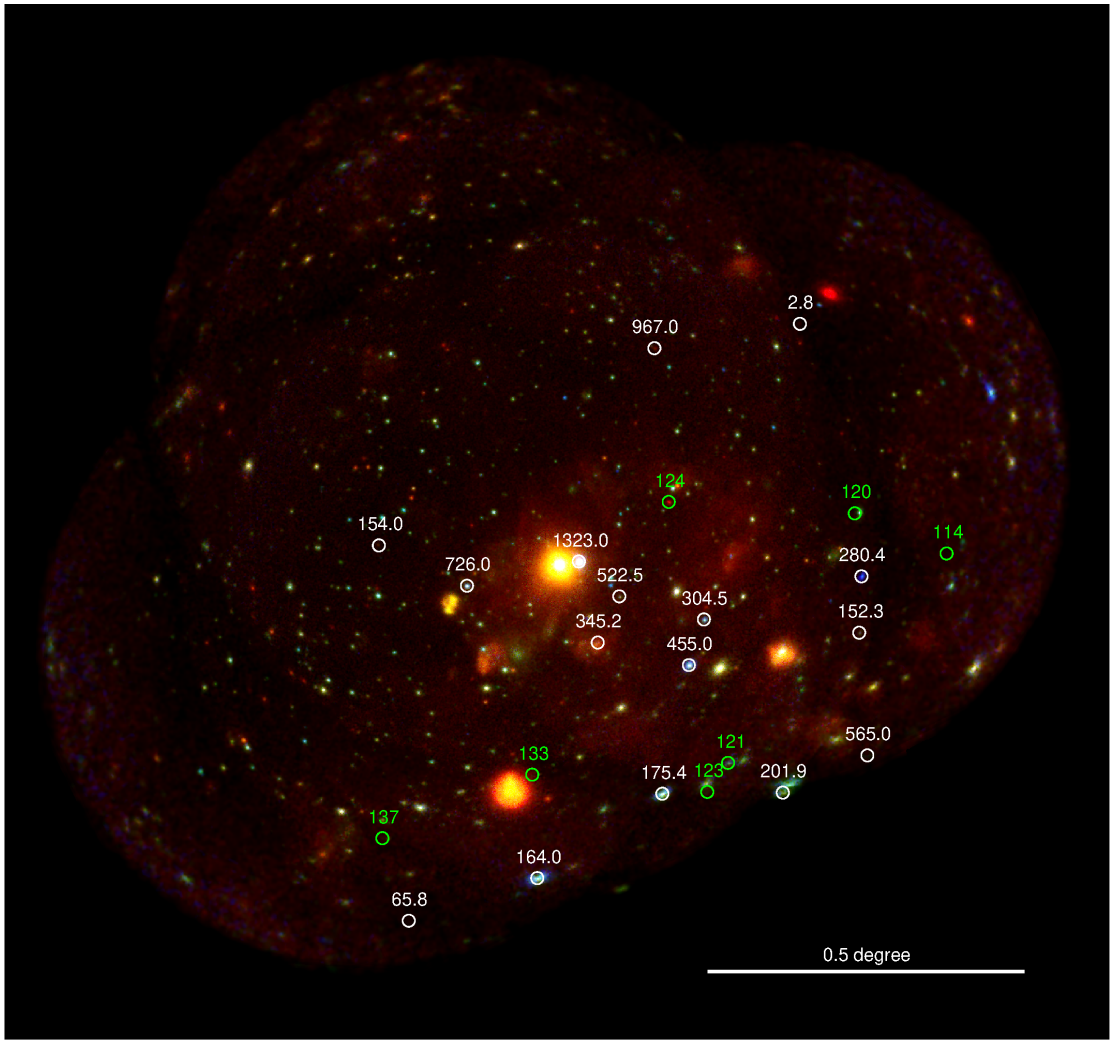


Fig. 2. SMC mosaic from eROSITA observations around the supernova remnant 1E 0102.2−7219, the brightest source near the image centre. Image colours and labels for the HMXB pulsars are as in Fig. 1. HMXBs without known pulse period are indicated by green circles and their entry number from HS16 (see Table 4).

data of the calibration observation 700183 of the supernova remnant N132D performed in November 2019 (Table 1). SRGEt J052829.5−690345 appears as a blue source in the eROSITA colour image (Fig. 3), indicating a hard X-ray spectrum. Source detection resulted in an X-ray source position of RA (2000) = $05^h28^m29^s.1$, Dec = $-69°03'51''$ with a statistical 1σ uncertainty of $1.2''$. The eROSITA position is thereby $7''$ from a star with $V = 15.70$ mag, $B = 15.90$ mag, $U = 15.08$ mag, and $R = 16.66$ mag (Massey 2002) with coordinates RA = $05^h28^m29^s.34$, Dec = $-69°03'44''.7$, as listed in the *Gaia* DR2 catalogue (Gaia Collaboration 2018). The brightness and colours of this star are typical for an early-B star in the LMC, suggesting a new BeXRB.

The observation also covers the supergiant fast X-ray transient (SFXT) XMMU J053108.3−690923 (Maitra et al. 2021) at a similar off-axis angle. The SFXT is securely identified with a supergiant in the LMC. The eROSITA position for this source is also shifted by a similar value ($6.6''$)[1] and in the same direction with respect to the optical counterpart. Therefore we used the SFXT for astrometric correction and obtained RA = $05^h28^m29^s.57$, Dec = $-69°03'45''.5$ for the refined coordinates of the new BeXRB candidate. The corrected X-ray position is $1.5''$ from that of the proposed optical counterpart, which is compatible within the errors. We use these coordinates for the

[1] This shift is consistent with the values obtained from other eROSITA observations (Brunner et al. 2022, Lamer et al., in prep.). These papers describe statistical methods for determining astrometric corrections using large samples of objects. In the case of the MCs, this is more difficult as only few sources in the FoV have secure optical counterparts (see Maitra et al. 2019b; Sturm et al. 2013b).

Manuscript 3

Table 2. HMXBs in the LMC.

No.	Type	X-ray source names	Spin (s)	AZ16	References
71	Be/SSS	XMMU J052016.0−692505	–	–	KHP06
5	Be/X	RX J0520.5−6932	8.04	14	VHS14
33	Be/X?	XMMU J052049.1−691930 Halpha?	–	–	[VBM18]7
35	Be/X?	XMMU J052417.1−692533 Halpha?	–	–	[VBM18]8
36	Be/X?	XMMU J052546.4−694450 Halpha?	–	–	[VBM18]9
37	Be/X??	XMMU J052550.7−692729 ID?	–	–	[VBM18]18
73	Be/X	SRGEt J052829.5−690345	–	–	This work
40	Be/X	XMMU J053010.8−694755	–	–	[VBM18]11
43	SFXT	XMMU J053108.3−690923	2013	–	VMH18, MHV20
18	Be/X?	CXOU J053833.4−691158	2567	46	CBB15
58	SG/BH	LMC X−1	–	37	
59	Be/X	XMMU J054045.4−691452	–	–	[VBM18]19
60	SG?	RX J0541.4−6936 ID?	–	39	SHP00
3	Be/X	IGR J05414−6858	4.42	38	RSG10, SHR12

Notes. HMXBs covered by the eROSITA calibration and performance verification observations of the LMC.

References. AZ16: Antoniou & Zezas (2016), CBB15: Clark et al. (2015), KHP06: Kahabka et al. (2006), MHV21: Maitra et al. (2021), RSG10: Rau et al. (2010), SHP00: Sasaki et al. (2000), SHR12: Sturm et al. (2012b), VBM18: van Jaarsveld et al. (2018), VHS14: Vasilopoulos et al. (2014), and VMH18: Vasilopoulos et al. (2018).

Table 3. HMXBs in the LMC: Variability between observations.

No.	700016 2019-09-15	700161 2019-10-18	700156 2019-10-10	700179 2019-11-22	700184 2019-11-23	700185 2019-11-25
71	–	–	$<4.6\times10^{-3}$	$<5.2\times10^{-3}$	$<2.0\times10^{-3}$	–
5	–	–	$<5.8\times10^{-3}$	$5.40\pm1.28\times10^{-3}$	$6.79\pm0.93\times10^{-3}$	–
33	–	–	$<2.9\times10^{-3}$	$<6.6\times10^{-3}$	$<1.6\times10^{-3}$	–
35	–	–	$1.14\pm0.15\times10^{-2}$	$1.51\pm0.09\times10^{-2}$	$1.33\pm0.10\times10^{-2}$	–
36	–	–	$<1.8\times10^{-3}$	$<2.9\times10^{-3}$	$<1.0\times10^{-2}$	$<3.0\times10^{-3}$
37	–	–	$<2.7\times10^{-3}$	$5.59\pm0.62\times10^{-3}$	$6.81\pm1.21\times10^{-3}$	$<5.7\times10^{-3}$
73	–	–	–	–	–	–
40	–	–	$1.47\pm0.31\times10^{-2}$	$1.05\pm0.09\times10^{-1}$	–	$7.34\pm1.29\times10^{-3}$
43	$1.27\pm0.04\times10^{-1}$	$5.61\pm0.81\times10^{-3}$	–	–	–	–
18	$<8.3\times10^{-3}$	$<7.4\times10^{-3}$	–	–	–	–
59	–	$<4.5\times10^{-3}$	–	–	–	–
60	–	–	–	–	–	–
3	–	–	–	–	–	–

No.	700183 2019-11-25	700182 2019-11-27	700205 2019-12-07	700206 2019-12-07	700207 2019-12-08
71	–	$<4.4\times10^{-3}$	–	–	–
5	–	$7.09\pm1.45\times10^{-3}$	–	–	–
33	–	–	–	–	–
35	$<3.8\times10^{-3}$	$<8.9\times10^{-3}$	–	–	–
36	$<8.3\times10^{-3}$	$<9.2\times10^{-3}$	–	–	–
37	$5.61\pm0.81\times10^{-3}$	–	–	–	–
73	$3.99\pm0.24\times10^{-2}$	–	–	–	–
40	$7.21\pm1.77\times10^{-3}$	–	–	–	–
43	$1.69\pm0.05\times10^{-1}$	–	–	–	–
18	–	–	$<2.7\times10^{-3}$	$<2.6\times10^{-3}$	$<2.2\times10^{-3}$
59	–	–	$<1.5\times10^{-3}$	$<4.2\times10^{-3}$	$<1.5\times10^{-3}$
60	–	–	$1.73\pm0.09\times10^{-1}$	$<6.6\times10^{-3}$	$2.11\pm0.11\times10^{-1}$
3	–	–	$<5.7\times10^{-3}$	$<9.0\times10^{-3}$	$<5.2\times10^{-3}$

Notes. Background-subtracted, PSF, and vignetting-corrected source count rates (cts s^{-1}) are obtained from source detection and are given for the 0.2–5.0 keV band normalised to seven telescope modules. We exclude LMC X-1 here due to its brightness, which causes strong photon pile-up effects. Numbers without error and marked with "<" denote upper limits (3σ) for undetected sources in the FoV, derived from sensitivity maps produced by the `eSASS` task `apetool`.

Manuscript 3

A&A 661, A25 (2022)

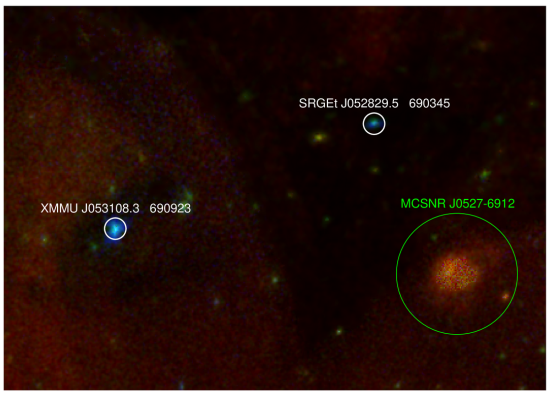


Fig. 3. eROSITA colour image (red: 0.2–1.0 keV, green: 1.0–2.0 keV, and blue: 2.0–4.5 keV) of the region around SRGEt J052829.5−690345. The transient source appears similar in colours to the SFXT XMMU J053108.3−690923 (Maitra et al. 2021), which is located at an angular distance of ∼15′. The soft extended X-ray emission from the supernova remnant MCSNR J0527-6912 (e.g. Maggi et al. 2016) is also marked.

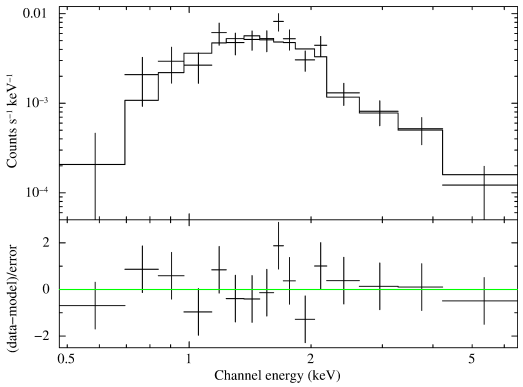


Fig. 4. Combined eROSITA spectrum of SRGEt J052829.5−690345 from the cameras with on-chip filter (TM1–4 and TM6). The best-fit absorbed power-law model is shown as a histogram, and the residuals are plotted in the bottom panel.

source name following the SRG/eROSITA convention for a new transient: SRGEt J052829.5−690345.

The position of the transient SRGEt J052829.5−690345 was covered by two *XMM-Newton* pointed observations (observation IDs 0690743501/3601) at large off-axis angles and during many slews with the European Photon Imaging Camera (EPIC; Strüder et al. 2001; Turner et al. 2001). The observations were performed consecutively between September 4, 2012, 16:55 and September 5, 2012, 11:25 as part of the *XMM-Newton* LMC survey (PI Haberl). The source was not detected, and we derived 3 σ upper limits in the 0.2–4.5 keV energy band of 1.6×10^{-3} cts s^{-1}, 1.6×10^{-3} cts s^{-1} and 3.4×10^{-3} cts s^{-1} from the EPIC-MOS1, MOS2, and pn sensitivity maps, respectively. The upper limits during slew are typically more than a factor 100 higher and not constraining.

Spectral analysis. As described above, we extracted eROSITA spectra (with a total net exposure of 28.4 ks) from circular regions around the source position (radius 25″)[2] and a nearby source-free background region (radius 50″). An absorbed power-law model yields an acceptable fit (reduced $\chi^2 = 0.8$ for 13 degrees of freedom, dof) to the eROSITA spectrum (Fig. 4). The power-law index of $0.66^{+0.74}_{-0.54}$, although with a large error, is within the range observed for BeXRBs in the Magellanic Clouds (e.g. Haberl & Sturm 2016), and the LMC absorption, required in addition to the Galactic foreground (fixed at 6.2×10^{20} cm^{-2}), is $1.0^{+1.0}_{-0.6} \times 10^{22}$ cm^{-2}. The observed 0.2–8.0 keV flux is 3.4×10^{-13} erg cm^{-2} s^{-1}, which results in a soft X-ray source luminosity of 1.2×10^{35} erg s^{-1}.

Using WebPIMMS[3] and the eROSITA best-fit parameters for a power law with a single column density, the expected 0.2–4.5 keV count rates for EPIC-MOS and pn are 1.3×10^{-2} cts s^{-1} and 3.3×10^{-2} cts s^{-1}, about a factor of 10 higher than the upper limits derived from the *XMM-Newton* observations. Considering the non-detection by *XMM-Newton*, we therefore conclude that the source is a transient, as expected for a BeXRB.

Considering that most known BeXRBs host accreting neutron stars, we also carried out a search for possible X-ray pulsations. Unfortunately, the search did not reveal any significant signal because of the low statistics. From the extraction region, a total of 330 counts is available, with ∼100 counts background contribution, which does not allow placing meaningful limits on the amplitude of possible pulsations either.

OGLE long-term monitoring. The region around the new BeXRB candidate SRGEt J052829.5−690345 was monitored regularly in the I and V bands with the Optical Gravitational Lensing Experiment (OGLE; Udalski et al. 2008, 2015). Images were taken in V- and I-filter bands, and photometric magnitudes are calibrated to the standard VI system.

The optical counterpart of SRGEt J052829.5−690345 was covered for about 18.5 yr during OGLE phases III (star lmc161.4.31169) and IV (lmc517.06.71858), as shown in Figs. 5 and 6. Both light curves exhibit remarkable variations by up to 0.75 mag in the I band. A Lomb-Scargle (LS) analysis of the I-band light curve reveals that these variations occur quasi-periodically and repeat every ∼511 days. The outbursts show different durations, which lead to phase shifts. This behaviour is very similar to that of the optical counterpart of another BeXRB: RX J0529.8−6556 (Treiber et al. 2021). The authors suggest this to be resulting from a misalignment of the Be star disc with respect to the orbital plane, which causes precession of the disc.

The OGLE V-band observations provided a less frequent coverage of the BeXRB system than the I-band observations. To compute the $I-V$ colour index, we chose the I-band magnitude nearest in time to the V-band measurement, disregarding those more than two days apart. The colour index $I-V$ is shown as a function of the I-band magnitude in Fig. 7. Large colour variations with brightness (redder when brighter) become apparent especially during the deep dips seen in the light curves.

4.2. XMMU J052417.1−692533, a BeXRB without significant Hα emission?

van Jaarsveld et al. (2018) selected 19 candidate BeXRBs from *XMM-Newton* observations of the LMC based on X-ray hardness

[2] The half-energy width of the telescope PSF is about 16″ at 1.5 keV (Predehl et al. 2021).
[3] https://heasarc.gsfc.nasa.gov/cgi-bin/Tools/w3pimms/w3pimms.pl

Manuscript 3

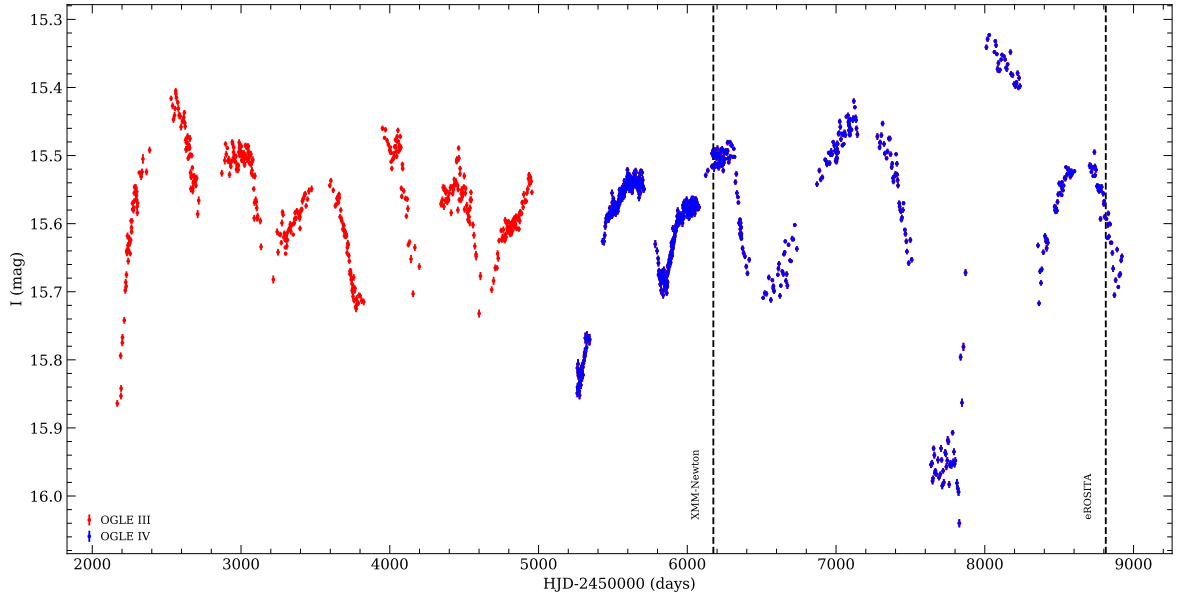


Fig. 5. OGLE *I*-band light curve of SRGEt J052829.5−690345 between September 15, 2001, and March 13, 2020. The vertical dashed lines indicate the times of the eROSITA and archival *XMM-Newton* observations.

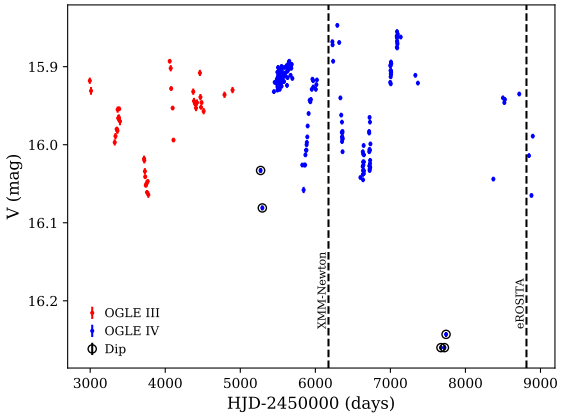


Fig. 6. OGLE *V*-band light curve of SRGEt J052829.5−690345. See also Fig. 5. The data points marked with additional black circles indicate two deep dips in the light curve that show extreme colours (see Fig. 7).

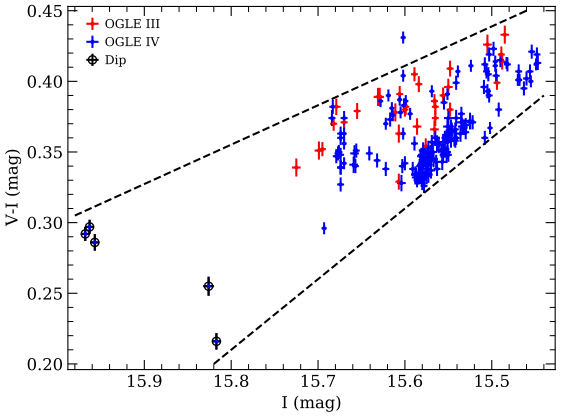


Fig. 7. OGLE $V - I$ colour index vs. I (interpolated linearly to the times of the *V*-band measurements). The data points marked with additional black circles originate from two deep dips in the light curve (see also Fig. 6). $V - I$ is correlated with I in a well-defined region of the parameter space, as indicated by the dashed lines.

ratio criteria. They present the results from optical spectroscopy and the analysis of the OGLE data of the proposed counterparts. Six of their candidates were covered by the eROSITA observations (reference [VBM18] in Table 2), and the proposed counterparts of three of these did not exhibit significant Hα emission (sources 33, 35, and 36), which makes their BeXRB identification doubtful. XMMU J052049.1−691930 (source 33) and XMMU J052546.4−694450 (source 36) were not detected in the eROSITA data, therefore we lack further information on their nature.

The position of XMMU J052417.1−692533 (source 35) was covered by three observations (700156, 700179, and 700184), from which similar count rates were obtained. Two observations yielded no detection (see Table 3). The upper limits indicate variability of at least a factor of four on a timescale of six weeks. The eROSITA positions obtained from the three detections have angular separations of 4.4″, 3.0″, and 6.5″ from the optical position of the $V = 16$ mag early-type star, which is proposed as optical counterpart (for more information on the star, see van Jaarsveld et al. 2018). Because of the current uncertainties in the astrometry of the CalPV observations (see Sect. 4.1), the X-ray position obtained from *XMM-Newton* is more reliable (see van Jaarsveld et al. 2018).

Manuscript 3

A&A 661, A25 (2022)

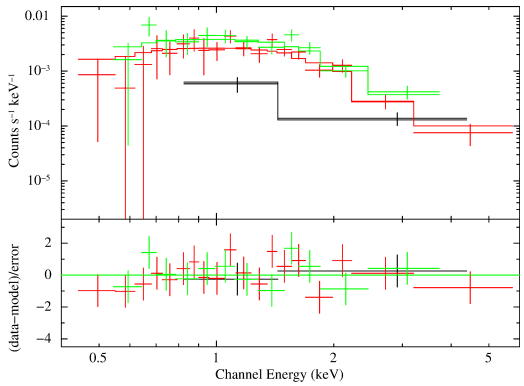


Fig. 8. Combined eROSITA spectra of XMMU J052417.1−692533 from the cameras with on-chip filter (TM1–4 and TM6). The best-fit absorbed power-law model is shown as a histogram, and the residuals are plotted in the bottom panel. The different colours indicate the observations 700156 (black), 700179 (red), and 700184 (green). The spectrum from observation 700156 includes data from TM6 only (see Table 1).

We extracted and analysed the eROSITA spectra of XMMU J052417.1−692533 in a similar way as for SRGEt J052829.5−690345 (Sect. 4.1). Because of a nearby source, the extraction regions were chosen smaller (15″ and 25″ for source and background regions, respectively). The spectra from the three observations (with a total net exposure of 135 ks) were fitted simultaneously with a power-law model. Absorption (foreground $N_{\rm H}$ fixed at 6.2×10^{20} cm^{-2}) and photon index were assumed to be constant between the observations, only the power-law normalisation was free in the fit to follow the flux variations. The spectra with the best-fit model are shown in Fig. 8. The model formally yields an acceptable fit (reduced $\chi^2=0.73$ for 29 dof) to the eROSITA spectra. The power-law index of 0.92 ± 0.22 is typical for BeXRBs in the MCs (e.g. Haberl & Sturm 2016), excluding a background active galactic nucleus and supporting the identification of the X-ray source with the early-type star. For the LMC absorption, no significant $N_{\rm H}$ was required in the fit, but the systematic residuals might indicate a more complex spectrum at energies below ∼1 keV. The 0.2–8.0 keV flux might vary slightly between observations, but is consistent within the 90% errors: $7.9^{+3.0}_{-2.6}\times10^{-14}$ erg cm^{-2} s^{-1}, $6.3^{+1.4}_{-1.5}\times10^{-14}$ erg cm^{-2} s^{-1}, and $7.2^{+1.5}_{-1.7}\times10^{-14}$ erg cm^{-2} s^{-1} (ordered in time), which corresponds to an average X-ray luminosity of 2.2×10^{34} erg s^{-1}.

5. SMC field

eROSITA performed five calibration observations consecutively in November 2019, one centred on 1E 0102.2−7219, and in the other four, the supernova remnant is offset in different directions (Table 1). This results in different off-axis angles for the sources covered by several observations and does not allow us to immediately handle the five observations as one long observation (duration ∼3.4 days). However, we concatenated light curves after they were background subtracted and corrected for vignetting and PSF losses. Similarly, spectra were extracted for each observation and were analysed simultaneously. A sixth observation in June 2020 was again centred on 1E 0102.2−7219, allowing further long-term studies of sources located within ∼30′ of the supernova remnant.

In total, the observations of the SMC cover 23 HMXBs, which include 20 well-confirmed cases of Be X-ray binaries (BeXRBs) and 16 X-ray pulsars (including XMMU J010429.4−723136, see below). The (candidate) HMXBs are summarised in Table 4 and are marked in the RGB image that is presented in Fig. 2. The image shows that one of the candidate HMXBs (XMMU J010147.5−715550, number 124; Sturm et al. 2012a) is characterised by a red colour, which indicates a super-soft X-ray source (SSS). SSSs with a Be star as optical counterpart are promising candidates for Be systems with a white dwarf (WD) as compact object (see also Kahabka et al. 2006; Coe et al. 2020). Moreover, in addition to the persistently bright supergiant system SMC X-1, several other classical BeXRBs are detected (with hard X-ray spectrum) that were sufficiently bright for a detailed spectroscopic and temporal analysis. All these are known to be BeXRB pulsars: RX J0101.0−7206, also known as SXP 304; RX J0101.3−721, also known as SXP 455; AX J0103−722, also known as SXP 522; RX J0105.9−720, also known as SXP 726,; and RX J0103.6−7201, also known as SXP 1323. The results from the HMXB XMMU J010429.4−723136, from which 164 s pulsations were discovered in the eROSITA CalPV data (Haberl et al. 2019), are presented in Carpano et al. (2022). The results from the other sources are described below.

5.1. RX J0101.0−7206, or SXP 304, or [HS16] 46

SXP 304 was discovered in ROSAT pointed observations as a highly variable source and was proposed to be a BeXRB (Kahabka & Pietsch 1996). Pulsations at 304 s were discovered using *Chandra*, confirming its nature as a BeXRB pulsar (Macomb et al. 2003).

In November 2019, SXP 304 was detected in the eROSITA observations 700001, 700002, and 700004 and had decreased in flux by more than a factor of two in June 2020 (ObsID 710000). The source was not covered during observation 700003 and was not detected during observation 700005, when it was located very close to the edge of the FoV (see Table 5). For the timing analysis, we used only the two observations with the best statistics, and for the spectral analysis, we analysed the spectra from all observations in which the source was detected. In order to look for periodic signals in the X-ray light curves of this source and other sources, an LS periodogram analysis (Lomb 1976; Scargle 1982) was performed. To determine the spin periods more precisely, an epoch-folding technique was applied (Leahy 1987).

The lower panel of Fig. 9 shows the light curve of SXP 304 obtained from the three observations with a detection. For the LS periodogram (upper panel of Fig. 9), we used only data from the first two observations with better statistical quality. A strong periodic signal at ∼302 s is visible. From the epoch-folding technique, the spin period and corresponding 1σ errors for ObsIDs 700001 and 700002 and combining the two were determined to be 302.21 ± 0.55 s, 302.33 ± 0.60 s, and 302.29 ± 0.27 s, respectively, and they are consistent with each other. This period is consistent with the shortest value of 302.6 ± 0.4 s measured from *XMM-Newton* data in November and December 2005 (Eger & Haberl 2008a), demonstrating that the pulsar shows little long-term period change on a timescale of 15 yr. The pulse profiles are single peaked and exhibit no change in shape between the eROSITA observations. The pulse profile in the energy range of 0.2–10 keV combining both observations is shown in Fig. 10, with a pulsed fraction of 51 ± 11%.

Manuscript 3

Table 4. HMXBs in the SMC.

Type	X-ray source names	Spin (s)	HS16	References
Be/X	XMMU J005605.8−720012	–	114	NLM11, MGB17
Be/X	CXOUJ005736.2-721 934	564.8	54	MFL03, CEG05
Be/X	RX J0057.8−7202 = AXJ0058−72.0	280.3	43	TIY99, SPH03
Be/X	RX J0057.8−7207 = CXOU J005750.3−720756	152.3	33	HS00, SPH03, MFL03
Be/X?	RX J0057.9−7156	–	120	HS00
Be/X	RX J0059.2−7138	2.76	4	H94, KYK00
Be/X	RX J0059.3−7223 = XMMU J005921.0-722 317	201.9	38	KPF99, SPH03, MLM04
Be/X	XMMU J010030.2−722035	–	121	SPH03
Be/X	XMMU J010055.8−722320	–	123	SHP13
Be/X	RX J0101.0−7206	304	46	KP96, MFL03
Be/X	RX J0101.3−7211	455	51	SHK01
Be/SSS	Be+WD? XMMU J010147.5−715550	–	124	SHP12
Be/X	RX J0101.8−7223 = AX J0101.8−7223 = XMMU J010152.4−722336	175	37	HS00, YIT03, TDC11
Be/X	CXOU J010206.6−714115	967	60	HEP08
Be/X	2XMM J010247.4−720449 = Suzaku J0102−7204	522	53	WTE13
Be/X	SAX J0103.2−7209 = AX J0103−722	345.2	50	ICC00, YK98
Be/X	RX J0103.6−7201	1323	62	HS00, HP05, CHS17
Be/X	XMMU J010429.4−723136	164	132	MSH13, MGB17, HCM19
Be/X	RX J0104.5−7221 = XMMU J010435.4−722147	–	133	HS00, SHP13
Be/X	RX J0105.9−7203 = AX J0105.8−7203	726	57	HS00, YIT03, EH08
Be/X	CXOU J010712.6−723533 = RX J0107.1−7235 = AX J0107.2−7234	65.8	24	MCS07
Be/X	XMMU J010743.1−715953	154	34	CHS12
Be/X	CXOU J010744.51−722741.7 = Swift J010745.0−722740	–	137	MSH14, VHM17

Notes. HMXBs covered by the eROSITA calibration observations of the supernova remnant 1E 0102.2−7219, extracted from Haberl & Sturm (2016, HS16).
References. CEG05: Coe et al. (2005), CHS12: Coe et al. (2012), CHS17: Carpano et al. (2017), EH08: Eger & Haberl (2008b), H94: Hughes (1994), HCM19: Haberl et al. (2019), HEP08: Haberl et al. (2008), HP05: Haberl & Pietsch (2005), HS00: Haberl & Sasaki (2000), ICC00: Israel et al. (2000), KP96: Kahabka & Pietsch (1996), KPF99: Kahabka et al. (1999), KYK00: Kohno et al. (2000), MCS07: McGowan et al. (2007), MFL03: Macomb et al. (2003), MGB17: McBride et al. (2017), MLM04: Majid et al. (2004), MSH13: Maggi et al. (2013), MSH14: Maggi et al. (2014), NLM11: Novara et al. (2011), SHK01: Sasaki et al. (2001), SHP12: Sturm et al. (2012a), SHP13: Sturm et al. (2013b), SPH03: Sasaki et al. (2003), TDC11: Townsend et al. (2011), TIY99: Tsujimoto et al. (1999), VHM: Vasilopoulos et al. (2017), WTE13: Wada et al. (2013), YIT03: Yokogawa et al. (2003), YK: Yokogawa & Koyama (1998).

Table 5. HMXBs in the SMC: Variability between observations.

HS16	700001 2019-11-07	700002 2019-11-08	700003 2019-11-09	700004 2019-11-09	700005 2019-11-10	710000 2020-06-18
114	–	$<2.3\times10^{-3}$	–	–	–	–
54	–	$1.14\pm1.76\times10^{-2}$	–	–	–	–
43	$1.90\pm0.20\times10^{-2}$	$2.38\pm1.07\times10^{-2}$	–	–	–	–
33	$4.50\pm1.64\times10^{-3}$	$7.00\pm7.90\times10^{-3}$	–	–	–	–
120	$<2.6\times10^{-3}$	$<2.3\times10^{-3}$	–	–	–	–
4	$<3.3\times10^{-3}$	$2.32\pm4.24\times10^{-3}$	–	$<1.4\times10^{-3}$	$<2.0\times10^{-3}$	–
38	–	$2.36\pm9.53\times10^{-1}$	–	–	–	–
121	$2.40\pm0.17\times10^{-2}$	$2.72\pm1.96\times10^{-2}$	–	–	–	$<3.2\times10^{-3}$
123	$5.11\pm1.37\times10^{-3}$	–	–	–	–	$<5.5\times10^{-3}$
46	$3.21\pm0.12\times10^{-2}$	$3.41\pm1.18\times10^{-2}$	–	$2.41\pm0.17\times10^{-2}$	$<4.0\times10^{-3}$	$1.56\pm0.13\times10^{-2}$
51	$8.68\pm0.20\times10^{-2}$	$1.10\pm2.37\times10^{-1}$	$4.82\pm0.37\times10^{-2}$	$9.27\pm0.30\times10^{-2}$	–	$1.57\pm0.04\times10^{-1}$
124	$6.42\pm0.55\times10^{-3}$	$7.36\pm4.94\times10^{-3}$	–	$8.59\pm0.70\times10^{-3}$	$1.00\pm0.10\times10^{-2}$	$6.89\pm0.89\times10^{-3}$
37	$1.74\pm0.03\times10^{-1}$	–	–	–	–	$2.07\pm0.05\times10^{-1}$
60	$2.84\pm0.73\times10^{-3}$	$2.00\pm3.79\times10^{-3}$	–	$2.60\pm0.58\times10^{-3}$	$<1.7\times10^{-3}$	$1.70\pm0.19\times10^{-2}$
53	$5.34\pm0.48\times10^{-3}$	$5.16\pm6.79\times10^{-3}$	$4.17\pm1.11\times10^{-3}$	$8.56\pm0.88\times10^{-3}$	$1.31\pm0.14\times10^{-2}$	$3.70\pm0.59\times10^{-3}$
50	$<1.4\times10^{-3}$	$<4.8\times10^{-3}$	$<4.2\times10^{-3}$	$<4.3\times10^{-3}$	$<6.6\times10^{-3}$	$<1.9\times10^{-3}$
62	$6.80\pm1.21\times10^{-1}$	$5.19\pm3.13\times10^{-1}$	$4.85\pm0.59\times10^{-1}$	$5.13\pm0.42\times10^{-1}$	$4.55\pm0.14\times10^{-1}$	$8.86\pm2.76\times10^{-2}$
132	$1.36\pm0.06\times10^{-1}$	–	$1.36\pm0.03\times10^{-1}$	–	–	$1.96\pm0.05\times10^{-1}$
133	$<2.4\times10^{-3}$	–	$<2.4\times10^{-3}$	–	–	$<3.0\times10^{-3}$
57	$1.49\pm0.07\times10^{-2}$	$9.33\pm1.53\times10^{-3}$	$1.63\pm0.08\times10^{-2}$	$1.41\pm0.08\times10^{-2}$	$1.65\pm0.11\times10^{-2}$	$1.34\pm0.12\times10^{-1}$
24	–	–	$3.71\pm0.81\times10^{-2}$	–	–	–
34	$1.35\pm0.39\times10^{-3}$	–	$<5.7\times10^{-4}$	$<1.0\times10^{-3}$	$2.49\pm0.57\times10^{-3}$	$5.55\pm0.68\times10^{-3}$
137	$<2.3\times10^{-3}$	–	$<1.8\times10^{-3}$	–	–	$1.12\pm0.17\times10^{-2}$

Notes. For a description of count rates and upper limits (numbers without error, marked with "<"), see Table 3.

Manuscript 3

A&A 661, A25 (2022)

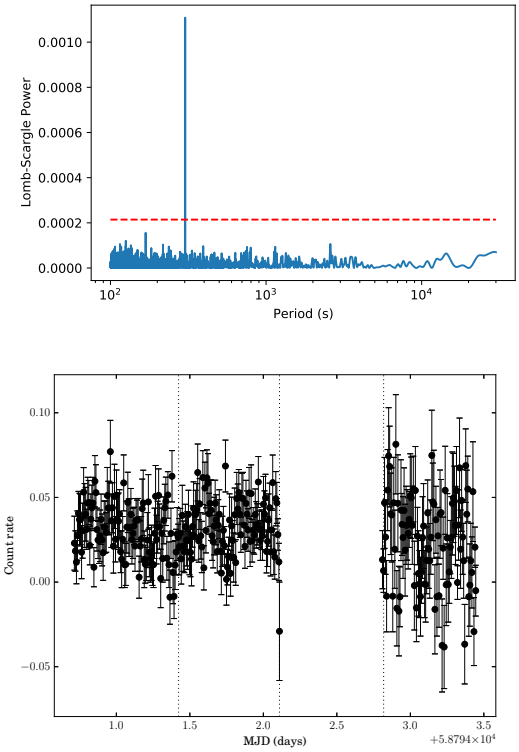


Fig. 9. *Top*: LS periodogram from the light curve of SXP 304, combining observations 700001 and 700002. The dashed red line indicates the 99% confidence level. *Bottom*: background-subtracted and vignetting-corrected light curve of SXP 304 (binned at twice the pulse period and including ObsID 700004) in the energy band of 0.2–8 keV. The dashed vertical lines separate the intervals corresponding to observations 700001–4. During observation 700003, the source was not in the FoV, and during observation 700005 it was not detected.

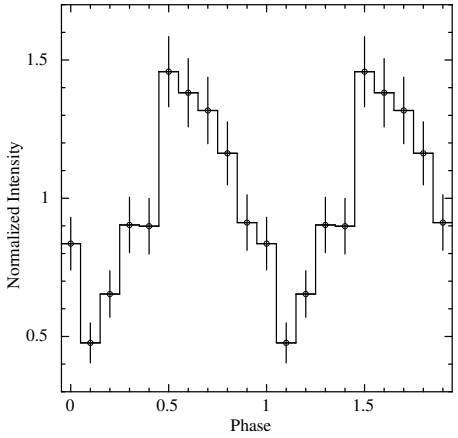


Fig. 10. Background-subtracted pulse profile of SXP 304 combined over observations 700001-2 in the energy range of 0.2–8 keV.

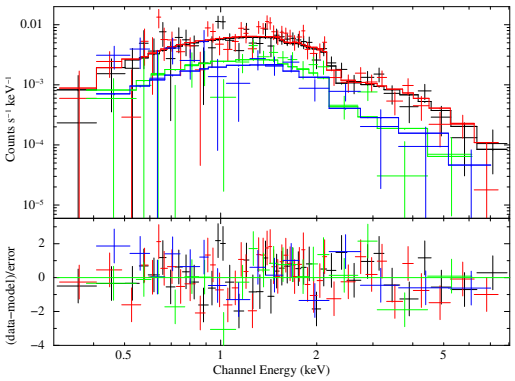


Fig. 11. Simultaneous spectral fit of SXP 304 spectra from observations 700001 (black), 700002 (red), 700004 (green), and 710000 (blue), showing the best-fit model as a histogram and the residuals in the bottom panel. Each spectrum was obtained by combining the data from TM1–4 and 6.

The spectra can be modelled with a simple absorbed power law. The absorption component was consistent with the Galactic foreground column density. No additional SMC component was required, and the $N_{\rm H}$ was fixed at 6×10^{20} cm^{-2}. From the simultaneous fit to the spectra of observations 700001, 700002, 700004 and 710000 a power-law index of $\Gamma = 0.31 \pm 0.11$ was derived. The observed flux (0.2–10 keV) varied from $\sim 3.6\times10^{-13}$ erg cm^{-2} s^{-1} in the first two observations to 3.2×10^{-13} erg cm^{-2} s^{-1} (700004) and 1.5×10^{-13} erg cm^{-2} s^{-1} (710000), corresponding to a luminosity between 6.5×10^{34} erg s^{-1} and 1.6×10^{35} erg s^{-1}. The spectra with best-fit model are shown in Fig. 11.

5.2. RX J0101.3−7211, or SXP 455, or [HS16] 51

SXP 455 was discovered as a BeXRB pulsar using *XMM-Newton* EPIC-pn observations (Sasaki et al. 2001). The source was detected in the FoV of observations 700001–4 and 710000 (see Table 5). In the case of 700003, we did not use the flag to select the circular FoV (as is applied to the released data) because the source was located just outside the selection mask and provides useful data for our temporal analysis. In November 2019, pulsations were significantly detected only from observations 700001 and 700002. The spin periods and corresponding 1σ errors measured for the two observations using an epoch-folding technique are 447.9 ± 1.0 s and 449.0 ± 1.9 s, respectively. These values are well within the range measured from the ROSAT and *XMM-Newton* observations reported by Eger & Haberl (2008a), and as in the case of SXP 304, they indicate little long-term spin period variations since 1993.

The combined light curve demonstrates the flaring behaviour of the source (Fig. 12). The pulse profiles also exhibit evidence for a change in pulse shape between observations 700001 and 700002, as shown in Fig. 13, which might be related to the flaring activity.

Because of the much reduced statistics due to the large off-axis angle of the source, we excluded observation 700003 from the spectral analysis. The spectra from observations 700001, 700002, 700004, and 710000 were fitted simultaneously. A simple absorbed power law did not provide an adequate fit to the data with an excess seen at low energies. Including an additional black-body component (with $kT \sim 1.7$), or alternatively, a partially covering absorbing component, improved the spectral fit.

Manuscript 3

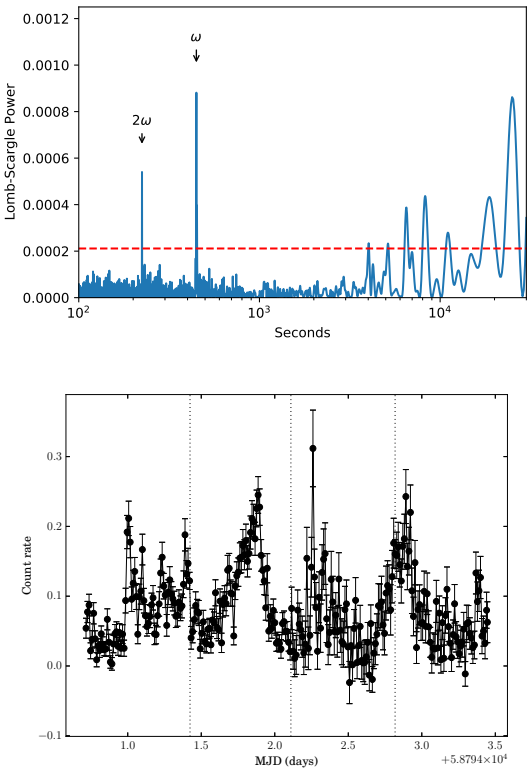


Fig. 12. *Top*: LS periodogram of SXP 455 from the combined light curve of observations 700001–2. The dashed red line indicates the 99% confidence level. *Bottom*: background-subtracted and vignetting-corrected light curve of SXP 455 (binned at twice the pulse period) in the energy band of 0.2–8 keV. The dashed vertical lines separate the intervals corresponding to observations 700001–4. During observation 700005, the source was not in the FoV.

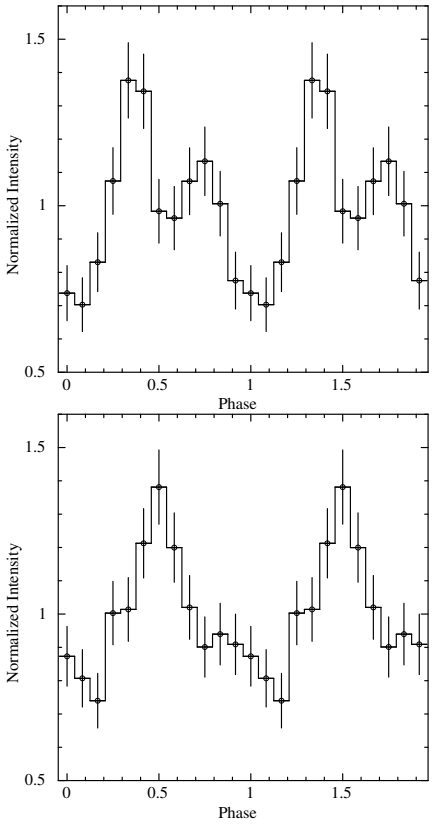


Fig. 13. Normalised pulse profiles of SXP 455 in the energy range of 0.2–8 keV (*top*: 700001 and *bottom*: 700002).

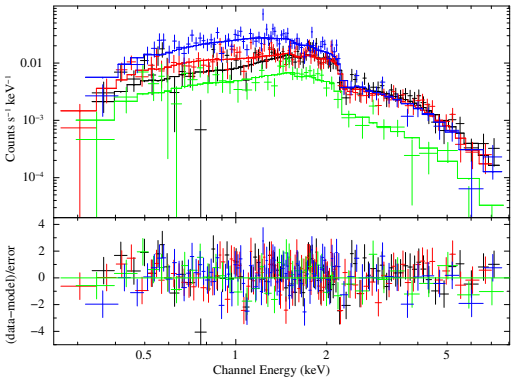


Fig. 14. Simultaneous analysis of the spectra of SXP 455 using a power-law model with a partially covering absorber (observation 700001: black, 700002: red, 700004: green, and 710000: blue). The best-fit model is plotted as a histogram, and residuals are shown in the lower panel. The spectrum from each observation is obtained by combining data from TM1–4 and 6.

As the partial absorbing component provided a better statistical fit (339.7/290 dof with respect to 387.5/295 dof), it was used as the final model for the spectral analysis. For the simultaneous fitting, only the power-law normalisation and the parameters of the partial covering absorber were left free. The obtained power-law index is 0.99 ± 0.16. The corresponding values of the partial absorber and the covering fraction (CF) for the four observations are summarised in Table 6, together with observed fluxes and luminosities. The eROSITA spectra with the best-fit model are presented in Fig. 14. The figure shows that the spectra mainly vary at energies below ~1.5 keV, which is also reflected in the parameters of the partially covering absorber. In particular the spectrum from June 2020 shows a lower absorption column density and a lower covering fraction, leading to the highest flux at low energies.

5.3. Suzaku J0102−7204, or SXP 522, or [HS16] 53

SXP 522 was detected in the November 2019 observations 700001–5 with increasing flux during the last two observations, while it was again weaker in June 2020 (see Table 5). The source was fainter than the other BeXRB pulsars studied in this work, and only data from observation 700001 (source was detected at smallest off-axis angle) were suitable for performing timing analysis. Pulsations are detected with a peak at ~517 s in the LS periodogram, as shown in Fig. 15. The precise spin period with 1σ error is 516.8 ± 2.0 s. The profile exhibits a simple

Manuscript 3

A&A 661, A25 (2022)

Table 6. SXP 455: Results for the partially covering absorber model.

ObsID	$N_{\rm H}$ (10^{22} cm^{-2})	CF	$F_{\rm observed}$ [(a)] (erg cm^{-2} s^{-1})	L [(a)] (erg s^{-1})
700001	2.24 ± 0.52	0.85 ± 0.05	8.2×10^{-13}	4.4×10^{35}
700002	$2.68^{+0.66}_{-0.57}$	0.76 ± 0.07	9.9×10^{-13}	4.3×10^{35}
700004	$2.14^{+0.80}_{-0.62}$	0.77 ± 0.09	8.1×10^{-13}	3.5×10^{35}
710000	$0.81^{+0.57}_{-0.50}$	$0.51^{+0.12}_{-0.17}$	8.9×10^{-13}	3.9×10^{35}

Notes. [(a)] 0.2–10 keV.

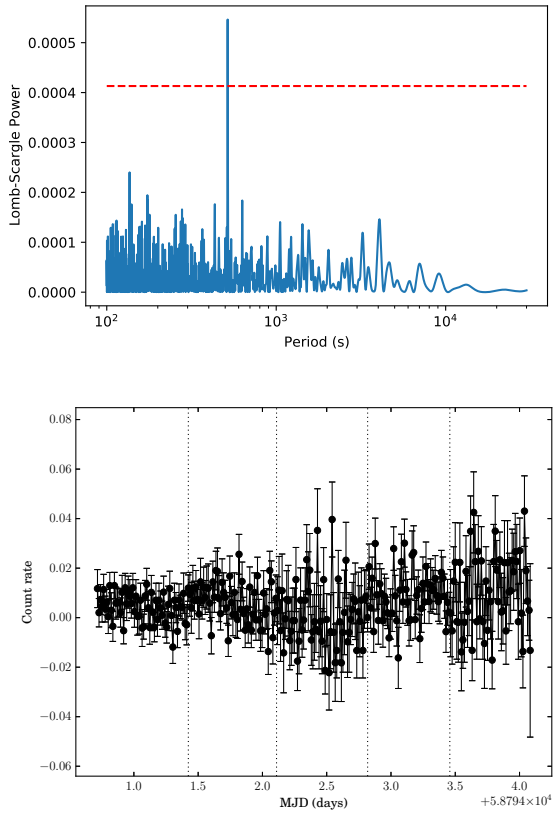


Fig. 15. *Top*: LS periodogram from ObsID 700001 for SXP 522. The dashed red line indicates the 99% confidence level. *Bottom*: background-subtracted and vignetting-corrected light curve of SXP 522 (binned at twice the pulse period) in the energy band of 0.2–8 keV for the five observations in November 2019.

sinusoidal profile (Fig. 16). The measured spin period indicates that SXP 522 experienced an episode of slight long-term spin-up since the discovery of the pulsations in October 2012 (522.5 ± 0.5 s; Wada et al. 2012, 2013) and an *XMM-Newton* detection in December 2012 (521.42 ± 0.21 s; Sturm et al. 2013a). To our knowledge, the new eROSITA spin measurement is the first reported since 2012.

The six spectra from all eROSITA observations can be modelled with a simple absorbed power law. The absorption column density was consistent with the Galactic foreground absorption and was fixed at 6×10^{20} cm^{-2}. The power-law index

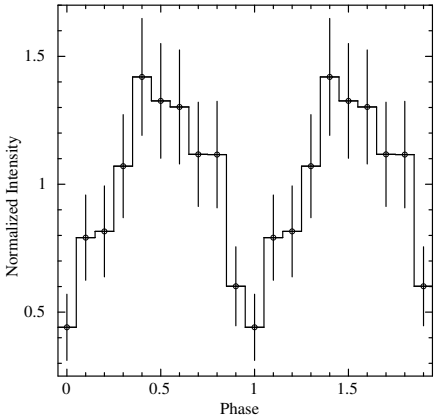


Fig. 16. Background-subtracted pulse profile of SXP 522 in the energy range of 0.2–8 keV.

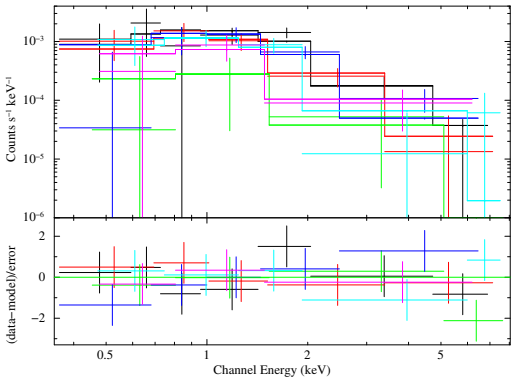


Fig. 17. eROSITA spectra of SXP 522 obtained from observations 700001–5 marked in black, red, green, blue, and cyan, respectively, and 710000 (magenta). Each spectrum includes data from TM1–4 and 6. The histograms show the best-fit model, and the residuals are drawn in the *lower panel*.

derived from a simultaneous fit is 0.93 ± 0.35. The low statistical quality of the spectra does not allow us to draw firm conclusions about variability between the observations. The observed average fluxes (0.2–10 keV) of ($2.7^{+1.5}_{-0.9}$, $3.1^{+1.8}_{-1.3}$, $1.4^{+1.7}_{-1.4}$, $4.1^{+2.4}_{-1.6}$, $5.4^{+3.7}_{-2.6}$, and $1.4^{+1.0}_{-0.8}$) $\times 10^{-14}$ erg cm^{-2} s^{-1} for the six observations are consistent within the errors and correspond to luminosities of (1.2, 1.4, 0.63, 1.8, 2.4, and 0.63) $\times 10^{34}$ erg s^{-1}. The spectra with the best-fit model are shown in Fig. 17.

5.4. RX J0105.9−7203, or SXP 726, or [HS16] 57

RX J0105.9−7203 was proposed to be a BeXRB by Haberl & Sasaki (2000) and was finally confirmed by the discovery of pulsations by Eger & Haberl (2008b) of ∼726 s. Seven detections of the period in *XMM-Newton* observations between April 2001 and November 2003 indicated a long-term spin-down rate of ∼3.2 s yr^{-1}, although it was of low significance due to large uncertainties in the individual period measurements.

Manuscript 3

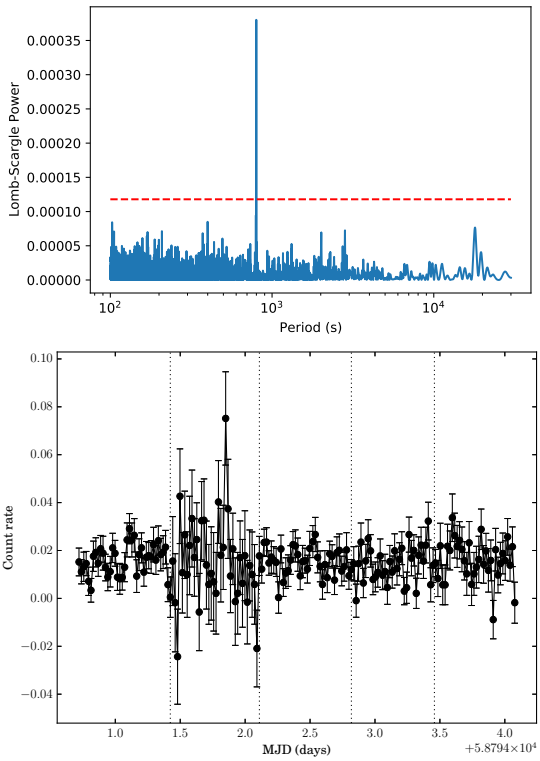


Fig. 18. *Top*: LS periodogram obtained from the combined light curve of SXP 726 shown below. The dashed red line indicates the 99% confidence level. *Bottom*: background-subtracted and vignetting-corrected light curve of SXP 726 (binned at twice the pulse period) in the energy band of 0.2–8 keV.

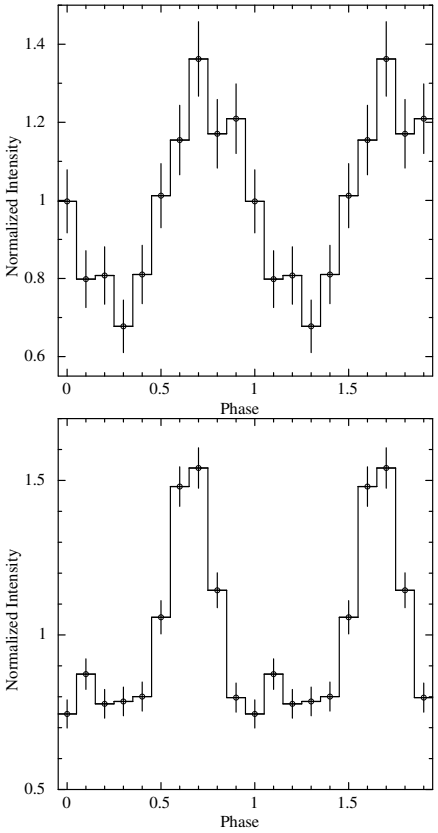


Fig. 19. Background-subtracted pulse profile of SXP 726 in the energy range of 0.2–8 keV averaged over all the observations in which pulsations were detected (*top*) and for ObsID 710000 (*bottom*).

SXP 726 was detected during the November 2019 observations 700001–5 at a similar flux level, while half a year later, it was a factor of ∼7 brighter (see Table 5). Pulsations are detected from all observations except 700002, where the source was located at a very large off-axis angle. The LS periodogram in Fig. 18 shows a strong periodic signal with the fundamental at ∼799 s, demonstrating that the pulsar has exhibited a significant spin-down by nearly 80 s since the time of the discovery of the period. The light curve exhibits a nearly constant count rate (Fig. 18). The precise spin periods with 1σ error from the November 2019 observations 700001, 700003, 700004, 700005, and from the merged data from these observations are 798.8 ± 4.0, 800.0 ± 3.8, 797.6 ± 6.6, 801.5 ± 4.4, and 799.9 ± 3.2 s, respectively. During observation 710000 in June 2020, the period had further increased to 803.0 ± 5.5 s.

No significant change in the spin period or the pulse shape is detected between the observations in November 2019, and the combined pulse profile is shown in Fig. 19 (top). The average profile is single peaked and the pulsed fraction (0.2–8 keV) is $30 \pm 8\%$. The pulse profile from observation 710000 shows a narrower peak with a pulsed fraction of $35 \pm 5\%$ (Fig. 19, bottom).

Considering the large spin-period deviation of SXP 726 inferred from eROSITA data with respect to published values, we re-visited all available archival *XMM-Newton* observations of the SMC covering the pulsar to investigate its evolution in more detail. In particular, we found 31 observations with counting statistics sufficient to search for periodicities. We re-processed the data from these observations using XMMSAS v.19, applying the standard screening criteria described in the documentation[4], and correcting photon arrival times to the Solar System barycentre assuming the position reported in Eger & Haberl (2008b). After this, source photons in the 0.2–10 keV energy band from a source-centred region with radius of 30″ were extracted for all EPIC cameras, and periodicity was searched in the 700–900 s range, using Z_2^2 statistics (Buccheri et al. 1983). The uncertainties for the strongest peak were estimated as width of the peak at a level corresponding to 1σ uncertainty, which was estimated assuming that the Z_2^2 statistics follows the χ^2 distribution for 4 dof (Buccheri et al. 1983).

The results, along with the values measured by eROSITA and values reported by Eger & Haberl (2008b) for some of the observations also reported here, are presented in Fig. 20. It is evident that the eROSITA measurements follow a general spin-down trend. To estimate the spin-down rate, we performed a linear fit to all data points obtained in this work (i.e. including *XMM-Newton* points), which resulted in $\dot{P} = 0.01178(6)$ s day^{-1}

[4] https://www.cosmos.esa.int/web/xmm-newton/sas-threads

Manuscript 3

A&A 661, A25 (2022)

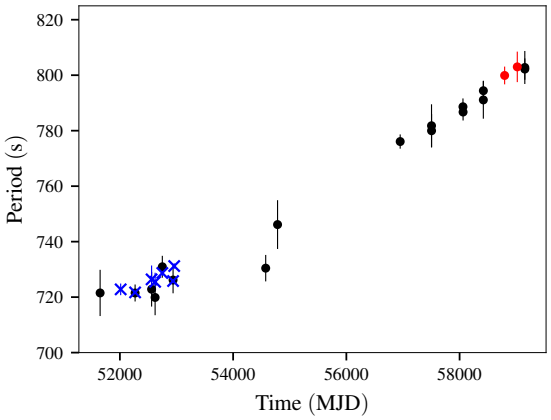


Fig. 20. Spin period evolution of SXP 726 measured in this work using the *XMM-Newton* (black) and eROSITA (red) data. The values reported by Eger & Haberl (2008b) for some of the *XMM-Newton* observations are also plotted for reference (blue crosses).

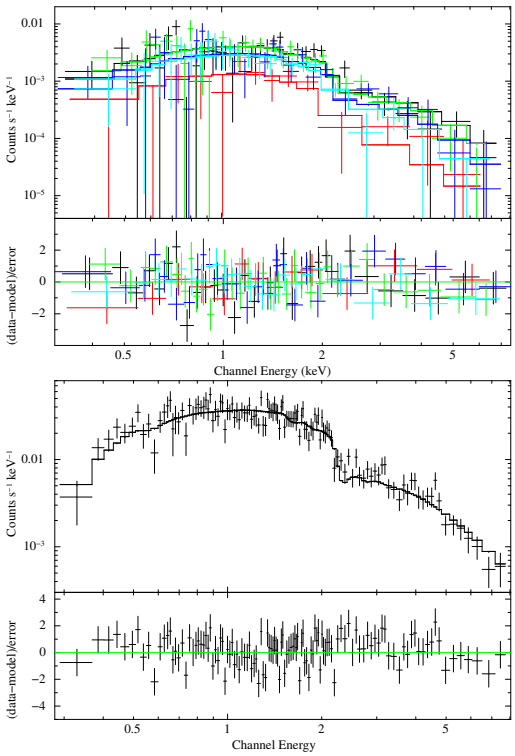


Fig. 21. *Top*: simultaneous spectral fit of an absorbed power law to the spectra of SXP 726 using observations 700001–5 (marked in black, red, green, blue, and cyan, respectively). *Bottom*: spectrum of SXP 726 from observation 710000. All spectra are obtained by combining data from TM1–4 and 6. The histograms trace the best-fit model, and the residuals are plotted in the narrow panels.

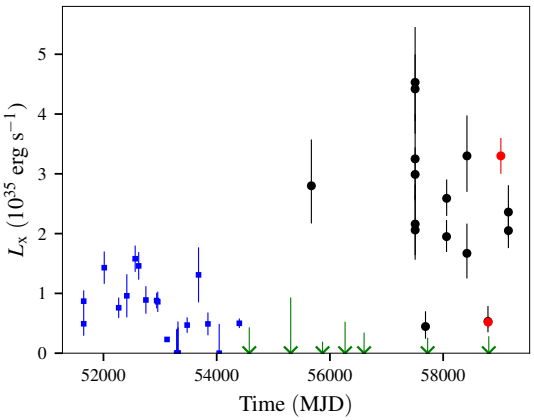


Fig. 22. Variability of SXP726 as observed by *XMM-Newton* and eROSITA (red). The blue points correspond to flux values reported by Eger & Haberl (2008b), whereas black points are reported here for the first time. The upper limits for observations when the source was not detected are also indicated (green arrows).

(4.3 s yr^{-1}). This means that the period change is highly significant and slightly higher in value than reported by Eger & Haberl (2008b).

To estimate the source flux observed by eROSITA, we fitted all observations of November 2019 simultaneously with a simple absorbed power-law model. The absorption component was consistent with the Galactic foreground absorption, and no additional absorbing material was required. The foreground column density was fixed at 6×10^{20} cm^{-2}, and the power-law normalisation was left free. The inferred power-law index was 0.63 ± 0.13 and the average observed flux (0.2–10 keV) $1.14 \pm 0.21 \times 10^{-13}$ erg cm^{-2} s^{-1}. This corresponds to a luminosity of 5.2×10^{34} erg s^{-1}. The spectra with the best-fit model are shown in Fig. 21.

During observation 710000, SXP 726 was sufficiently bright to analyse the spectrum individually. The power-law index was 0.70 ± 0.06, consistent within errors with the value obtained from the observations in November 2019. The observed flux was $7.5^{+0.61}_{-0.56} \times 10^{-13}$ erg cm^{-2} s^{-1} and the luminosity 3.3×10^{35} erg s^{-1}.

To place the eROSITA flux in the context of the historical flux evolution of SXP 726, we also analysed the available *XMM-Newton* observations of the source. To estimate the source flux, we used the same procedure as for the eROSITA data, that is, we fitted source spectra using the absorbed power-law model. For observations in which the source was detected by multiple EPIC cameras, the spectra were modelled simultaneously by linking the model parameters. The source flux in the 0.2–10 keV band and its uncertainty were then estimated using the `cflux` component in `XSPEC`. The results are presented in Fig. 22. It is evident that the source is generally quite variable, and the eROSITA observations occurred at flux levels typically observed from SXP 726 during recent years.

5.5. RX J0103.6−7201, or SXP 1323, or [HS16] 62

SXP 1323 has been extensively monitored by various X-ray observatories due its close angular distance to supernova remnant 1E 0102.2−7219, which is used as calibration standard

Manuscript 3

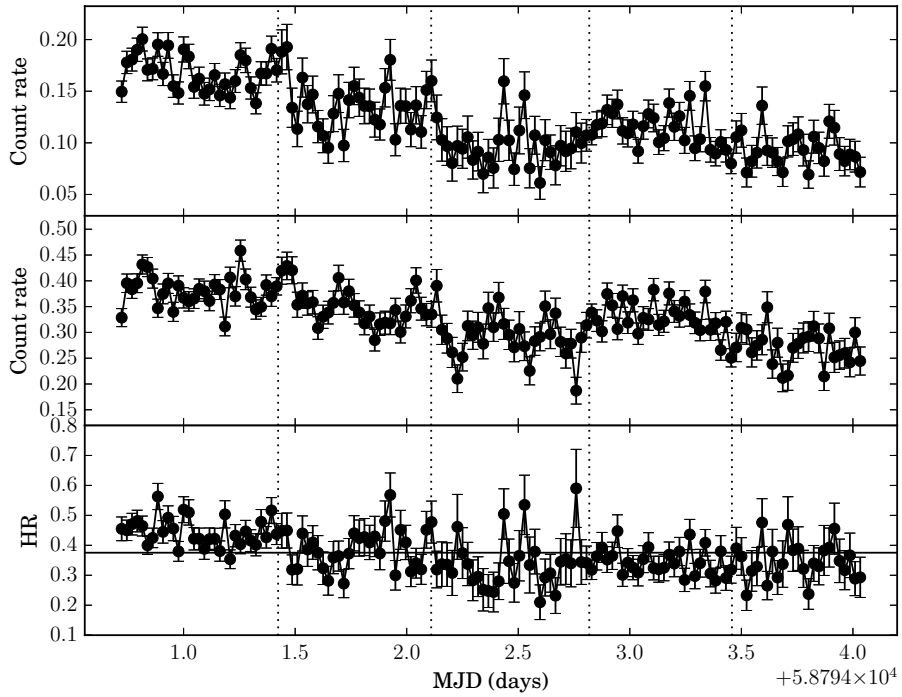


Fig. 23. Background-subtracted and vignetting-corrected light curves of SXP 1323 from observations 700001–5, binned at twice the pulse period in the energy range of 2.5–8 keV (*top*) and 0.2–2.5 keV (*middle*). *Bottom*: hardness ratio (H/S) of SXP 1323.

by many X-ray observatories (Plucinsky et al. 2017). X-ray pulsations were discovered by Haberl & Pietsch (2005) in *XMM-Newton* data. Their long-term light curve created from ROSAT, *Chandra*, and *XMM-Newton* data from 1991–2004 was extended by Carpano et al. (2017) until the end of 2016. Their study of the Suzaku, *Chandra*, and *XMM-Newton* data showed that the pulse period stayed relatively stable around 1323 s from 2000 to 2006, but afterwards, the source started to spin-up rapidly and reached 1110 s by mid 2016. Since then, the source continued to spin-up at a similar rate, and the pulse period of 1005 s during the eROSITA CalPV phase was already announced by Haberl et al. (2019).

SXP 1323 was detected in all the November 2019 observations (700001–5) and the June 2020 observation (710000) performed by eROSITA with count rates in the range between 0.09 cts s^{-1} and 0.68 cts s^{-1} (Table 5). The combined light curve from November 2019 is shown in Fig. 23 for two energy bands, a soft band (0.2–2 keV) and a hard band (2.5–8 keV). The hard band was chosen to avoid any possible residual contribution from the nearby supernova remnant (see Fig. 24), which exhibits a soft X-ray spectrum. Some variability by a factor of ~3 is seen in the hard-band light curve of the pulsar, while in the soft band, variations are reduced to a factor of ~2. The hardness ratio (ratio of count rates in the hard and soft bands) shows a slight decreasing (softening) trend during the 3.4 days, but caution is required due to the large PSF at the large off-axis angles during observations 700002–5 (see also below).

In the eROSITA data, pulsations are detected most significantly during observation 700001 from November 7, 2019, when the source was brightest and close to the telescope optical axis. Our timing analysis revealed the pulse period at 1006.3 ± 5.6 s. The LS periodogram is presented in Fig. 25 and shows signal at the fundamental frequency and the second harmonic (3ω), but not at the first harmonic (2ω). This is different from periodograms obtained from *XMM-Newton* observations in the first years of this century (Haberl & Pietsch 2005), when the fundamental and the first harmonic were seen. Correspondingly, the pulse profile from the eROSITA observation 700001 (presented in Fig. 26) shows two narrow peaks, while the *XMM-Newton* profiles were characterised by a structured broader peak.

Figure 27 shows the long-term evolution of the pulse period of SXP 1323, as in Carpano et al. (2017), but including the latest *XMM-Newton* and eROSITA measurements. The ten new *XMM-Newton* observations are spanning from October 26, 2016 (ObsID: 0412983201) to October 30, 2020 (ObsID: 0810880701), when the pulse period monotonically decreased from 1090.86 s to 976.91 s (note that pulsations are not detected significantly in all ten observations). Using the latest data, the spin up rate is now $\dot{P} = -23.2\,\mathrm{s\,yr^{-1}}$, as inferred from a linear fit to the data in the 2005–2021 time interval. With a mean value of 1168 s, the corresponding relative spin period change is $|\dot{P}/P| = 0.0199\,\mathrm{yr^{-1}}$. Between 2010 and 2014, pulsations were only occasionally detected if at all, and were at a low confidence level (Carpano et al. 2017). A comparison of the spin-up trend from the epochs before and after this break suggests that the spin-up rate was reduced during the break (Fig. 27). The first measured period after the break is about 50 s longer than expected from the extrapolation of the data before the break. This also implies even higher spin-up rates before and after the break compared to the 16-yr average (see also Mereminskiy et al. 2022).

Manuscript 3

A&A 661, A25 (2022)

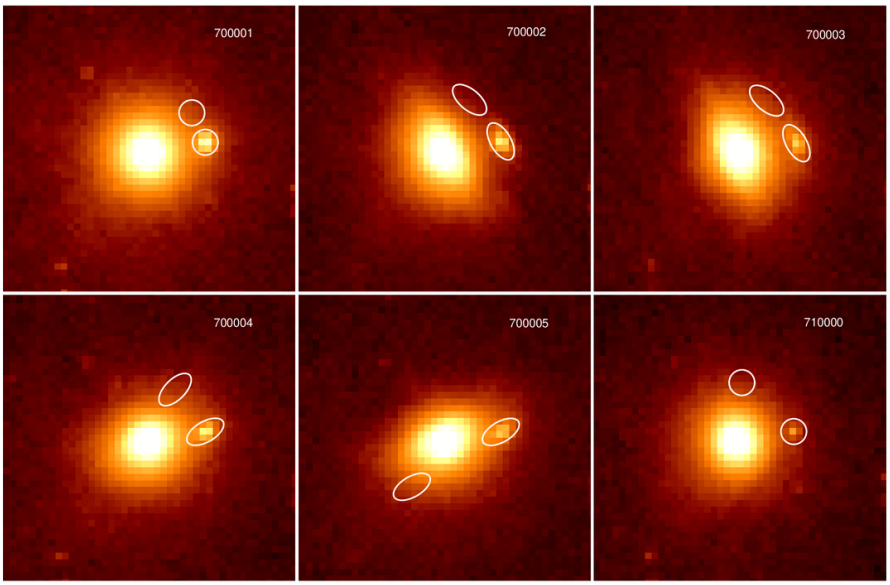


Fig. 24. Images of the region around 1E 0102.2−7219 and SXP 1323 from the six CalPV observations. The source and background-extraction regions we used for the temporal and spectral analyses of SXP 1323 are marked.

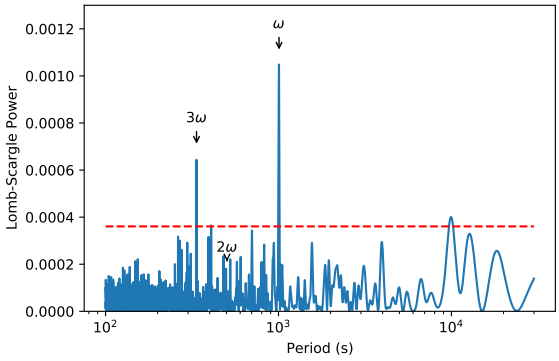


Fig. 25. LS periodogram obtained from the light curve extracted from ObsID 700001 of SXP 1323. The dashed red line indicates the 99% confidence level.

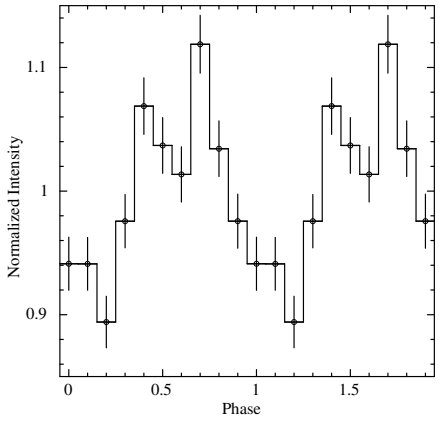


Fig. 26. Background-subtracted pulse profile of SXP 1323 in the energy range of 0.2–10 keV from observation 700001, in which pulsations were detected.

Because of the vicinity of SXP 1323 to 1E 0102.2−7219, special care has to be taken for the definition of the extraction regions for source and background spectra. In particular, for the off-axis observations of 1E 0102.2−7219, the larger PSF causes a significant contribution of the supernova remnant flux to the spectra of SXP 1323, as shown in Fig. 24. The background regions were carefully selected to remove this emission, taking into account the distance of SXP 1323 to 1E 0102.2−7219 and also the asymmetric shape of the PSF at large off-axis angles.

The spectra extracted from observations 700001–5 and 710000 were fitted simultaneously. An absorbed power-law provided an adequate description to the spectrum. For this purpose, we used two absorption components: one to describe the Galactic foreground absorption (fixed at 6×10^{20} cm^{-2}), and another to account for the column density of both the interstellar medium along the line of sight in the SMC and the local absorption near the source. For the latter absorption component, the abundances were set to 0.2 solar for elements heavier than helium, as described before. In the fits only the power-law normalisation was left free to vary between observations. The obtained power-law photon index is 0.50 ± 0.02, and $N_{\rm H} = 9.8 \pm 2.5 \times 10^{20}$ cm^{-2} (reduced $\chi^2 = 1.1$ for 1581 dof). During the November 2019 observations, the observed flux (0.2–10 keV) decreased from 4.5×10^{-12} erg cm^{-2} s^{-1} (700001) to 3.1×10^{-12} erg cm^{-2} s^{-1} (700005), as already indicated by the light curve (Fig. 23), and was even lower at 5.7×10^{-13} erg cm^{-2} s^{-1} in June 2020. This corresponds to luminosities of 2.0×10^{36} erg s^{-1}, 1.3×10^{36} erg s^{-1}, and 2.5×10^{35} erg s^{-1}. The result of the simultaneous spectral fit with the best-fit model is shown in Fig. 28.

Manuscript 3

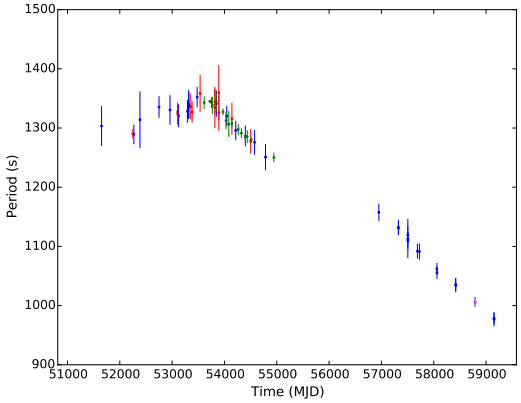


Fig. 27. Long-term spin period evolution of SXP 1323, following Carpano et al. (2017), which includes Suzaku (green), *XMM-Newton* (blue), *Chandra* (red), and eROSITA (pink) observations.

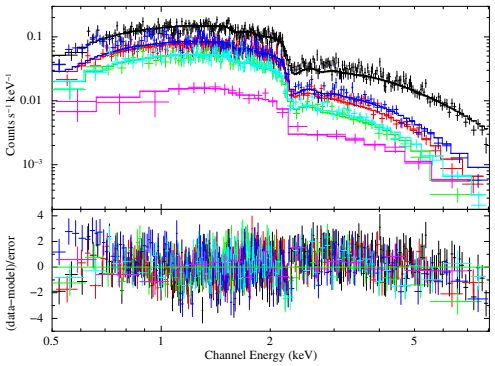


Fig. 28. eROSITA spectra of SXP 1323 (observations 700001–5 marked in black, red, green, blue, and cyan, respectively, and 710000 in magenta), together with the best-fit power-law model and the residuals from the simultaneous fit. The spectrum from each observation is obtained by combining data from TM1–4 and 6.

6. Discussion

6.1. HMXBs in the Magellanic Clouds as seen during eROSITA CalPV observations

The eROSITA observations around SN 1987A and N 132D in the LMC covered 14 known (candidate) HMXBs. Six of them were not detected in any of the observations, and upper limits between 1.5×10^{-3} cts s^{-1} and 1.1×10^{-2} cts s^{-1} were derived. Assuming the spectral parameters derived for the new transient SRGEt J052829.5−690345 (see below), these correspond to fluxes from 1.2×10^{-14} erg cm^{-2} s^{-1} to 8.8×10^{-14} erg cm^{-2} s^{-1}, or luminosities from 4.2×10^{33} erg s^{-1} to 3.1×10^{34} erg s^{-1} (0.2–8.0 keV). All other sources (we exclude LMC X-1 from our analysis) were detected in at least one of the observations with fluxes (luminosities) in the range of 4.3×10^{-14} erg cm^{-2} s^{-1} to 1.7×10^{-12} erg cm^{-2} s^{-1} (1.5×10^{34} erg s^{-1} to 5.9×10^{35} erg s^{-1}). The brightest sources were the SFXT XMMU J053108.3−690923 (Maitra et al. 2021) and the supergiant HMXB candidate RX J0541.4−6936, the latter being undetected in one observation with an upper limit a factor of ∼30 below the two detections.

The SMC observations around 1E 0102.2−7219 covered 23 HMXBs, most likely all BeXRBs. The SMC observations were more sensitive for point source detection than those of the LMC, resulting in a factor 2–3 smaller upper limits (5.7×10^{-4} cts s^{-1} to 6.6×10^{-3} cts s^{-1}, 4.5×10^{-15} erg cm^{-2} s^{-1} to 5.3×10^{-14} erg cm^{-2} s^{-1}, 2.2×10^{33} erg s^{-1} to 2.6×10^{34} erg s^{-1}). This is caused not only by the deeper exposures, but is also due to the stronger diffuse X-ray emission in the LMC. Only one of the known SMC BeXRB pulsars was not detected, although it was in the FoV of all observations (SXP 345, [HS16] 50). Of the HMXBs without a known spin period, three were not detected ([HS16] 114, 120 and 133). Haberl & Sturm (2016) listed [HS16] 120 in their lowest confidence class for being a genuine HMXB. Nineteen (83%) of the HMXBs covered by the eROSITA observations were detected, with fluxes (luminosities) in the range of 1.1×10^{-14} erg cm^{-2} s^{-1} to 5.4×10^{-12} erg cm^{-2} s^{-1} (5.2×10^{33} erg s^{-1} to 2.6×10^{36} erg s^{-1}), with SXP 1323 the brightest in the SMC. These moderate flux levels (Haberl & Sturm 2016) indicate that none of the sources was in a strong outburst during the eROSITA observations, as expected for long-period, low-luminosity BeXRBs.

One of the LMC calibration observations in November 2019 revealed a new hard X-ray transient, SRGEt J052829.5−690345, with the typical characteristics of a BeXRB, but with a relatively faint X-ray luminosity of 1.2×10^{35} erg s^{-1}. The X-ray spectrum can be modelled with a power law with photon index of $0.66^{+0.74}_{-0.54}$, and as optical counterpart, we identified a $V\sim15.7$ mag star, which shows large brightness variations in the V and I bands as monitored by the OGLE project over 18.5 yr (Figs. 5 to 7). The star varies in colour as indicated by the $V-I$ index, which is correlated with the brightness of the star. There is some scatter in $V-I$ for a given I, which is limited to a well-defined band, as shown in Fig. 7. This behaviour of reddening with brightness was reported from several other BeXRBs in the MCs with large variations in brightness (Treiber et al. 2021; Haberl et al. 2017; Vasilopoulos et al. 2014; Coe et al. 2012) and is interpreted as a changing size of the circum-stellar disc, which leads to variations in the infrared excess with respect to the emission from the stellar photo-sphere.

The eROSITA CalPV observations also covered three HMXB candidates in the LMC, which were selected based on X-ray hardness ratios and early-type star as likely counterpart, but did not show significant Hα emission during the spectroscopic observations performed by van Jaarsveld et al. (2018). XMMU J052417.1−692533, one of the candidates, was detected in three eROSITA observations, and the spectra can be well represented by an absorbed power law with photon index 0.83 ± 0.17, consistent with the average value found for BeXRBs in the SMC by Haberl et al. (2008). This supports the proposed HMXB nature of the source, although no Hα emission was observed. Simultaneous X-ray and optical observations are required to verify if X-ray luminosities of $\sim10^{34}$ erg s^{-1} can be powered when no significant circum-stellar disc is present.

In the SMC, the eROSITA observations covered 16 BeXRB pulsars, including XMMU J010429.4−723136, from which 164 s pulsations were discovered in eROSITA data (Carpano et al. 2022; Haberl et al. 2019). We present detailed spectral and temporal analyses for SXP 304, SXP 455, SXP 522, SXP 726, and SXP 1323. All five belong to a group of long-period ($\gtrsim$100 s) and low-luminosity ($\lesssim5\times10^{36}$ erg s^{-1}) pulsars, which usually do not exhibit very strong outbursts with amplitudes $F_{\rm max}/F_{\rm min}$

Manuscript 3

A&A 661, A25 (2022)

larger than ∼500, unlike short-period BeXRB pulsars, which can reach factors larger than 10^4 (see Fig. 5 in Haberl & Sturm 2016).

The current pulse periods measured for SXP 304 and SXP 455 are within the range published previously, indicating little long-term spin changes over the last one to two decades. Their X-ray luminosities of $\sim 1–5 \times 10^{35}$ erg s^{-1} are also within the typical range observed in the past (Eger & Haberl 2008a).

SXP 455 showed the largest flare-like flux variations of all investigated BeXRBs covered by the long November 2019 observations (Fig. 12). In particular, during observation 700002, a strong flare occurred, which increased by a factor of five in flux and lasted for about 10 hours. During the flare, the pulse profile changed from double peaked to more single peaked (Fig. 13). During previous *XMM-Newton* observations in April and October 2000, the source was a factor of more than 2 fainter than in 2019, and the pulse profile showed indications for two peaks, in particular, at energies below 2 keV (Sasaki et al. 2003, 2001). This indicates a dependence of the pulse profile on source luminosity, but it should be noted that during the eROSITA observation, the weaker peak followed the stronger one, while during the *XMM-Newton* observations this order was reversed. A similar flaring activity and a luminosity dependence of the pulse profile was reported from the Galactic transient 2.76 s X-ray pulsar 4U 1901+03 (Ji et al. 2020), which the authors interpreted as changes in the pulsed beaming pattern due to transitions between the sub- and super-critical accretion regimes. However, there are some differences between the flares of SXP 455 and 4U 1901+03: The flares of the SMC pulsar are stronger than the persistent emission and last longer (10 h versus a few hundred seconds). It is remarkable that the ratio of the flare durations is similar to the ratio of the spin periods of the two neutron stars.

The newly measured period of SXP 522 indicates a small spin-up of approximately -6 ± 2 s over the last seven years. However, the luminosity seen by eROSITA in 2019 is a factor of 40–100 lower than the maximum in 2012, suggesting that the source has returned to a low state after some more active period when the pulsations were discovered.

6.2. Long-term spin-period evolution of SXP 726 and SXP 1323

The spin history of SXP 726 and SXP 1323 is very different from the other three pulsars. While SXP 726 shows a nearly linear spin-down rate of 4.3 s yr^{-1} for about 17 yr, SXP 1323 is spinning up on average with -23.2 s yr^{-1} for about 16 yr.

The low X-ray luminosity of X-ray pulsars in the SMC ($\sim 10^{35}$–10^{36} erg s^{-1}) and the long pulse periods (exceeding ∼70–100 s) suggest that they may be quasi-spherically accreting from stellar winds. In this case, the plasma entry in the neutron star magnetospheres is regulated by the plasma cooling rate (Elsner & Lamb 1977). At X-ray luminosities below $\sim 4 \times 10^{36}$ erg s^{-1}, the Compton cooling of plasma above the magnetosphere is insufficient to keep pace with freely falling fresh matter that is gravitationally captured from the stellar wind, and a quasi-spherical subsonic turbulent shell is formed around the magnetosphere (Shakura et al. 2012). The accretion through the shell occurs subsonically (the settling accretion), no shock arises above the neutron star magnetosphere, and the accretion rate onto the neutron star $\dot{M}$ is lower than the potential mass accretion rate determined by the standard Bondi-Hoyle-Littleton value. Turbulent stresses mediate the angular momentum exchange between the shell and the magnetosphere, leading to the spin-up or spin-down of the neutron star. The angular momentum balance in this case is written as (Shakura et al. 2012, 2018; Shakura & Postnov 2018)

$$\dot{\omega} = A(\mu, v, P_\mathrm{b}) \dot{M}^{7/11} - B(\mu, P) \dot{M}^{3/11} . \quad (1)$$

Here $\omega = 2\pi/P$, the coefficients A and B depend on the system parameters (the neutron star magnetic moment μ[5] and moment of inertia, the stellar wind velocity v, the binary orbital period P_b, and details of the shell structure; see below).

The equilibrium pulsar period reads

$$P_\mathrm{eq} \approx 1000[\mathrm{s}]\, \mu_{30}^{12/11} \left(\frac{P_\mathrm{b}}{10\,\mathrm{d}}\right) \dot{M}_{16}^{-4/11} v_8^4 . \quad (2)$$

Here the parameters are normalised to the typical values; $\mu_{30} \equiv \mu\ /\ (10^{30}\,\mathrm{G\,cm^3})$, P_b is the binary orbital period (the orbit is assumed to be circular), $\dot{M}_{16} \equiv \dot{M}\ /\ (10^{16}\,\mathrm{g\,s^{-1}})$ is the accretion rate onto the neutron star surface corresponding to an X-ray luminosity of $L_x = 0.1 \dot{M} c^2$, and $v_8 \equiv v\ /\ (1000\,\mathrm{km\,s^{-1}})$ is the stellar wind velocity relative to the neutron star.

For accretion rates below the equilibrium value, $\dot{M} < \dot{M}_\mathrm{eq} = (B/A)^{11/4}$, the spin-up torque can be neglected. The spin-down torque $\dot{\omega}_\mathrm{sd}$ (Shakura et al. 2012, 2018; Shakura & Postnov 2018) reads (see Eq. (6.9) in Shakura & Postnov 2018)

$$\dot{\omega}_\mathrm{sd} \approx -0.54 \times 10^{-12} [\mathrm{rad\,s^{-2}}]\, \Pi_0\, \mu_{30}^{13/11} \dot{M}_{16}^{3/11} \left(\frac{P}{100\,\mathrm{s}}\right) , \quad (3)$$

where the dimensionless combination of the theory parameters $\Pi_0 \sim 1$ (see Shakura et al. 2018, for more detail). This torque can be recast to the fractional period change rate as

$$\left(\frac{\dot{P}}{P}\right)_\mathrm{sd} = -\frac{\dot{\omega}_\mathrm{sd}}{2\pi} P \approx 8.6 \times 10^{-12}\, \Pi_0\, \mu_{30}^{13/11} \dot{M}_{16}^{3/11} . \quad (4)$$

When the X-ray luminosity is known, formula (4) can therefore be used to estimate the neutron star magnetic moment,

$$\mu_{30} \approx 0.16 \left[\frac{(\dot{P}/P)_\mathrm{sd}}{10^{-12}\mathrm{s^{-1}}}\right]^{11/13} \Pi_0^{-11/13} \dot{M}_{16}^{-3/13} . \quad (5)$$

In the case of SXP 726, we have $P \approx 800$ s, $L_x \approx (3-5) \times 10^{34}$ erg s^{-1}, corresponding to $\dot{M}_{16} \approx (3-5) \times 10^{-2}$, and $(\dot{P}/P)_\mathrm{sd} \approx 1.7 \times 10^{-10}$ s^{-1}, which yields an estimate of the magnetic moment of the neutron star of $\mu_{30} \simeq 2.7$ (corresponding to the surface polar magnetic field $B \simeq 5.4 \times 10^{12}$ G), independent of the unknown binary orbital period and stellar wind velocity.

For SXP 1323, a period of $P \approx 1000$ s for which an almost steady spin-up is measured at a rate of $(\dot{P}/P)_\mathrm{su} \approx 0.0199\,\mathrm{yr^{-1}} = 6.31 \times 10^{-10}\,\mathrm{s^{-1}}$ at an X-ray luminosity of $\sim 10^{36}$ erg s^{-1}. The spin-up torque $\dot{\omega}_\mathrm{su}$ at the quasi-spherical settling accretion stage reads (see Eq. (4.15) in Shakura & Postnov 2018)

$$\dot{\omega}_\mathrm{su} \approx 5.3 \times 10^{-13} [\mathrm{rad\,s^{-2}}] \left(\frac{\Pi_0}{\zeta^{4/11}}\right) \mu_{30}^{1/11} \left(\frac{P_\mathrm{b}}{10\,\mathrm{d}}\right)^{-1} \dot{M}_{16}^{7/11} v_8^{-4} , \quad (6)$$

corresponding to a fractional period change rate of

$$\left(\frac{\dot{P}}{P}\right)_\mathrm{su} = -\frac{\dot{\omega}_\mathrm{su}}{2\pi} P \approx -8.44 \times 10^{-12} \left(\frac{\Pi_0}{\zeta^{4/11}}\right) \mu_{30}^{1/11} \left(\frac{P/100\,\mathrm{s}}{P_\mathrm{b}/10\,\mathrm{d}}\right) \dot{M}_{16}^{7/11} v_8^{-4} . \quad (7)$$

[5] The neutron star dipole magnetic moment is defined as $\mu = BR^3/2$, where R and B are the neutron star surface polar field and radius. For the typical values of $B = 10^{12}$ G and $R = 10$ km, $\mu = 0.5 \times 10^{30}$ G cm^3.

Manuscript 3

Clearly, the strongest dependence in Eq. (7) is on the stellar wind velocity, which enables us to estimate it from measurements of the fractional period spin-up rate and X-ray luminosity,

$$v_8 \simeq 1.7 \left(\frac{10^{-12}\mathrm{s}^{-1}}{-(\dot{P}/P)_{\mathrm{su}}}\right)^{1/4} \left(\frac{P/100\,\mathrm{s}}{P_{\mathrm{b}}/10\,\mathrm{d}}\right)^{1/4} \dot{M}_{16}^{7/44} \mu_{30}^{1/44} \left(\frac{\Pi_0}{\zeta^{4/11}}\right)^{1/4} . \quad (8)$$

Substituting parameters for SXP 1323 ($P \approx 1000$ s, $\dot{M}_{16} \simeq 1$, $P_{\mathrm{b}} = 26.2$ d; Carpano et al. 2017) and ignoring dimensionless theory parameters Π_0, ζ of about unity, we find

$$v_8 \simeq 0.5 \mu_{30}^{1/44} . \quad (9)$$

We note the virtual independence of this estimate of the unknown magnetic field of the neutron star. The long-term spin evolution of SXP 1323 presented in Fig. 27 and suggests a torque reversal at around MJD 53500. Therefore the equilibrium period of this pulsar could be close to ~1000 s. Then Eq. (2) with the velocity estimate Eq. (9) may suggest a magnetic moment of $\mu_{30} \sim 10$ for this pulsar.

Thus, the quasi-spherical subsonic accretion theory (Shakura et al. 2012) applied to observations of the spin-up and spin-down of the slowly rotating X-ray pulsars SXP 1323 and SXP 726 gives reasonable (standard) estimates for the magnetic field of the neutron star and the stellar wind velocity in these systems, without making additional assumptions on the spin-up or spin-down mechanisms or involving extraordinary values of the system parameters. Further observations of such BeXRB pulsars, especially to measure their orbital periods, neutron star magnetic fields, and stellar wind velocities, can be used to test this theory in more detail.

7. Conclusions

The eROSITA pointed observations of the CalPV phase of fields in the LMC and SMC demonstrate the strength of the telescopes for the investigation of the HMXB population in the MCs, namely high sensitivity especially at energies below ~2 keV and a wide FoV. This also holds for the eROSITA all-sky survey, which is currently in progress and covers the whole Magellanic system, LMC, SMC, and the Magellanic bridge. Because of the location of the LMC in the vicinity of the south ecliptic pole (SEP), where the survey scans cross, the sources there are scanned for a much longer time than most of the sky, for instance, three weeks of scans in the northern part of the LMC per survey visit lead to a 20 times higher exposure and accumulates to ~40 ks over four years. This is similar to the exposures of the CalPV observations and opens discovery space for the faint end of the HMXB luminosity function. The various timescales involved in the survey, from ~40 s per scan, six scans per day over many days in the LMC (depending on the distance to the SEP, two days in the SMC), to the eight half-yearly visits of the survey will allow us to discover new transient HMXBs and to investigate their duty cycles.

Acknowledgements. This work is based on data from eROSITA, the soft X-ray instrument aboard SRG, a joint Russian-German science mission supported by the Russian Space Agency (Roskosmos), in the interests of the Russian Academy of Sciences represented by its Space Research Institute (IKI), and the Deutsches Zentrum für Luft- und Raumfahrt (DLR). The SRG spacecraft was built by Lavochkin Association (NPOL) and its subcontractors, and is operated by NPOL with support from the Max Planck Institute for Extraterrestrial Physics (MPE). The development and construction of the eROSITA X-ray instrument was led by MPE, with contributions from the Dr. Karl Remeis Observatory Bamberg and ECAP (FAU Erlangen-Nürnberg), the University of Hamburg Observatory, the Leibniz Institute for Astrophysics Potsdam (AIP), and the Institute for Astronomy and Astrophysics of the University of Tübingen, with the support of DLR and the Max Planck Society. The Argelander Institute for Astronomy of the University of Bonn and the Ludwig Maximilians Universität Munich also participated in the science preparation for eROSITA. The eROSITA data shown here were processed using the eSASS software system developed by the German eROSITA consortium. The OGLE project has received funding from the National Science Centre, Poland, grant MAESTRO 2014/14/A/ST9/00121 to AU. N.Sh. is partially supported by RSF grant 21-12-00141. K.P. is partially supported by the RFBR grant 19-02-00790. NSh and KP also acknowledge the support from the Scientific and Educational School of M.V. Lomonosov Moscow State University 'Fundamental and applied space research'.

References

Antoniou, V., & Zezas, A. 2016, MNRAS, 459, 528
Antoniou, V., Zezas, A., Hatzidimitriou, D., & Kalogera, V. 2010, ApJ, 716, L140
Arnaud, K. A. 1996, ASP Conf. Ser., 101 17
Brunner, H., Liu, T., Lamer, G., et al. 2022, A&A, 661, A1 (eROSITA EDR SI)
Buccheri, R., Bennett, K., Bignami, G. F., et al. 1983, A&A, 128, 245
Carpano, S., Haberl, F., & Sturm, R. 2017, A&A, 602, A81
Carpano, S., Haberl, F., Maitra, C., et al. 2022, A&A, 661, A20 (eROSITA EDR SI)
Clark, J. S., Bartlett, E. S., Broos, P. S., et al. 2015, A&A, 579, A131
Coe, M. J., Edge, W. R. T., Galache, J. L., & McBride, V. A. 2005, MNRAS, 356, 502
Coe, M. J., Haberl, F., Sturm, R., et al. 2012, MNRAS, 424, 282
Coe, M. J., Kennea, J. A., Evans, P. A., & Udalski, A. 2020, MNRAS, 497, L50
Dickey, J. M., & Lockman, F. J. 1990, ARA&A, 28, 215
Eger, P., & Haberl, F. 2008a, A&A, 491, 841
Eger, P., & Haberl, F. 2008b, A&A, 485, 807
Elsner, R. F., & Lamb, F. K. 1977, ApJ, 215, 897
Gaia Collaboration (Helmi, A., et al.) 2018, A&A, 616, A12
Graczyk, D., Pietrzyński, G., Thompson, I. B., et al. 2014, ApJ, 780, 59
Haberl, F., & Pietsch, W. 2005, A&A, 438, 211
Haberl, F., & Sasaki, M. 2000, A&A, 359, 573
Haberl, F., & Sturm, R. 2016, A&A, 586, A81
Haberl, F., Eger, P., & Pietsch, W. 2008, A&A, 489, 327
Haberl, F., Sturm, R., Ballet, J., et al. 2012, A&A, 545, A128
Haberl, F., Israel, G. L., Rodriguez Castillo, G. A., et al. 2017, A&A, 598, A69
Haberl, F., Carpano, S., Maitra, C., et al. 2019, ATel, 13312, 1
Hughes, J. P. 1994, ApJ, 427, L25
Israel, G. L., Campana, S., Covino, S., et al. 2000, ApJ, 531, L131
Ji, L., Ducci, L., Santangelo, A., et al. 2020, MNRAS, 493, 5680
Kahabka, P., & Pietsch, W. 1996, A&A, 312, 919
Kahabka, P., Pietsch, W., Filipović, M. D., & Haberl, F. 1999, A&AS, 136, 81
Kahabka, P., Haberl, F., Payne, J. L., & Filipović, M. D. 2006, A&A, 458, 285
Kohno, M., Yokogawa, J., & Koyama, K. 2000, PASJ, 52, 299
Leahy, D. A. 1987, A&A, 180, 275
Lomb, N. R. 1976, Ap&SS, 39, 447
Luck, R. E., Moffett, T. J., Barnes, Thomas G., I., & Gieren, W. P. 1998, AJ, 115, 605
Macomb, D. J., Fox, D. W., Lamb, R. C., & Prince, T. A. 2003, ApJ, 584, L79
Maggi, P., Sturm, R., Haberl, F., & Vasilopoulos, G. 2013, ATel, 5674, 1
Maggi, P., Sturm, R., Haberl, F., Vasilopoulos, G., & Udalski, A. 2014, ATel, 5778, 1
Maggi, P., Haberl, F., Kavanagh, P. J., et al. 2016, A&A, 585, A162
Maitra, C., Haberl, F., Filipović, M. D., et al. 2019a, MNRAS, 490, 5494
Maitra, C., Haberl, F., Ivanov, V. D., Cioni, M.-R. L., & van Loon J. T. 2019b, A&A, 622, A29
Maitra, C., Haberl, F., Vasilopoulos, G., et al. 2021, A&A, 647, A8
Maitra, C., Haberl, F., Sasaki, M., et al. 2022, A&A, 661, A30 (eROSITA EDR SI)
Majid, W. A., Lamb, R. C., & Macomb, D. J. 2004, ApJ, 609, 133
Massey, P. 2002, ApJS, 141, 81
McBride, V. A., González-Galán, A., Bird, A. J., et al. 2017, MNRAS, 467, 1526
McGowan, K. E., Coe, M. J., Schurch, M., et al. 2007, MNRAS, 376, 759
Mereminskiy, I. A., Mushtukov, A. A., Lutovinov, A. A., et al. 2022, A&A, 661, A33 (eROSITA EDR SI)
Novara, G., La Palombara, N., Mereghetti, S., et al. 2011, A&A, 532, A153
Pietrzyński, G., Graczyk, D., Gallenne, A., et al. 2019, Nature, 567, 200

Manuscript 3

Plucinsky, P. P., Beardmore, A. P., Foster, A., et al. 2017, A&A, 597, A35
Predehl, P., Andritschke, R., Arefiev, V., et al. 2021, A&A, 647, A1
Rau, A., Schady, P., Greiner, J., Haberl, F., & Updike, A. 2010, ATel, 2704, 1
Reig, P. 2011, Ap&SS, 332, 1
Rolleston, W. R. J., Trundle, C., & Dufton, P. L. 2002, A&A, 396, 53
Sasaki, M., Haberl, F., & Pietsch, W. 2000, A&AS, 143, 391
Sasaki, M., Haberl, F., Keller, S., & Pietsch, W. 2001, A&A, 369, L29
Sasaki, M., Pietsch, W., & Haberl, F. 2003, A&A, 403, 901
Scargle, J. D. 1982, ApJ, 263, 835
Shakura, N., & Postnov, K. 2018, Proc. Sci., 288 (APCS2016), 040
Shakura, N., Postnov, K., Kochetkova, A., & Hjalmarsdotter, L. 2012, MNRAS, 420, 216
Shakura, N., Postnov, K., Kochetkova, A., & Hjalmarsdotter, L. 2018, Quasi-Spherical Subsonic Accretion onto Magnetized Neutron Stars, ed. N. Shakura (Berlin: Springer), 454, 331
Strüder, L., Briel, U., Dennerl, K., et al. 2001, A&A, 365, L18
Sturm, R., Haberl, F., Pietsch, W., et al. 2012a, A&A, 537, A76
Sturm, R., Haberl, F., Rau, A., et al. 2012b, A&A, 542, A109
Sturm, R., Haberl, F., Freyberg, M., Coe, M., & Udalski, A. 2013a, ATel, 4719, 1
Sturm, R., Haberl, F., Pietsch, W., et al. 2013b, A&A, 558, A3
Subramanian, S., & Subramaniam, A. 2009, A&A, 496, 399
Tatton, B. L., van Loon, J. T., Cioni, M. R. L., et al. 2021, MNRAS, 504, 2983
Townsend, L. J., Drave, S. P., Corbet, R. H. D., Coe, M. J., & Bird, A. J. 2011, ATel, 3311, 1
Treiber, H., Vasilopoulos, G., Bailyn, C. D., et al. 2021, MNRAS, 503, 6187
Tsujimoto, M., Imanishi, K., Yokogawa, J., & Koyama, K. 1999, PASJ, 51, L21
Turner, M. J. L., Abbey, A., Arnaud, M., et al. 2001, A&A, 365, L27
Udalski, A., Szymanski, M. K., Soszynski, I., & Poleski, R. 2008, Acta Astron., 58, 69
Udalski, A., Szymański, M. K., & Szymański, G. 2015, Acta Astron., 65, 1
van Jaarsveld, N., Buckley, D. A. H., McBride, V. A., et al. 2018, MNRAS, 475, 3253
Vasilopoulos, G., Haberl, F., Sturm, R., Maggi, P., & Udalski, A. 2014, A&A, 567, A129
Vasilopoulos, G., Haberl, F., & Maggi, P. 2017, ATel, 10 253, 1
Vasilopoulos, G., Maitra, C., Haberl, F., Hatzidimitriou, D., & Petropoulou, M. 2018, MNRAS, 475, 220
Verner, D. A., Ferland, G. J., Korista, K. T., & Yakovlev, D. G. 1996, ApJ, 465, 487
Wada, Q., Tsujimoto, M., & Ebisawa, K. 2012, ATel, 4628, 1
Wada, Q., Tsujimoto, M., Ebisawa, K., & Miller, E. D. 2013, PASJ, 65, L2
Wilms, J., Allen, A., & McCray, R. 2000, ApJ, 542, 914
Yokogawa, J., & Koyama, K. 1998, IAU Circ., 7009, 3
Yokogawa, J., Imanishi, K., Tsujimoto, M., Koyama, K., & Nishiuchi, M. 2003, PASJ, 55, 161

Manuscript 3

Appendix A: Electronic chopper

To reduce telemetry load, for example, when a very bright source is observed, part of the read-out frames recorded by the eROSITA cameras can be discarded from transmission. To do this, an electronic chopper is set to a value of n, which causes only every nth frame to be processed. This results in a reduction of the net exposure time by a factor of n, which needs to be considered by the ground software. In the eSASS pipeline version that processed the CalPV data that were publicly released[6], the correction for the chopper setting was applied twice, once to the good time interval extension, and once to the dead-time correction extension in the event files. Of the CalPV data used here, three observations in the LMC (Table 1) were affected by a chopper setting of 2 (part of the time, part of the cameras). As a workaround, we multiplied the dead-time values by 2 for the corresponding time intervals to finally obtain the correct exposure times, which were used to compute count rates and fluxes. The problem has been fixed in the eSASS software, and after a future re-processing of the data, the event files will have the correct extensions.

[6] https://erosita.mpe.mpg.de/edr

Declaration of contributions

Last Name, First Name: Dai Xiaohang

List of Publications

1. **Dai Xiaohang**, Kong L, Ji L, Zhou M, Shui Q, Wang P, Zhang S, and Santangelo A, 2024, *Astronomy & Astrophysics*, title: **Unveiling the rebrightening mechanism of GRS 1915+105: Insights from a change in the quasi-periodic oscillations and from a wind analysis**.

2. **Dai Xiaohang**, Kong L, Bu Q, Santangelo A, Zhang S, Ji L, Zhang S, and Yorgancioglu ES, 2023, *Monthly Notices of the Royal Astronomical Society*, title: **Evolution of disc and corona in MAXI J1348-630 during the 2019 reflare: NICER and Insight-HXMT view**.

3. Haberl F, Maitra C, Carpano S, **Dai Xiaohang**, Doroshenko V, Dennerl K, Freyberg MJ, Sasaki M, Udalski A, Postnov KA, and Shakura NI, 2022, *Astronomy & Astrophysics*, title: **eROSITA calibration and performance verification phase: High-mass X-ray binaries in the Magellanic Clouds**.

All authors of the papers participated in the discussion of the paper.

In publications (1) and (2), the author Dai Xiaohang is the first author and the main contributor, responsible for more than 80% of the scientific ideas, data generation, analysis, and interpretation, as well as almost all of the paper writing.

In publication (3), the author Dai Xiaohang is the fourth author, with the main contribution being in Chapter 5.4, including almost all scientific ideas, data generation, analysis, interpretation, and paper writing for this chapter.

I confirm that the above-stated is correct.

Date, Signature of the Candidate

I/We certify that the above-stated is correct.

Date, Signature of the Doctoral Committee or at least one of the members